UNIVERSITY OF SOUTHAMPTON

FACULTY OF ENGINEERING AND APPLIED SCIENCE

SCHOOL OF ENGINEERING SCIENCE

Thesis submitted for the Degree of Doctor of Philosophy

WEAR/CORROSION SENSING IN FLOWING SEAWATER

By Andrew James Speyer

November 2002

UNIVERSITY OF SOUTHAMPTON

ABSTRACT

FACULTY OF ENGINEERING AND APPLIED SCIENCE
SCHOOL OF ENGINEERING SCIENCE
Doctor of Philosophy

WEAR/CORROSION SENSING IN FLOWING SEAWATER

By Andrew James Speyer

Pipework for cooling and firefighting purposes in naval vessels is typically subject to corrosion by pumped seawater. Close to land, erosion by ingested sand also occurs. The expensive alloys presently used to resist corrosion do not resist erosion very well. There are requirements both to understand conjoint erosion and corrosion better and to develop improved materials. This Thesis examines the possibilities for using metal-on-steel claddings for this duty, and also the possibilities for the use of Electrochemical Noise techniques to evaluate their performance.

The literature is reviewed for relevant aspects of erosion, corrosion, their interaction ('synergy'), electrochemical methods, appropriate experimental equipment and the materials requirements for such claddings. It is concluded in the latter case that the key properties are that claddings should be as hard as possible and that, since porosity can never be wholly eliminated, that they should be anodic to the substrate (carbon steel).

For practical investigations, a series of model claddings have been used – HVOF spayed aluminium, aluminium/12%silicon alloy, a composite of this alloy with particulate alumina and hot-dipped zinc. Characterisation of the experimental composite showed it had high porosity; it also did not perform well in early tests, so its use was discontinued.

Erosion failure of the metal claddings was found to be entirely ductile, though the angular dependency of this was not classical; this was probably associated with the relatively dense slurries used. Corrosion behaviour under static conditions was heavily influenced by the deposition of solid corrosion deposits, especially in pores in the cladding, and by the aeration of the corroding solution.

Flow corrosion and erosion-corrosion were examined in a newly built test rig, specially adapted for electrochemical measurements. Zinc claddings were found to suffer severely from flow corrosion; aluminium-based claddings do not. Neither metal performs very adequately under erosion-corrosion conditions; hardening by alloying or composite formation will be required in practical systems, as will be protection against pitting.

Simple erosion is non-Faradaic, so direct prediction of mass loss by electrochemical means is not possible where this process dominates. However, in brine pitting occurs and impacts cause depassivation/repassivation events. These can be monitored using Electrochemical Noise techniques. A new application of the wavelet transform allows separation of these effects, and a preliminary quantitative understanding of how the chloride inhibition of impact scar repassivation can result in increased corrosion..

Proposals are made as to how this work may be further developed, in terms of more realistic materials, improved experimental technique and better data analysis.

CONTENTS

LIST OF FIGURES

LIST OF TABLES

NOMENCLATURE

A unified nomenclature has been used for this Thesis, set out below. This implies that the symbols used in some papers quoted from the literature are not the same as those in the original papers. While an effort has been made to retain the symbols most commonly used for important quantities, the interdisciplinary nature of this work has meant that this has not always been possible.

a,b,c… are used for uncharacterised constants in various equations.

j is used for $\sqrt{-1}$.

x,y… are used for uncharacterised variables in various equations.

- Suffix n is used to denote the nth value of x.
- Suffix r is used to denote a lag in x.

θ is used as an uncharacterised angle in various equations.

A	Autocorrelation function	(None)
A_0	Normalised autocorrelation function	(None)
A_r	Autocorrelation function for lag r	(None)
A_{scar}	Scar area	(m^{-2})
a_n	Noise amplitude	(μA)
C	Capacitance	(Farads)
C_B	Material constant, from density and elastic load limit (Bitter)	($kg^{-1}.m^{0.5}.s^{2.5}$)
C_{dl}	Double layer capacitance	(Farads)
C_{pass}	Passivation layer capacitance.	(Farads).
c_p	Specific heat at constant pressure	($J.kg^{-1}.K^{-1}$)
D	Diffusion coefficient	($m^2.s^{-1}$)
d_p	Diameter of particle	(m)
d_j	Diameter of jet	(m)
d_n	Wavelet detail number n	(None)

E	Electrochemical Potential	(V)
E_p	Polarised potential	(V)
E_{corr}	Corrosion potential	(V)
E_{rest}	Rest potential	(V)
E_M	Dimensionless erosion rate (mass removed/mass impacting)	(None)
E_k	Particle energy/nominal impact	(μJ)
$E(t)$	Free corrosion potential	(V)
F	Faraday's constant	($C.mol^{-1}$)
f	Fanning friction factor	(None)
f_p	Pulse repetition frequency	(s^{-1})
f_s	Sampling frequency	(s^{-1})
H_V	Vicker's Hardness	($kg.mm^{-2}$)
h	Pulse height	(μA)
h_j	Stand-off distance of jet from plate	(m)
h_T	Heat transfer coefficient	($J.m^{-2}.s^{-1}.K^{-1}$)
I	Current density	($A.m^{-2}$)
I_{anodic}	Current density on anode	($A.m^{-2}$)
$I_{cathodic}$	Current density on cathode	($A.m^{-2}$)
I_{corr}	Corrosion current density	($A.m^{-2}$)
I_{pore}	Current density in pore	($A.m^{-2}$)
I_{lc}	Local current density	($A.m^{-2}$)
I_0	Exchange current density	($A.m^{-2}$)
i	Current	(A)
i_{pore}	Pit current	(A)
h_{jet}	Stand-off distance of jet	(m)
l	Depth of particle contact (Finnie).	(m)
l_{corr}	corrosion rate	($m.s^{-1}$)
k	Thermal conductivity	($J.m^{-1}.s^{-1}.K^{-1}$)
K_F	Ratio of vertical to horizontal force components (Finnie, Bitter)	(None)
Ku	Kurtosis	(None)
M	Mass loss	(kg)

M_B	Mass loss in flowing 'brine' (this work)	(mg)
M_{B+S}	Mass loss in flowing 'brine/sand' (this work)	(mg)
M_T	Total mass loss	(kg).
M_E	Mass loss due to erosion	(kg)
M_{MEM}	Order parameter (filter length), Maximum Entropy Method	(None)
ΔM_E	'Synergistic mass loss', effect of corrosion on erosion rate (Stack)	(kg)
M_C	Mass loss due to corrosion	(kg)
ΔM_C	'Additive mass loss', effect of erosion on corrosion rate (Stack)	(kg)
M_S	Mass loss due to synergy effect	(kg)
M_W	Mass loss in flowing 'water' (this work)	(mg)
M_{W+S}	Mass loss in flowing 'water/sand' (this work).	(mg).
m	Particle mass	(kg)
N	Number of data points	(None)
N_x	Number of data points in range $x \pm W/2$	(None)
n	Velocity exponent	(None)
n_m	Number of moles of substance	(mol)
P	'Power' or data variance ($= \sigma^2$)	((as data)^2))
P_{xx}	Power Spectral Density	((as data)^2/Hz)
p	Particle radius exponent.	(None)
Pr	Prandtl Number	(None)
q_{conv}	Convective energy flux	(J.s^{-1})
r	Radius of particle	(m)
r_{pore}	Pore radius	(m)
r_j	Radial distance from stagnation point	(m)
R	Resistance	(Ohms)
R_a	Surface flatness	(μm)
R_{ct}	Charge transfer resistance	(Ohms)
R_{pol}	Polarisation resistance.	(Ohms)
R_N	Noise Resistance.	(Ohms)
R_{soln}	Solution(cell) resistance	(Ohms)
R_0	Gas constant	(J.K^{-1})

Re	Reynolds Number	(None)
r^2	Correlation coefficient	(None)
Sc	Schmidt Number	(None)
Sh	Sherwood Number	(None)
St	Stanton Number	(None)
Sk	Skewness.	(None)
$Syn\text{-}E$	Electrochemical synergy (this work)	(A)
$Syn\text{-}M$	Mass loss synergy (this work)	(mg)
T	Temperature	(^{0}C)
T_K	Absolute temperature	(K)
t	Time	(s)
t_p	Length of synthetic pulse train	(s)
V	Volume	(m^3)
V_s	Volume of impact scar	(m^3)
V_u	Volume removed by single particle impact	(m^3)
V_{ud}	Volume removed by single particle impact, by deformation (Bitter)	(μm^3)
V_{uc1}	Volume removed by single particle impact, by cutting, $\alpha < \alpha_0$	(μm^3)
V_{uc2}	Volume removed by single particle impact, by cutting, $\alpha > \alpha_0$	(μm^3)
v	Velocity	($m.s^{-1}$)
v_e	Maximum velocity for purely elastic impact	($m.s^{-1}$)
v_{el}	Impact velocity at which the elastic limit is just reached. (Bitter)	($m.s^{-1}$)
W	Bandwidth	(None)
w	Pulse width	(s)
x	Co-ordinate parallel to surface (Finnie)	(m)
x_t	x position at time t. (Finnie)	(m).
y	Co-ordinate normal to surface (Finnie)	(m)
y_{pore}	Pore depth.	(m)
y_t	y position at time t. (Finnie)	(m).
Z	Impedance	(Ohms)

α	Angle of impact (measured from plane of surface)	(^{0})
α_A	Anodic transfer coefficient	(None)
α_C	Cathodic transfer coefficient	(None)
α_0	Critical angle of impact when particle horizontal exit velocity $\rightarrow$ 0.	(^{0})
δ_{max}	Maximum scar depth	(μm)
ε_B	Deformation wear factor (Bitter)	($J.m^{-3}$)
ε_p	Plastic true strain	(None)
η	Overpotential	(V)
μ	Mean value of data	(As data)
μ_v	Absolute viscosity	(Pa.s)
ν	Kinematic viscosity	($m^2.s^{-1}$)
ρ	Density	($kg.m^{-3}$)
ρ_B	Integrated product of stress and strain (Bitter)	(Pa)
σ	Standard deviation	(As data)
σ_V	Standard deviation of potential	(V)
σ_I	Standard deviation of current	(A)
τ_w	Wall stress	(Pa)
σ_p	Plastic flow stress on impact (Finnie, Sundararajan)	(Pa)
ψ	Ratio of depth of contact (l) to depth of cut (y_t) (Finnie)	(None)

ACKNOWLEDGEMENTS

I am grateful to the Ministry of Defence, and particularly their representative, Mr Keith Stokes ([dstl]), for financial support and for the basis of this project.

I am grateful also to Dr Robert Wood for his supervision of this work, and his persistence in the face of an industrial person, incorrigibly non-academic.

I am particularly grateful to Mr Stephen Pilcher, who built the erosion-corrosion test rig, without which this work would not have been possible, and to my colleagues, especially Dr Julian Wharton and Mr K.S. Tan, for their advice, encouragement and general cheerfulness.

1 INTRODUCTION

Background

Naval ships contain pipework, carrying seawater for such purposes as firefighting and cooling items of machinery. Because seawater is corrosive, expensive alloys are currently used for this duty. However, if a ship is situated over a sandbank, sand may be pumped in along with the water. Although filters are used, fine sand passes through and erodes the pipes' internal surfaces, the alloys used not being particularly resistant to erosion. The conjoint action of corrosion and erosion is termed erosion-corrosion. An example is shown in Figure 1.1. It is desired to improve the understanding of the processes of erosion-corrosion in this context, and to identify materials that will resist these conditions. Preferably, for cost reasons, this should be a coating on carbon steel. This Thesis investigates the possibilities for the use of metallic coatings on steel, and develops methods for characterising their degradation.

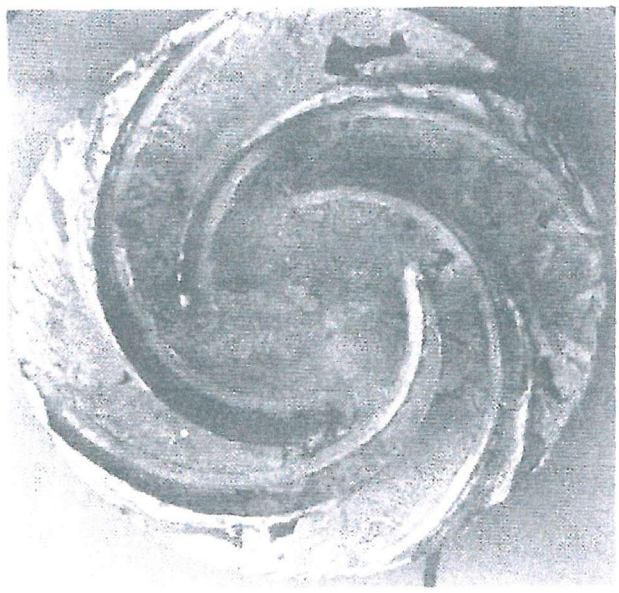

Figure 1.1: Erosion-corrosion on a pump impeller.
From: G.A. Minick and D.L. Olsen, Metals Handbook, 9th Edition, Volume 13, ASM International, 1987.

Objectives

The objectives of this work have been:

- To investigate materials issues of metal-on-steel coating systems for slurry corrosion duties.

- To develop equipment suitable for investigating such systems.

- To investigate synergies between erosion and corrosion in sand/seawater slurries.

- To investigate the application of advanced signal processing techniques to Electrochemical Noise data from slurry-erosion studies, to characterise degradation.

Scope of Thesis

Erosion-corrosion work encompasses a very large number of possible variables. To make this situation manageable, the work in this Thesis has been limited as follows:

- The basic principles governing materials choice for this duty have been assessed on the basis of literature review; some possible candidate materials have been identified by the same means. Practical work has been limited to the investigation of model materials.

- The liquid used has been either water or a 3.5% solution of sodium chloride in water (hereafter referred to as 'brine'), rather than real seawater. Therefore, complexities due to calcareous scaling or biofouling have been avoided.

- Mass loss has generally been limited to situations where the coating is not perforated, in order to characterise the coating performance. Actual behaviour at breakdown is not covered.

- Most variables have been limited to one or two values only. In particular, in the erosion-corrosion work, only one slurry density has been used, only one chloride concentration and all experiments have been carried out under fully aerated conditions at one flow velocity and at ambient temperature. Cathodic protection has not been investigated. The implications of these limitations, are, however, discussed.

Structure of Thesis

The literature is reviewed in Section 2 for significant aspects of the science. This is done under the heads; Erosion, Static corrosion, Corrosion under Flow conditions, Electrochemical Methods, Equipment and Metal Claddings for Erosion-Corrosion Protection. Conclusions are drawn from this review.

Section 3 describes sample preparation and characterisation.

Sections 4 and 5 describe preliminary erosion and (static) corrosion experiments carried out separately, to obtain baseline data for further investigation of the combined effects, to develop suitable methods and to characterise equipment (particularly, electrochemical equipment).

Section 6 describes the main experimental part of this work. Design and construction of a new test rig is described. Various experimental difficulties encountered, and the means used to control/allow for these are reviewed. An experimental program is defined, and the results obtained from this reported and discussed, under the heads: Appearance of samples, Mass loss and Electrochemical Noise data. Particular conclusions are noted, by Section.

Sections 7 and 8 summarise Overall Conclusions and make proposals for Further Work.

References are collected in Section 9.

Associated Publications

- A.J. Speyer, R.J.K. Wood, K.R. Stokes and A.J. Sturgeon, "Corrosion of aluminium-based coatings for use in marine pipework", presented at *Eurocorr 2000,* London, 2000, [1].

- A.J. Speyer, R.J.K. Wood and K.R. Stokes, "Erosion of aluminium-based claddings on steel by sand in water", presented at *Wear of Materials,* Vancouver 2001; published in *Wear,* 250 (2001), 802-808, [2].

- R.J.K. Wood, J.A. Wharton, A.J. Speyer and K.S. Tan, "Investigation of erosion-corrosion processes using electrochemical noise measurements", *Tribology International,* 35, (2002), 631-641, [3].

- R.J.K. Wood and A.J. Speyer, "Erosion-corrosion of Marine Coatings", to be submitted to a special Tribo-corrosion issue of *Wear* (2002), [4].

2 LITERATURE REVIEW

2.1 EROSION

2.1.1 Introduction

Erosion is defined to be wear caused by hard particles striking a surface, carried by a gas stream or entrained in a flowing liquid [5].

The response of solid bodies to impact has been a matter of scientific interest at least since the time of Thomas Young [6], better known for his work on Optics. As noted by Lord Rayleigh [7], Young in 1807 pointed out that:

> "There is, however, a limit beyond which the velocity of a body striking another cannot be increased without overcoming its resilience and breaking it, however small the bulk of the first body may be, and this limit depends on the inertia of the parts of the second body, which must not be disregarded when they are impelled with a considerable velocity."

Rayleigh used a form of dimensional analysis to show that the relative sizes of the two bodies do not matter, so this observation is pertinent to the erosion of extended solid bodies by sand-blasts or slurries. He also noted that the behaviour might be dependent on strain rate as well as strain magnitude.

Young and Rayleigh both seem to have envisaged solid wastage under erosion as resulting from a mechanism akin to cavitation in liquids. Further consideration of how erosion actually occurs has had to wait for more than another half century.

Erosion of solid surfaces by slurries is an extremely complex phenomenon, and has attracted a large literature. Detailed reviews exist [8,9]. More specifically, Meng and

Ludema [10] have reviewed more than 28 erosion models with over 100 variables and constants – their principal conclusions were that no general quantitative models exist and that there is no convergence of thought regarding the general form an erosion model should have. Partly this is because there is no general agreement as to the precise meaning of terms, and partly because many of the material properties used in equations are interdependent. Hardness is the most widely used variable, but is clearly not the only important factor.

The present review will limit itself to a qualitative discussion of issues relevant to the characterisation of erosion-corrosion under jet impingement conditions.

Variables involved in slurry erosion may be listed (adapted from [8]):

Slurry Parameters:

Liquid:

Viscosity, density, surface tension, composition, corrosivity, aeration

Particles:

Size, shape (angularity), density, brittleness, relative hardness, concentration, degradation

Flow Field:

Relative velocity, angle of impingement, particle impingement efficiency, boundary layer, particle/particle interactions, particle drop-out, turbulence intensity

Target parameters:

Bulk Properties:

Ductility or brittleness, hardness and toughness, melting point, microstructure

Surface Properties:

Roughness, work hardening (shot peening effect), corrodibility, oxide and other corrosion surface layers (including biofouling)

Coatings:

Type, mode of application, bonding to substrate, thickness, porosity/permeability, degradation

System parameters:

Overall system geometry

Temperature/Pressure

2.1.2 Early Work

I. Finnie

The earliest clear discussion of erosion phenomena was made by Finnie in 1960 [11].

As he pointed out, the prior literature was mostly of a purely practical nature, with little consideration of fundamental behaviour. The only useful observation, made by Wellinger [12] was that results could vary with angle of impingement – under bombardment by quartz sand in air, soft steels eroded faster than hard ones at glancing angles of impingement, reflecting field experience of wear in pipes; conversely, at normal incidence, as used by previous investigators, there was little difference.

Finnie first of all considered fluid flow conditions. He recognised clearly that:

> "The erosion of a surface by abrasive particles in an inert fluid should depend on the number of particles striking the surface, their velocity and their direction relative to the surface. These quantities are largely determined by the flow conditions."

Turbulence can promote erosion, so surface finish is an important parameter, as is the overall system geometry. So is erodent particle size (and shape). Furthermore, particle velocity is not necessarily the same as fluid velocity, owing to the interplay of drag and inertia effects. The effects of particle velocity and impact angle are, therefore, not at all clear, as the real values of these quantities are not easily recovered from experiments. Finnie satisfied himself that for small particles in air, the particle velocity is likely to be only a small fraction of air velocities under bench-top test conditions (larger scales are necessary for these experiments). He did not do the corresponding calculations for particles in water, but one would expect that relatively increased drag forces would lead particles to more nearly follow liquid streamlines. How this applies to particular situations in practice is a key issue for the understanding of erosion (and erosion-corrosion) phenomena.

Finnie made a clear-cut distinction between ductile materials on the one hand and brittle materials on the other.

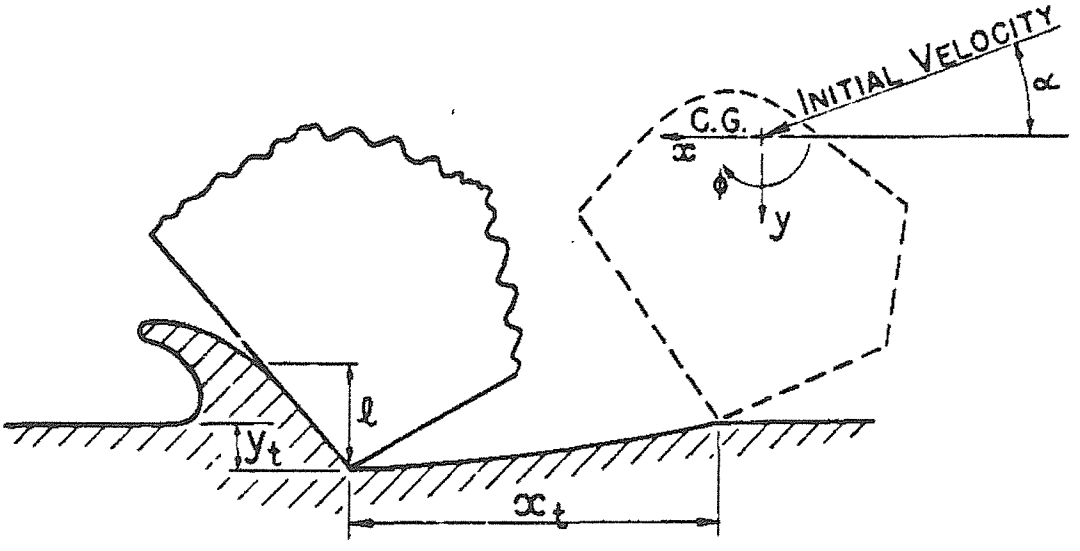

Figure 2.1: Geometry of microcutting by impacting particle
From I. Finnie, *Wear* 3 (1960), 87-103

For ductile materials, erosion is by a process of microcutting. The geometry envisaged is as Figure 2.1, taken from [11]. Consideration of the equation of motion for the particle leads to the following expressions for the volume of material removed from the target (regarded as the product of the area swept out by the particle tip and the width of the cutting face):

$$V_u = \frac{mv^2}{p\psi K_F}\left(\sin 2\alpha - \frac{6}{K_F}\sin^2\alpha\right) \quad \text{if} \quad \tan\alpha \le \frac{K_F}{6} \qquad (2.1)$$

$$V_u = \frac{mv^2}{p\psi K_F}\left(\frac{K_F \cos^2\alpha}{6}\right) \quad \text{if} \quad \tan\alpha \ge \frac{K_F}{6} \qquad (2.2)$$

where V_u is the volume of material removed by a single impact (m^3).

m is the particle mass (kg).

v is the particle velocity ($m.s^{-1}$).

p is the plastic flow stress immediately on impact ($N.m^{-2}$).

ψ is the ratio of the depth of contact l to the depth of cut y_t

(taken as 2, by analogy with metal cutting experiments)

K_F is the ratio of vertical to horizontal force components.

α is the angle of impact.

The first equation, for lower angles, predicts behaviour when the particle leaves the surface still cutting; the second, for higher angles, predicts behaviour when the particle comes to rest during the cutting operation.

Figure 2.2, from [10], shows how these equations predict a peak in volume removal at relatively small angles, typically 20°-30°. Also shown are experimental data from erosion of copper, AISI 1020 steel and aluminium by angular silicon carbide grains entrained in air

Figure 2.2 shows two things. Firstly it shows that the theory correctly predicts the low angle peak in erosion for ductile metals, with close to the experimental angle for peak erosion. Secondly, it shows that, while the theory predicts zero erosion at normal incidence, in reality quite significant levels of erosion occur. Any theory which depends only on the effects of a component of velocity parallel to the surface is bound to be inadequate at normal incidence – some other mechanism must be present to account for normal incidence erosion.

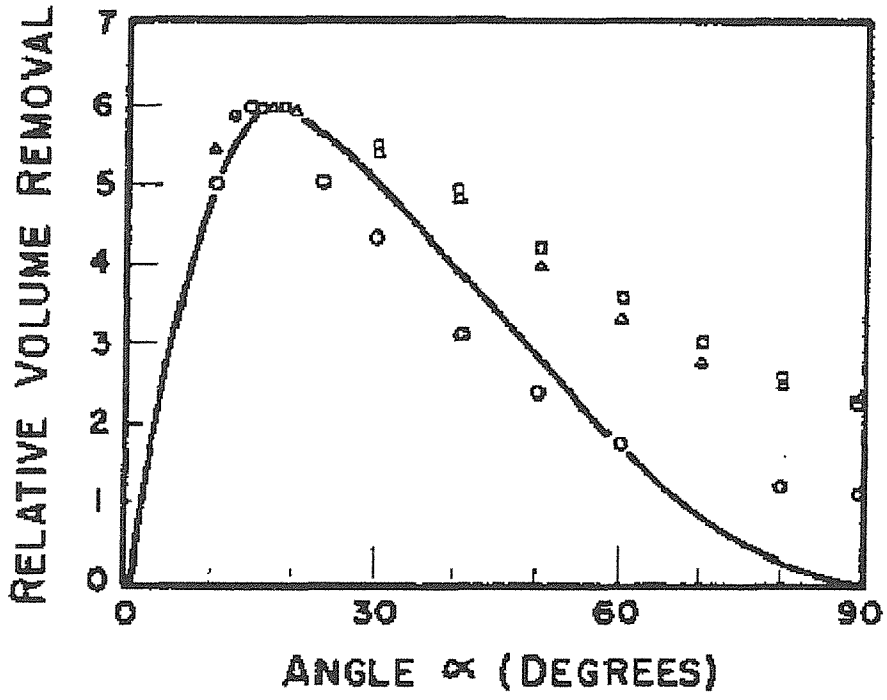

Figure 2.2: Predicted variation of volume removal with angle for a single abrasive grain (solid line). Experimental points for erosion by many grains are plotted so that the maximum erosion is the same in all cases.

(Δ copper, □ AISI 1020 steel, O aluminium)

From: I. Finnie, *Wear* 3 (1960), 87-103

Finnie's equations also predict a linear dependence on kinetic energy (or, equivalently, a 'velocity exponent' of 2). For the particular test conditions Finnie used - erosion of AISI 1020 steel by angular silicon carbide in air at 20° incidence,

particle velocities being determined photographically – this relationship was closely observed.

Finnie observed also that sharp particles cause more erosion than round ones, that particle hardness only matters in a gross sense (particles are either harder than the target, in which case excess hardness does not make any difference, or softer than the target, in which case little erosion occurs) and that weak particles may shatter rather than cause erosion (independent of hardness).

Analysis of the erosion of brittle materials was much less satisfactory. Qualitatively, mass loss occurs as a result of the formation of cracks, and their subsequent intersection. The latter depends on how cracks propagate within the material. Initial cracking may be predicted for elastic impact by spherical erodents by using Hertzian stress analysis [5], but further cracking and mass loss cannot be easily modelled. Experimental work showed that mass loss peaked at near normal incidence (with a lot of scatter in the data), and that 'velocity exponents' around 6.5 were obtained, quite different from the ductile erosion case.

Overall, Finnie's work is important in identifying most of the important parameters in erosion situations, and in modelling the erosion of ductile materials at low impingement angles. It is unsuccessful at modelling ductile erosion at normal incidence, or brittle erosion, other than qualitatively, under any conditions.

Subsequent work can be seen as elaborating the successful parts of Finnie's work and trying to resolve the difficult areas.

J.G.A. Bitter

The most important single contribution subsequent to this has been made in a pair of papers by Bitter [13,14].

Bitter distinguished two modes of erosion; one by repeated deformation leading to pieces of material breaking loose, the other caused by the cutting action of the erodent. In practice these wear modes occur together.

For deformation wear only, Bitter derived equation (2.3):

$$V_{ud} = \frac{1}{2}\frac{M(v\sin\alpha - v_e)^2}{\varepsilon_B} \qquad (2.3)$$

where V_{ud} is the volume eroded by deformation (m^3).
M is the total mass of impinging particles (kg).
v is the velocity of particles before collision ($m.s^{-1}$).
v_e is the maximum velocity for purely elastic impact ($m.s^{-1}$).
α is the impingement angle
ε_B is a deformation wear factor, i.e. the amount of energy required to remove unit volume of material by this mechanism ($J.m^{-3}$).

Equation (2.3) says that the volume removed depends on the kinetic energy of the erodent stream, less an allowance for the elastic deformation, which does not result in wear.

v_e is closely related to the elastic load limit of the material near its surface, hence its hardness. Continuous deformation of the surface leads to local work hardening, and it is important that it is the hardness close to the surface (as, for example, measured on a section of the sample) that is considered, rather than the bulk hardness. Also, the work hardness of the surface takes time to develop, so experiments should be allowed to run for long enough for this not to be an issue.

ε_B is the energy required to remove unit volume of target. This is only partly deformation energy; some of it may relate to recrystallisation and to formation of new surface area. For brittle materials there is no deformation and failure of homogeneous

materials, e.g. glass, is by cracking. According to Bitter, the cracks occur in such a way that ε_B is proportional to the square of the elastic load limit divided by Young's modulus for the material. Similarly, for cements (i.e. brittle particles in a brittle binder) the particles are dislodged whole and it is the elastic load limit and Young's modulus of the binder only that are important in this case.

For metals, deformation wear is always associated with cutting wear. This is the situation considered by Finnie. Bitter gives a somewhat more elaborate analysis, leading to the two equations:

$$V_{uc1} = \frac{2MC_B(v\sin\alpha - v_e)^2}{\sqrt{v\sin\alpha}}\left(v\cos\alpha - \frac{C_B(v\sin\alpha - v_e)^2}{\sqrt{v\sin\alpha}}\rho_B\right) \qquad (2.4)$$

when $\alpha \leq \alpha_0$, and:

$$V_{uc2} = \frac{1/2Mv^2\cos^2\alpha - K_F(v\sin\alpha - v_e)^{3/2}}{\rho_B} \qquad (2.5)$$

when $\alpha \geq \alpha_0$

where the nomenclature is as in the previous equation, except that:

V_{uc} is the volume eroded by cutting (m^3).
C_B is a material constant, which depends on the density and the elastic load limit ($kg^{-1}.m^{0.5}.s^{2.5}$).
ρ_B is the integrated product of stress and strain (cutting wear factor)(Pa).
α_0 is the angle at which the horizontal component of velocity just becomes zero as the particle leaves the body; this is the same condition as used by Finnie.

For the case: $\alpha \geq \alpha_0$, it can be shown that the treatments of Finnie and of Bitter are essentially identical.

For the case: $\alpha \leq \alpha_0$, Bitter considers the role of elastic forces (neglected by Finnie) in ejecting the erodent particle and obtains a more complicated equation: however, he claims that v_e, C_B are constants of the target material, whereas Finnie's ψ and K_F are variables, strongly dependant on angle. Bitter's equation should therefore be more useable in practice.

Erosive wear is the sum of deformation wear and cutting wear, and Bitter shows evidence to show that his theory successfully accounts for the finite wear that occurs in ductile materials at 90^0 impact, unlike Finnie's.

2.1.3 Nature of Fluid.

Fluid considerations fall into two groups, relating to physical and chemical properties.

Physical properties such as density and viscosity mainly affect particle behaviour in the flow field and will be dealt with under that heading (Section 2.1.5). The major distinction is between gas phase erosion (not discussed in detail in this review), where particle-fluid interactions are relatively small, and liquid phase (particularly aqueous) erosion where particle trajectories are strongly influenced by the liquid flow field.

Chemical properties affect corrosion behaviour and erosion-corrosion synergy and will be dealt with under those heads (Section 2.2 and 2.3). Both impacting particles and target materials need to be considered under this head.

2.1.4 Nature of Impacting Particles

The key parameters here are size, shape, hardness/softness, strength and concentration in the fluid/particle-particle interactions.

Lin and Shao [15] found, using quartz sand in water to erode a variety of targets, that erosion rate rises rapidly with erodent size in the range 80-250 μm; also the impingement angle for peak erosion shifts to lower values with increasing grit size. This is consistent with Finnie's predictions. These authors also found a regular transition in erosion behaviour over a range of materials from pure aluminium (very ductile) to glass (brittle), as illustrated in Figure 2.3.

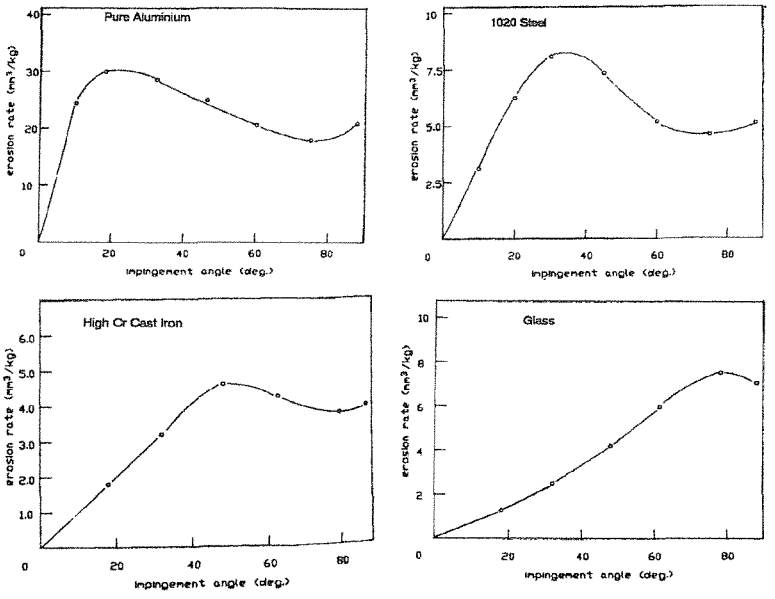

Figure 2.3: Trends in peak erosion angle with ductility/brittleness.
From: F. Lin and H. Shao, *Wear*, 141 (1991), 279-289

These results clearly show a regular trend in behaviour as one goes from predominately ductile to predominately brittle, as predicted by Bitter but not by Finnie. Note also that for the most brittle material (glass) peak erosion occurs at about 80°, not at normal incidence; the reason for this is not understood.

Lynn *et al* [16] made a particular study of particle size effects, using silicon carbide abrasives in oil to erode API P110 casing steel in a slurry pot. They found that in

their system, for particles larger than about 100 μm, mass loss was proportional to the dissipation of kinetic energy. However, for smaller particles both the collision efficiency (i.e. the ratio of the number of particles striking unit area of surface in unit time to the number of particles within the volume of the suspension sweeping that area in unit time) and the impact velocity decreased with decreasing size. This is largely due to flow field effects (see below, Section 2.1.5) resulting in very fine particles in a dense medium being swept away from the target surface without ever contacting it. It is asserted also that small particles lack the energy to rebound from the surface after impact, accumulate in the boundary layer and that these particles then make multiple impacts with the surface, thus enhancing the erosion rate; some evidence is adduced to support this view, in the shape of calculated *vs* measured erosion rates as a function of particle size. In some ways this conclusion is surprising, since collisions within a particle-laden boundary layer should redistribute the energy of the most energetic (most erosive) particles impacting on it. It would be interesting to know how experimental erosion rates for fine particles varied as a function of slurry concentration, but this experiment seems not to have been carried out.

It is common experience in slurry erosion work [5,11] that particle shape is important. Sharp particles are more erosive than rounded ones, so that, if slurries are recycled, their erosivity decreases [17]. Nevertheless, little systematic work has been carried out on the effects of particle shape, possibly due to the difficulty of defining particle shape. A possible approach by Stachowiak [18] has been to attempt to define the angularity of projections; some success has been claimed for this, so long as the erodent particles are not agglomerates (do not have low fracture toughness). The qualitative effect is clearly due to energy transfer from the impacting particle to the target being concentrated in a smaller area resulting in higher impact pressures.

2.1.5 Flow field considerations

The flow field in dilute slurries.

Benchaita *et al* [18] have considered in detail the fluid dynamics of the erosion of a metallic plate by solid particles entrained in a liquid jet, in air. The system investigated was sand in water (at very low concentrations, to minimise particle/particle interactions), impinging normally (vertically downward) on a copper plate. The plate had been machined to a surface finish of 1 μm before testing and therefore contained some surface strain. Erosion profiles typically of the 'W' shape indicated in Figure 2.4 were obtained. Note the central maximum, and the flanking minima outside the width of the impinging jet, i.e. the maximum erosion is displaced laterally from the stagnation point, directly beneath the jet.

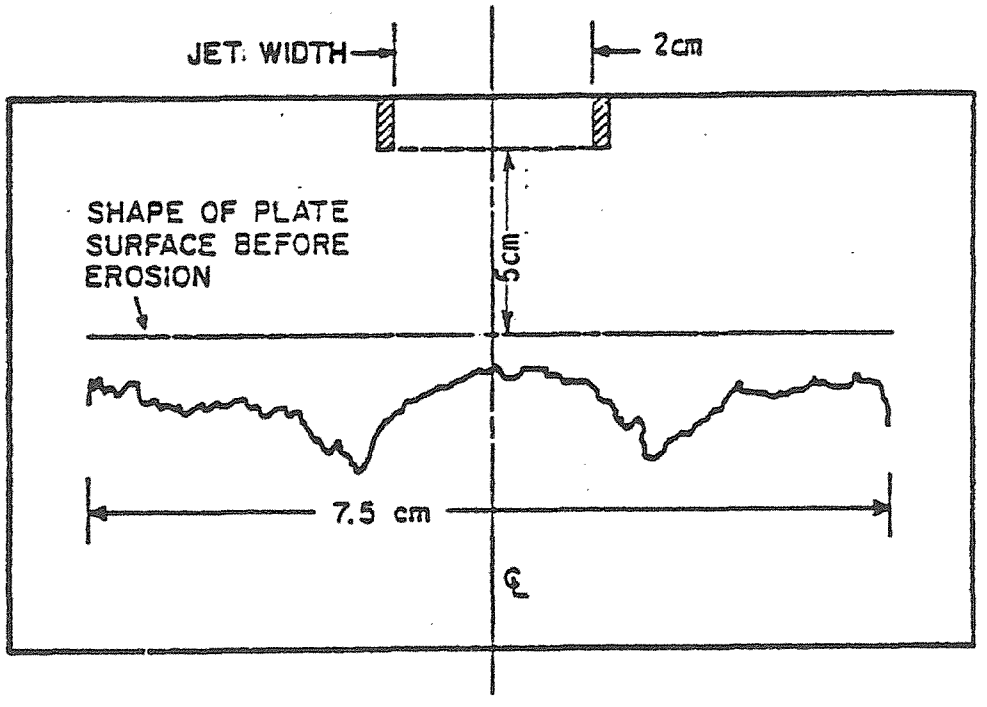

Figure 2.4: Wear profile of sand in water impinging normally on copper plate. From Benchaita *et al*, "Erosion of a metallic plate by solid particles entrained in a liquid jet", *J. Eng. Ind* 105 (1983), 215-227

The procedure used to model this was to:

a) Evaluate the liquid velocity distribution in the absence of particles.
b) Determine the erodent trajectories within the jet
c) Apply a suitable erosion model, first to one impact only, then summing over all impacts.

To evaluate the liquid flows, laminar inlet and exit flows were assumed, with a transition region between them in which vertical flow decreased linearly to rest, while horizontal flow increased linearly from rest at the stagnation point (the symmetrically central point on the plate surface, away from which all horizontal flow occurs). The geometry is shown in Figure 2.5. A boundary layer develops, but is calculated to be thin, relative to the dimensions of the erodent particles used in this study, and may therefore be neglected. Note that this may not always be true – calculation of boundary layer thickness depends on a 'flow parameter', not defined in this paper, and quite small changes in this parameter could make the boundary layer significant.

Once the liquid flow pattern is established, particle trajectories can be calculated by momentum analysis, i.e. by balancing inertial and drag forces. The latter are related to Reynolds Numbers (in this case for spherical particles – assumed for simplicity of calculation and not necessarily realistic). The differential equations of motion are non-linear and must be solved numerically. It is found that large particles are little affected by the flow and strike the plate at near normal incidence, small particles are carried by the flow out of the system without impact; it is only a range of particles of intermediate sizes that have intermediate trajectories and strike the plate at shallow angles and peripheral sites. Figure 2.6 shows this for particles initially on the central axis. For particles of intermediate size, the behaviour is influenced by how far off the central axis the particle was when it left the jet, as shown for a particular case in Figure 2.7.

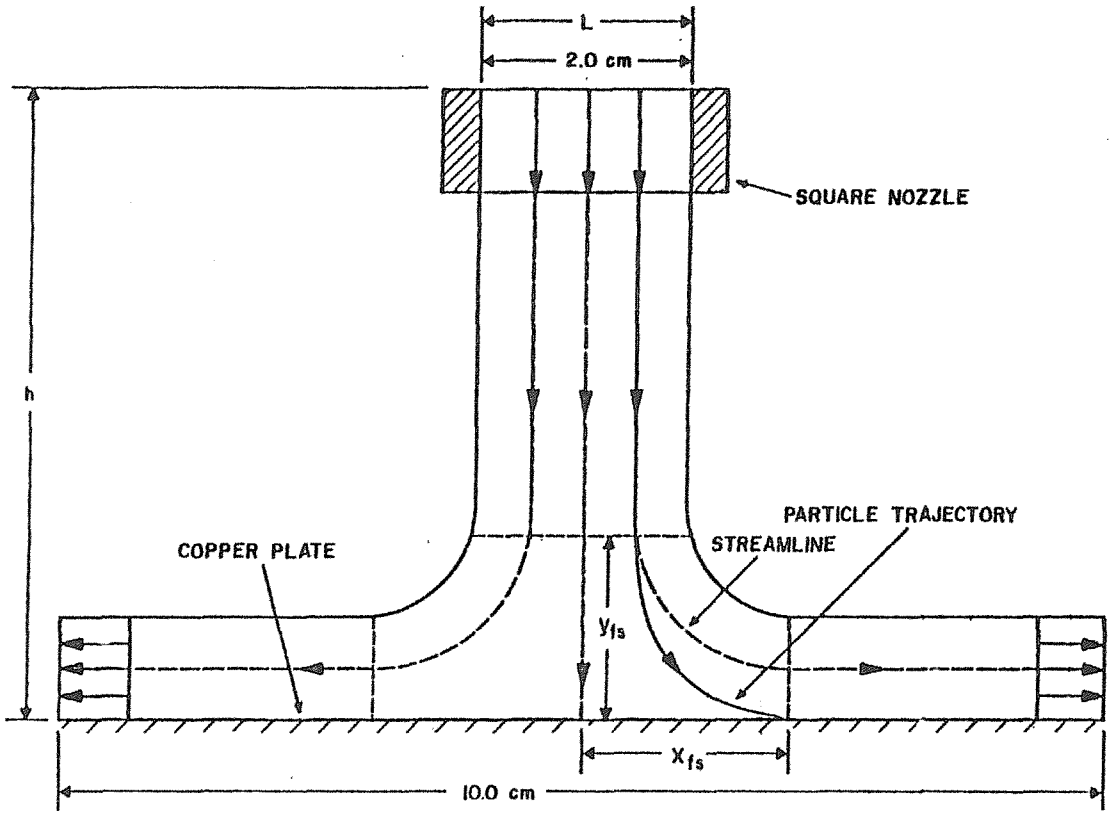

Figure 2.5: Geometry of normally impinging jet
From Benchaita *et al*, "Erosion of a metallic plate by solid particles entrained in a liquid jet", *J. Eng. Ind* 105 (1983), 215-227

The particular numerical conclusions reached in this paper reflect the particular situation studied; what is important is the methodology and the general trend of the results.

Having established the particle trajectories, it remains to describe the consequences of impact. Essentially here Benchaita *et al* follow Finnie [11], though they spell out the assumptions more clearly:

- the erodent particle is rigid (or harder than the target material)
- the erodent particle impinges with a sharp edge, rather than with a flat face

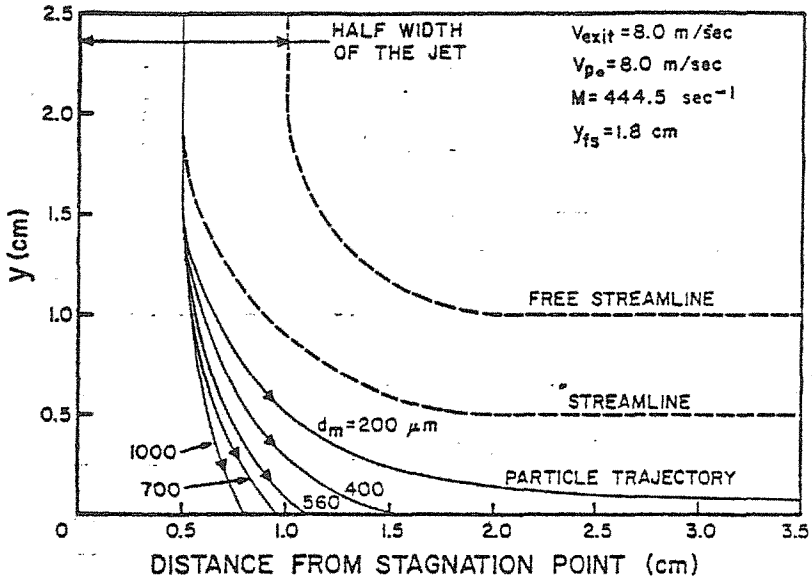

Figure 2.6: Particle trajectory as a function of particle size.
From Benchaita *et al*, "Erosion of a metallic plate by solid particles entrained in a liquid jet", *J. Eng. Ind* 105 (1983), 215-227

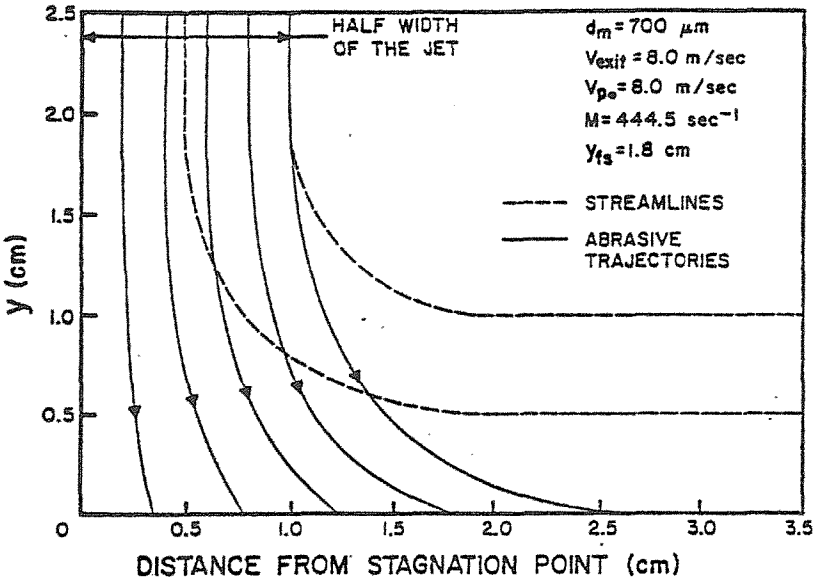

Figure 2.7: Intermediate size particle trajectory as a function of starting position.
From Benchaita *et al*, "Erosion of a metallic plate by solid particles entrained in a liquid jet", *J. Eng. Ind* 105 (1983), 215-227

- any oxide or other layer at the surface may be neglected.
- the target deforms entirely plastically.
- all motions are two dimensional.
- boundary layer, vorticity and other secondary flow effects may be neglected.

Since Benchaita *et al* follow Finnie in this part of the analysis, their results have the same defect of incorrectly predicting zero erosion at the stagnation point; the micro-cutting mechanism cannot be the only one.

The erosion distribution over the plate is taken to be the sum of all the individual impact effects. This is calculated numerically for given flow rates and erodent sizes. It is anticipated that the result will overestimate erosion, because the calculation neglects:

- work hardening of the surface
- particle shape and orientation at impact (sharp edge leading?)
- squeeze layer effects
- the possibility that it may take more than one impact to detach material from the target

The eventual result of this calculation is a calculated erosion profile. It is found to be in qualitative agreement with experiment, and calculated values for the position of maximum erosion depth relate reasonably well to real values. However, the experimental erosion scar is distinctly sharper than that calculated, and, contrary to calculation, erosion does take place at the stagnation point (evidently by a mass removal mechanism not considered by this paper).

This paper has been considered at some length, since further work would have to follow essentially the same methodology, allowing for different geometries and attempting to allow for the complexities noted but not allowed for in this treatment.

It may also be noted that the erosion scar itself, once developed, alters the geometry of the system, both in terms of overall shape and also the target surface roughness. Moreover, this effect will vary across the erosion scar, and so will be non-uniform in space as well as in time; perhaps this complexity accounts for the fact that this consideration appears not to have been addressed in this paper or elsewhere.

Dense slurries.

The bulk of published work has been devoted to the behaviour of dilute slurries, as in the paper of Benchaita above, since in these it is possible to follow the behaviour of individual particle trajectories and the consequences of individual impacts. Indeed, there is a noticeable trend in recent research to concentrate on individual particle impacts, e.g. [20,21,22]. However, most erosion-corrosion situations of practical interest involve relatively dense slurries, in which particle/particle interactions are important. Relatively little has been published about the behaviour of dense slurries, but in general, it is found that erosion mass loss increases less rapidly than slurry concentration [23,24,25], i.e. the efficiency of nominal particle impacts decreases. This is partly due to particle shielding effects and partly due to particle blunting, resulting from particle/particle collisions [17,23].

More work has been reported on dense solid-in-gas systems, in the context of fluidised bed erosion. While, obviously, the numerical results from these calculations are not applicable to solid-in-liquid systems, some general principles have been found which should be relevant.

Firstly, what is meant by 'dense' in this context? Shipway and Hutchings [26] introduced the idea of relative spacing between particles, i.e. the ratio of mean particle/particle distance to mean particle diameter. This has been further developed by Oka *et al* [27], who concluded that for non-interference particle relative spacing should be greater than 17. As will be seen in the experimental parts of this Thesis, actual relative spacing under the conditions used is much less than this, so actual

particle impact velocities, impact angles and impact efficiencies will differ from the nominal conditions of the experiment.

The fluid dynamics of impact under dense particle laminar flow (solid-in-gas) have been very recently considered by Gustavsson [28]. He considered that following the behaviour of individual particles under these conditions was impracticable, so a two-fluid approach was used in which the particles are regarded as constituting a continuous phase interpenetrating with the carrier phase. The erosion process results from the normal and shearing components of the viscous dissipation of the particulate phase, resulting in deformation and cutting wear processes respectively.

2.1.6 Kinetic Energy and the velocity exponent.

Clark in a review article [22] pointed out that the erosion rate is some power function of velocity:

$$\text{Mass loss} \propto v^n \qquad (2.6)$$

Here v is the jet velocity, and n is known as the velocity exponent. "It is generally acknowledged that the exponent derives from the expression for the kinetic energy of solid particles, and other things being equal, should have a value of 2.0". However, various workers have found values for n greater than 2, and a variety of explanations have been proposed for this.

That, on a per-particle basis, mass loss is approximately proportional to kinetic energy input seems to have been first recognised by van Riemsdijk and Bitter in 1959 [29], who also showed that it is the energy associated with the normal component of velocity that is responsible for deformation wear and the parallel component with cutting wear. Subsequent to this, both Finnie [11] and Bitter [13,14] produced theories of erosion (see above, Sections 2.1.2) which predicted $n = 2$ (with a small adjustment for elastic losses in the case of Bitter's theory).

Experience has shown that n is often slightly greater than 2, particularly at high flow rates. Several explanations have been suggested for this:

- Finnie and McFadden [30], using a complicated theoretical analysis, showed that, under suitable conditions '$n > 2$' could be obtained if the impacting particle rolled forward during impact. However, the effect is small (and under the experimental conditions used in this Thesis would be entirely negligable).

- Hashish [31] found that, under water jetting conditions (typically $v = 500$ $m.s^{-1}$ i.e. about two orders of magnitude greater than the conditions used in this work), considerations of particle shape, material strength (flow stress) and hydrodynamic loading combined to give '$n = 2.5$'.

- Sundararajan [32] developed a theory for the erosion of ductile metals, based on the formation and fracture of lips. This theory leads to an explicit '$n = 2$' velocity dependence, but Sundararajan argues for '$n > 2$' on the basis that several of the target material properties used in the theory (e.g. coefficient of restitution, coefficient of friction) are also velocity dependent. The excess of n over 2 is not explicit and is not expected to be large.

- Laitone [33] studied the aerodynamics of gas-blast sand erosion testing at normal incidence, and was able to show that particle impact speeds can vary with the square of the nominal stream velocity. This is because the fluid stream is actually accelerated as it leaves the stagnation point. Subsequent calculations by Hojo [34] indicate that the point of maximum erosion is not the stagnation point but that at which impact is at about 40^0. Hydrodynamic effects alone, particularly at high fluid flow rates, can give values of n in the range 2-4.

- A more fundamental advance has been made in connection with solid-in-gas systems (fluidised beds). The key point recognised has been that erosion loss is proportional to kinetic energy loss *locally* [35] – the 'monolayer kinetic energy dissipation model'. Values of 'n' greater than 2 then arise mainly from the non-uniform distribution of kinetic energy flux across the surface. This is naturally largest with large fluid velocities. Gustavsson [28] has used these ideas to calculate the effect of a dense solid-in-gas jet on an obliquely angled plate, by setting up a grid of points all over the plate surface, calculating normal and shearing components of viscous dissipation at each point and deducing deformation and cutting wear rates from these. It is found that the modelling of the particulate phase boundary is particularly important for cutting wear, and is affected by particle size and angularity, and by surface roughness. Extension of this sort of calculation to solid-in-liquid systems with turbulent flow would be valuable.

Overall, the evidence suggests that the velocity exponent can take values greater than 2, but will generally only do so at fluid flow velocities significantly higher than those used in this work.

2.1.7 Target material considerations.

Ductile materials.

It is noted above that the principle distinctions to be made relate to the ductility or brittleness of the target material and the angle of incidence of incoming erodent particles. Hutchings [5] has reviewed some more detailed considerations.

Firstly, under low angle, 'ductile' conditions, several different types of metal removal may be distinguished:

- Rounded particles cause *'ploughing'*, displacing material to the side and front.

- Angular particles, rolling forward, cause *'type 1 cutting'*, forming a prominent lip ahead of the particle.

- Angular particles, rolling backward, may give a true machining action, *'type 2 cutting'*, cleanly removing a chip of material; this is quite rare.

Useful SEM photographs for comparison purposes are given by Hutchings for ploughing and Types 1 and 2 cutting erosion on mild steel in air in [36]. Some impact scars do not fit easily into these categories. Oltra *et al* [37] illustrate scars with more prominent lateral lips obtained in a dense medium (erosion of iron by SiC in sulphuric acid).

Hutchings [38] considering Finnie type models, and elaborations of them, found that they typically predict an inverse dependence on hardness and possibly ductility, defined as a failure strain. This inverse hardness dependence is not general. For some pure metals the relationship is found, provided the correlation is made with the work-hardened surface rather than the annealed metal. Alloys show a much weaker dependence, and materials hardened by heat treatment, almost no dependence at all. This is thought to be a consequence of strain-rate effects. Strain rates during erosion can reach 10^6 s^{-1}. Conventional strengthening mechanisms, such as precipitation, solid solution and grain boundary hardening are relatively ineffective at these rates.

Where lips are formed, repeated impacts may remove material more readily than from the bulk of the target. Levy [39,40], writing principally about gas blast erosion, has called this *'platelet erosion'*. The process is one of micro-extrusion and forging, leading to lips which are easily fractured. The mechanism proposed is largely qualitative, but shows good agreement with the physical features observed (by SEM) on gas-phase eroded mild and stainless steel and aluminium. Under these conditions

Levy finds that sometimes softer, more ductile alloys resist erosion better than harder, stronger ones; this he attributes to the ability of the more ductile alloys to redistribute the kinetic energy of impacting particles by the plastic deformation of a large subsurface region beneath the impact area, thereby reducing the concentration of force at the immediate point of impact and thence reducing platelet formation also. (Clearly, in the case of a coated sample, this mechanism may be compromised if the coating is thin and forces are not efficiently transmitted to the substrate, if the substrate is unable to undergo the necessary deformation or if disbondment occurs).

Platelet erosion on aluminium at normal incidence is illustrated by Finnie *et al* [40], who also points out that material removed is only about 1% of scar volume in this case, i.e. this mechanism is a very inefficient process.

A study by Cousens and Hutchings [42] of the very particular case of erosion of aluminium alloy by solid spherical particles at normal incidence concluded that, in this case, platelet formation resulted from work hardening of the surface by the impacting particles (with some particle embedment), fracture of this relatively brittle surface and back-extrusion of the softer underlying material into platelets. Mass loss was by subsequent fracture of these platelets. For non-spherical particles or non-normal incidence, other erosion mechanisms, e.g. micro-cutting are expected to compete with this one.

This picture has been elaborated by Sundararajan [32], who has developed a theoretical model to account for lip formation, based on strain localisation. This model asserts that:

- Erosion occurs by extrusion of lips and their subsequent fracture.

- Erosion rate is controlled by lip formation rather than lip fracture, since the latter occurs easily in a lip already containing a high level of frozen-in stress.

- Lip formation is controlled by the localisation of plastic deformation.

- This localisation is controlled by the strain hardening behaviour of the metal. If $d\sigma_p/d\varepsilon_p$ (strain hardening capacity; σ_p is flow stress, ε_p is plastic true strain) is positive plastic deformation spreads uniformly over a large volume; if $d\sigma_p/d\varepsilon_p$ is zero or negative strain is localised. Sundararajan maintains that the most likely behaviour is strain hardening at low strains, but strain softening at high strains; there is therefore a (calculable) critical strain, ε_c, beyond which lip formation occurs.

- This strain hardening behaviour is explained by assuming that material properties are functions of temperature, such that the local heating induced by particle impact causes a transition from strain hardening to strain softening as local temperature rises. Qualitatively, this seems reasonable, but no justification is given for the particular relation assumed (linear reduction of flow stress with temperature).

In general terms, this model explains experimental findings quite well. In particular, it explains why the erosion resistance of pure metals is related to their annealed hardness, but strength increases in such metals due to cold work or heat treatment are ineffective in reducing erosion.

Both Levy [40] and Sundararajan [32] note that temperature may be important because of its effects on the material properties of the target material. This is likely to be more of an issue under gas-phase erosion than in liquids, in which local heating may be more readily dissipated. An interesting example of temperature dependent behaviour is given as an unexplained observation by Misra and Finnie [43], who studied 3-body abrasion on aluminium. At ambient temperature the workpiece suffered a mixture of cutting and deformation wear. When the entire apparatus was heated to a temperature of 290 ^{0}C (0.6 $\times$ absolute melting point of aluminium), the wear mode changed to the formation of platelets with subsequent lip removal.

Similarly, Hearley *et al* [44] studying the erosion of HVOF nickel aluminide claddings by silica sand (nominal diameter, 120-150 μm) in air, found platelet formation ("overlapping lamellae") under conditions of high intensity impact (v = 25 – 71 $m.s^{-1}$) under which local temperatures might have become significantly raised (though this was not measured).

Brittle materials.

For 'brittle' fracture, a distinction is drawn between genuine brittle fracture by hard, angular particles, which results in crack patterns similar to those shown in Figure 2.8, and the 'Hertzian' crack pattern, shown in Figure 2.9. However, in either case, equations of the general form:

$$V_u \propto d_p^m \, v^n \qquad (2.7)$$

are obtained, where d_p is the radius (m) of the impacting particle, and v is its velocity ($m.s^{-1}$). Models for material removal by cracks suggest that the values of m and n should be related to the Weibull constants of the material, and that fracture toughness is a more important parameter than hardness. Qualitatively, this is borne out, but quantitative agreement with theory is poor.

For composite materials, e.g. cemented carbides, behaviour is complicated, and depends on the relative sizes of impacting particles and composite components. For very small erodent particles, wear can occur by preferential erosion of the binder phase, leading to carbide grains falling out; for intermediate sized particles, overall wear occurs, usually by 'ductile' mechanisms: for large particles, brittle fracture of the carbide grains may be important.

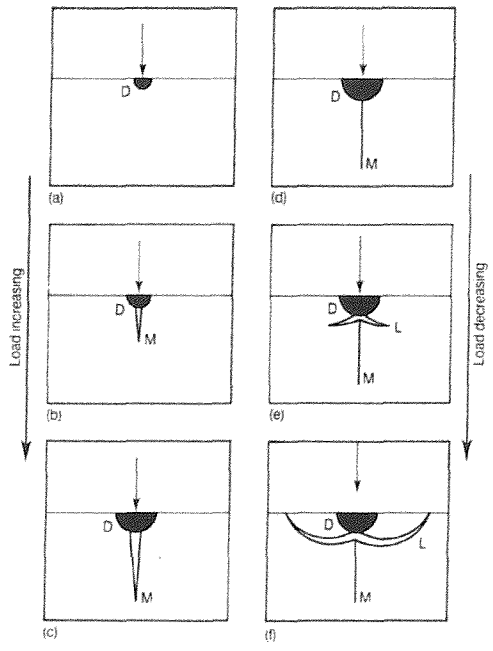

Figure 2.8: Crack pattern in a brittle material due to point indentation.
Load increased from a)-c), then decreased from d)-f).
From: I.M. Hutchings, "Tribology: Friction and Wear of Materials"
Arnold (1992).

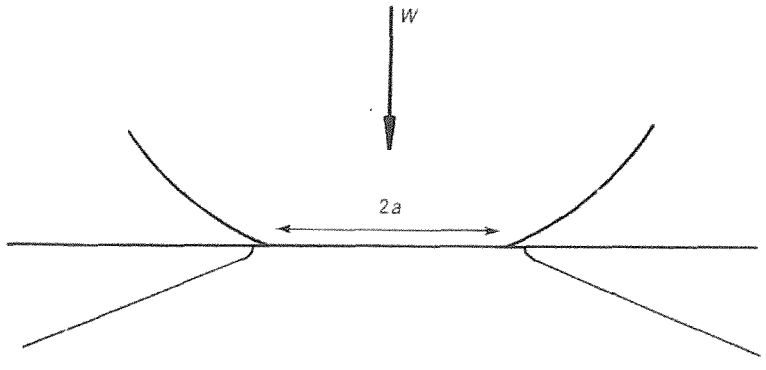

Figure 2.9: Geometry of Herzian stress crack.
From: I.M. Hutchings, "Tribology: Friction and Wear of Materials"
Arnold (1992).

2.2 STATIC CORROSION

2.2.1 Introduction

Corrosion is the destruction or deterioration of a material by reaction with its environment [45].

It is not intended to review corrosion problems and investigational methods as a whole. Good general books on corrosion exist [45,46,47]. Specific corrosion topics, relevant to this thesis, will be reviewed briefly, concentrating on static corrosion issues in this section and specific issues related to flowing media in the next one. Electrochemical methods relevant to characterising this scenario will be reviewed in Section 2.4.

2.2.2 Mass transfer and charge transfer

Corrosion reactions are electrochemical in nature, and take place at solid/solution interfaces. For corrosion to occur, corrosive reagents must be transported to the interface, reaction occur and product species be transported away from the reaction zone. Any of these processes may be rate limiting, and it is by no means always the case that the actual charge transfer step of the corrosion process is rate limiting. In fact, in corrosion of bare metals, it is more often than not the case that diffusion of oxygen to the reaction site is the critical consideration. This may be complicated by the presence of insoluble corrosion products, if they occur, or the presence of surface films, deliberately introduced or otherwise, any of which may impede diffusion.

2.2.3 Passivation, depassivation and repassivation

Most structural metals are so reactive in air that they are always covered with an invisible ultra-thin film of oxide. In some cases (e.g. aluminium, stainless steel) this is inert and impermeable to electrolytes, and is therefore protective toward the metal.

Such a protective film is called a passivation layer. Not all oxide layers are passivating – that of iron is not under ordinary circumstances, and iron is said to be non-passivating. These terms are not absolute, and there is a sizeable industry devoted to mitigating the effects of those influences that tend to interfere with the natural passivation of some metals, and to promoting the improved passivation of those metals that do not passivate naturally; inhibition lies outside the scope of this review and will not be considered further.

Most passivation films are weakened by the presence of chloride ion (from seawater, or elsewhere) in the solution. This is true of the oxide film on aluminium, and the chromium oxide film on ordinary stainless steels. Film resistance can be improved by suitable additions to the system – e.g. zirconium for aluminium and molybdenum for stainless steel. The mechanism by which this works is not well understood, but there is a balance between depassivating and repassivating influences.

When passivation films break down, this may occur as localised corrosion, in the form of pits or cracks. There are two important characteristics of this phenomenon. First, because the corrosion is local, the depth of the corrosion feature (pit or crack) may be relatively large and, hence, damaging. Secondly, it should be understood that localised corrosion is a behaviour intermediate between having a fully active surface and a fully passive one – a consequence of this is that the conditions required to support localised corrosion in any given case may be difficult to predict. However, two situations in which pitting commonly occurs [48] are at the transition between general corrosion and full passivation ('active state pit') and the transition between the passive and transpassive states ('polishing state pit'). Pits, once formed may be stable, i.e. continue growing, or unstable, i.e. they may 'die'.

Erosion may have the effect of disrupting passive films. The literature does not make completely clear whether passive film failure in this way is equivalent to pitting failure or not. Nor is it clear whether an erosion defect can become a corrosion pit,

though this seems likely, nor whether, once formed, such 'erosion pits' go directly into a growth phase.

2.2.4 Coatings and their effects on Corrosion

Figure 2.10 shows an outline of some of the basic corrosion behaviours that can occur in the presence of coatings.

Figure 2.10a shows bare metal. The important point here is that the anodic reaction (in a corrosion context, metal dissolution – shown here as iron dissolving from steel) and the cathodic reaction (shown here, as is most commonly the case, as oxygen reduction – note the necessary co-presence of water and metal cations) occur in separate places. This is characteristic of corrosion processes; the interaction of anionic and cationic sites, electrically in series, determines behaviour.

The fundamental difference between different types of coating in corrosion terms lies in whether the coating is a dielectric (organics, most ceramics) or a conductor (metals, a few ceramics). A dielectric coating may be either an organic coating, an applied ceramic coating or a self-grown passivation layer. Typically this lies uniformly over the surface, covering both anodic and cathodic areas and is itself electrochemically inactive. Typically, also, such coatings contain flaws. The behaviours of different dielectric types differ because the nature of the flaws differs. Organic coatings typically have some porosity and are also permeable to oxygen and water. This is always true, though the extent of permeability may vary widely between coatings. Failure is typically by coating disbondment ('blistering'), mainly because cathodic reduction of oxygen leads to the formation of hydroxyl ions and very high pH under the coating. Ceramic coatings are brittle and will contain cracks, especially if the solid has been subject to forming after coating. Some of these cracks will expose anodic and some cathodic areas, as shown in Figure 2.10b. Failure occurs as pitting at exposed anodic sites. The overall effect is that the coating acts as a mask, reducing corrosion activity roughly by the ratio of exposed areas to total area.

2.10 a) Bare metal

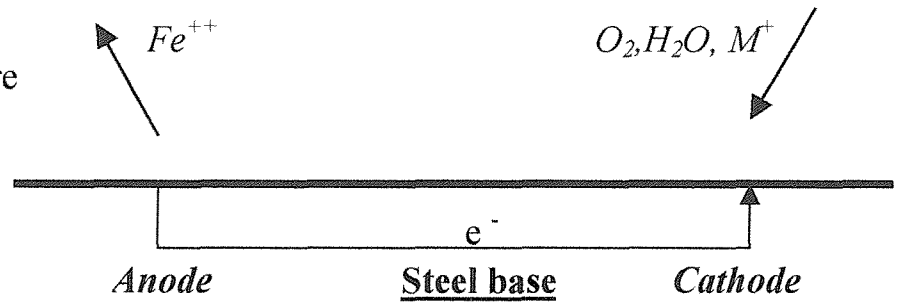

2.10 b) Cracked non-conductive coating.

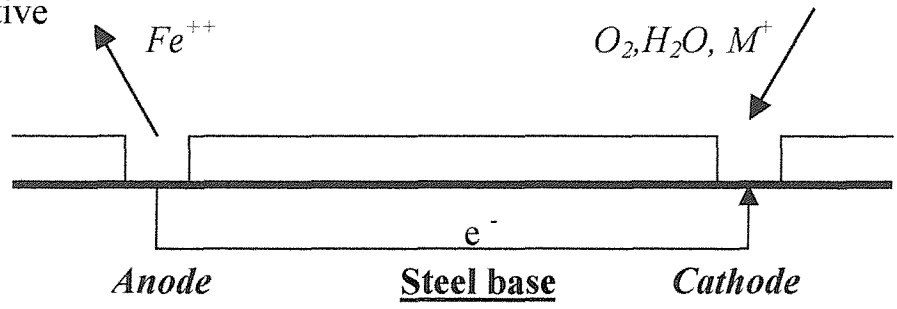

2.10 c) Anodic coating

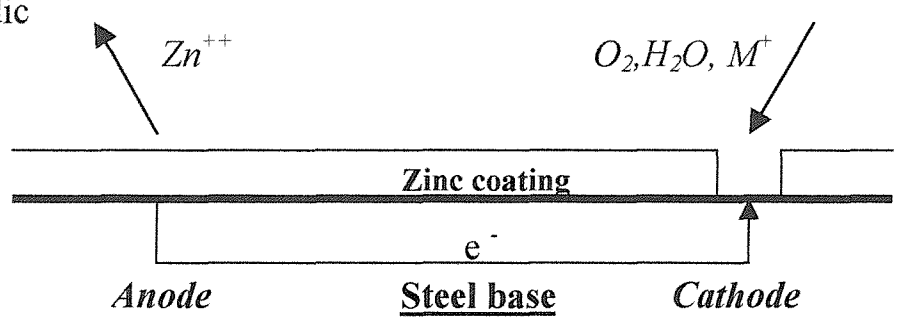

2.10 d) Cathodic coating

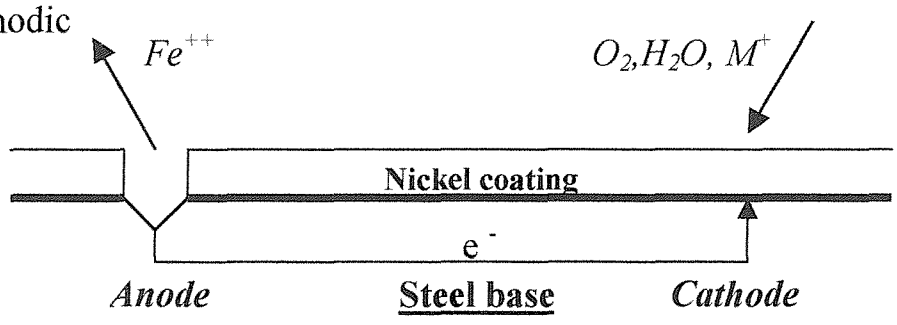

Figure 2.10: Coatings and Corrosion.

Dielectric coatings are not the subject of this Thesis and will not be considered further.

Conductive coatings interact with the substrate electrochemically at any location where both coating and substrate are exposed to the corrosive electrolyte. This is called galvanic corrosion and will always occur when suitable conditions are present. Practical aspects in a marine context have been discussed in detail by Francis [49]. It is very likely to occur in metal clad pipework carrying aerated seawater, because practical claddings always have some level of flaws in the coating.

In Figure 2.10c the coating (shown here as zinc) is more active in this electrolyte than is the steel substrate. It therefore tends to dissolve preferentially, protecting the substrate. This can be very effective and is robust toward damage, since holes in the coating are automatically protected, unless they become too large. Herein lies the principal problem with this sort of coating – if the coating is lost over an area, protection is lost. The coating may be lost because of excess electrochemical activity (and therefore it helps to use coatings which are not too electroactive), or removed by erosion.

In Figure 2.10d the coating (shown here as nickel) is less active than the steel substrate. Unrestricted oxygen reduction can take place on the nickel surface, driving a rapid reaction on the steel. This large cathode/small anode scenario can lead to very rapid deep pitting and potential component failure. In this case the coating acts purely as a mechanical barrier and must not contain flaws. Metallic coatings tend to be relatively ductile, which is helpful as regards maintaining coating integrity during component forming, but may be less helpful when low angle erosion is an issue.

In all the above examples, it has been assumed that the products of corrosion are soluble in the electrolyte. If this is not the case, further complications may arise. In particular the pores in coatings may become clogged with corrosion product. Alternatively, alkalinity at the cathode can result in deposition of low solubility solids

('calcareous scaling' in seawater). These processes can greatly slow down or even stop otherwise facile corrosion reactions. So, even though a corrosion film on a bare metal surface might be swept away under erosion-corrosion conditions, leading to rapid mass loss, the same surface with a suitable coating might survive, because corrosion product blocks the pores in the coating and the coating protects the corrosion product from erosion.

2.2.5 Cathodic Protection

Cathodic protection, i.e. polarisation in a cathodic direction relative to a stable reference electrode, is often used to protect metal structures in engineering practice, particularly in a marine context. This same technique has been widely used in erosion-corrosion studies, with the unsupported assertion that this practice suppresses corrosion mass loss entirely, and can therefore be used to obtain a 'pure' erosion baseline.

A paper of general importance in this context is that of Naerheim and Kendig [50], who investigated the effects of wear (in a pin-on-disc apparatus) in a model system (nickel in sodium perchlorate) that allowed a wide range of polarisation, but suffered little corrosion in the absence of wear. Unsurprisingly, anodic polarisation promoted wear, but the important finding in this context was that, under some circumstances, cathodic polarisation could also promote wear. This was attributed to reduction of self-formed surface oxides exposing new and softer underlying metal to wear; at large cathodic polarisations, hydrogen embrittlement may also be a factor. The claim that cathodic polarisation completely suppresses corrosion, so a cathodically protected sample in a corrosive medium may be assumed to suffer erosion only is evidently not safe, in the absence of supporting evidence, e.g. from weight loss measurements.

2.3 CORROSION UNDER FLOW CONDITIONS

2.3.1 Introduction

When corrosion occurs in flowing media, certain extra effects can occur. For the purposes of this Thesis:

Flow Corrosion is corrosion occurring in a flowing electrolyte with no solids present.

Erosion-corrosion refers to mass loss occurring in solid-in-liquid dispersions (slurries), whether this occurs primarily by erosion, by corrosion or by some interaction between the two.

Synergy (to some authors 'synergism') is the extra material loss resulting from the interaction of erosion and corrosion processes. This definition is adapted from [51]. It is sufficient for a qualitative discussion – more will be said about prior literature discussion of a more detailed definition in Section 2.3.5, and about the implementation of this concept in the current work in Section 6.3.2 (mass loss definition) and Section 6.3.3 (electrochemical definition). Synergy may be positive or negative.

2.3.2 Mass transfer to a free surface

Where mass transport of reagents to, or of products from the reaction site is limiting, then the presence of hydrodynamic boundary layers will be of importance. As a generality, the more rapid the flow is past the corroding surface, the more mass transport will be enhanced. This will be particularly the case if flow is so rapid, or the system geometry or solid surface roughness is such as to render the flow turbulent, as this leads to substantial boundary layer thinning.

For laminar flow, the behaviour of boundary layers is discussed extensively in textbooks on fluid mechanics, e.g. [52]. Correlations are generally expressed in terms of dimensionless groups.

For example, Rao and Trass [53] and Dawson and Trass [54] have investigated jet impingement on a flat plate, as illustrated in Figure 2.11.

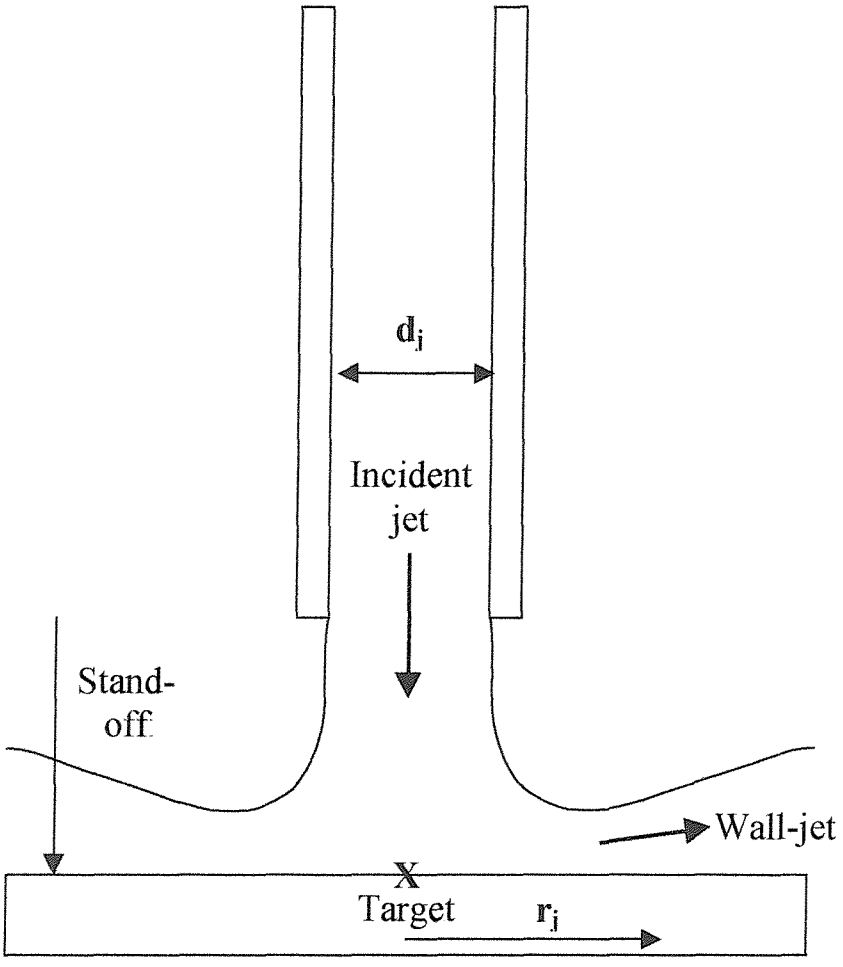

Figure 2.11: Nomenclature for jet impingement.
X marks the 'stagnation point'.

The latter, more general, paper found that, for Schmidt Numbers > 100:

In the 'wall-jet' region, where: $\left(\frac{r_j}{d_j}\right)^{-1} \geq 4.5$

$$Sh = 0.0294\,\mathrm{Re}^{0.93}\,Sc^{0.25}\left(\frac{r_j}{d_j}\right)^{-1} \qquad (2.8)$$

In the 'stagnation' region, where: $\left(\frac{r_j}{d_j}\right)^{-1} \leq 4.5$

$$Sh = 0.107\,\mathrm{Re}^{1.06}\left(\frac{h_t}{d_j}\right)^{-0.54} \qquad (2.9)$$

Here: Sh = Sherwood Number = $\frac{ad_j}{D}$

Re = Reynolds Number = $\frac{vd_j}{\nu}$

Sc = Schmidt Number = $\frac{\nu}{D}$

Where r_j is the radius on the plate from in stagnation point (m)

d_j is the jet diameter (m)

h_j is the stand-off distance (m)

D is the diffusion coefficient of the fluid ($m^2.s^{-1}$)

v is fluid velocity at nozzle ($m.s^{-1}$)

ν is kinematic viscosity ($m^2.s^{-1)}$

In principle, these equations should allow the calculation of the mass transport of reactive species across boundary layers, but in practice even Dawson and Trass were unable to obtain better than moderate agreement with experimental results, especially in the stagnation zone. They attributed this to the effects of flow corrosion in this zone.

Application of this type of approach to jet impingement flow corrosion has also been made by Dawson *et al* [55], with particular reference to the use of inhibitors. These

authors attempted to correlate calculated flow parameters with electrochemical (impedance) measurements made with a segmented electrode, with moderate success. The important aspect of this work lies in the recognition that the working electrode is spatially inhomogeneous. Further development of this approach, including the use of electrochemical noise measurements, which does not seem to have been attempted, would be highly desirable.

Correlation of flow corrosion in various geometries is sometimes expressed in terms of 'wall shear stress'. For example, Efird *et al* [56] studied the flow corrosion of mild steel in pipes, under jet impingement and on rotating cylinders, in sodium chloride/carbonate solutions. They found that:

$$l_{corr} = a\tau_w^b \qquad (2.10)$$

where l_{corr} is the corrosion rate (mm/year).

τ_w is the wall shear stress (Pa).

a, b are constants, not fully characterised by experiment.

The wall shear stress is a hydrodynamic parameter; it is the isothermal pressure loss in turbulent fluid flow within an incremental length due to fluid friction resulting from contact with a solid wall. It is not a force on the wall; it is a force within the flowing fluid at the wall. It is defined at the wall by:

$$\tau_w = \nu \left.\frac{\partial v}{\partial y}\right|_{y=0} \qquad (2.11)$$

where ν is kinematic viscosity ($m^2.s^{-1}$).

v is fluid velocity ($m.s^{-1}$).

y is normal distance from the wall (m).

This may be evaluated for appropriate geometries. In particular, Efird found for an impinging jet:

$$\tau_w = 0.179 \rho v^2 \, \mathrm{Re}_j^{-0.182} \left(\frac{r_j}{d_j} \right)^{-2.0} \qquad (2.12)$$

where: $\mathrm{Re}_j = \dfrac{2 r_j \, v}{\nu}$ is the jet Reynolds Number.

r_j, d_j v are defined as before.

ρ is the fluid density (kg.m^{-3}).

τ_w is not well defined near the stagnation point (because the flow vector changes very rapidly with radial distance), nor is it useful at large radii (because turbulence decays very rapidly in this zone). However, there is an annular zone of high turbulence for which this correlation should be useful.

This theory should support a geometry independent description of flow corrosion. However, Efird *et al*'s own experimental data (corrosion penetration data, supported electrochemically (EIS)) do not really give confidence in this. While the power law dependence of corrosion on wall shear stress is found for each of the geometries studied separately, the fit constants differed in ways not predictable from this theory. The EIS data suggested that the systems studied are not well characterised electrochemically.

Further developments of these approaches may be useful but are not attempted in this Thesis.

2.3.3 Effects of flow on corrosion

Fontana [45] shows that there are two distinct effects that can occur in solids-free flow. These are based on the premise, normally fulfilled, that metal corrosion rates are controlled by the diffusion of oxygen to the cathode.

For actively dissolving metals in which the reduction process is under diffusion control, e.g. oxygen reduction, corrosion rate increases continuously with flow

velocity up to a limit imposed by concentration polarisation. Beyond this limit, corrosion remains constant. These metals are safest at low flow velocities.

For metals which passivate, a completely different behaviour is observed. In this case, corrosion increases with flow up to a limit, then declines precipitously. For these metals, notably stainless steels, within the potential range in which they are passive, safe usage depends on keeping flow velocities *above* a certain limit.

Legat [57] has established that the direct effect of electrolyte movement on Electrochemical Noise data (to be discussed more fully later) is small, but large changes may occur if the corrosion mechanism changes, as is often the case.

2.3.4 Erosion-corrosion

More complicated effects can occur when solids are entrained in the liquid flow.

This was apparently first recognised by Zelders [58], who studied metal wastage in a coal washing plant. Zelders was unable to alter either the materials in the system or its geometry. Nevertheless, he correctly deduced that in the absence of solids, the important factors were oxygen concentration in the mine water, water conductivity, flow rates, turbulence and the porosity/adhesion characteristics of surface oxide layers. Flow corrosion of carbon steel could be as much as 20 times greater than static corrosion under otherwise similar conditions. In the presence of coal slurries (about 5% w/v) mass losses were increased considerably further. While attributing most of this to direct erosion and (particularly) corrosion losses, Zelders recognised that his data could not be modelled without a further quantity, which would subsequently be termed 'synergy'. In practice, some of Zelders' corrosion loss under these circumstances was undoubtedly erosion-enhanced, so the various contributions to his mass loss are not cleanly separated.

This is a particular (very common) case where erosion removes surface oxide layers. Other mechanisms exist that can result in 'synergy' effects. Wood [59] has listed possible causes of such 'synergy':

- Erosion of protective films of corrosion product, notably oxides (passivation layers). Erosion produces fresh reactive surfaces.

- Local acidification in erosion scars, promoting pitting corrosion.

- Surface roughness promotes turbulence, increasing oxygen and ion transport to the surface. Greater oxygen access may result in either positive or negative synergy, depending on whether oxidised corrosion products are soluble or not.

- Lowering the fatigue strength of the metal by corrosion.

- Removal of work hardened surfaces by corrosion.

- Grain loosening by selective grain boundary dissolution.

- Increased density of stress raisers due to micropitting.

- Shot peening effects may lead to negative synergy.

Generally, while it is well recognised that synergistic effects do occur, detailed mechanisms are not well understood in particular cases, and rational design of materials to resist combined erosion and corrosion is in its infancy.

The balance between erosion and corrosion, and the damage resulting, depend on the energy and frequency of impacts. Figure 2.12, from Heitz [60], illustrates some of the effects that may occur. At very low energies, passivation layers may be sufficient to protect the underlying metal (Fig 2.12a). At somewhat higher energies (Fig 2.12b),

passivation layer disruption and healing may occur, or selective damage to heterogeneous materials (e.g. dissolution of the binder phase in composites). At the highest energies (Fig 2.12c), erosion dominates, surface layers are entirely removed and corrosion is typical of the unprotected metal.

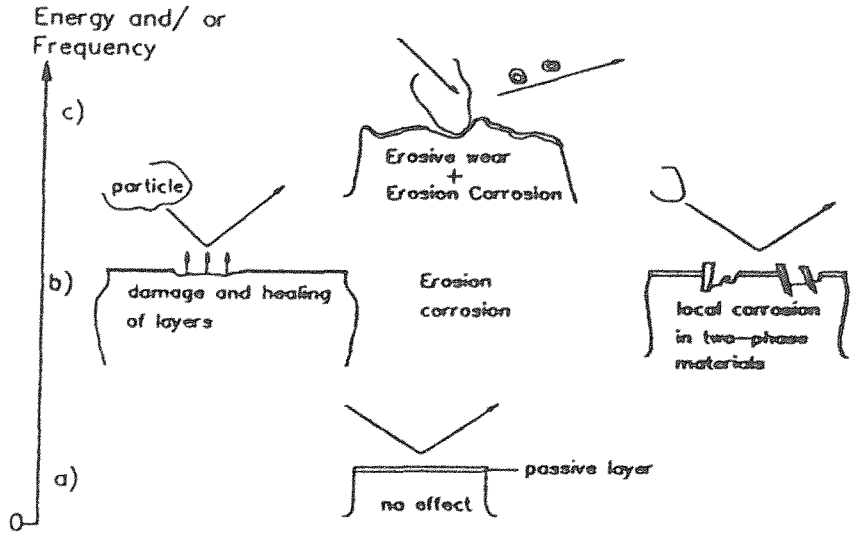

Figure 2.12: Effects of erosion-corrosion on materials with surface layers.
From: E. Heitz, *Corrosion* 47(2) (1991), 135-145

Another study, by Batchelor and Stachowiak [61], of the wear rates of mild steel, zinc and magnesium under two- and three-body abrasion conditions in sulphuric acid, again where removal of oxide films is important, showed large differences in 'synergy', measured by mass loss. These authors concluded that 'synergy' effects were only significant when the static corrosion rate exceeded half the dry abrasion rate, but that 'synergy' magnitudes could not be predicted from pure corrosion and dry abrasion data alone.

Matsumura *et al* [62], using an unusual type of jet apparatus (see Section 2.5.1), compared the erosion-corrosion of 304 stainless steel in sulphuric and hydrochloric acids, i.e. under conditions which would stabilise or destabilise the passive film. They were only able to interpret their data by assuming that chloride ion adsorption

plays an important part in the process. This acts, at least in part *via* differences in coefficient of friction, which they were able to measure, resulting from this adsorption.

Modelling of erosion-corrosion of passive surfaces has been attempted by Novak and Macenauer [63]. They used an erosion-depassivation/repassivation model, based on a matrix of target points, with the (implicit) assumption that most of the surface is passive most of the time, i.e. a very low impact rate. Under these (not very relevant) conditions they asserted that, given a passive layer damage rate (obtained by microscopical examination after pure erosion experiments) and data from potentiostatic measurements under pure erosion conditions, they could estimate 'the corrosion part of erosion-corrosion'. Their comment on the low impact rates assumed was that higher impact rates should not be allowed!

A quite different synergy mechanism was invoked by Li *et al* [64] in a study of the erosion-corrosion of aluminium. Mass loss behaviours in 0.5 M NaCl, 0.5 M acetic acid and 0.1 M Na_2CO_3 were compared. In non-corrosive media the basic mechanism of mass loss was the ductile fracture of flakes formed at the surface. In corrosive slurries, although the 'pure' corrosion component was very small, mass loss was greatly enhanced by flake cracking due combined stress and corrosion.

In general, the degradation of aluminium is expected to depend on flow velocity, qualitatively as shown in Figure 2.13. In water, very small mass losses occur, slowly increasing with flow velocity. In brine, mass losses are larger, but may be (more than) balanced by mass gains from precipitation of corrosion products; in general, the latter dominate at low velocities, but mass losses dominate at higher flow rates. When sand is present, insolubles are swept away; mass losses are always positive and increase rapidly with flow rate (approximately $\propto v^2$ if erosion dominates).

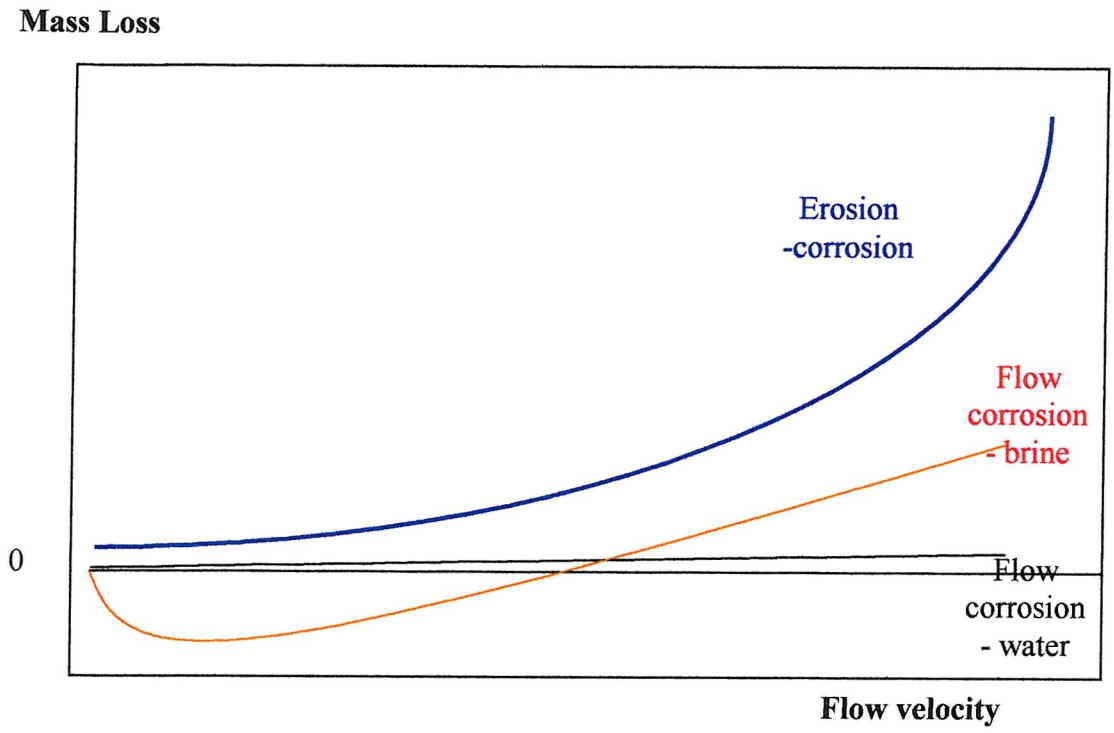

Figure 2.13: Schematic of expected variation of mass loss with velocity. Aluminium target, various erodents.

'Erosion-corrosion maps' have been constructed, e.g. by Stack [65], setting out the conditions under which erosion predominates, corrosion predominates or synergistic effects are most important. These have not, in general, been applied to sea water systems, or to any great extent to coatings, and are not considered further here. However, the point made above concerning mass loss under cathodic protection conditions being sometimes greater than that attributable solely to erosion is further illustrated in this paper in the case of alumina erosion of steel in sodium carbonate/bicarbonate.

Detailed studies of the erosion-corrosion of stainless steel in sodium chloride have been carried out by Burstein and Sasaki [20]. Using a 2-electrode set-up under potential control (see Section 2.5.2), analysis of electrochemical current noise at very high data rates (up to 5×10^5 s^{-1}, apparently without anti-aliasing) resolved different types of transient for particle impact and for metastable pitting. It was shown that

metastable pitting occurred under flow conditions, but became much more frequent when erodent particles were injected. This was attributed to mechanical disruption of the passive film providing access to potential nucleation sites for pits, e.g. sulphide inclusions. The noise features for metastable pitting and for impact features were found to be distinguishably different. A further paper by these authors [66] demonstrated the existence of a threshold impact energy required to cause passive film disruption.

2.3.5 Synergy

As noted above, synergy (to some authors 'synergism') is the extra material loss resulting from the interaction of erosion and corrosion processes. Attempts to define synergy more closely and quantify it have led to a variety of different detailed treatments.

According to Wood [59]:

$$M_T = M_E + M_C + M_S \qquad (2.13)$$

Where: M_T is the total mass loss (kg).

M_E is the mass loss due to erosion only (kg).

M_C is the mass loss due to corrosion only (kg).

M_S is the mass loss due to 'synergy' (kg).

This is a natural definition, provided that the 'erosion', 'corrosion' and 'erosion-corrosion' measurements are all made under comparable conditions. Note that the definition is entirely gravimetric, and does not involve assumptions about electrochemistry. However, note also that M_S is determined as the difference between typically much larger quantities, and is therefore likely to be difficult to determine precisely. Finally, difficulties arise when solid corrosion products are present.

A more complicated expression has sometimes been used [67,68,69]:

$$M_T = M_E + M_C + (\Delta M_E + \Delta M_C) \quad (2.14)$$

Where: ΔM_E is described as the 'synergistic effect' and is 'the effect of the corrosion on the erosion rate' (kg).
ΔM_C is described as the 'additive effect' and is 'the effect of the erosion on the corrosion rate' (kg).

This is essentially the same as the expression used in ASTM Standard G119 – 93 [51].

Apart from the assumptions made by Wood, some others are introduced. Apart from the purely philosophical point that it is not entirely clear that an interaction between erosion and corrosion can always be split in the manner suggested, there are electrochemical issues. It is claimed that the pure erosion term, M_E, can be measured by carrying out slurry testing under cathodic protection conditions, but see the paper of Naerheim and Kendig [50], referred to earlier (Section 2.2.5). ASTM recommends an imposed potential of –1.0 V *vs* SCE, but this is likely to produce hydrogen effects. Equally, it is claimed that M_C and $(M_C + \Delta M_C)$ can be estimated from polarisation curves, making use of Faradaic equivalence, without and with solid erodent in the flow. This involves further assumptions:

- That there are no side reactions, i.e. that the Faradaic efficiency is 100%.
- That the electrochemistry is wholly under charge transfer control.
- That there are no parasitic resistances (iR drop) in the system.
- That polarisation does not change the surface irreversibly.
- That potentiodynamic polarisation, a relatively slow process, is appropriate in a dynamic erosion-corrosion context.

This is a long list of assumptions, which should be established case-by-case – not often done! For the purposes of this Thesis, a gravimetric approach will be preferred,

to be discussed further in Section 6.3.2. Some further remarks will also be made in Section 6.3.3 regarding electrochemical aspects of synergy.

2.3.6 Ripple formation

Under flow corrosion or erosion-corrosion conditions a surface having a rippled topography is sometimes formed. This is extensively discussed by Karimi and Schmidt [70]. They concluded that:

- Ripple formation can be reproduced experimentally.
- Ripple formation can occur in all types of material, ductile or brittle.
- Ripples arise as a result of an interaction between erosion induced microroughness and turbulent eddies in fluid flow.
- Ripples can arise in the absence of solids by means of cavitation processes alone.

2.4 ELECTROCHEMICAL METHODS

2.4.1 Introduction

General books on Corrosion [44,45,46] give outline information on electrochemical methods relevant to corrosion studies. More specialised information can be found in [71], which includes guidance on cell design and on choice of electrodes. Choice of reference electrodes is addressed specifically by Ives and Janz [72]. There are a large number of electrochemical techniques available, and it is not proposed to review them all. Three particular techniques that may be of value in characterising erosion-corrosion in coated systems will be considered here, Potentiodynamic Polarisation, Electrochemical Impedance Spectroscopy and the main technique used in this work and considered in more detail, Electrochemical Noise. Their relative advantages and limitations are considered in the context of the present work.

2.4.2 Theory

When a metal is immersed in an aqueous solution, there is a tendency for metal atoms to dissolve in the solution as aquo-ions. There is also an opposing tendency for such aquo-ions to discharge as atoms on the existing solid. If the rates of these processes are unequal, a charge separation builds up at the metal/solution interface, the so-called electrical double layer. This results in an electric field perpendicular to the surface, which acts so as to lead to equalisation of dissolution and discharge rates, setting up a dynamic equilibrium. The potential at which this equilibrium is reached is called the rest or equilibrium potential. It depends on many factors, including the nature of the metal and solution species, e.g. pH, complexants, etc.

If a cell is constructed in which the metal of interest is made the working electrode, together with suitable counter and reference electrodes, the rest potential of the test metal may be measured relative to the reference (suitably, Ag/AgCl in brine solutions). If the potential of the system is then displaced from equilibrium, a current

will flow through the system. The potential difference from equilibrium, η, is called the overpotential:

$$\eta = E_p - E_{rest} \tag{2.15}$$

where E_p is the polarised potential and E_{rest} is the rest potential.

Using electrochemist's conventions, if the overpotential is positive, an anodic (positive) current flows and oxidation reactions occur at the metal surface. Similarly, if the overpotential is negative, cathodic (negative) currents flow, metal plating may occur, or, more relevantly for present purposes, reduction of oxygen or hydrogen ions.

A plot of the current response to variations in overpotential is called a polarisation curve. Under ideal conditions such curves have characteristic shapes, from which useful data may be obtained. At the rest potential, no net current flows:

$$I_{anodic} = -I_{cathodic} = I_0 \tag{2.16}$$

I_0 is called the exchange current density, and is an important parameter of the system.

Away from the rest potential, it can be shown [46] that (for thermodynamically reversible reactions, entirely under charge transfer control):

$$I = I_0\left[\exp\left(\frac{\alpha_A n_m F\eta}{R_0 T_K}\right) - \exp\left(\frac{-\alpha_C n_m F\eta}{R_0 T_K}\right)\right] \tag{2.17}$$

Here: I is the current density ($A.m^{-2}$) at overpotential η (V).

I_0 is the current density ($A.m^{-2}$) at $\eta = 0$.

α_A and α_C are constants known as anodic and cathodic transfer coefficients.

n_m is the number of electrons transferred in the charge transfer process.

F is Faraday's constant.

R_0 is the Gas constant.

T_K is the absolute temperature.

This is the Butler-Volmer equation, the fundamental equation of electrode kinetics.

It consists of two terms, representing the anodic and cathodic current densities. Far away from the rest potential, one term or the other becomes very small and can be neglected. Under such conditions, two simpler and more useful relations result:

$$Log_{10} I = Log_{10} I_0 + \frac{\alpha_A n_m F \eta}{2.303 R_0 T_K} \qquad \text{at positive } \eta \qquad (2.18)$$

$$Log_{10}(-I) = Log_{10} I_0 - \frac{\alpha_C n_m F \eta}{2.303 R_0 T} \qquad \text{at negative } \eta \qquad (2.19)$$

These are called the Tafel equations, after Tafel, who originally discovered them empirically.

α_A and α_C are often approximately equal, with a value of 0.5, so that at 25°C:

$$Log_{10} | I | = Log_{10} I_0 \pm \frac{n_m}{120} | \eta | \qquad (2.20)$$

i.e. the slopes of the Tafel lines should be close to $120/n_m$ mV/decade of current.

2.4.3 Potentiodynamic Polarisation

Procedure.

If a piece of metal – a 'working electrode' (WE) - is immersed in an electrolyte, and connected to another electrode – a 'counter electrode' (CE) - and, *via* a potentiostat, to a stable potential reference – a 'reference electrode' (RE) - the behaviour of the working electrode can be controlled. The counter and reference electrodes need to have particular properties for effective operation; these are detailed in [71], but essentially the CE needs to have a low impedance and pass current freely, while the RE needs to have a very high impedance and pass no more current than is required for potential estimation.

Such a 3-electrode cell may be used to generate a polarisation curve, as defined above. To do this, the potential of the working electrode is allowed to settle to its rest value (minimum net current) at open circuit (the open circuit potential – OCP). The potentiostat is then switched in and the potential slowly swept away from OCP, while the current is measured. A slow sweep (typically at 1 $mV.s^{-1}$) is necessary so that the data represent quasi-static conditions. Both cathodic and anodic sweeps are carried out (usually cathodic first, as this generally causes less damage to the working electrode). Making use of the Tafel relationships, above, $\log(|I|)$ is then plotted against the potential, relative to the reference electrode, to obtain the polarisation curve. Figure 2.14 shows idealised polarisation curves for two metals (it must be emphasised that real polarisation curves are *never* as tidy as this). In practice, the two metals would be tested separately in the electrolyte of interest. For a single metal measured alone, two useful pieces of data result. Firstly, the 'rest potential' is that at which the deep minimum in the plot occurs. Comparison between rest potentials shows unequivocally which metal of the two will protect the other in a galvanic couple– in this case, metal 1 protects metal 2. Secondly, if tangents are fitted to the straight line portions of the curves (not explicitly shown), these tangents should intersect at a point at the rest potential, and define a current density for the metal. This

'exchange current density' (I_0) is a measure of how active the metal surface is in this particular electrolyte – here anodic and cathodic currents balance under no external polarisation.

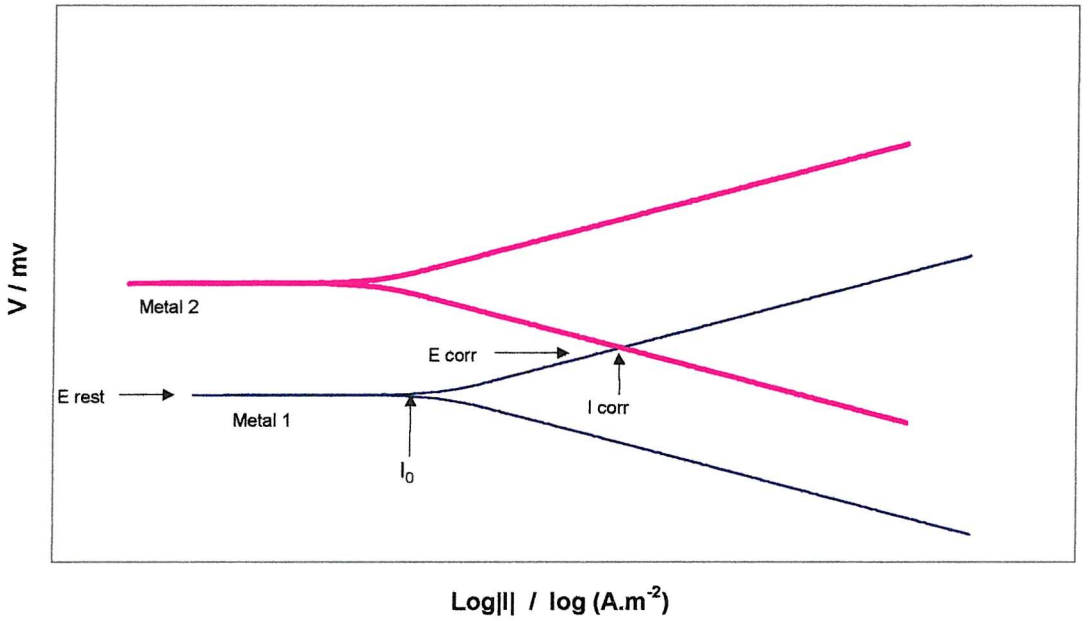

Figure 2.14: Schematic of form of Polarisation Curves.

If two metals are present, in contact, in the electrolyte together then each will 'polarise' the other. The potentials shift until they meet at a 'corrosion potential' (E_{corr} in Figure 2.14, such that the anodic current from one metal (metal 1 in this case) exactly balances the cathodic current on the other metal (metal 2). Care needs to be taken in carrying out this current matching operation to ensure that any mismatch in areas is allowed for. At E_{corr} a specific current density, I_{corr}, exists on the anode. This defines, by Faradaic equivalence, the rate at which metal will be lost from the anode (in the absence of side reactions and such other effects as erosion). If it is further assumed, as is often (probably too often) done, that corrosion occurs uniformly, this can be further converted into a penetration rate. This procedure is widely used to characterise galvanic corrosion.

Limitations

- Mass Transfer. The simple theory above assumes that this is not important. The practical effect, if mass transfer limitation is present, is to 'bend over' the ends of the Tafel lines away from the rest potential. This can easily be so severe that no Tafel lines are available at all, particularly in stagnant, viscous solutions of low ionic strength; fortunately, the electrolyte concerned in this study (3.5% NaCl) is likely not to be troublesome in this regard.

- Thermodynamic reversibility. This is assumed, and is reasonable for a metal dissolving into an electrolyte containing its own ions. However, it is not valid where reactions creating (or consuming) gases or solids are involved. Oxygen reduction is not a thermodynamically reversible process, nor is solid oxide (passivation layer) formation. Where such processes exist, the corresponding polarisation curves may be strongly curved, and no simple theory will suffice.

- Non-repeatability. Allied to the previous point is the fact that this method is very intrusive. Large polarisations are commonly used – 250mV or more – and these will alter the surface irreversibly. For example, if the polarisation process induces pitting, repeat sweeps may be very different from the original one – indeed, this may be used as a means of assessing pit stability [73]. The consequence of this non-repeatability is that, not only can this experiment not be repeated on the same sample, but neither can any other surface sensitive experiment (such as an erosion trial). It is possible that if the effects of erosion were to effectively make new surface at a rate so fast that the measurement was always at a quasi-equilibrium, this limitation would be avoided, but no discussion of this has been found.

- Non-locality. The experiment averages results over quite a large sample area, and is incapable of distinguishing between general and localised corrosion. Where the latter is present, serious errors of interpretation may be made.

- Sweep rate. When slow processes are present, sweeping potential at conventional rates will give misleading results, since the assumption of quasi-equilibrium assumed at each measurement point will be violated. For this reason, the sharpness of the 'V' shape of the calculated curves in Figure 2.14 is rarely encountered in practice.

- Stationarity. Polarisation curves typically take an appreciable fraction of an hour to carry out. If rapid processes are present, the curves will be distorted, since features present at the start of the experiment, e.g. passivation layers, may have altered during the measurement.

2.4.4 Electrochemical Impedance Spectroscopy (EIS)

Electrochemical test methods, in general (with one exception, see Section 2.6, below), either impose a potential on an electrochemical system and observe the current response, or impress a current and observe the resulting potentials. Measurement of polarisation curves, as seen above, involves applying large potentials across the cell, which change the system under study, and is necessarily slow, because establishment of quasi-equilibrium conditions at each cell potential should be attempted (even if it is not always achieved). Electrochemical Impedance Spectroscopy (EIS), formerly known also as AC Impedance, Immittance Spectroscopy and by other names, was originally developed to provide means of investigating rapid processes, not otherwise accessible. More recently, it has found favour in investigating complex processes, such as corrosion (particularly under organic coatings), because of its ability to resolve processes occurring on different time scales. It also provides an unequivocal means of measuring the cell solution resistance, a quantity not otherwise easily accessible.

AC techniques have a long history, but relatively little progress was possible until the development of the modern electronics and computing techniques necessary to handle the large amounts of data involved, in real time. The pre-history of the subject will

not be reviewed here. A good recent treatment of EIS is to be found in a NACE publication by Cottis and Turgoose [74].

The experiment is carried out by applying a small amplitude sinusoidal AC potential of known frequency, and measuring the current response at that frequency. A range of frequencies is used, within the span 10MHz-10μHz. Modern instrumentation automatically generates the required AC potential input, analyses the resulting AC current output (rejecting both DC current and any noise there may be, of whatever origin), sweeps frequency over a pre-set range and records the results for subsequent analysis. Because small amplitudes are used, the sample is only a little disturbed (but not 'not disturbed', as asserted in some older literature), and, because high frequencies may be used, fast processes may be characterised.

Impedance, Z, is the AC equivalent of resistance:

$$E = IZ \tag{2.21}$$

Z is a complex quantity, having a phase as well as a magnitude.

$$Z = a + jb \tag{2.22}$$

$$|Z| = \sqrt{a^2 + b^2} = \frac{|E|}{|I|} \tag{2.23}$$

$$\tan\theta = \frac{b}{a} \tag{2.24}$$

Real and imaginary parts of impedance are recorded as a function of frequency, and equivalent circuit models used to model the electrical behaviour.

It is important to realise that this modelling process is incapable of leading to a unique explanation of system behaviour in all but the simplest cases, owing to fundamental mathematical ambiguities [75]. Fortunately, by using other information about the system, it is often possible to associate particular AC features with particular aspects of behaviour. Ultimately, probably the best way of using EIS in a particular context will be to regard it as a means of parameterising the system response to a given input.

There are a number of different ways of representing impedance data. The most common ones are the so-called Nyquist and Bode plots. In Nyquist plots, the (negative) imaginary part of the impedance is plotted *vs* the real part, as a function of frequency. In Bode plots, the (log) magnitude of the impedance and its phase angle are plotted separately *vs* (log) frequency. It is usually easier to analyse data from their Nyquist representation, but the Bode plot, particularly in its phase angle form, is more sensitive to the presence of small features. There has in the past been considerable, rather sterile, discussion of which form is 'better'; nowadays, with modern computing power, it is straightforward to produce either or both for presentational purposes, but better to do the data analysis with one of the specialist programmes commercially available, e.g. the EQUIVCRT program [75] from the University of Twente.

Figure 2.15 shows sample Nyquist and Bode plots, to illustrate their form [76]. The system here is bare carbon steel corroding in an unidentified waste stream, and is as simple as real systems get. The Nyquist plot shows a single semi-circle, more or less centred on the real axis, but slightly displaced from the origin. The Bode plot shows a single step in the magnitude plot with a slope close to -1, and a single peak in the phase angle plot. There is some distinctly poor quality data at both ends of the frequency spectrum, which may hide the edges of further features. Ignoring these, the data has a form that may be modelled using a very simple equivalent circuit, as shown in Figure 2.15. The offset of the semi-circle from the origin corresponds to the uncompensated solution resistance - this is the best way of measuring this quantity.

The semi-circle itself can be shown to represent the AC behaviour of a parallel RC circuit [71,77]. This, in turn, can be shown to be the equivalent circuit representation of an idealised (thermodynamically reversible) charge transfer reaction. Within the parallel RC component, the resistance, R_{ct}, represents the charge transfer resistance, inversely proportional to the reaction rate and to area, while the capacitance, C_{dl} represents the double layer capacitance, proportional to the electroactive area over which the reaction occurs.

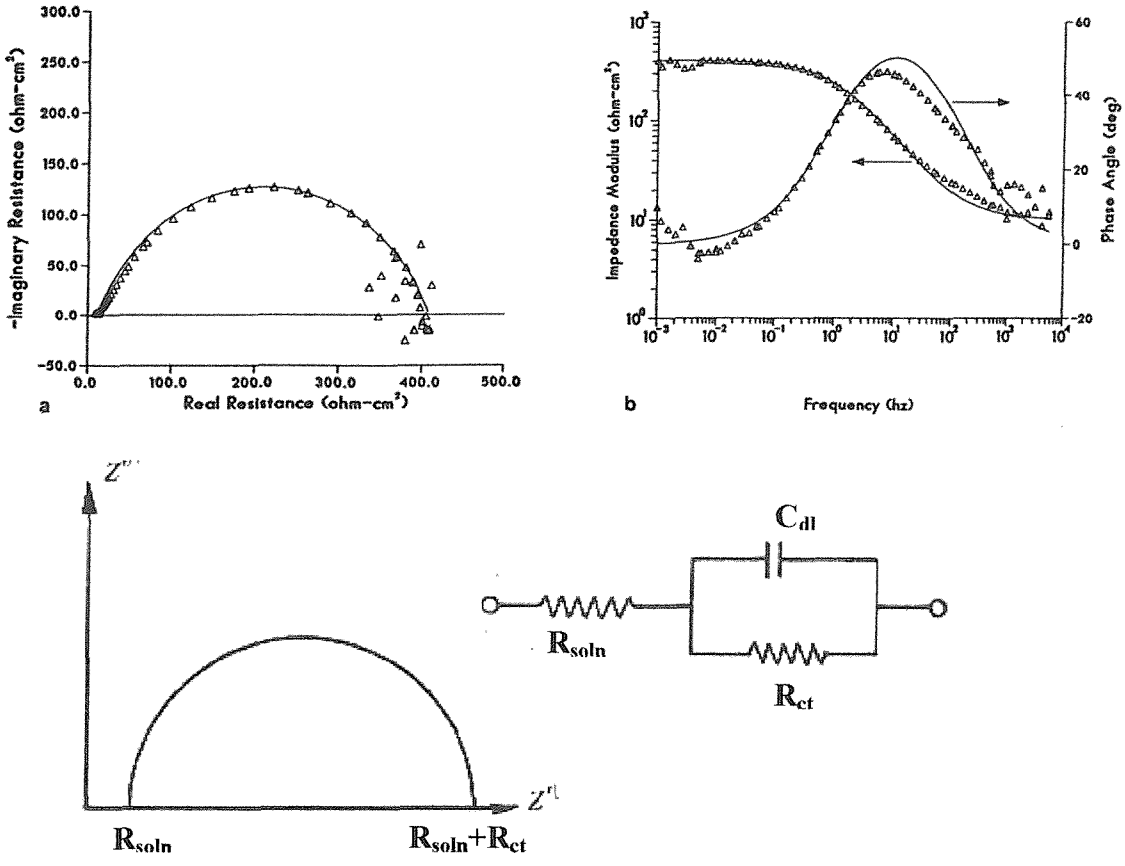

Figure 2.15. Sample Nyquist and Bode plots. Carbon steel in unidentified waste.
From: D.C. Silverman, "Rapid Corrosion Screening in poorly defined systems by Electrochemical Impedance Technique", *Corrosion*, 46(7), 589-598
Added: Schematic Nyquist plot and equivalent circuit, to match this data.

More complicated systems have more complicated spectra. EIS may be used to characterise a very wide range of situations, but in this work has been used mainly to characterise the cell resistance.

2.4.5 Electrochemical Noise Analysis (ENA)

Introduction

In general, electrochemical experiments either apply a potential difference to a cell and measure the resulting current flows, or impress a current across the cell and measure the resulting potentials. Either way, the test sample is to some extent disturbed by the experiment, and to that extent results obtained will be distorted. However, electrodes are not passive electrical components. They generate potential and current fluctuations spontaneously, and these can be measured. These fluctuations are described as Electrochemical Noise.

It is usually held that such phenomena were first systematically investigated by Iverson [78] (but see Section 2.6.4, reference [150]), who investigated potential fluctuations between a platinum electrode and working electrodes of platinum, aluminium, magnesium, iron, mild steel and zinc. He recorded fluctuations characteristic of the corroding metal (> 100 μV at 1-2 Hz for aluminium and magnesium, ~ 50 μV, at ~ 0.5 Hz for iron, steel and zinc and none for the non-corroding platinum). He concluded that these derived from minute changes in the charge on the corroding electrode caused by momentary imbalances between the anodic and cathodic reactions; these should be quantitatively relatable to the corrosion rate.

Other early workers to investigate these phenomena were Barker [79], Fleischmann and Oldfield [80], Tyagai [81], and Blanc *et al* [82], who between them went a long way toward characterising the theoretical nature of these fluctuations as the results of various stochastic processes occurring on an electrode surface.

At a more practical level, early papers of importance include Williams *et al* [83], concerning pitting phenomena, and Bertocci [84] and Uruchurtu and Dawson [85], concerning aluminium dissolution.

Particular publications that have been of importance have been patents by Hladky [86], concerning practical measurement of Electrochemical Noise, and by Eden *et al* [87], concerning analysis of ENA data, particularly the concept of Noise Resistance. While, in view of the prior art noted above (which is not an exhaustive list), the strength of these patents must be questionable, they have had the practical effect of inhibiting development of commercial Electrochemical Noise measurement equipment.

A good recent coverage of the subject is to be found in a NACE publication by Cottis and Turgoose [74].

Experimental considerations

Two experimental configurations are commonly used [88], shown in Figure 2.15:

- Use of two 'identical' electrodes connected via a zero resistance ammeter (ZRA), with the electrochemical potential measured relative to a third 'identical' electrode - favoured by field users - or to a reversible reference electrode (RE) – favoured by laboratory workers. Measurement is always at OCP, i.e. the current minimum of the polarisation curve.

- Use of a working electrode (WE), connected *via* a potentiostat to a counter electrode (CE - ideally non-noisy), with the electrochemical potential of the WE fixed relative to a RE. This configuration measures current noise only. Measurement may be made at OCP or at any other set potential desired, e.g. under cathodic protection conditions.

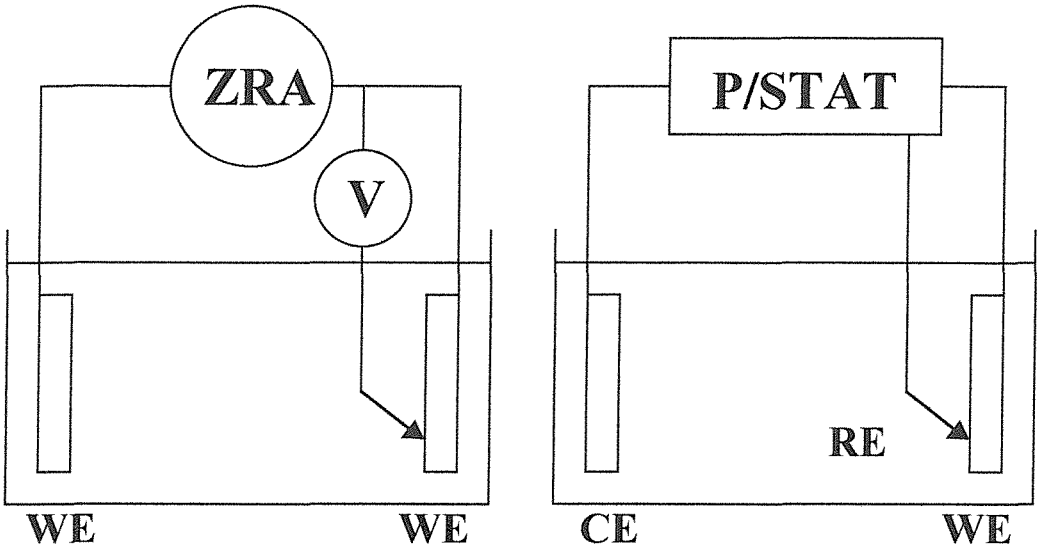

2 Identical Working Electrodes. (V and I noise, common OCP)

Single Potentiostatted Working electrode. (I noise only, any potential)

Figure 2.16: ENA cell layouts.

The first approach has traditionally been favoured by electrochemical noise researchers, because, if the various electrodes really are identical, analysis of the noise data is greatly simplified. However, this assumption is rarely, if ever, justified, because:

- It is impossible to prepare identical electrodes; even in the simplest cases this is an approximation and for coated systems it is impossible even to get close, particularly because of differences in coating porosity.

- Even in the case that near identical electrodes can be prepared, they generally do not remain identical for very long. Consider the case of two 'identical' stainless steel electrodes in brine [89]. If an active pit appears on one electrode, it is found that its corrosion potential drops dramatically (by several hundred millivolts). In effect one electrode becomes anodic and the other cathodic; this behaviour tends to be self reinforcing.

- Additionally, in some cases, e.g. the present one, it is not possible to arrange to have a symmetrical cell; intrinsically, there is a flow of fluid from the CE (and RE, if present) to the WE.

Where two non-identical electrodes are present, Pistorius [90] has shown that the noise output is dominated by the electrode of lower impedance (larger area). This favours the use of large working electrodes and small counter electrodes. Pistorius states without discussion that his findings do not apply to situations where high impedance is the result of the presence of an organic coating.

For the present work, it is considered necessary to use the second electrode configuration, with a WE connected, *via* a potentiostat, to a CE and RE. This configuration has previously been used to study erosion-corrosion by Oltra *et al* [36]. More recently, Burstein and Sasaki [20,66] have also studied erosion-corrosion under potential control using a 2-electrode system.

The potentiostat is required for the following reason [88]. Since the WE and CE are not identical in this configuration, there will be a galvanic potential between them and, in the absence of a large impedance in the system (such as would be provided by, e.g. an intact insulating coating) a significant couple current will flow. Unless a potentiostat is employed to hold the WE at its open circuit potential (OCP), the WE will be polarised to a significant and, in general, unknown extent away from its OCP. This will result in the current noise amplitude (on top of the galvanic current) being different from that expected at the OCP – in general, ignoring complications due to such phenomena as passivation layers, polarisation in the anodic direction would be expected to lead to higher levels of current noise and cathodic polarisation to lower levels. For this project, a potentiostatted WE is essential. The inclusion of a potentiostat also allows investigation of system behaviour under externally impressed cathodic protection conditions, should this be desired, though in this case, careful consideration of the separation of deterministic processes due to the impressed

galvanic potential from stochastic processes would be necessary; Bertocci [84] has used cross-correlation calculations to achieve this.

Nevertheless, a difficulty arises. When the metallic coating being used breaks down, the OCP of the WE will change, but the actual potentiostat-controlled potential will not. There is no way of avoiding this, without introducing polarisation by the CE. The best that can be done is to hold the potential for as short a time as is consistent with obtaining a useable noise trace. For present purposes, this consideration probably does not matter, so long as a characteristic electrochemical signature can be associated with coating breakdown. This, however is, likely to inhibit theoretical understanding.

System considerations

Sampling rate. The bulk of published literature on the application of electrochemical noise to corrosion studies has reported measurements limited to a sampling rate of 2 s^{-1}. This frequency seems to have been first used by Hladky and Dawson [91] in 1981, using self-built equipment based on available components. This apparently arbitrary frequency, driven as much by equipment availability as anything else, has become an accepted standard, typically accompanied by vague unsupported remarks to the effect that there is no activity of interest at higher frequencies.

However, EIS data on plain metal surfaces usually contain charge transfer loops peaking at frequencies of the order of 100 Hz, suggesting that this frequency range should be investigated. Moreover, there is a small amount of published work suggesting that there is indeed noise activity at frequencies higher than 2 s^{-1}:

- W.P. Iverson 1968 [78].
  Equipment: High impedance voltmeter, with a home-made chopper stabilised circuit. Found: Transients on Al, Mg at 2 s^{-1} or higher.

- R. Oltra *et al* 1986 [37].

  Equipment: Home-made ultra low noise potentiostat with extensive filtering, applied to an erosion-corrosion scenario, on steel.

  Found: Evidence for electrochemical activity at two frequencies. Activity at ~ 3 Hz attributed to pitting. Activity at ~ 30 KHz attributed to depassivation/repassivation resulting from particle impact. Need to measure to 10^5 s^{-1} to get all of this.

- A. Neville *et al* 1995 [92].

  Equipment: Oscilloscope

  Found: Oscillations at millisecond timescales, on steel.

- P.C. Pistorius 1997 [90,93]

  Equipment: 'Digital recorder', sampling at 50 $secs^{-1}$ or 10^3 $secs^{-1}$.

  Found: Diffuse peak in *psd* plot at ~ 40 Hz, on steel. Data well recorded if sampled at 10^3 $secs^{-1}$.

- A. Burkert *et al* 1998 [94]

  Equipment: Datalogger, bandwidth limited to 0.1-40 s^{-1}.

  Found: *psd* plots suggest that useful data range would extend to at least 100 Hz. On aluminium coated steel.

- G.T Burstein and K. Sasaki (2000) [20,66]

  Equipment: Potentiostatted 2-electrode recording of electrochemical noise at 5×10^5 s^{-1}.

  Found: Distinguishably different current transients from impacts and metastable pitting. On 304L stainless steel wire electrode.

Danielson [95] has modelled both the potentiostatted single WE and the two WE configurations. His calculations suggest that, for steel in 3.5% NaCl, measurements at $>10^3$ s^{-1} will be unreliable because part of the cell current will be shorted within the

cell by the double layer capacitance of the WE. This sampling frequency should not be taken too literally, since the actual numbers will depend on the details of the experimental materials involved. Also, a static cell was considered, and as noted above (Section 2.3.3), Legat [57] has shown that changes in mechanism can result in changes in Electrochemical Noise data. Nevertheless, there is an unexplained discrepancy between this calculation and the results of Oltra [37], noted above.

Between them, these papers suggest that noise measurements should initially be made at the highest frequencies that can conveniently be achieved. If no noise is observed at high frequencies, the sampling frequency should be reduced as far as possible, consistent with anti-aliasing requirements (see below) to minimise data logging requirements. The low frequency limit is, in practice, determined by stationarity considerations (see below) and the size of the data file that can be accumulated.

Anti-aliasing. It is explained in books on digital signal processing [e.g. 93] that an effect of digital sampling is to introduce artefacts into the recorded signal ('aliasing', i.e. power belonging at higher frequencies), unless suitable filtering is used. In general, if this filtering is carried out correctly and the sampling frequency is f_s, then the maximum frequency at which reliable data may be obtained is, in principle, $f_s/2$ (the Nyquist frequency). It is essential that this filtering is applied before analog-to-digital conversion, since aliasing cannot be removed once it has been introduced. This $f_s/2$ criterion is applicable to an ideal system; for real systems with imperfect filters, reliable data will not be obtained above (0.2-0.4) $\times f_s$ depending on filter type.

This is discussed in detail in the context of Electrochemical Noise by Bastos *et al.* [94], who used synthetic signals of known characteristics to define the effects of various kinds of filters. For systems which produce 'white noise', i.e. flat *psd* plots, system power is overestimated in unfiltered systems to an extent which is a function of the sampling rate, but may typically be × 4. Furthermore the time record is also affected, so that time record statistics, such as standard deviation, skewness and kurtosis, will also be incorrect; this may be less than obvious from inspection of the

recorded data. For systems showing 'pink noise', i.e. sloped *psd* plots, both the slope and the power levels may be incorrect. If mains frequency (and harmonic) effects are not filtered out, complicated low frequency 'beat' artefacts may be introduced if mains frequency is not an exact multiple of the sampling rate. The slope of the filter characteristic is of prime importance in determining filter efficiency; Chebychev filters are recommended. By contrast, the low-slope data averaging filters commonly implemented in DVMs do not prevent aliasing effectively.

Detrending. Similarly, data often show long-term drift, which is no part of the required signal. This is best removed by mathematical detrending on the recorded data [94], e.g. using MATLAB. (High pass analogue filters with long time constants have been used in the past, but lead to experimental problems owing to their long recovery times).

Resolution. The electronics should have sufficient resolution to cope with the dynamic range of the data, to avoid quantisation error. In practice, all available equipment has 16-bit resolution or near. Procedures for estimating effects of quantisation error are given in [99].

Background Noise. It is essential to minimise and characterise the background noise in the system (not just in the electronics, which are not normally limiting). Procedures for estimating background noise are given in [99]. Steps to do this include:

- Use of a Faraday cage to exclude through-space electric fields. Consideration should be given to whether magnetic fields are likely to be problem.

- Exclusion of light from light sensitive electrodes, e.g. Ag/AgCl REs.

- Filtering the mains input to the system to exclude starting transients from other equipment (notably lighting) in the building. Measurement equipment should also filter 50 Hz and its harmonics from the data signal.

Data Analysis – Stationary data. A variety of methods have been used to analyse noise data. Most of these have been conveniently summarised by Searson and Dawson [100].

If both the mean current and its standard deviation are invariant over time, the signal is said to be stationary [101]. Most analytical methods assume this. Most real data only approximates it. The most straightforward mode of analysis is to compute a mean current (which should ideally be invariant, but is often not, in which case de-trending is required – see above), and then to compute standard statistical parameters about this detrended mean – standard deviation or variance ('power' in signal processing language), skewness and kurtosis. Calculation of these quantities, whose variability over time is required, involves careful consideration of the length of data sets. The lowest frequency that can be estimated is defined by the length of the data set, so that if low frequencies are important, long data sets are needed, but this precludes following rapidly changing (non-stationary) situations. Factors influencing lengths of data sets are discussed in standard textbooks on digital signal processing, e.g. [96].

Probability density functions (*pdf*) describe information about the data in the amplitude domain and describe the probability that the data will assume a value within a defined range at any instant of time. For zero mean:

$$pdf = \frac{N_x}{NW} \tag{2.25}$$

where N_x is the number of points which fall within the range $(x \pm W/2)$

N is the total number of points (within the window)

W is the bandwidth centred at x.

The *pdf* is usually used just to check that the noise spectrum is genuinely random and not deterministic – its shape should be roughly Gaussian. However, in a real experiment more than one source of random noise will exist. In particular, there will be instrument noise as well as electrochemical noise in the signal. In a well designed experiment the large amplitude noise will be all electrochemical, but the small amplitude noise will include a component of instrument noise. In a complex corrosion situation, involving more than one anode (or more than one current path), the *pdf* may provide a route to separating various simultaneous processes, or processes occurring at different times within the experimental period; this is unexplored.

The autocorrelation function of a stochastic process describes the general dependence of values of the data at any instant with previous values, i.e. the 'memory' of the system. The autocorrelation function of a system with zero mean can be estimated from:

$$A(r) = \frac{1}{N}\sum_{n=1}^{N-r} x_n x_{n+r} \tag{2.26}$$

for x_n; = 1,2,....N

lag r = 0,1,2,....m, where m is the maximum lag number

This value can be positive or negative, so a normalised autocorrelation function, A_0, is often used:

$$A_0 = \frac{A\ (r)}{A(0)} \tag{2.27}$$

$$\text{where } A(0) = \frac{1}{N}\sum_{n=1}^{N} x_n^2 - x^2 \tag{2.28}$$

A widely used function for noise analysis is the power spectral density (*psd*). This is, in general, the Fourier transform of the autocorrelation function. There are several algorithms for estimating the *psd*, and there has been extensive discussion concerning the most appropriate one to use [e.g. 98,99]. Most common is the Fast Fourier Transform, usually estimated by the Cooley-Tukey FFT algorithm. So long as aliasing is avoided, this gives a reliable result, but can require long acquisition times for ensemble averaging to reduce otherwise large errors, especially at the high frequency end of the spectrum. If ensembles are arrived at by taking sections of a very long stationary data set, then a 'windowing' process is necessary to make the ends of the individual sections 'match up' – a variety of windowing functions are available [96], but their behaviour varies very little; a Hanning function (a half-cycle cosine function) is commonly used. An alternative means of estimating the *psd* is the Maximum Entropy Method (MEM), derived from information theory. This yields a smooth spectrum, with relatively short acquisition times, but at the cost that an 'order' parameter, M_{MEM}, has to be introduced; the value to be given to this is unknown. It is claimed [98] that, since corrosion electrochemical noise is random, small values of M_{MEM} may be used, since they produce a smooth spectrum from computer generated white noise – but this is to assume the answer one wishes to obtain. Schauer *et al* [102] review a variety of algorithms for deciding M_{MEM}, called by them the optimum filter length, objectively, but it is rather doubtful whether any of these methods really justify the considerable computational effort involved. If this approach is to be used, they recommend the criterion autoregressive transfer function (CAT). Probably the safest approach is to use the MEM, if at all, only for direct comparison of similar samples to identify trends, where the same values of M_{MEM} can be used for each, and only relative values are required; for quantitative work the FFT should be used.

If, by whatever means, a believable *psd* function can be obtained, several parameters can be extracted, illustrated in Figure 2.17.

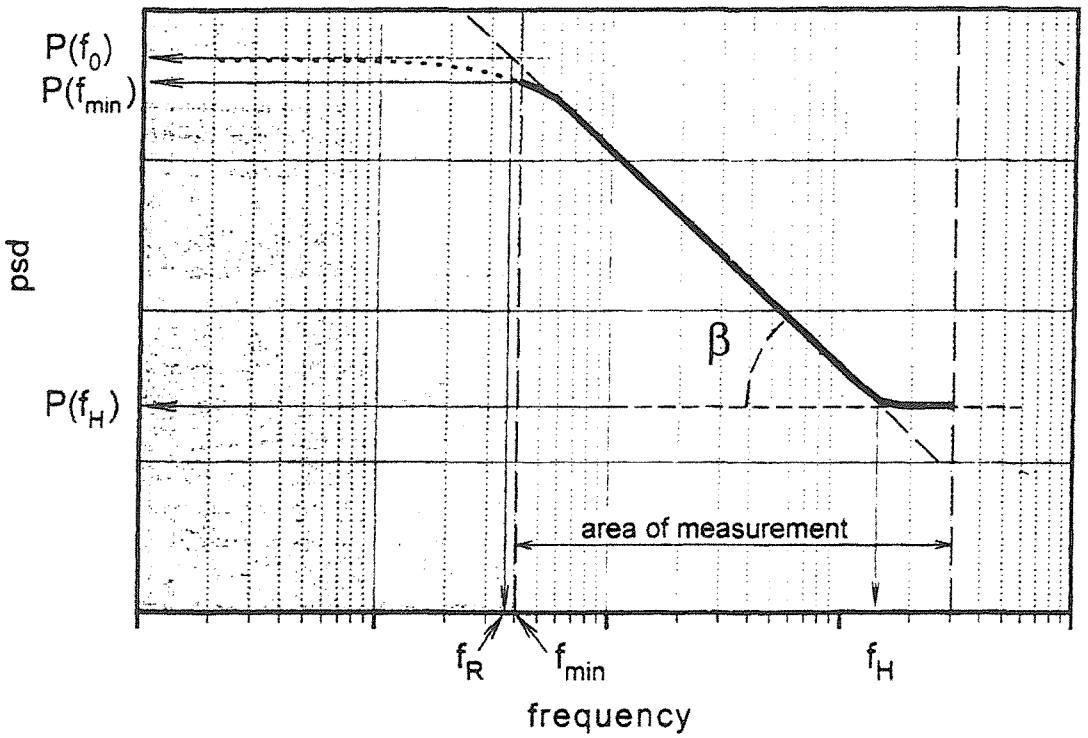

Figure 2.17: Schematic of power spectral density plot.

From: T. Schauer *et al, Electrochimica Acta,* 43 (1998) 2423-2433

Attempts are made to correlate $P(f_0)$ (or $P(f_{min})$) and $P(f_H)$ with polarisation resistance, but the results of such claims, (e.g. [103]), are, at best, disputable. Of more interest is the slope of the middle part of the curve, from which mechanistic information may be obtained [100,104,105,106]. There is an important distinction here between potential noise and current noise, most clearly explained by Legat and Dolecek [105]. For potential noise, general corrosion yields nearly flat *psd* plots, whereas passivation and pitting both yield steeply sloped plots. Conversely, for current noise (whose magnitude is held to correlate with mass loss better than potential noise) general corrosion yields flat or nearly flat *psd* plots ("white noise"), as does passivation, whereas localisation leads to steep plots – the greater the localisation the steeper the plot. There has been much discussion of these findings and other authors, working mainly with stainless steel, have disputed these conclusions; they do not agree amongst themselves – a possible reason for this will be suggested in Section 5.4.5.

However, if consideration is limited to current noise on aluminium, a reasonably consistent picture emerges (see Section 2.6.4).

Data Analysis – Non-stationary data. All of the above methods require that the signal is stationary in the sense indicated at the beginning of this Section. If it is not, then more complex analysis methods are required, known as Joint Time-Frequency Analysis (JTFA). These are reviewed in a book by Chen and Qian [107]. Some of the methods in this book are used in the Gamry potentiostat software employed in this work.

A particular form of JTFA, the 'wavelet transform' has been used to a minor extent [108-116] to describe Electrochemical Noise data, mostly descriptively. Its relevance is not yet clear. The mathematics of the wavelet transform is presented at length in a book by Mallat [117], and its practical operation in a more user-friendly form in the MATLAB Wavelet Toolbox Manual [118]. The wavelet transform, and particularly the Discrete Wavelet Transform (for which MATLAB provides a graphical user interface), allow a means to isolate data features, characterised by their occurrence on a particular timescale, from other processes that may be present on other timescales. The Discrete Wavelet Transform can be shown to be equivalent to a filter bank; design of such a filter bank is discussed in detail in a book by Strang and Nguyen [119]. It is important that this technique separates on the basis of time scale, and is therefore complementary to Fourier Transform techniques, which separate on a frequency basis.

Aballe *et al* [108,109,113,115] have developed a particular data representation, called by them (incorrectly) an 'energy distribution plot', also used by Dong *et al* [114] (who, more correctly, call it a 'power distribution fraction'), which illustrates the dependence of Electrochemical Noise power on transient timescale. These authors have concentrated on the signal processing aspects of the technique, with relatively little chemical interpretation. However, Aballe *et al* [115] have used this to study the

inhibition of corrosion of Al/Mg AA5083 alloy by $CeCl_3$, and this sort of study could clearly be developed further.

The operation of this technique will be discussed further in Section 6.3.4.

A particular problem that arises with the use of wavelets is that the wavelet transform is a class of techniques, and mathematicians have developed several dozen different versions of it, mainly for image compression applications. These applications have particular requirements, which it is not at all clear are shared by electrochemical data. There is no accepted way of deciding which wavelet to use for an arbitrary application. A very recent development by Huang *et al* [120] may resolve this difficulty in future. This is a technique, based on calculating instantaneous frequencies, which calculates an appropriate scaling function for a particular data set from the data themselves. It is not yet implemented in MATLAB, though this is expected in future.

Data Analysis – General Comments. It is important to recognise that parameters derived by any of these methods, e.g. slopes from psd plots, are in themselves no more than convenient ways of describing the data. They may then be correlated *empirically* with different corrosion conditions. They say nothing about underlying processes. The latter may be modelled to demonstrate that a particular proposed process would result in an electrochemical signal of particular form, which may be consistent with observed data (or not). Even if consistency is demonstrated, it is not possible by these means alone to show that a model is *uniquely* consistent with the data. Furthermore, information about individual localised events can only be obtained in cases where single non-overlapping transients can be obtained. When, as often occurs, transients occur so frequently that they overlap, then only general information about corrosion processes will be obtainable, e.g. concerning the degree of localisation.

From a corrosion perspective, clear parametisation of electrochemical data, and empirical correlation of estimated parameters with particular observed corrosion modes are probably as much as can be expected, except in particular, very favourable cases. Even at this quite modest level, there are so many experimental and data processing constraints that have to be satisfied that comparisons with work carried out in different laboratories should only be done with extreme caution. For example, a round robin experiment [121] carried out on standardised corrosion experiments resulted in quite large discrepancies between ENA results obtained by different laboratories. These were traced to differences in data acquisition and data handling.

2.5 EQUIPMENT

2.5.1 Equipment for Erosion testing.

Historically, equipment for erosion testing was designed to simulate a particular problem scenario, and provided results difficult or impossible to use in any other context. For results to be useful in a wider context, the impact conditions need to be well defined. These include particle velocity, flux and impact angle. Figure 2.18, taken from Hutchings [5], illustrates four equipment designs which have been used to achieve this.

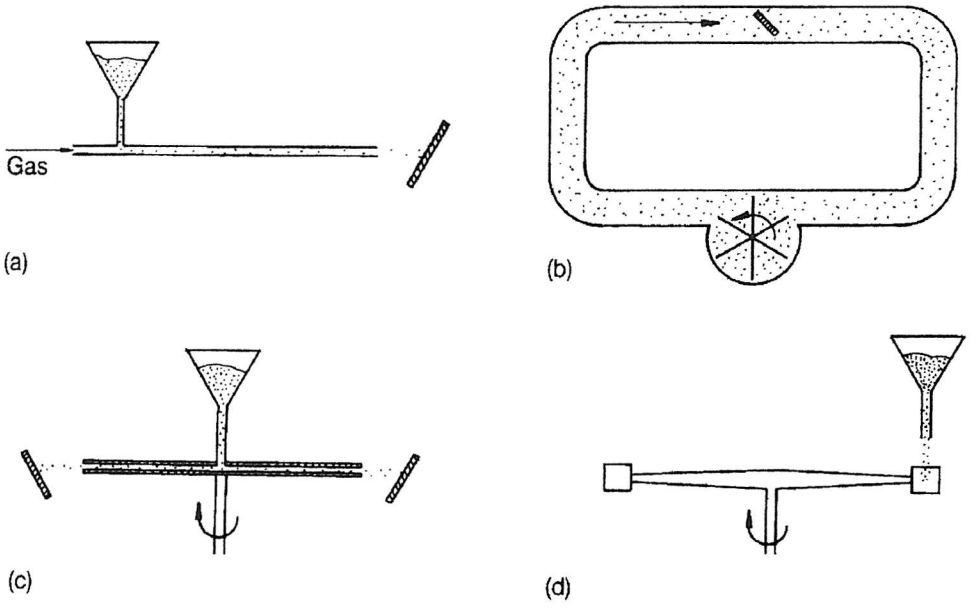

Figure 2.18: Schematic illustrations of erosion testing test arrangements.
From: I.M. Hutchings, Tribology: Friction and Wear of Engineering Materials.

Arrangement a), the jet-impingement apparatus, may be used with gas or liquid as the carrier fluid. It generally has the best defined geometry of all the arrangements, but even here, as noted in Section 2.1.5, the flow field is quite complicated. Solid feed

arrangements are usually made in such a way that solid is used only once, thus avoiding complications due to the erodent itself becoming worn.

Arrangement b), the recirculating loop arrangement, is useful for testing pipes and pipe fittings. The solid may pass through the pump, as shown, or may be separated from the fluid and reinjected.

Arrangement c), the centrifugal accelerator, and d), the whirling arm arrangement are also sometimes used, but the impact conditions are difficult to define, and these arrangements are less preferred. Another variant of this, described as the 'sample rotation method', with samples embedded in a wheel rotated in the slurry, has been used by Prasad *et al* [122]. Slurry-pot testers, with a geometry similar to d), have been quite widely used to compare materials. Madsen [123] has used such a device to measure erosion-corrosion synergism, polarisation curves being obtained within the slurry pot (though it is questionable how valid these curves were, since sweep rate and stationarity issues were not addressed – see Section 2.4.3).

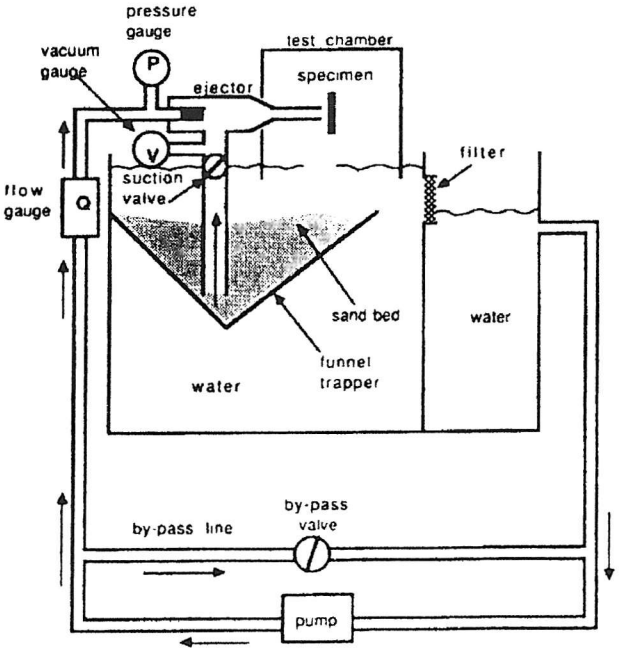

Figure 2.19: Slurry erosion test rig.
From: Zu *et al, Wear* 140 (1990), 331-344

Zu *et al* [124] have designed a slurry erosion test rig, which incorporates features of arrangements a) and b), above. Figure 2.19 illustrates this.

A recirculating system has been constructed to feed a nozzle, the jet from which impacts on the test sample. In this case the pump circulates water. Just upstream of the jet-forming nozzle is an ejector, used to entrain a sand slurry. The concentration of sand in the jet is controlled by altering the ejector dimensions (inlet and outlet diameters and inlet jet position relative to the sand intake). Downstream from the sample, sand is filtered out before it reaches the pump. This arrangement allows control of all the important erosion variables, and relatively simple operation.

Puget [125] has built a metal-free version of this rig, suitable for erosion-corrosion and electrochemical measurements – see further below.

A very strange variant of this type of equipment has been used by Matsumura et al [62], in which an ejector is used to suck a sand slurry over a target. It is hard to see the advantage of this arrangement, in which the flow field is poorly defined.

A recent trend in erosion testing has been to design equipment to study very dilute slurries or single impacts. One example is the equipment used by Burstein and Sasaki in their electrochemical noise work, noted previously [20]. In this, particles from a very dilute slurry maintained in suspension in a separate vessel were transferred by dropper to an injection port in a conventional ejector.

A more radical design is the 'Coriolis tester', originally designed by Tuzson [126] and developed by Xie *et al* [127] and by Clark *et al* [128]. It is illustrated schematically in Figure 2.20. In this, a very dilute slurry is supplied to the centre of a disc, rapidly spinning on an horizontal axis (up to 7500 rpm), and is allowed to escape to the edge by means of shallow channels in the disc surface. The target(s) to be eroded are inserted into the disc, flush with the channel bottoms. This allows well

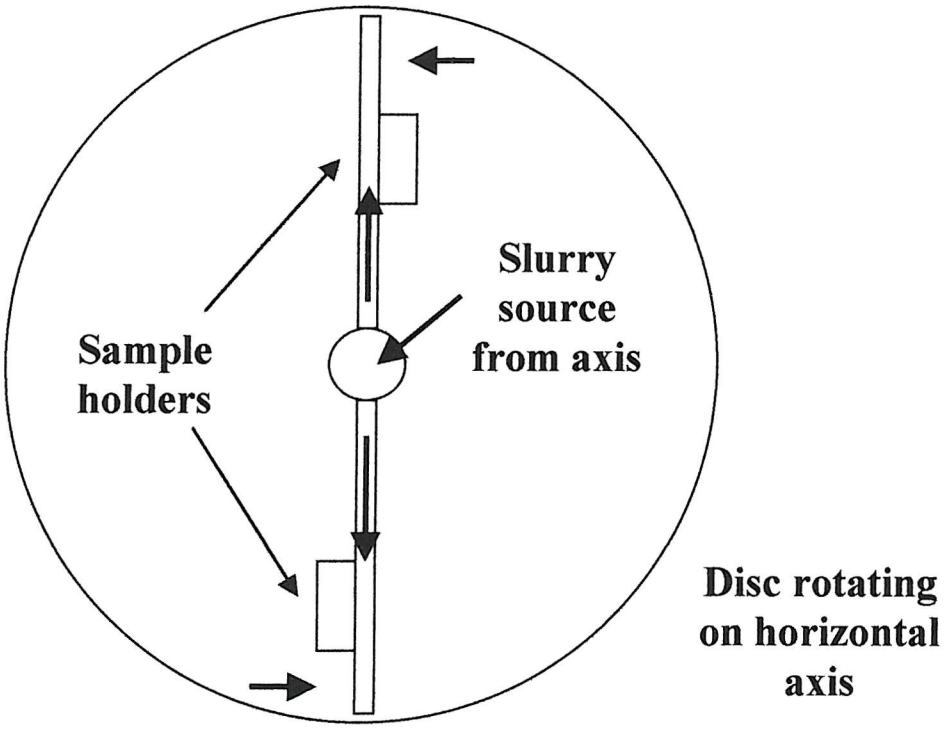

Figure 2.20: Schematic of 'Coriolis tester'.

Redrawn from: H. McI. Clark, J. Tuzson and K.K. Wong, "Measurements of specific energies for erosive wear using a Coriolis tester", *Wear*, 241 (2000), 1-9

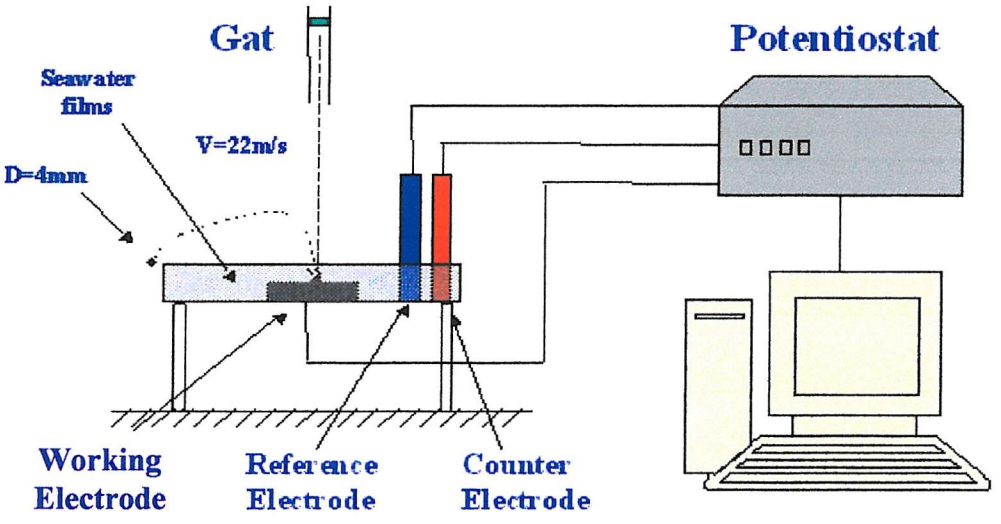

Figure 2.21: Schematic of air gun tester

Courtesy: Prof. A. Neville, U. Heriot-Watt

characterised single impacts to be recorded, albeit only at very grazing angles of incidence. Specific erosion energies are estimated from frictional losses.

A further design is that of Neville *et al* [22], in which an air gun is used to project single particles at a target surface, which may be covered with a film of electrolyte. This is illustrated schematically in Figure 2.21. This allows angular flexibility, but it is not clear how the impact of a rapidly moving particle through a static film will compare with that in a moving slurry – the hydrodynamics and therefore the oxygen access will be quite different.

All these single particle techniques aim to abstract a simplified impact situation from slurry corrosion, so that basic interactions may be studied. Nonetheless, most real slurry corrosion situations of interest involve relatively dense slurries (1-50% w/v), so this simplification cannot provide all the answers. There remains a need to study dense slurry systems where co-operative effects between particles may be important or even dominant.

2.5.2 Equipment for erosion-corrosion testing

Essentially, this should be equipment similar to that discussed in Section 2.5.1, but metal-free and with provision for carrying out electrochemical experiments. Various approaches have been made to this.

Pitt and Chang [129] constructed an immersed jet slurry apparatus, in which the sample was the working electrode. The counter electrode was a platinum mesh, mounted immediately upstream of the jet – and therefore in the mineral concentrate slurry, where it must have been eroded itself and been very vulnerable. The reference electrode was a 'calomel' electrode (not further defined), connected to the slurry stream via a Luggin capillary. This equipment was used to measure open-circuit potentials, and to polarise the test sample with a view to suppressing corrosion in some experiments.

Madsen [127], as noted above, built a slurry pot tester with provision for electrochemical testing. The slurry pot contained a number of sample holders, most of which were occupied by test samples, each of which could be used as the working electrode, via a switching arrangement. Two of the holders were replaced by mild steel blanks (subject to erosion), which served as counter electrodes. Reference electrodes were made by drilling holes through the centre of each working electrode and inserting a capillary, connected to a saturated calomel electrode (SCE). This arrangement was used to measure polarisation curves *in situ,* a questionable procedure in a dynamic system, as noted above, quite apart from the unusual cell geometry.

Li *et al* [130] have modified the Zu *et al* jet slurry erosion rig, in order to be able to carry out electrochemical experiments. The stainless steel nozzle of the ejector (in the slurry stream) was used as the counter electrode, whereas the reference electrode was an SCE connected to the liquid stream upstream of the sand injection. Polarisation curves were obtained under erosion conditions.

Puget [125] has, as noted above, constructed a metal-free version of a jet slurry erosion rig. This was set up to carry out electrochemical current noise experiments, and had a counter electrode in the form of a carbon rod, set into the liquid stream upstream of the ejector. No reference electrode was provided, so the rig as described was not suitable for making measurements under potential control. Couple-current measurements, incorporating some element of galvanic current between working and counter electrodes, were carried out.

Burstein and Sasaki [20,66] have used a ejector system, designed as a 2-electrode cell under potential control, to measure Electrochemical Current Noise in very dilute slurries. The conventional counter and reference (Ag/AgCl) electrodes were combined in order to minimise external noise and the instrumentation response time. This was possible because the combined electrode was made 25000× the area of the working electrode and therefore the current density on it was too small to cause

polarisation (the validity of this uncheckable assumption is crucial to the acceptability of this cell design).

The Neville *et al* [22] single particle design, noted above, is designed to be used to obtain an electrochemical response (a current transient), with counter and reference electrodes immersed in the electrolyte film relatively distant from the particle impact point, implying significant iR drop in the film, even in brine.

Submerged jet rigs have been used by Pitt and Chang [129], Oltra *et al* [37] and by Neville *et al* [92]. These come closer to reproducing the real condition in fluid pipework and would in principle allow control of oxygen concentrations, but are typically less convenient to build and operate.

The use of segmented electrodes in jet impingement apparatuses has been advocated by Dawson *et al* [55], to investigate the heterogeneity of the jet, but does not seem to have been followed up. This is a difficult experiment, not least because segmented electrodes are very prone to crevice corrosion with attendant noise, but success with this approach could be very informative.

In summary, several attempts have been made to carry out electrochemical experiments under erosion-corrosion conditions. This is intrinsically difficult, as it is awkward to arrange for suitable cell geometries, without involving erosion of counter and reference electrodes. Also, insufficient care seems to have been taken to ensure that equilibrium and stationarity requirements have been met, when measuring polarisation curves. Relatively little work has been done on more complex electrochemical techniques.

2.6 METAL CLADDINGS FOR EROSION-CORROSION PROTECTION

2.6.1 Basic considerations for materials selection

As noted in the introduction to this report, the specific focus of this work is the performance of internal pipework in naval ships, subject to simultaneous erosion and corrosion. It is desired to replace expensive alloys, which do not resist erosion-corrosion particularly well, with cheaper systems, based on coated mild steel. For metallic coatings, there are four considerations:

Erosion resistance – hardness is a rough guide to this.
Corrosion resistance – anodic or cathodic nature w.r.t mild steel.
Synergy effects – unknown.
Cost.

For pure metals, Hutchings [5] gives a correlation of erosion loss with the Vickers Hardness of the eroded (work hardened) surface, showing, on a log-log scale, a linear decrease of weight loss with increasing hardness. For the most likely coating metals (on cost grounds) – aluminium, copper, nickel, zinc – this shows nickel as the hardest, most erosion resistant metal, followed by copper and then aluminium (zinc not given). He also points out that conventional hardening means (by alloying or heat treatment) do not always have the expected effect on reducing erosion, probably because of the very high local straining rates involved. Table 2.1 gives some further data obtained at Southampton University (E_k and V_u are kinetic energy/nominal impact and volume removed/nominal impact respectively).

In terms of corrosion, the important distinction is between anodic and cathodic coatings, see Figures 2.10c and 2.10d. Of the four metals considered, zinc and aluminium are both anodic, i.e. they will protect steel galvanically in seawater, and are indeed used in offshore applications for this purpose. Copper and nickel are both

SELECTED METALS EROSION

Normal Incidence

MATERIAL	DENSITY / kg.m^{-3}	SURFACE HARDNESS H_{v30}	V_u / μm^3/impact at E_k = 0.48 μJ	V_u / μm^3/impact at E_k = 8.0 μJ
Cast Stellite 6	8360	415	0.105-0.417	1.05-1.35
Zeron 100	7870	270	0.249-0.251	3.3-3.9
Inconel 625	8440	275	0.41	9.6
AISI 1020	7850	220	0.41-0.55	8.5-9.4
Ferralium 255	7810	300	0.44-0.46	11.2-12.3
Nickel	8810		0.7	20
Titanium alloy	4460		0.66-0.80	19-23
316 SS	7840	200	0.55-0.566	35-45
Zinc (h/d galv)	7100	220		103
Cupronickel 90/10	8000	98	1.2	4.25
Chromium (pulsed)	6920	900	0.061	
ENP/SiC	7950	450	0.127	

Table 2.1

cathodic coatings, i.e. they are not protective to steel (even though as bulk materials they may be corrosion resistant in themselves), and, moreover, where holidays in the coating occur, exposed steel is likely to be rapidly corroded; it would be a condition for using copper or nickel (or their likely alloys), either that a situation is guaranteed that there are no holidays (implausible), or that an additional coating (probably organic) is used to protect the holidays.

There is thus a conflict in the material requirements, in that the galvanically protective metals are soft and the hard metals will promote corrosion on steel where steel is exposed. This is shown schematically in Figure 2.22. The options are to harden zinc or aluminium by alloying or composite formation, or to modify copper or nickel to change or disguise their electrochemical properties. No means are apparent to achieve the latter, so the remainder of this section will concentrate on reviewing what is known of the behaviour of anodically protective metals.

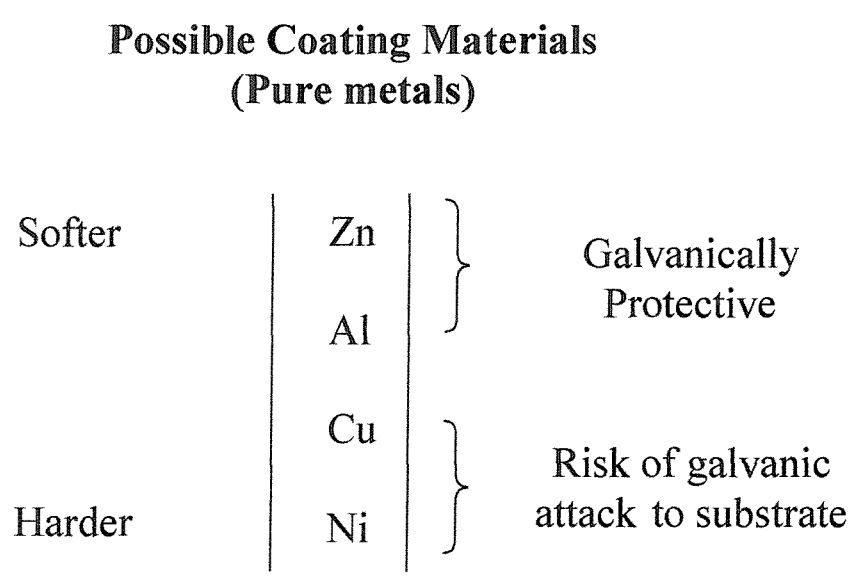

Figure 2.22: Schematic of material properties

2.6.2 Metal claddings for steel protection – US practical experience

The American Welding Society [131] has issued a long term test report on the performance of metallised test coupons in seawater and marine atmospheres. The main conclusions after 19 years exposure were:

- Unsealed zinc coatings required 0.30 mm thickness to give complete protection in seawater for 19 years. Application of vinyl based sealants to thinner coatings could extend lifetimes by up to 100%.

- Aluminium sprayed coatings (0.08 – 0.15 mm thick), sealed and unsealed gave complete base metal protection from corrosion in seawater and also in severe marine and industrial atmospheres, including at sites of mechanical damage. Thin aluminium coatings performed better than thick ones, allegedly due to a reduced tendency to pit or blister. The effect of sealants was mainly cosmetic.

It is understood that these test coupons are still under test and will be re-examined on the 50th anniversary of their immersion in 2002; this is not yet reported.

The United States Army Corps of Engineers (USACE) is responsible for the maintenance of many civil and military installations throughout the USA. They have issued extensive technical guidance for the use of thermal sprayed coatings in river and seawater [133]. This guidance emphasises the importance of using anodic coatings with good adhesion and low porosity. Zinc, aluminium and zinc-aluminium alloy coatings are used, with and without organic sealers. Aluminium is preferred to zinc in seawater because "aluminium coatings are harder, have better adhesion to steel and form a protective oxide layer that prevents self corrosion". Organic sealers are generally not used. Al/Zn alloys "are also quite widely used", though this document does not detail the circumstances in which they would be preferred. However, it is noted that zinc containing coatings can prevent marine fouling. HVOF spraying is recommended.

Similarly, the US Navy specifies [133] aluminium sprayed coatings for corrosion protection, mainly in topside areas. A review [135] of coatings performance under this specification is available. To date, performance over more than 20 years has been wholly acceptable and the procedure is seen as very cost effective.

In a development of this practice, USACE has reported [136] very large scale trials, involving the thermal spraying of whole lock gates on the Ohio River, downstream of

Pittsburgh, i.e. in very dirty (though not saline) water. These lock gates, approximately 30 m wide, are subject to impact by logs, up to 1 m in diameter from upstream felling operations (note that the scale does not matter [7]). The river flow was about 10 $m.s^{-1}$. Individual lock gates were sprayed with zinc, 85/15 Zn/Al alloy (expected to be harder than pure zinc), aluminium bronze and 18/8 stainless steel. The zinc-based systems were anodic to the steel lock gates while the others were cathodic. The metallic coatings were applied with and without organic sealers. After 2 years, the zinc based coatings showed substantial algal growth but no corrosion. Both the aluminium bronze and stainless steel coatings showed extensive "pinpoint rusting" at coating flaws, and some delamination at locations which suffered the maximum impact damage. The behaviour of the organic sealers seems to have been somewhat equivocal.

2.6.3 Zinc

Zinc in marine use.

Apart from the use of galvanised structures, the major marine use of zinc is as sacrificial anodes [49]. Very large anodes are used to protect static structures, such as oil rigs. Much smaller anodes, often distributed about a hull to minimise the effects of resistive losses, are used to protect ships' hulls, particularly smaller ones (larger vessels tend to use impressed current cathodic protection systems). The zinc used for this purpose is an alloy [136] containing 0.1 - 0.5% aluminium and 0.02 – 0.07% cadmium. These additives are present to ensure uniform dissolution of the zinc. It is reported that mass loss in use is approximately 4 times mass loss 'pierside' (for the reason for which, see next Section).

Zinc Corrosion

Surprisingly little has been reported about the corrosion of zinc in brine. The definitive published work remains that of Bengough and May [137], published as long ago as 1924!

Under static conditions they found that initially rapid corrosion became strongly inhibited by a gelatinous layer of white corrosion product. It was established that this consisted mainly of (hydrous) zinc oxide/hydroxide, admixed with zinc carbonate and some zinc chloride (oxychloride?). The degree of corrosion inhibition under these circumstances was strongly dependent on the carbonate content of the film, carbonate-free-films inhibiting pitting entirely. Pits were more numerous but smaller on specimens exposed to distilled water than on specimens exposed to seawater. This was related to the greater solubility of carbon dioxide in distilled as opposed to seawater. At high levels of carbon dioxide, the film becomes uniformly pervious, and pitting is dispersed. At lower levels, only weak spots in the film become pervious, and corrosion is more localised.

It was noted that when zinc coupons were exposed to aerated water jets (~ 1.7 $m.s^{-1}$), most of the flow corrosion took place away from the point of jet impingement. Experiments with multiple linked electrodes suggested that zinc surfaces distant from the jet became anodic (by 7 – 8 mV) to the area directly exposed to the jet. This was attributed to greater oxide growth under the jet (because of greater oxygen transport to the surface) than at more distant points.

If the flow of aerated water was increased to ~ 3 $m.s^{-1}$ a different result was obtained. Now the flow was sufficient to wash the corrosion product away, and pitting was concentrated under the jet. A similar, but more intense corrosion behaviour was observed from a solution of 3.0% NaCl flowing at ~ 8.3 $m.s^{-1}$.

Overall, Bengough and May found that the corrosion behaviour of zinc depended on the existence of a film of corrosion product. The existence and porosity of this film depends in a complicated way on flow conditions (high flow tends to remove the film) and the composition of the electrolyte (chloride causes 'perviousness' of the film, oxygen reinforces it, but the last effect may be opposed by dissolved carbon dioxide).

This work was repeated (on brass) in real seawater by LaQue [138,139], who, unsurprisingly, obtained similar results. He did, however, make the additional observation that when his seawater contained silaceous diatoms, as it did seasonally, mass losses were substantially increased. This is one of the earliest notices of erosion-corrosion (and seems to have caused some surprise at the time).

It would be of interest to know how these factors affect the corrosion performance of the alloy used in sacrificial anodes.

Only one paper has been found on the application of Electrochemical Noise to zinc or zinc coatings. Diaz-Ballotte and Garfias-Mesias [140] measured the Electrochemical Noise characteristics of hot-dipped galvanised steel in saturated calcium hydroxide solutions, in the context of galvanised rebar corrosion. Both potential and current noise were measured. Discussion centred on the passivity or otherwise of the zinc in these very alkaline systems. It is claimed that corrosion rates (assumed to be of zinc only) were roughly correlated with potential noise changes and more reliably with current noise changes, though no weight loss data are quoted.

Prasad [122] has investigated the erosion-corrosion behaviour of zinc/37.5% aluminium alloys in synthetic minewaters (containing chloride and sulphate ions). Addition of 4% silicon made a large improvement to the 'wear resistance' of the alloy, though the measuring equipment used makes this a rather qualitative finding.

2.6.4 Aluminium

Aluminium in marine use

Aluminium is used in marine duties either structurally or for its galvanic properties relative to steel. Structural uses have been recently reviewed [141] and are not considered further. Galvanic applications may be as sacrificial anodes or as thermally sprayed claddings.

When aluminium is used for making sacrificial anodes for use in marine conditions, it is used in the form of an aluminium/zinc/indium alloy [142]. Zinc is added to control the behaviour of the passivation layer, to prevent pitting. Similarly, indium (and sometimes gallium) is added to activate aluminium dissolution (reduce charge transfer resistance), possibly through cyclic dissolution and redeposition of indium (gallium) compounds in variable valence states. How these additions will behave in an erosion-corrosion situation, in which the passivation layer is being continuously removed is not clear, but in the real shipborne application erosion-corrosion will not occur either over the whole immersed area or all of the time.

However, papers relating to the use of thermal sprayed aluminium claddings in submerged marine environments, e.g. for tension leg elements for North Sea oil production platforms, [143,145] advocate the use of commercially pure aluminium or aluminium/5% magnesium. Use of zinc containing alloys would increase anodic efficiency at the expense of barrier properties – the coating would break down too rapidly to give desired service lifetimes (of the order of 10-30 years). These papers also emphasise the importance of coating adhesion, and of factors tending to plug the porosity inherent in sprayed coatings (typically a few per cent). In this latter respect, the following points are made:

- Aluminium sprayed coatings perform better than zinc sprayed coatings in the splash zone or in submerged service, because their corrosion products are better at plugging porosity.

- Use of a suitable sealer over the sprayed coating is seen as essential; these authors found that silicone based sealants performed better than vinyl based materials – whether this would still be true under sand erosion is unknown.

- In real seawater, cathodic pores tend to become clogged by calcareous deposits.

Other authors [145] have recommended aluminium phosphate as a sealer.

Aluminium metal

Zu *et al* [146] studied the erosion of aluminium by silica sand in air and in water. They found that, under otherwise similar conditions, erosion in water took place several times faster in water than it did in air, the exact rate depending strongly on impact angle. This was because, in air, sand particles became embedded in the surface of the aluminium in a way that did not occur in water. This result suggests that deliberate embedment of hard particles in aluminium might be beneficial, but that it might be difficult to avoid loss of this reinforcement under erosion(-corrosion). Lubrication of the impacting surfaces by water (squeeze film effect) appears to be minimal.

Li *et al* [130,147] have extended this work to more aggressive slurries, including salt water slurries. They found that, in 0.5M NaCl, below –2.0V *vs* SCE erosion-corrosion rates were independent of potential (fully filmed surface), between –2.0V and –0.75V (the pitting potential) rates increased slowly (film thinning), and above the pitting potential rates increased rapidly. Mass loss is ductile in nature (flake

forming) and it is suggested that the increased roughness caused by pitting facilitates flake detachment (this roughening mechanism for increasing erosion loss has previously been proposed by Postlethwaite [148,149] in the context of coal slurries in pipelines). It is also suggested that localised corrosion promotes cracking at the base of the flakes, which are in any case highly stressed.

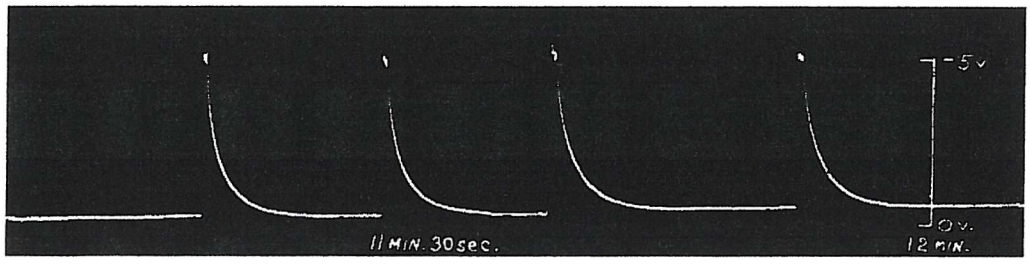

Figure 2.23: Potential transients on an aluminium micro-electrode
From T. Hagyard and M.J. Prior, *Trans Faraday Soc,* 57, (1961), 2288-2294

The earliest identified study of electrochemical noise (not so called) on aluminium is a paper by Hagyard and Prior [150], who studied potential transients at open circuit on aluminium micro-electrodes. Very sharp transients were observed, see Figure 2.23, in the negative (active) direction. These were attributed to localised breaking and re-sealing of the passive film. These sharp, well formed transients were not observed on larger electrodes, where there is too much activity to resolve individual events.

A related study by Hagyard and Williams [151], using relatively large scratched electrodes to obtain fresh aluminium surfaces, related sharp potential changes to a series of processes, identified as aluminium ionisation, hydrogen formation and passive film formation, on progressively increasing time scales. The potentials observed (hydrogen scale) indicate that a fresh aluminium surface should have a potential around –1.6 V, a passive surface in the presence of oxygen around –0.5 V and a passive surface in a de-oxygenated environment around –1.1 V. This means that the behaviour of aluminium claddings in seawater will be a sensitive function of

the oxygenation of the water. Under low oxygen conditions aluminium will be fully protective galvanically. Under fully aerated conditions aluminium will be barely protective to steel, if at all, but will form a barrier layer of surface oxide, self-healing unless this is compromised by chloride ions.

Bertocci [84] has investigated electrochemical current noise on aluminium in borate buffer with chloride additions, using a potentiostatted system, and used cross-correlation analysis to separate the deterministic and stochastic parts of the process. While this paper was mainly concerned with theoretical developments, Bertocci did find a *1/f* dependance in the random fluctuations under pitting conditions with a slope of approximately –20 dB/decade.

Uruchurtu and Dawson [85] used a three electrode system to measure potential noise on pure aluminium under various pitting conditions. They used Maximum Entropy Methods, without adequate explanation or experimental specification, to analyse their data. They found that shallow slopes (< 20 dB/decade) indicated pitting, whereas steeper slopes represented either passivation or general corrosion. More speculative conclusions were also drawn regarding mechanisms of passivation/healing, though it is hard to see how these are really supported by their data.

Legat and Dolecek [105] found that electrochemical current noise on aluminium (not potentiostatted) was related to localisation. Shallow or zero slopes related to general corrosion or passivation, whereas steeper slopes (-7 to -14 dB/decade) related to pitting corrosion.

Corrosion of thin (~1μm) aluminium coatings on steel has been characterised using electrochemical current noise under potentiostatic conditions, in circumstances in which steel was more active than aluminium (acetate buffer with chloride additions), by Burkert *et al* [94. Slurry erosion conditions were not used. This was particularly valuable as a coating production monitoring method to minimise flaws and pores, the main parameter used being the overall power level in the current noise. It was found

that corrosion usually started at the base of a defect and spread laterally under the coating; aggregation of corrosion products causes lifting of the coating and subsequent collapse.

In some respects conditions within the porosity inherent in sprayed coatings or within impact scars resemble those within pits, notwithstanding that the typical dimensions of HVOF pores (tens of μm) are larger than those of pits (typically tenths of μm for metastable pits, μm or more for stable pits [152]). In particular, there is a confined geometry, which may result in local chemistry different from the bulk chemistry, and also in restricted diffusion within the pore, particularly if solid corrosion products are present. A difference is that the pores are preformed by the production process, rather than by the corrosion process, and are sufficiently larger than pits that both anodes and cathodes may be present within them; pore chemistry is therefore going to be difficult to predict. To the extent that these resemblances are more important than the differences, understanding of pitting corrosion, and its electrochemical signatures may be relevant to corrosion of porous coatings.

Pitting corrosion in aluminium has been reviewed by Szklarska-Smialowska [153], and for metals more generally in book form by the same author [154]. Relevant aspects of her discussion include the finding by Galvele [155] that stable pits will grow continuously if the quantity $(y_{pore}.I_{pore})$ is larger than about 10^{-8} A.m^{-1}, where y_{pore} is the pore (pit) depth (m) and I_{pore} is the current density (A.m^{-2}) within the pore. This results from transport calculations coupled to considerations of pH and chloride ion concentration. Practically, larger pores are likely to be more vulnerable to corrosion than smaller ones. Pride *et al* [156] found by consideration of current noise (analysis of individual peaks) that the magnitude and frequency of anodic current 'spikes' on pure aluminium were related to chloride concentration and potential; also, there was a relationship between peak 'spike' current and apparent pit radius at the time of the 'spike'. Furthermore, at least in very dilute NaCl (10^{-4}M), pits only became stable when the quantity (i_{pore}/r_{pore}), where i_{pore} is the pit current (A) and r_{pore} is the pit radius (m), exceeded 10^{-4} A.m^{-1}, implying, according to them, a

sustained high concentration of $AlCl_3$ in the pit – this would be helped by a re-entrant pit geometry. Their stable pits were always larger than 2 μm. Buzza and Alkire [157] showed that on pure aluminium in 1M NaCl a critical concentration of aluminium oxychloride must be maintained next to the surface, and that when pits of different sizes compete, it is always the large pits which survive and the small ones which repassivate. Collectively, these papers suggest that the relatively large HVOF pores will behave like stable actively growing pits, so long as cathodes are not present within the pit to upset the local chemistry. As regards the latter, silicon lamellae (potential micro-cathodes), when present, may intersect the pore surface, but oxygen is likely to be depleted within narrow tortuous porosity – the anticipated importance of internal cathodes is not clear. Relatively large HVOF pores may also cause impact scars to repassivate more rapidly than they otherwise would; comparative testing of HVOF claddings and bulk metal/alloy would be required to establish this.

Oltra *et al* [157] have noted that noise generated, e.g. by pitting effects, may be modified by system effects, notably by potentiostat time constants and by the effects of surface capacitance. They consider equivalent circuits for isolated active pits, surrounded by a passive surface, under free corrosion conditions or connected to a potentiostat.

To avoid complications due to the potentiostat, they show that as fast as possible a potentiostat should be used, and iR drop in the cell should be minimised.

The effects of surface capacitance depend on the cathode reaction kinetics. Where these are 'rapid' (e.g. involving Fe^{++}/Fe^{+++}), the potential transient is directly related to current changes. However, where cathodic reaction kinetics are 'very slow' (e.g. involving oxygen reduction on a passive surface), potential changes are dominated by charge resupply from the passive layer). The latter situation has been shown, e.g. [158], to apply to a variety of passivating metals, and is expected to apply to pitting of aluminium under stagnant conditions. What is not addressed in this paper, and is not at all clear, is what the effect of intense erosion will be. Clearly, much of the passive

layer will be removed. If the whole surface is 'active', how will this logic apply (if at all) and how will anodic and cathodic areas be disposed on it? Presumably, these will be dictated by the geometry of the erosion scar and possibly by the local hydrodynamics. There is likely to be an overall increase in corrosion activity, but the extent to which this might be localised (and thereby made more dangerous) by erosion effects is entirely unknown.

It has been found that corrosion of aluminium and its alloys in seawater can be inhibited by treatment with salts of rare earths, especially cerium or yttrium [159,160]. To the extent that the synergistic part of erosion-corrosion is strongly linked to corrosion, this sort of surface treatment may help. Given the likelihood of the loss of surface films by erosion, alloying with these elements may be more satisfactory. The Electrochemical Noise behaviour of a cerium based inhibitor has been investigated by Aballe *et al* [115].

Aluminium–silicon alloys.

It is generally found [5] that there is a crude correlation between erosion resistance and hardness. Silicon is therefore added to aluminium to improve wear resistance in such applications as pistons for automotive use. Traditionally, pistons have been made using eutectic (11-13% silicon) alloy, which is easy to cast and to machine, but has limited wear resistance; use of hypereutectic alloy (16-20% silicon) can greatly improve wear performance [161]. This is because the eutectic alloy contains silicon only as a very fine dispersion in an aluminium matrix, whereas hypereutectic alloy contains a dispersion of larger silicon particles. The properties of hypereutectic alloy are very sensitive to control of the dispersion. If a very uniform dispersion can be obtained, good wear performance results, at the expense of requiring diamond tooling to machine products. At least two papers have been published on spray forming hypereutectic aluminium/silicon alloys [162,163]. These conclude that spray-formed hypereutectic alloys generally have properties, including wear properties, superior to

those of conventionally cast alloys, because silicon dispersion is more uniform, leading to enhanced superficial hardness (about 230 H_V).

The dry erosion behaviours of pure aluminium and of aluminum/12% silicon alloy have been compared by Hovis *et al* [164]. This work was carried out using alumina particles in an air blast at 30^0 impingement angle. They found that alloy erosion under these conditions could be higher than for pure aluminium, even though the indentation hardness of the alloy was up to three times higher than that of aluminium. This was because in pure aluminium impact causes extensive lateral displacement and folding before fracture, whereas this is much less apparent in the alloy, where the finely dispersed silicon platelets act as initiation sites for micromachining chip fractures (this effect is expected to be more pronounced for hyper-eutectic alloys, which have a coarser silicon microstructure). This effect is to some extent a function of the relative scales of the alloy microstructure and the erodent particle size.

Little work appears to have been done on the corrosion performance of aluminium/silicon alloys, but Meyer-Rodenbeck *et al* [165] studied a range of aluminium alloys in comparison with mild steel in simulated corrosive mine-waters. They concluded that: "Under abrasive-corrosive conditions aluminium alloys, with their superior corrosion resistance, outperform mild steel by a factor of up to 2.2 times. The alloys with superior corrosion resistance provide the better performances". Unfortunately, aluminium/silicon alloys are not identified as having superior corrosion performance, owing to micro-galvanic effects (i.e. silicon acts as a cathode for aluminium dissolution); other cast alloys have similar problems. "The ideal alloy is not commercially available" – a low copper version of alloy 7017 is suggested (this is a wrought alloy, not suitable for flame spraying), but this must be questionable since copper is typically an excellent cathode for aluminium. These authors suggest that this is an area ripe for new alloy development.

Some further information is available in a paper by Bhattamishra *et al* [166], who studied the effects of impurities on the corrosion behaviour of Al/Si alloys. They

concluded that the presence of iron in the alloy was very deleterious, possibly because of the action of iron containing intermetallics as micro-cathodes. Minor alloying with rare earth elements improved corrosion performance, possibly by altering the morphology of intermetallic phases.

Aluminium based composites

Turenne *et al* [167] investigated the erosion behaviour of metal matrix composites (alumina or silica fibres in aluminium alloy) in a jet type apparatus, under non-corrosive conditions. The behaviour found depends on the relative scales of the erodent particles and the fibre reinforcement. Large particles caused fibre fracture and removal. Small particles selectively eroded the matrix, resulting in a rough surface, especially at low impingement angles. However, the fibres remained in place, resulting in improved erosion performance.

In extension of this work, Turenne *et al* [168] have studied the slurry erosion behaviour of aluminium alloy (5083)/alumina composites. The reinforcement helps to protect the alloy under shallow angle impingement conditions. At large angles fine particles deviate from the nominal angle of impingement, being carried by the liquid flow (see Section 3.5 above), but coarse particles impinge nearly normally and shatter the reinforcement. This suggests that either this sort of composite should be restricted to low-angle impingement situations or that it needs to be protected against 'large' particulates.

Bester and Ball [169] investigated the performance of aluminium alloys and particulate reinforced metal matrix composites in erosive-corrosive slurry conditions, obtaining polarisation curves for their samples under erosion-corrosion by silica in a jet type apparatus. They concluded that the effects of corrosion alone are not significant, but under erosion conditions there is a significant reinforcement (~30%) in material loss (synergy) by corrosion; this is accurately reflected by corrosion current densities. Normally, corrosion of aluminium alloys is not uniform, but is

characterised by pitting where passivation is discontinuous. Under erosion, the surface is constantly renewed and passivation is not allowed to develop. These authors did not attempt Electrochemical Noise measurements, but changes in localisation may well result in changes in behaviour identifiable by this technique. In their case, addition of particulate alumina resulted in worse erosion-corrosion performance, owing to reduced fracture toughness. It was also suggested that protrusion of reinforcement particles from the specimen surface would inhibit formation of a passive layer.

Monticelli *et al* [170,171] have investigated the corrosion behaviour of aluminium composites (reinforced with SiC or Al_2O_3 particles or Al_2O_3 fibres) – not under erosion conditions. Electrochemical potential noise measurements [173] correlated with linear polarisation resistance and weight loss measurements and with appearance, as seen under the SEM. Polarisation curves indicated that the limiting factor in corrosion was oxygen reduction at cathodic sites, and that this can be affected by the nature and shape of the reinforcement. Current noise measurements [174] yielded *psd* plots with slopes of around -20 dB/decade when corrosion was mainly localised in pits, reducing to near zero when general corrosion was dominant.

Ahmad and Aleem [172] studying the degradation of Al 6013-20SiC metal matrix composites in seawater found that erosion-corrosion (polystyrene balls) was strongly correlated with flow velocity and concentrated on the metal/reinforcement interface. Degradation was strongly suppressed by treatment of the composite with $CeCl_3$.

As noted above, surface treatment of aluminium alloys with yttrium compounds can reduce corrosion by seawater and inclusion of particulates can improve wear characteristics, at least in favourable circumstances. Perhaps surprisingly, it is claimed by Zhang and Li [173]. that inclusion of yttria particles can do both. Yttria reinforced aluminium was found to perform better than aluminium metal or 6061 alloy in sliding wear, both dry and in dilute nitric acid. It would be very interesting to observe this material's performance in sand erosion in brine.

Generally, reinforcement helps if the slurry energy is not sufficient to fracture the reinforcement, but causes inferior performance, sometimes spectacularly so, when fracture does occur. It is also emphasised that corrosion by itself usually has only minor effects, but there is considerable synergy under erosion conditions, thought to result from corrosion promoted fracture of platelets.

Aluminium – Electrochemical current Noise

It is convenient to collect together the scattered references to the application of Electrochemical Current Noise techniques to aluminium based materials, to demonstrate that, irrespective of what may have been found with other materials, in this limited field findings are relatively consistent:

- Bertocci [84] has investigated electrochemical current noise on aluminium in borate buffer with chloride additions, using a potentiostatted system, and used cross-correlation analysis to separate the deterministic and stochastic parts of the process. While this paper was mainly concerned with theoretical developments, Bertocci did find an inverse frequency dependence in the random fluctuations under pitting conditions with a slope of approximately –20 dB/decade in the range 1-50 Hz.

- Legat and Dolecek [105] found that electrochemical current noise on aluminium (not potentiostatted) in 3.5% NaCl was related to localisation. Shallow or zero slopes related to general corrosion or passivation, whereas steeper slopes (-7 to –14 dB/decade) related to pitting corrosion. Frequency range 0.5 - 500 mHz. In spite of the low frequencies used, reasonably stationary data appear to have been obtained (though this is not commented on), once starting transients were eliminated.

- Monticelli *et al* [170] have investigated the corrosion behaviour of aluminium composites (reinforced with SiC or Al_2O_3 particles or Al_2O_3

fibres). Electrochemical Current Noise measurements (not potentiostatted) yielded *psd* plots with slopes of around -20 dB/decade when corrosion was mainly localised in pits, reducing to near zero when general corrosion was dominant. Frequency range 0.1-10 Hz.

None of these authors used anti-aliasing filters.

- Corrosion of thin (~1μm) aluminium coatings on steel has been characterised using electrochemical current noise, under potentiostatic conditions with anti-aliasing filters, in circumstances where steel was more active than aluminium, by Burkert *et al* [94]. Frequency range 0.1-40 Hz. This was particularly valuable as a coating production monitoring method to minimise flaws and pores, the main parameter used being the overall power level in the current noise. Burkert's *psd* plots did not have well defined straight sections but possessed generally negative slopes, which tended to become steeper as his coatings broke down.

All of these authors have found that uniform corrosion on aluminium based materials is associated with flat current *psd* plots, and that pitting is associated with negatively sloped plots. Less well established is the relationship between 'degree of localisation' (a term widely used, without definition) and the actual value of the negative slope. It appears to be commonly thought that as pitting transforms itself into general corrosion, i.e. becomes less localised, then the *psd* slope becomes flatter. However, Burkert's data appear to contradict this, since his *psd* slopes became steeper (and non-linear) as corrosion progressed; however, this was associated with increasing steel exposure, which must modify the Noise behaviour in ways not at present at all understood.

2.7 CONCLUSIONS from LITERATURE REVIEW

The focus of this work is the performance of internal pipework in naval ships, subject to simultaneous erosion and corrosion. It is desired to replace expensive alloys, which do not resist erosion-corrosion well, with cheaper systems, based on coated carbon steel. There is a particular interest in metallic coatings.

Coatings need to be: erosion resistant
corrosion resistant
cheap enough

The primary function of a coating is to act as a barrier. It must therefore have a good resistance to erosion. Erosion resistance correlates very roughly with hardness. This works quite well for pure metals, especially if hardness is measured on the eroded (work-hardened) surface, but much less well for alloys. For the metals likely to be cheap enough to consider, hardness varies as:

Softest: Zinc, Aluminium, Copper, Nickel :Hardest

Erosion also varies with angle of impingement. For ductile materials, including metals, erosion is generally greatest at relatively low angles of incidence (typically 30^0), whereas brittle materials suffer greatest erosion at normal incidence. Different material solutions may be appropriate to different duties.

Much reported erosion work relates to rather dilute slurries and there is a trend toward studying single particle impacts; however, situations of practical importance usually involve relatively dense slurries where co-operative particle effects may be important or even dominant.

Once the coating has been penetrated, behaviour depends on electrochemistry. Corrosion behaviour for metallic coatings is governed by whether the coating is

anodic or cathodic to the steel substrate. Zinc and aluminium are anodic to carbon steel in seawater, so the coating is protective. Copper and nickel form cathodic coatings; the substrate steel may suffer rapid attack if the coating is penetrated.

The options are to harden anodic coatings, or to try to modify (or disguise, by organic coating) the electrochemical behaviour of cathodic coatings. In practical terms, it is difficult to see how one could make copper or nickel anodic by alloying. The most practical option for development is expected to be to attempt to harden an anodic coating by alloying or composite formation.

Erosion can be characterised by weight loss, microscopy and profilometry.

Electrochemical methods which may be useful in characterising the degradation of metal-coated metal pipes are potentiodynamic polarisation, electrochemical impedance spectroscopy and electrochemical noise.

Polarisation methods are limited because they combine large potential excursions (which will themselves alter the surface, usually irreversibly) with being slow compared with the processes likely to occur under erosion-corrosion conditions.

Electrochemical Impedance Spectroscopy is useful to separate processes occurring simultaneously on different time scales. In the present context, determination of the cell resistance and possibly a charge transfer resistance, if the system is sufficiently simple, is as much as seems likely to be obtainable from this technique.

Electrochemical Noise is principally useful to investigate localised corrosion. It has been used to investigate pitting, crevice corrosion and stress corrosion cracking, and there are claims, somewhat controversial, to be able to distinguish between them.

Electrochemical Noise can be measured as current noise or potential noise, and it is not at all clear which of these, or some combination of them, is to be preferred,

though several claims have been made that mass loss correlates better with current noise. The erosion-corrosion experiment itself, however, precludes the use of identical working electrodes. A single potentiostatted working electrode will be used. It is not clear at what sampling rate measurements should be made – rates of 2 s^{-1} are conventional, but several papers have been found suggesting that relevant noise activity could occur requiring rates up to 10^6 s^{-1}. Unless correct data acquisition and data manipulation techniques are used (e.g. anti-aliasing filters, proper detrending means) meaningless results will be obtained; this has not always been recognised in the electrochemical literature. Furthermore, the theory of this technique is underdeveloped, there being no agreement whether simple statistical treatments or more elaborate procedures, based on Fourier Transforms or wavelet methods are to be preferred. Essentially none of the published work is quantitative. Experience of the use of the technique with erosion-corrosion is very limited.

Equipment to study erosion-corrosion is basically modified erosion equipment. This is designed to define impingement conditions as closely as possible in terms of slurry composition, flow rate and impingement angle. Jet impingement designs offer the best available experiment definition. For erosion-corrosion work with electrochemical monitoring the primary modification required is that all metallic parts, other than the sample under test, should be removed from the fluid circuit. Additionally, means of electrically contacting the test sample are required, together with such additional electrodes in the flow circuit as may be necessary. Since corrosion currents are typically small (μA), the test apparatus should normally be enclosed in a Faraday cage. The disposition of counter and reference electrodes in suitable positions relative to the test sample, but out of the erosive flow, is an inherent problem of this type of experiment, and there is no general agreement as to how they should be arranged. Testing will be carried out using a jet impingement erosion-corrosion rig, with some modifications to aid sample handling and to facilitate electrochemical measurements. Optimisation of this may require considerable experimentation.

Zinc is used in a marine context as a sacrificial anode, usually as an alloy with trace additions of aluminium and cadmium. Zinc suffers very severely from flow corrosion, but only very old papers address this. A single paper suggests that a Zn/Al/Si alloy may have good erosion-corrosion resistance in minewaters.

Aluminium (alloy) is used in a marine context both structurally and as a sacrificial anode. In the latter context, it is usually used as a flame-sprayed cladding, and there is extensive experience of its use (mainly US). Several papers have been identified relating to the erosion-corrosion of aluminium, its alloys and composites. Erosion is very angle dependant and ductile in nature. Several electrochemical methods have been used to study these materials, including polarisation measurements, EIS and electrochemical noise. Only one paper has been found relating to electrochemical measurements (current noise) on a cladding (pure aluminium) on steel; this was carried out under static conditions at a sampling rate up to 40 s^{-1}, with indications of activity at higher frequencies – a correlation was claimed with coating porosity. There does not appear to be any electrochemical study of aluminium, its alloys or composites, as claddings on steel, under erosion-corrosion conditions.

In view of the above, the objectives of the practical work are:

- To develop equipment suitable for investigating the erosion-corrosion of metal claddings on steel.

- To investigate synergies between erosion and corrosion in sand/seawater slurries on these materials.

- To investigate the application of advanced signal processing techniques to Electrochemical Noise data from slurry-erosion studies, to characterise degradation.

3 SAMPLE MATERIALS

3.1 SAMPLE PRODUCTION

3.1.1 Sample manufacture

For reasons discussed above (Section 2.6.1), the practical work associated with this project concentrates on HVOF claddings of aluminium, aluminium/silicon alloy, a composite of aluminium/silicon alloy with alumina and galvanised zinc, all on mild steel blanks. These blanks have also been included, as made, for comparison purposes.

The steel used is AISI 1020 mild steel (0.2% C steel). In order to fit pre-existing test equipment, it has been prepared as 40 × 40 × 5 mm blanks, ground on the working face to < 1 μm R_a and with provision on the rear for making an electrical connection.

Cladding has been carried out by TWI Ltd, using High Velocity Oxy-Fuel (HVOF) spraying (Topgun). This is a procedure which provides denser, more uniform coatings than ordinary flame spraying. Figure 3.1 illustrates the gun used.

Oxygen and fuel gas (in this case propylene) are mixed in the flame nozzle just prior to burning. The nozzle design gives good mixing and high efficiency combustion. Powder is injected in a stream of carrier gas along the central axis of the ring of flame jets. This ensures efficient heating and melting of the material and good acceleration of the particles into a tight uniform spray pattern. Materials are sprayed in a raster pattern at a stand-off distance of about 280 mm and normal incidence. Thickness is built up progressively; this allows layered coatings to be built up by alternating powder feeds.

The steel blanks were grit blasted before spraying to roughen the surface, in order to improve cladding adhesion.

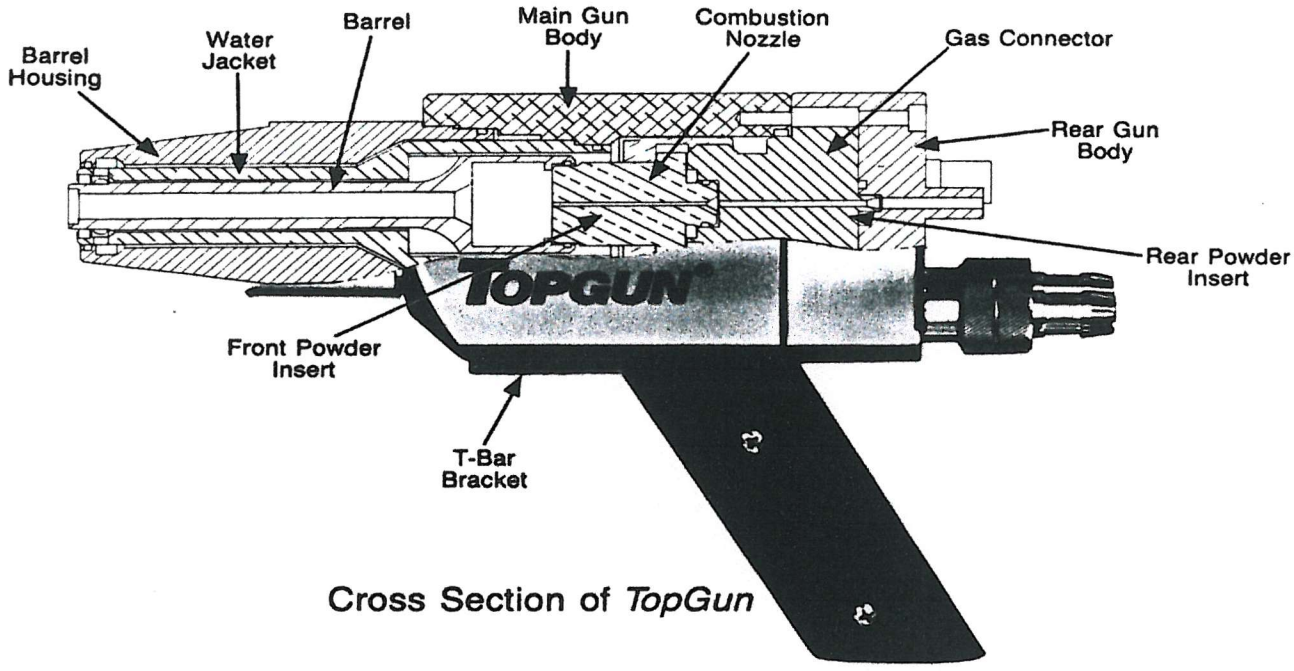

Figure 3.1: Miller Thermal *Topgun* as used by TWI Ltd for HVOF spraying

Initially, 3 series of samples have been made. These were:

- Aluminium metal, commercially pure (>99%).
- Aluminium/12% silicon alloy (eutectic alloy).
- A composite of aluminium/12% silicon alloy and alumina, sprayed alternately to give a multi-layer sandwich structure. This novel product, with an alumina layer at the top (for best erosion resistance) and an aluminium layer at the bottom (to provide galvanic protection to the steel) was designed to offer superior performance, avoiding some of the difficulties encountered by earlier workers with random particulate dispersions.

Details of the powders used are given in Table 3.1, and of spraying conditions in Table 3.2. Target cladding thickness was 300 μm.

Subsequent examination (see below) showed that the layering of the composite was not very well developed. Neither did the composite perform very well in preliminary

tests (Sections 4.5). Since composite development, as such, was not a principal aim of this project, use of this variable was discontinued in the main part of the work (Section 6).

Galvanised (hot dipped) zinc samples were obtained from Wyatt Ltd, based on the same steel blanks. These coatings were typically ~ 80 μm in thickness.

3.1.2 Further sample preparation

Some of the clad samples have been subjected to erosion testing, as supplied, but, since the surfaces of these materials were quite rough (up to ~ 25 μm R_a) an attempt was made to grind them to a more acceptable degree of flatness.

Flatness is important for several reasons:

- Non-flat surfaces yield non-typical initial erosion rates, which can be very misleading, because:
    - Particles erode asperities faster than the bulk material.
    - Roughness alters the local angle at which impingement occurs, which can change the erosion mechanism, e.g. from microcutting to cracking.
    - Fluid flow can erode the surface over a much larger area than the apparent erosion scar; this is most easily identified on a flat surface (by observing the presence/absence of grinding/lapping marks).
- Pressure losses in pipes are minimised by having a smooth internal surface.
- Rough surfaces can cause micro-cavitation, a serious source of erosion.

TABLE 3.1

Powder materials used for HVOF spraying

Aluminium (Supplier: Praxair.)

Composition: Certified 99 % minimum. Actual test: 99.7 %

Particle size: Certified -90+45 μm. Actual test distribution (ASTM B214):

+170	Mesh	0.0 %
-170+200	Mesh	2.16 %
-200+325	Mesh	91.93 %
+325	Mesh	5.91 %

Aluminium/12.5 % Silicon (Supplier: Praxair.)

Composition:	Certified %	Actual %
Aluminium		Balance
Silicon	11.0-13.0	11.53
Iron	0-0.8	0.13
Copper	0-0.3	0.01
Zinc	0-0.2	0.01
Magnesium	0-0.1	0.02

Particle size: Certified -106+45 μm. Actual test distribution (ASTM B214):

+140	Mesh	0.2 %
+170	Mesh	3 %
+325	Mesh	97 %
-325	Mesh	3 %

Alumina (Alloys International)

Composition: None available

Particle size: -15+5 μm

This was not wholly successful, for two reasons:

- It was found that the samples had become slightly bowed by the HVOF spraying process. This resulted in the grinding process being more effective in removing peaks at the centre of the samples than at the edges (the amount of grinding in the composite being limited by the sandwich layer thickness – about 25 μm nominal).
- New porosity was created by the grinding process. The overall result was a surface flat to < 1 μm R_a in general, but containing isolated pits, typically 25 μm across and at least 25 μm deep. The nature of these pits varied with sample type, as discussed further below (Section 3.2.1). If such a material were to be used in a real application, some means of sealing this porosity would be required.

TABLE 3.2 - Spraying Conditions

(for all variables)

Gun:	Topgun	
Fuel:	Propylene	9.5×10^{-4} $m^3.s^{-1}$
	Oxygen:	25.6×10^{-4} $m^3.s^{-1}$
Traverse conditions:		
Turntable:		665 mm diameter.
Rotation:		30 rpm
Vertical speed		2.53 $mm.s^{-1}$
Spray	Distance:	285 mm.
	Angle:	90^0

3.2 SAMPLE CHARACTERISATION

3.2.1 Optical Microscopy

Microscopy in plan.

Figure 3.2 shows the general appearance of the centres of the coated samples after grinding (approximately 15 mm × 15 mm areas). Note that, although these images are all reproduced to the same scale, the brightness and contrast have been adjusted individually. This is because the aluminium sample is very reflective and contrasty, whereas the composite sample is very dull and lacks contrast, the alloy sample being intermediate.

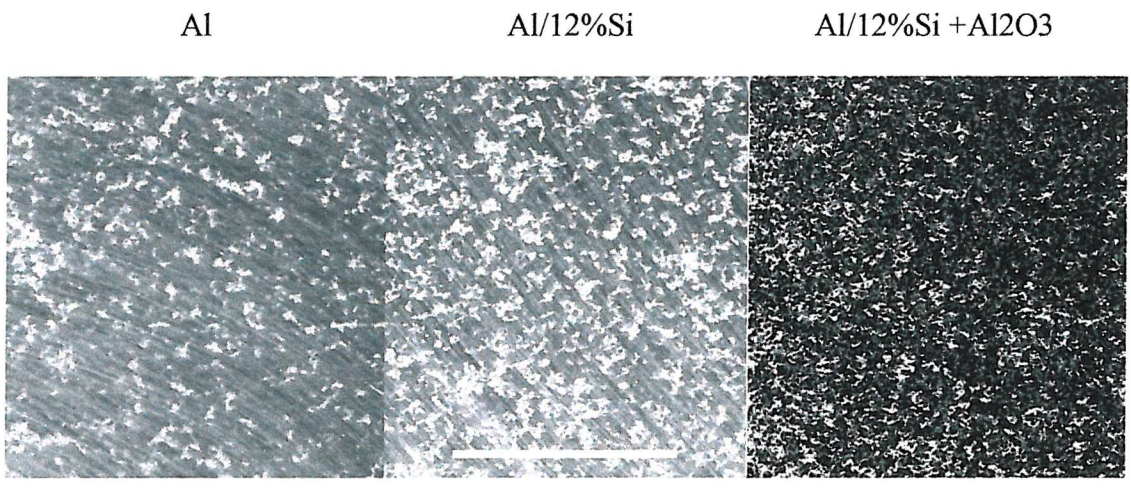

Figure 3.2: General appearance of HVOF coatings after grinding.
10 mm scale bar.

The aluminium metal and alloy images show a ground metal surface with scattered bright patches; these bright patches are depressions resulting from inter-splat porosity. The appearance of the composite surface is more complicated; it is significantly rougher since grinding has not been taken quite far enough, and there are two kinds of height deviation. There are gaps between not completely ground down

peaks, and within this there are gaps between aluminium alloy splats, partially filled with alumina (illustrated in more detail below, Section 3.2.2).
Figure 3.3 (at end of Section) shows these surface defects in more detail. The images (Olympus B061) are to the same scale as the μm scale to the left. The aluminium and alloy images show very irregular voids (dark areas) of typically 30-50 μm scale, voids in the alloy being somewhat larger. In the case of the composite, the dark (lower) areas appear to occupy most of the surface, but this is because the peaks are not wholly ground down; the actual voidage is not visible on this image.

Microscopy of Sections.

Figure 3.4 (at end of Section) shows sections of the same materials. The section of aluminium shows an almost fully dense coating (too thick to wholly fit into this image). Aluminium/12% silicon eutectic alloy shows two principle phases, of which the darker one is evidently aluminium metal, while the lighter phase contains a fine precipitate, thought to be silicon. The lighter phase occurs as large particles, ~ 50μm in size, which appear to be the remains of the larger original powder particles, not flowed out, or agglomerations of smaller ones. The composite section also shows these 'melt packets' (relatively dark in this image), but with a white material in between – this appears to be alumina; as can be seen, in these samples, the desired laminar structure has not been achieved.

The photographs of sections were made using a digital camera, which results in an image that can be subjected to further analysis. Figure 3.5 (at end of Section) shows two examples of this, produced using a commercial image analysis program – (Carl Zeiss Vision KS300).

The top image is a straightforward image of a composite section (same as bottom image in Figure 3.4).

The middle image is a version of this, which has been manipulated to emphasise edges; it shows that while the lighter phase is made up of single particles, the intervening matrix is not – and may be reasonably expected to be vulnerable to erosion.

The bottom image is one of the porosity in the top image. The procedure for producing and using this image is:

- To identify (by moving the microscope focus up and down) which areas on the image correspond to porosity – the darkest areas in this case.
- To construct a 'grey-scale' histogram of the top image.
- To identify a greyness threshold on this histogram which will just pick out the areas identified as porosity.
- Application of this threshold to the original image produces the bottom image in Figure 3.5.
- If a rectangular box is inscribed on the 'porosity' image, the software will calculate the percentage area represented by dark image within the box, i.e. the percentage porosity.

Some precautions need to be taken to obtain consistent results with this procedure:

- As large a box as possible should be used, i.e. one considerably larger than the porosity.
- The box should be narrow enough to exclude both upper and lower surfaces (and therefore all the steel and epoxy)
- Several estimates should be made from different parts of the coating.

Several further considerations result from this:

- The section should be a typical one. A random section is fair for a new sample, but might not be after erosion, owing to differential plastic flow

beneath different regions of an erosion scar; indeed, mapping of the differential voidage under such a scar might be instructive.

- Any voidage particularly associated with the coating/substrate interface, such as might result from erosion induced cracking will be missed. This could be assessed separately, if desired.

With these caveats, the following porosity data have been obtained.

TABLE 3.3 – Sample Porosity

Material	Porosity %	Mean %
Aluminium	0.73, 0.73, 0.55	0.67
Aluminium/12%silicon	1.29, 1.34, 1.11	1.25
Aluminium/12%silicon + alumina	5.86, 7.23, 6.03	6.37

While this sample is too small to be really reliable, it is clear that these materials are different, with the composite having significantly more porosity than the other coatings. If this porosity is connected, which is not established, then clearly there will be implications both for the mechanical strength of the coating and for its ability to protect the substrate from corrosion.

This is a reasonably simple means for characterising a significant parameter relevant to coating behaviour. As at present implemented, there is a minor degree of 'art' in the procedure; if the method were to be adopted as being generally useful, a more rigorous measurement procedure would be required to ensure reproducibility between different operators.

3.2.2 Electron Microscopy

Figure 3.6 shows electron images (JEOL JSM 6400) of the surfaces of the same samples as those shown in Figure 3.3. These show the porosity in the aluminium (Fig 3.6a), aluminium/12%silicon (Fig 4.6b) and aluminium/12%silicon + alumina composite (Fig 4.6c,). The greater depth of field of the SEM shows that these pores are very irregular and choked with loose material. In the case of the composite, this loose material is very fine and charges up (in spite of the sample having been carbon shadowed) and is evidently unbonded alumina. The reason why there appears to be more porosity at the surface than internally is that the coating contains loose material, which can fall away from the surface, but is retained in the internal porosity.

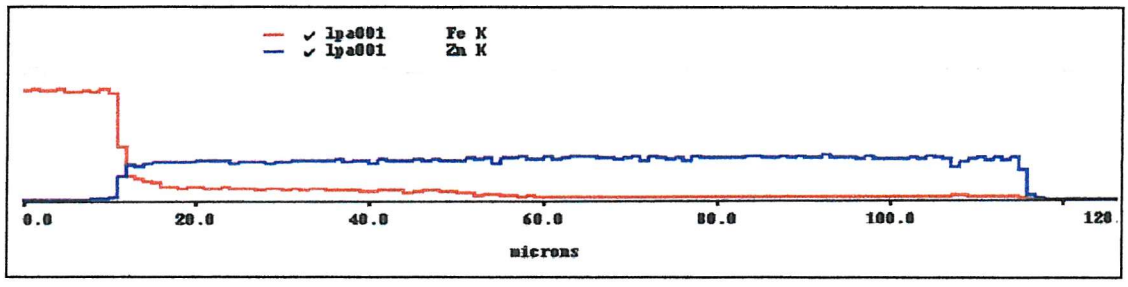

Figure 3.7: SEM-EDS Linescan. Relative electron intensities of iron and zinc across a hot-dipped zinc coating section, showing iron diffusion into zinc.

SEM examination of sections in general showed no detail that was not observable optically. The exception to this concerned the hot-dipped zinc material. A line-scan across the section (Figure 3.7) revealed that the zinc coating contained a significant proportion of iron close to the steel substrate, decreasing toward the coating outer surface. This is important, because, as will be shown below (Section 4.3.1), the hot-dipped zinc coating proved more erosion resistant than expected. This is probably due to zinc/iron alloy formation, zinc/iron being known to be harder than pure zinc [174] (Knoop Hardness Number = 63 for pure zinc, 324-370 for Zn/Fe). While it falls outside the scope of this Thesis, investigation of the erosion-corrosion properties of Zn/Fe (and possibly other zinc alloys such as Zn/Ni) would be of interest. Zn/Fe

alloy can be made relatively easily, either by holding the sample to be galvanised at elevated temperature for an extended time or, better, by using silicon containing steels that promote alloy formation [175].

3.2.3 Surface Roughness and Hardness Measurements

Surface roughness (Rank Taylor Hobson Form Talysurf 120L) and Vickers microhardness (10 gm load on a transverse section) measurements have been made on AISI 1020 steel and on coatings on this substrate. Results are given in Table 3.4.

SAMPLE	R_a /μm		H_v
	As Received	Ground	
AISI 1020 Steel	N/a	0.13	268
HVOF aluminium on steel	9.0	< 0.1 + pores	83
HVOF aluminium/12%silicon on steel	14.1	< 0.1 + pores	155
HVOF (aluminium/12%silicon + alumina) on steel	18.7	< 0.1 + pores	N/a
Hot-dipped zinc on steel	1.3	N/a	220

Table 3.4: Surface Roughness and Hardness data for erosion samples.

All steel samples were used in the ground condition. As noted above (Section 3.1.2), grinding the HVOF sprayed samples, produced a complex surface structure, with porosity intersecting an otherwise flat surface. Zinc coated samples were not ground, because of their very soft outer surface and relative thinness, compared with the aluminium-based claddings. No hardness measurement was made on the sprayed

composite sample, because its extreme heterogeneity would have resulted in a meaningless result on this measurement scale.

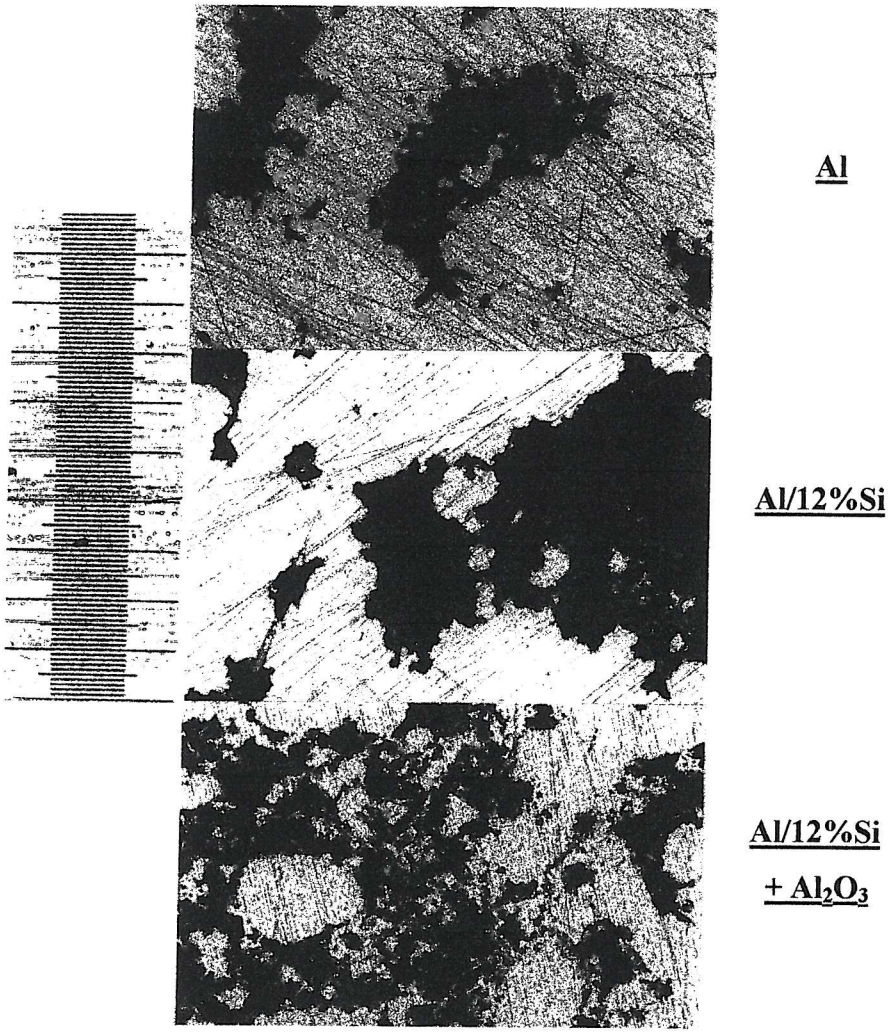

Figure 3.3: Detailed view of ground coating surfaces.
μm scale (smallest gradation).

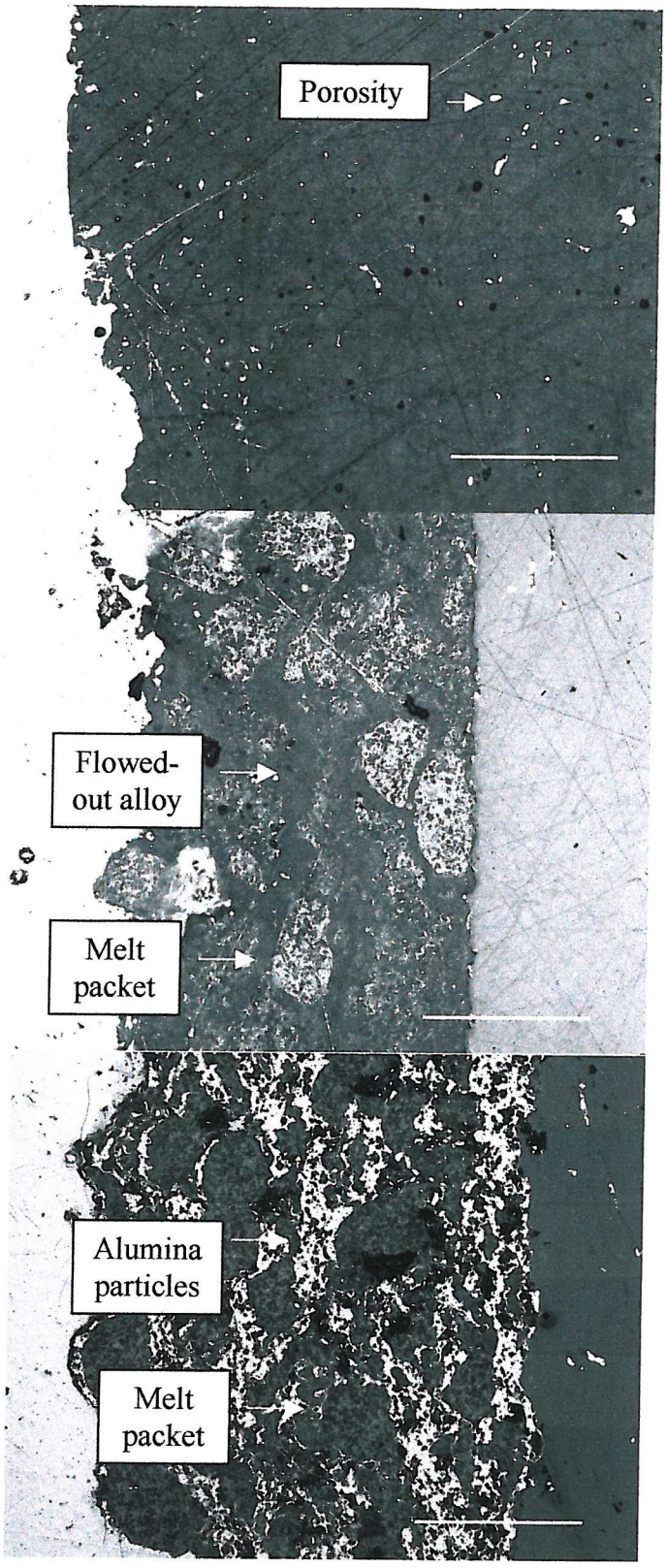

Figure 3.4: Optical transverse sections through HVOF coatings

Scale bars: 100 μm

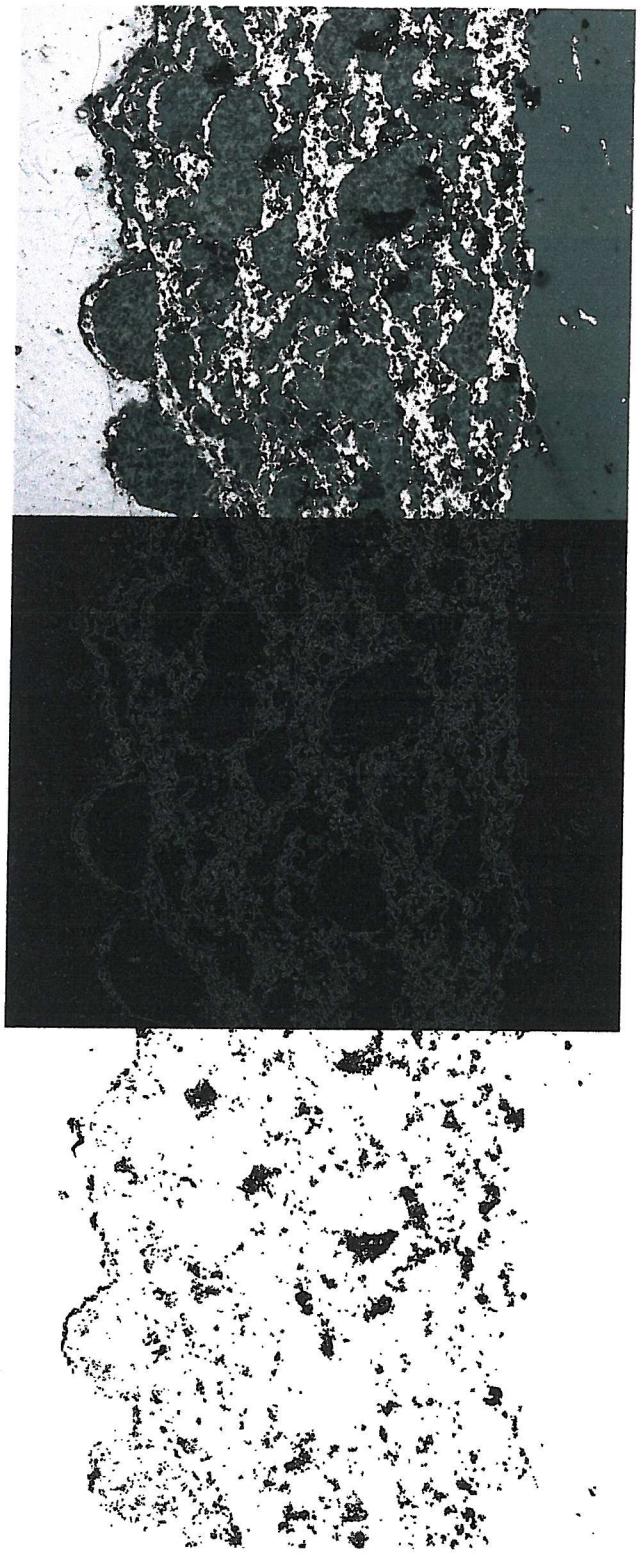

Original

Edges

Porosity

Figure 3.5: Derived images from image analyser

Scale as for Figure 3.4

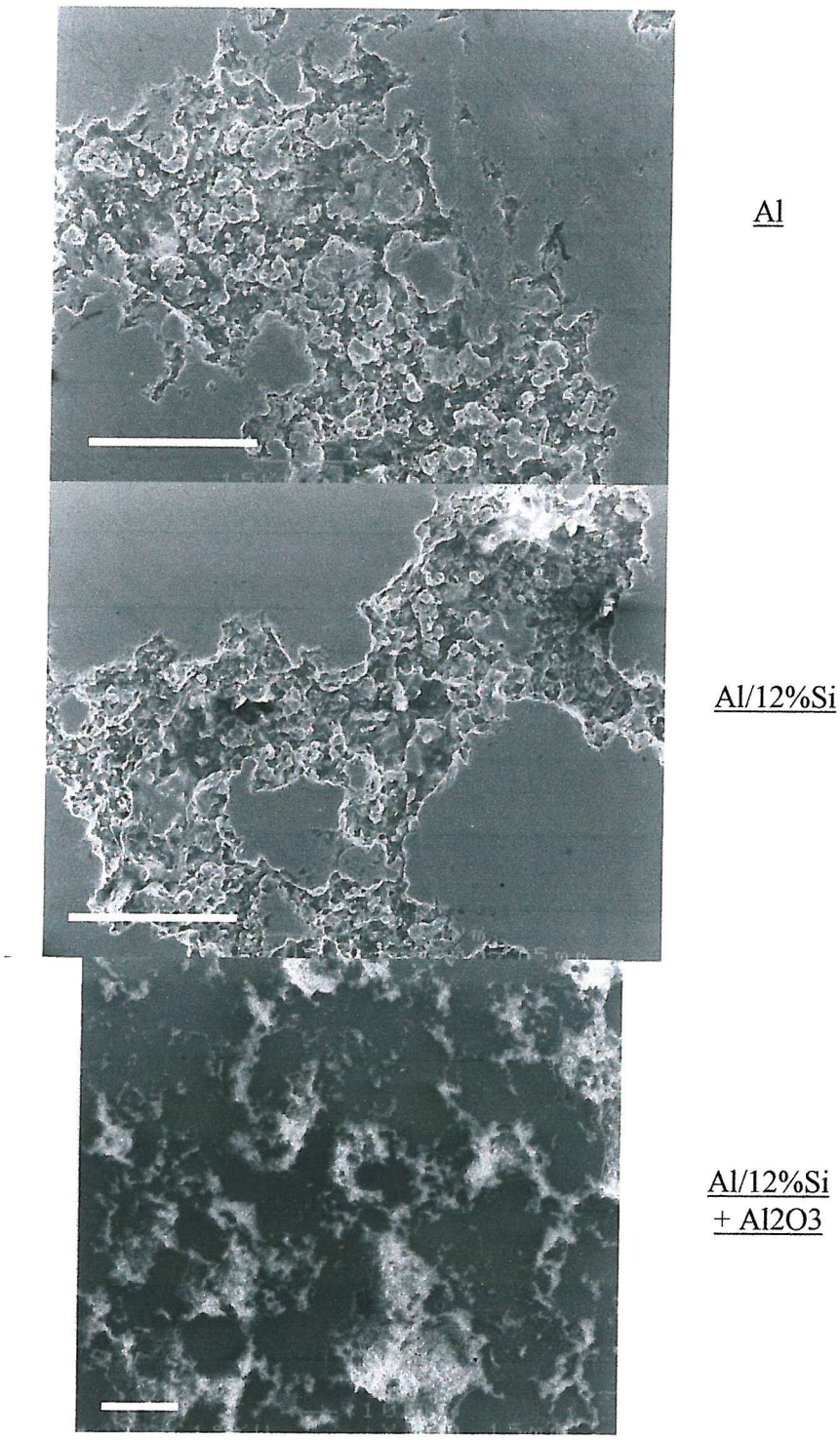

Figure 3.6: SEM images of porosity in HVOF coatings.

20 μm scale bars.

4 EROSION

4.1 INTRODUCTION

This Section describes preliminary erosion experiments carried out in order to obtain an initial idea of the changes that occur on these materials as a baseline for future erosion-corrosion experiments, to compare the initially chosen aluminium based claddings with previous work on other materials, and to develop suitable means for evaluating eroded surfaces.

4.2 EXPERIMENTAL

Erosion measurements have been made in Southampton (Chilworth) tap water, using an existing jet erosion rig with a circulating sand slurry, described in previous work [176]. A consistent set of operating conditions has been used for these tests:

Redhill 50 silica sand

Mean diameter 235 μm, angular, density 2700 $kg.m^{-3}$

Source: Redhill Quarry, Hepworth Minerals, Ltd

2.5 % w/w slurry in tap water

Flow: 0.73 $kg.s^{-1}$ (27 $m.s^{-1}$ jet velocity, 5.9 mm nozzle diameter)

Orientation: vertically down, in air

30^0 and 90^0 impact angles, 37 mm stand-off

Room Temperature

Test duration: 60 s

These operating conditions equate to a sand kinetic energy /nominal particle impact, E_k = 6.5 μJ/particle. This is a nominal particle impact rate of about 1000 s^{-1}, or about 37 $mm^{-2}.s^{-1}$. Relative particle separation [26,27] is ~ 4.1, so there is expected to be considerable inter-particle interaction.

The flow corresponds to a water jet Reynolds number = 166000. According to Townsend [177] the critical Reynolds Number for a circular jet is 1000, with some fluctuations down to 300. The flow in the jet is therefore expected to be turbulent.

This represents a severe set of erosion conditions and it has been necessary to limit the duration of the test, in order not to penetrate the coatings. The HVOF coatings have been tested in both as-received and in ground form (see Section 3).

Erosion has been characterised by mass loss (by direct weighing on a precision balance, ±0.02 mg), by form profilometry and by optical and electron microscopy.

4.3 RESULTS AND DISCUSSION

4.3.1 Mass Loss

Erosion results are presented in Table 4.1. Results obtained are shown as mass losses and as volume loss per nominal impact (V_u), and compared with surface roughness and microhardness values.

A number of comments may be made on the data in Table 4.1:

- Erosion losses on aluminium are comparable to those found by Zu *et al* [124], whose data, converted to the same form, give V_u values of 83 μm^3/impact, independent of angle of incidence. Zu *et al* used sand of average diameter 750 μm at an estimated impact velocity of 4.5 $m.s^{-1}$, i.e. larger particles at a lower energy. This is equivalent to E_k = 11.9 μJ/nominal impact, at a relative separation of 1.9. So V_u/E_k in this work, having values in the range 10 – 17 $\mu m^3/\mu J$, compares with V_u/E_k in Zu's work of 7 $\mu m^3/\mu J$, i.e. these data are broadly similar.

EROSION RESULTS High Energy Conditions – E_k = 6.6 μJ/nominal impact						
Target (Coating on steel)	**R_a / μm**	**H_v**	**Weight Loss / mg**		**Volume Loss/Impact V_u / μm³/impact**	
			30^0	**90^0**	**30^0**	**90^0**
As Supplied						
Aluminium	8.9	83	15.6	12.7	114	92
Al/12%Si Alloy	14.1	155	13.0	11.1	94	81
Al/12%Si Alloy+ Al_2O_3	18.7	n/a	13.6	14.5	90	97
Zinc	1.3	220	16.6	19.0	46	53
Ground						
Aluminium	N/a	83	15.4	12.2	103	81
Al/12%Si Alloy	N/a	155	7.2	7.7	48	52
Al/12%Si Alloy + Al_2O_3	N/a	N/a	10.0	15.2	67	101
AISI 1020 Steel	0.13	268	4.7	9.0	12	22

Table 4.1: Measured Erosion mass loss data.

COMPARATIVE EROSION DATA All using 235 μm Redhill sand at 0.73 $kg.s^{-1}$ slurry flow. E_k = 6.5 μJ/nominal impact.			
Sample	**H_v**	**V_u / μm^3/nominal impact**	
		30^0 impact	**90^0 impact**
Cr_3C_2/Ni-Cr (plasma-sprayed)	520		88
Co superalloy (HVOF)	550		81
Ni-WC/Co (HVOF)	560		53
ENP + SiC (Heat treated)	950	2.5	23
Hard Cr (pulsed)	1100	1.8	20
WC/Co/Cr (D-gun)	1300	1.0	8.8
WC/Co/Cr (HVOF)	940	0.4	3.9
Stellite 20	670		2.3

Table 4.2: Comparative erosion data

Given the differences between these two pieces of work (different operating conditions, different equipment, different operators), it is not clear that these loss rates are actually different. If the difference is real, it is in the sense expected; material loss from the sprayed coating is higher than from bulk aluminium, presumably because the porosity of the sprayed coating both reduces the strength of the aluminium and because it provides surface roughness which promotes erosion.

- Alloying improves performance. Use of a harder, hypereutectic alloy would be expected to provide further improvement (with respect to erosion), but no commercial source of such alloys in sprayable form has been identified. They are, however, being developed for automotive applications [161,162], so this may change.

- Compositing, in this case, reduces performance (relative to the alloyed samples). The poor performance appears to have resulted from the high porosity of the composite and the apparently poor alumina/matrix bonding.

- Grinding is helpful with respect to the alloy samples, but not for pure aluminium. Presumably, the pure metal is so soft that even a very small amount of erosion is sufficient to re-introduce enough surface roughness to negate the effects of grinding.

- The best results were obtained from the alloy samples, ground, with no reinforcement. This material's performance was not very angle sensitive. Volume loss/nominal impact, V_u is about 3 times greater than for steel, but the mass loss is about the same, i.e. the difference is entirely accounted for by density.

- There is no straightforward relationship between V_u and surface roughness, but there does appear to be one between V_u and microhardness. Figure 4.1 shows this. Erosion (as volume removed per impact) appears to decrease roughly linearly with increasing hardness. This trend is more pronounced at 30^0 impingement angle than at 90^0.

  Aluminium is, as expected, very soft; addition of 12% silicon has increased hardness and decreased erosion, but only by a rather small amount. Hot-dipped zinc has produced a coating that is surprisingly hard

and erosion resistant. The measured hardness is considerably higher than is expected for bulk zinc metal. This is attributed to partial alloying with the base steel, as shown in Section 3 (Figure 3.7). Alloying with other materials might result in better performance.

- None of the above provides any indication of likely salt water performance. In particular, the presence of alloying elements may result in microgalvanic effects, which may alter corrosion behaviour dramatically.

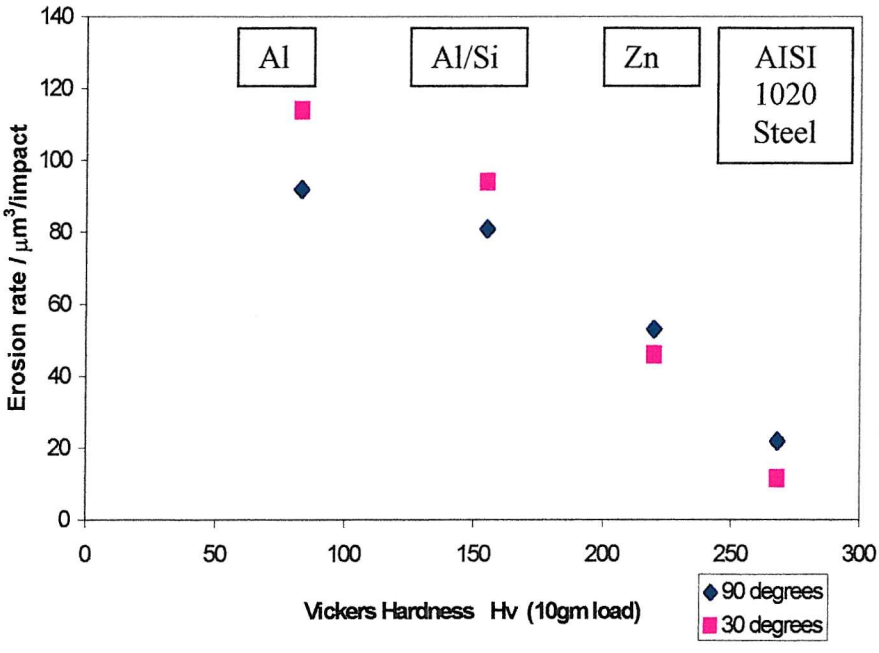

Figure 4.1: Dependence of erosion loss on hardness.
This work.

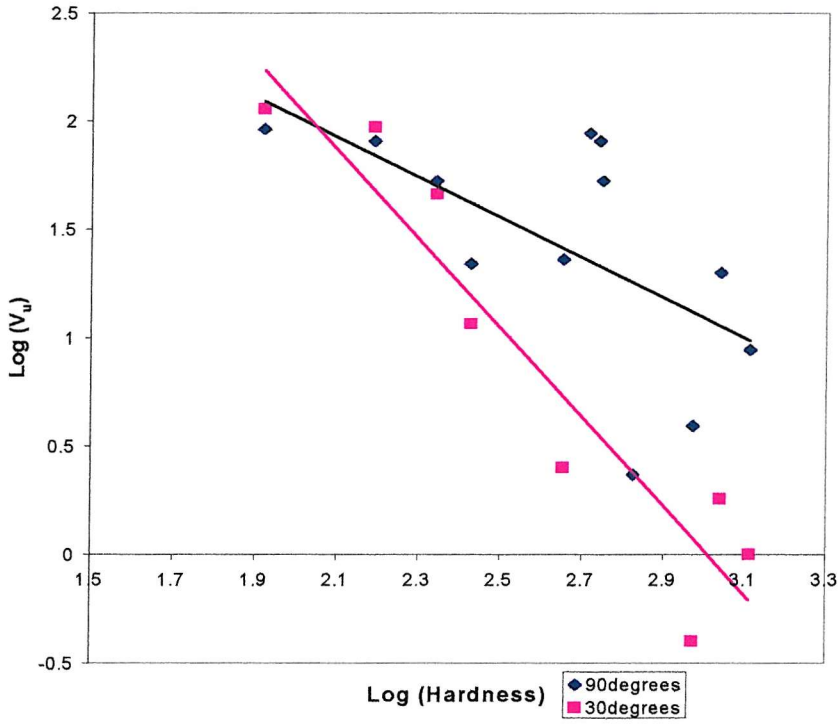

Figure 4.2: Coating erosion *vs* Hardness: comparative data.

For comparison, data for some other materials, obtained by other workers using the same equipment, are presented in Table 4.2 [176]. These data mainly show that use of much harder materials typically results in lower mass/volume losses.

Figure 4.2 plots these data (on a log-log scale to compress the data onto one sheet), together with the trend lines for the 90^0 and 30^0 degree data separately. The present data are the points at the top left hand corner of the plot, that is to say they are the softest and amongst the least erosion resistant members of this group. They are, however the only members of this group likely to be anodic to the steel base.

Approximately, At 90^0 $$V_u \propto \frac{1}{H_V} \qquad (4.1)$$

At 30^0 $$V_u \propto \frac{1}{H_V^{\,2}} \qquad (4.2)$$

No data is available for intermediate angles.

There is considerable scatter in these plots, which may be attributed in part to the difficulties in obtaining consistent operating conditions, especially between different operators, and in part to the composite nature of some of these materials.

The implication for pipework use is that, for the relatively soft materials being considered in this project, angle of impingement is not very critical, so the materials would be robust in terms of pipework configurations. This would not be true for the harder materials compared here. On the other hand, the strong dependence of erosion resistance on material hardness at small angles suggests that quite modest increases in hardness at grazing incidence (i.e. in straight pipe runs) would be beneficial.

It is found that, in general, erosion of sprayed coatings tends to lie above the trend line, at any rate at 90^0 impingement incidence. This may be related to the fact that these coatings are not fully dense and typically contain some oxidised material; these defects may constitute sites at which erosion may be initiated, and may also reduce the strength of the material.

Hawthorne et al [178] have compared slurry and dry erosion behaviour of a range of HVOF coatings. They found that erosion weight loss decreases with increasing (Knoop) hardness. For 'large' (200μm) particles, there was not much difference with impact angle and weight loss varied roughly as H^{-2}. For 'small' particles, behaviour at 90^0 impact angle was similar, but at 20^0 there was no such clear trend. The reasons for the differences between Hawthorne's work and that reported here are not altogether clear, but Hawthorne's coatings were mostly carbides, much harder than the mostly metallic coatings reported here. He comments that only the small number of metallic coatings in his study showed any sign of ductile failure, so the differences are probably due to different failure mechanisms.

4.3.2 Profilometry

2-D Profilometry

The erosion scars resulting from the experiments described above have been characterised using a Rank Taylor Hobson Form Talysurf 120L. The profiles obtained are, in each case, sections down the mid-line of the scar.

The forms obtained are, in every case, those expected for ductile materials [11,15,19].

Figures 4.3a and 4.3b, for ground aluminium at 30^0 and 90^0 respectively, are representative. In particular, the scar at 90^0 shows the typical 'W' shape of ductile materials, resulting from variable impact angles within the scar, while the 30^0 scar is essentially featureless (the jet enters from the left hand side of Figure 1b – the scar is perhaps more symmetrical than might have been anticipated).

Aluminium/12%silicon shows very similar scars, except that at 30^0 there is apparent roughening upjet of the scar. Figure 4.4 shows this with the 'roughening' clearly visible on the left. As will be shown later, this 'roughening' is actually an accidental concentration of pits on this particular sample and has no special significance.

The corresponding composite scar (Figure 4.5) is similar to Figure 4.3b, except that it appears somewhat rougher inside the scar.

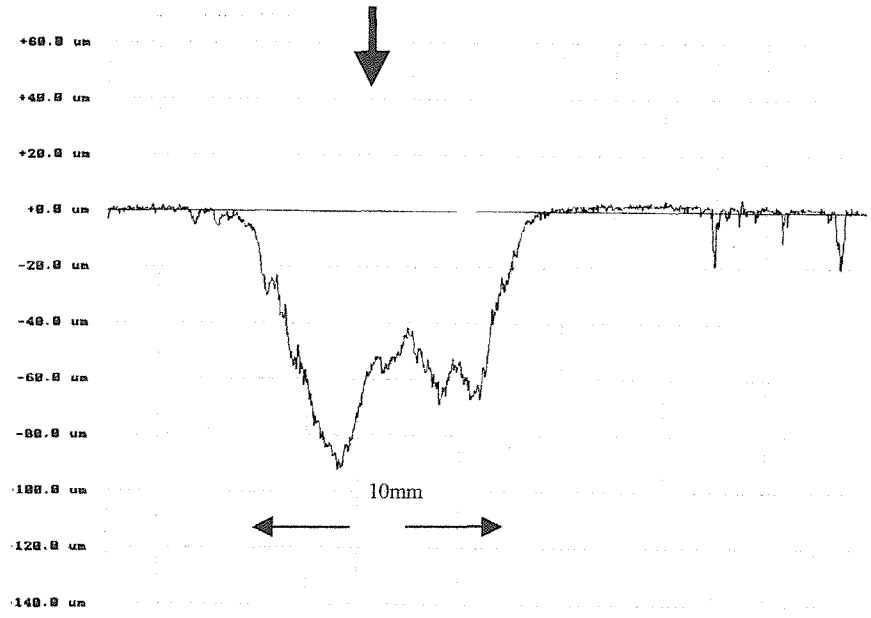

Figure 4.3a: 90 degree impact

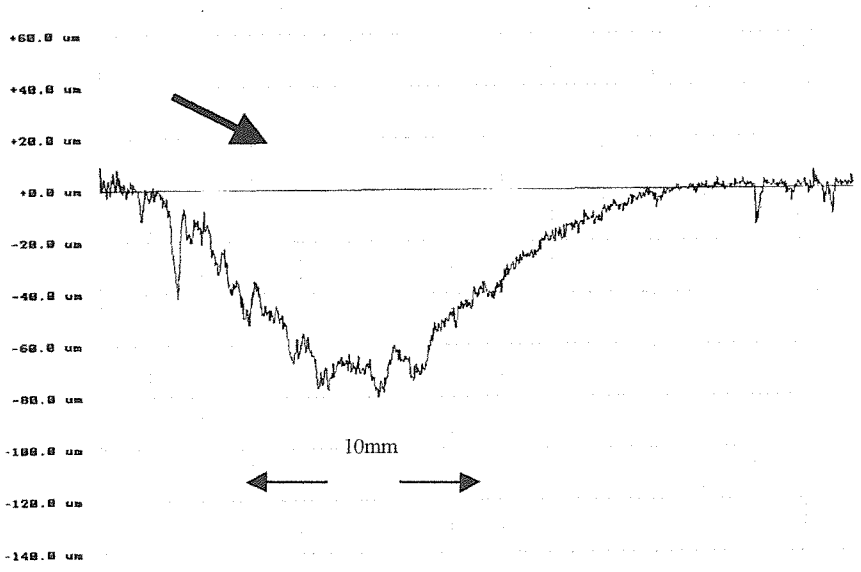

Figure 4.3b:30 degree impact

Form Talysurf traces of erosion scars:
Redhill 50 sand in tap water;
Ground Aluminium HVOF coating on steel

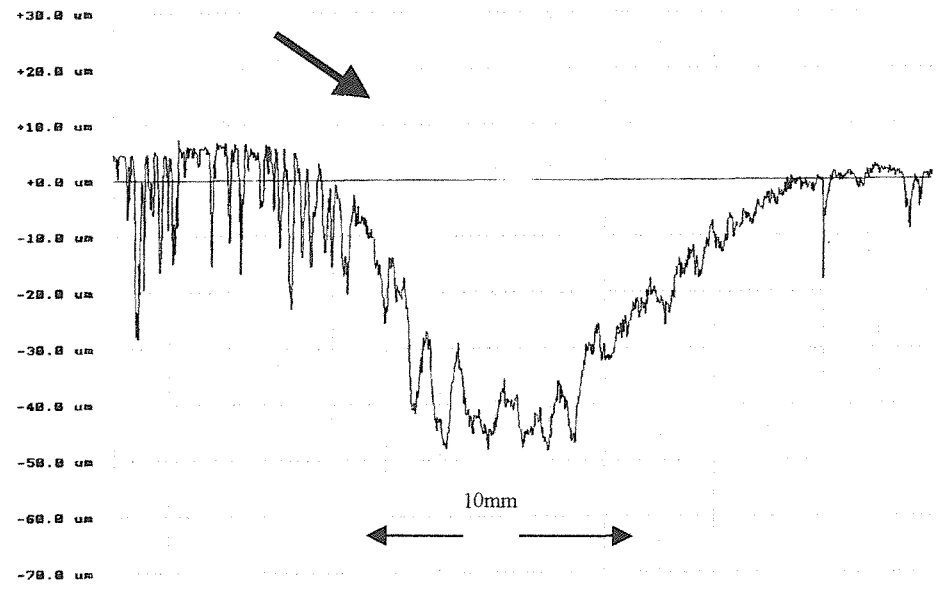

Figure 4.4: Form Talysurf trace of erosion scar: 30^0 impact
Redhill 50 sand in tap water
Aluminium/12%Silicon alloy, ground; HVOF coating on steel

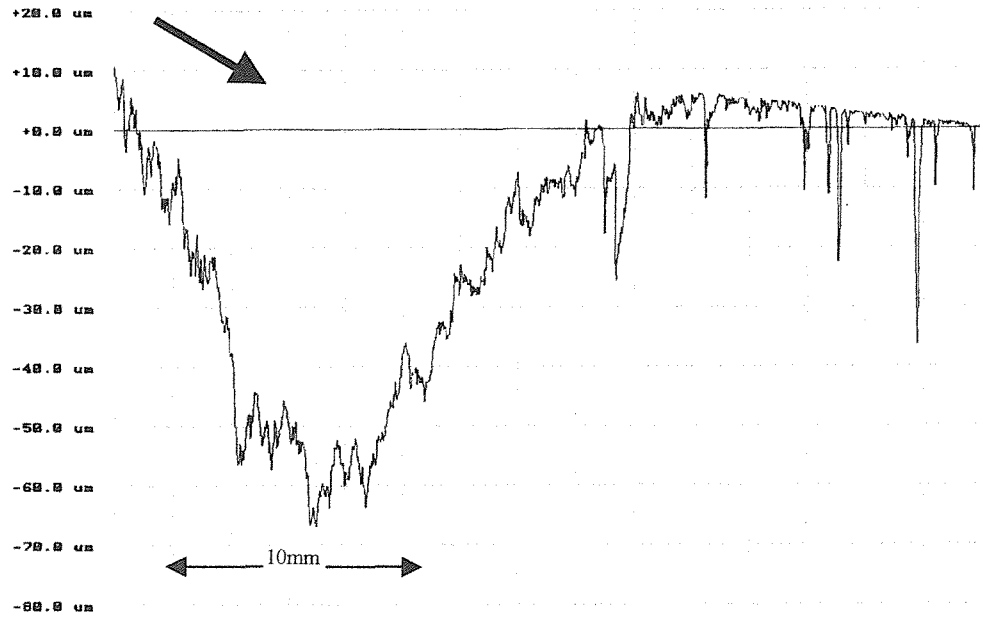

Figure 4.5: Form Talyform trace of erosion scar: 30^0 impact.
Redhill 50 sand in tap water;
Aluminium/12%Silicon alloy + Alumina, ground; HVOF coating on steel

3-D Profilometry.

The form of the erosion scars has been characterised by 3-D profilometry, using the RTH Form Talysurf and the CASA (Computer Aided Surface Assessment) software package [179], written under MATLAB v5.0. This has been somewhat compromised by the following factors:

- The measured scars are very shallow relative to their lateral extent. Typically, they are of the order of 0.1 – 0.15 mm deep, compared with a scar diameter of about 8 mm for a vertical impact scar and about 10 × 30 mm for an oblique impact scar. Scar depth was deliberately limited, so that the coating should not be completely penetrated.

- As noted above (Section 3.2), HVOF spraying left the samples slightly bowed; this bowing is of comparable order of depth to shallow scars.

- An experimental artefact was encountered in making the Talysurf traces. This manifested itself as pronounced parallel lines on the traced profile (parallel to the scan direction). At the time of experiment, it was thought that these lines were related to the sample bowing (all samples being similarly oriented) and represented some kind of 'quantisation' error in the instrumentation. However, it has subsequently been established that poor temperature control; associated with the room air conditioning, was responsible. Unfortunately, by the time this was discovered, the samples had been destroyed by sectioning and it was no longer possible to re-scan them.

Nevertheless, an overall impression can be obtained. Two series of profiles have been measured:

- 20 × 20 mm profiles to obtain overall scar profiles (122.7 μm point spacing)

- and, (for oblique scars only) 2 × 2 mm profiles (12.27 μm point spacing), to try to get a better idea of the nature of the surface. These scans were carried out at the leading edge of the erosion scars, where it was thought interesting features might occur.

Note that this instrument does not have the lateral resolution (at best about 6 μm between points) to resolve individual impact features (typically about 1 μm wide).

Figure 4.6 shows 20 × 20 mm profiles of erosion scars obtained on the steel substrate at 90^0 and at 30^0 impact. They are typical of ductile behaviour, as expected [19]. At 90^0 a circular scar is found with a central hump at the stagnation point. At 30^0 a smooth elliptical scar is obtained with no other features. The linear artefactual features noted above are visible at the edges of the image.

Figure 4.7 shows comparable erosion scars for HVOF sprayed aluminium. Their general form is very similar to those for steel. The main difference is that, in the case of 90^0 incidence, steel produces a relatively smooth central hump, whereas the sprayed aluminium produces a central hump that appears to be fragmented into a number of smaller peaks. The reason for this is unknown, but may be related to the splat structure of the coating. Since, in the case of commercially pure aluminium, there is little porosity, splat oxidation may be involved.

Profilometry images for Al/12%Si alloy and for (Al/12%Si + alumina) composite coatings are not reproduced, since they are qualitatively very similar to the images shown for the commercially pure aluminium coating. In detail, the scars are less well defined and their interiors appear rougher, probably due to the coarser nature of the structures.

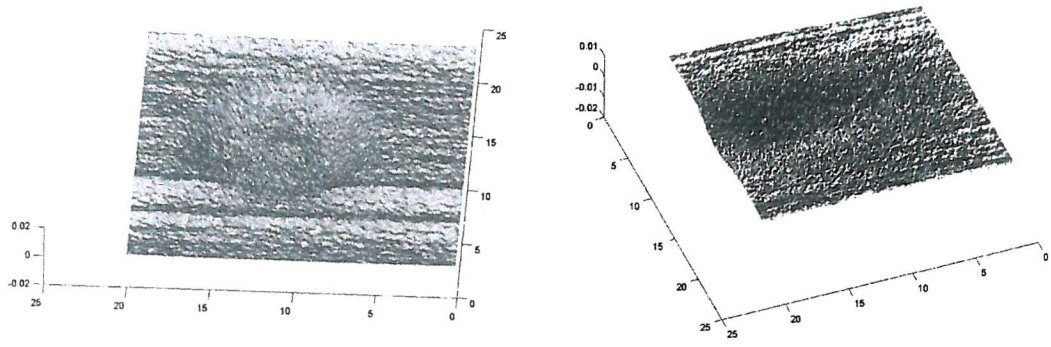

a) 90^0 impact. b) 30^0 impact

Figure 4.6: Erosion scars (mm scales).
Silica sand in tapwater on AISI 1020 steel

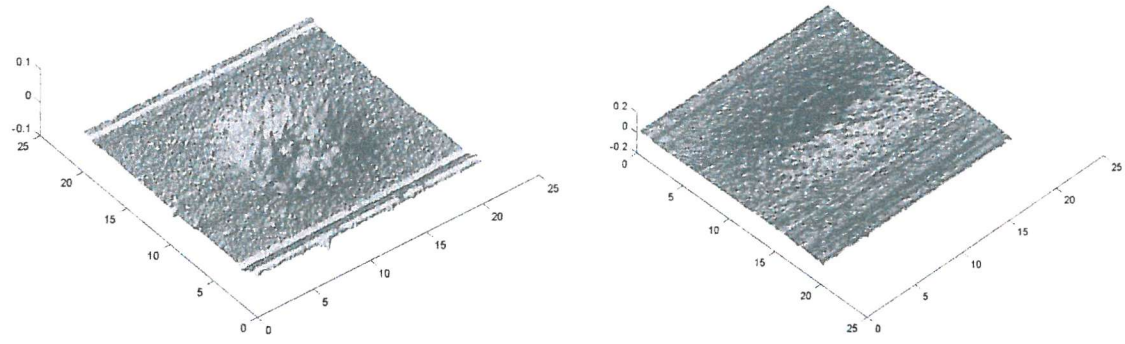

a) 90^0 impact b) 30^0 impact

Figure 4.7: Erosion scars (mm scales).
Silica sand in tapwater on HVOF aluminium.

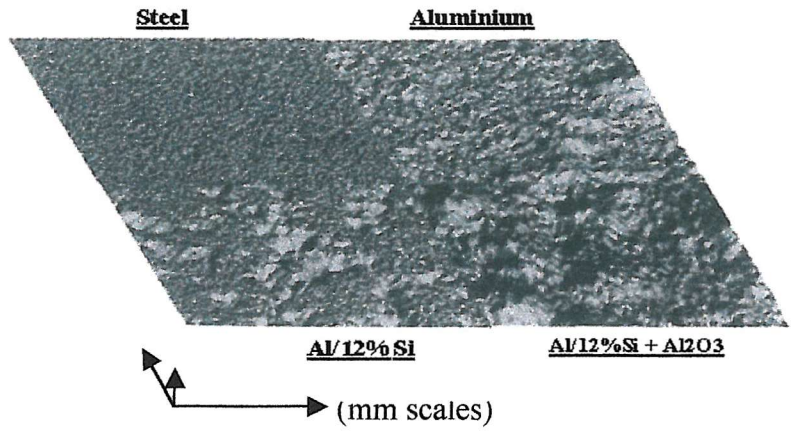

Figure 4.8: Mosaic of 3-D Talysurf images (CASA)

That the surfaces of the eroded samples are very different is illustrated by Figure 4.8. This is a mosaic of 2 × 2 mm squares, scanned at the leading edge of 30^0 erosion scars, shown at the same scale and viewing angle. Steel after erosion has very much the smoothest surface. Aluminium is noticeably coarser. Al/12%Si is generally similar to aluminium, but with conspicuous holes in it; these are several 10 μm across and are thought to correspond to wholesale removal of the 'melt packets' seen in Figure 3.4. There is texture on a similar scale on the composite coating, but it is less well defined because the surface is rougher on a variety of scales.

An attempt has been made to compare the volume lost from the sample, assessed from weight loss, and the volume of the scar (estimated as a spherical cap and ignoring the central hump). For 90^0 impacts on aluminium-based materials, the volumes shown in Table 5.3 were obtained. For the aluminium and aluminium/12% silicon alloy samples, the agreement is extremely good. The implication is that, for these materials, all the erosion takes place within the scar and not generally over the surface. In the case of the composite coating, total volume loss is estimated to be about 180% of the scar volume, implying that considerable erosion took place outside the scar. The volume loss from the scar itself is barely different from that of the unreinforced alloy, so for this particular composition the reinforcement is not doing anything useful.

Sample	Volume Removed / $m^3 \times 10^{-9}$	
	From Weight Loss	From Scar Volume
Aluminium	4.5	4.6
Al/12%Si	2.9	2.9
Al/12%Si + Al_2O_3	5.6	3.1

Table 4.3: Volumes of material removed; 90^0 impacts.

Other authors [168,170] have also found that when erodent particles are much larger than (randomly dispersed) reinforcement particles, the latter are not effective. The excess weight loss outside the scar is probably related to the greater surface roughness of this sample. Losses of non-bonded alumina from surface porosity may also have contributed.

4.3.3 Microscopy.

Optical Microscopy.

Eroded samples have been examined under a low power binocular microscope (×8 – ×40), as this gives the best overall idea of how the surface has changed.

Erosion of the steel substrate resulted in smooth scars, with no indication of cracking. Erosion appeared to be entirely ductile.

The ground aluminium samples showed a common appearance. Away from the scar, some porosity was evident – this appeared to be associated with splat boundaries, suggesting incomplete flow-out. Within the erosion scar this porosity was not visible, i.e. the erosion process had caused plastic flow in the surface to such an extent that

the porosity had become (at least largely) sealed. This is, of course, a desirable phenomenon from a corrosion point of view as it reduces available area (shot-peening would have the same effect). Previous workers [124,125,130] have also found erosion of aluminium, both in tap water and in brine, to be ductile in nature. Generally, within the scar the form was very smooth, apart from the central peak in the 90^0 impingement case and a slight indication of waviness at right angles to the scar axis (possibly associated with turbulence [70]) in the 30^0 case – this has also been seen by Zu *et al* [124].

The ground alloy samples have generally similar appearance to the aluminium samples. They show the same splat boundary associated porosity, but there is less of it and the pores have better defined edges. Within the erosion scar, the porosity has not been wholly eroded away or sealed, which may indicate that alloying has reduced plastic flow.

The ground composite samples showed a somewhat different appearance. Within the scar, the surface appeared wholly smooth, with no sign of the reinforcement at all. It appears that the rather large (235 μm mean), high energy particles have removed the smaller (approximately 25 μm) reinforcement particles completely, leaving a smooth metallic surface behind. Turenne *et al* have considered the erosion of alumina-in-aluminium composites [168], at much lower energy conditions. He found that reinforcement was helpful at low angles of incidence, owing to a 'picket-fence' effect, but not at normal incidence, because the reinforcement fractured under erodent impact. The 'picket-fence' is clearly not a factor here. It is possible that Turenne's mechanism may be more appropriate to filtered flows at lower energies.

One interesting observation was made from the as-made composite sample eroded at 30^0. Without grinding, the surface away from the scar exhibits protruberent lumps of material. Close to the scar, 'down-jet', these lumps are seen to be spattered with metallic debris. Some of these spatters are quite large – comparable in size with the 'lumps'. These spatters demonstrate both that material is being removed bodily in

sufficient sizes for it to be easy to understand how the erodent flow can just wash away the reinforcement, and also that redeposition of metallic material is possible on a suitable surface.

At higher magnifications, differences in optical appearance reflect the location of the imaged area relative to the visible scar much more strongly than composition.

For all materials studied, within the scar the surface was intensely disturbed by multiple impacts and resulting ductile flow, so that no individual impact sites could be resolved. Given that the estimated impact rate was in excess of 37 $mm^{-2}.s^{-1}$, this is not surprising. Ductile flow is so pronounced that, near the centre of the scar, it is not easy to tell which sample is which, nor what the sand impact angle was (i.e. there is no visible orientation). No cracking was observed in any sample.

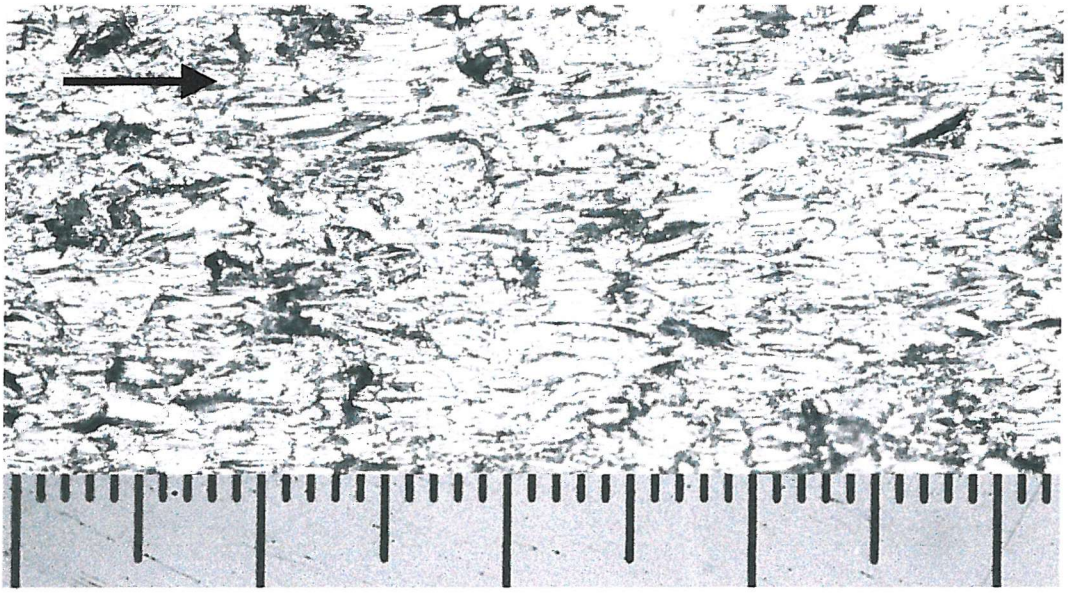

Figure 4.9: Impact scar field (flow direction as shown).
HVOF Al/12%Si on steel, 30^0 impact.
Trailing edge of scar – beyond visibly eroded area.
Scale: 1 small graticule division is 1 μm.

Away from the visible scar, fields of individual erosion impact sites are visible out to quite large distances from the visible scar. Figure 4.9 shows a typical example of such a scar field (HVOF Al/12%Si on steel, 30^0 impact, trailing edge of scar – beyond the visibly eroded area). It has not proved possible to obtain good images of individual scars optically, owing to depth of field considerations.

Electron Microscopy

In practice, the most useful information obtained relates to the different types of impact site observed. Detailed consideration of this topic will be deferred to Section 6, where impact sites obtained under these conditions will be compared with those found under the lower energy conditions used for the erosion-corrosion work.

However, some conclusions will be drawn here.

It is possible to make some very crude estimates of the volumes of individual scars (V_s) from SEM images, by direct measurement of scar length and breadth and assuming that scar depth is comparable to scar width. V_s may be compared with V_u, the volume removed per nominal impact as estimated by total weight loss, to obtain some idea of the efficiency of metal removal, and thereby get some indication of mechanism. This comparison is shown in Table 4.4.

It is not immediately obvious whether most material in these outer locations is removed *via* a small number of large sites or a large number of small sites. However, it is clear that, overall, if the small sites dominate then material removal must approach 100% efficiency – i.e. this is a true machining operation. Hutchings [36] has suggested that this can occur, but only under a very limited range of conditions. On the other hand, if large sites dominate, then the total scar volume excavated (scar volume × number of scars) is around 100 × the volume of material actually removed, as estimated from weight loss. This is in agreement with the observations of Finnie

Target (Coating on steel)	Volume Loss/ Impact, V_u / μm^3/impact, from overall weight loss	Scar Volumes from SEM imaging. Scar Volume V_s / μm^3		Volume Ratio V_u/V_s	
		Large	Small	Large	Small
Aluminium	103	11000	102	0.009	1.0
Al/12%Si	48	5800	160	0.008	0.3
AISI 1020 Steel substrate	12	1800	22	0.007	0.5

Table 4.4: Analysis of metal deformation/removal, 30^0impacts.

[38], for erosion of aluminium at normal incidence in air. In this case, most of the excavated volume represents material displacement (plastic flow into lips) rather than material loss. The likely mechanism for material loss is breaking off of lips under repeated impact.

The above represents the situation distant from the centre of the visible scar, but of course, most of the material loss is from the visible scar. Here the balance between large and small features (or, at least, large and small impacting particles) will be different. As shown by Benchaita *et al* [19] large particles are less deflected by the flow field than small particles, so the effects of large particle impacts, i.e. ductile flow into lips, which are subsequently broken off, are expected to predominate. This is consistent with the disturbed platelet-like surface actually observed.

It is therefore concluded that the mechanism of material loss is predominately by lip formation and fracture in the manner of Sundararajan [32] rather than directly by micro-cutting.

A further conclusion relevant to an electrochemical context may be deduced from the SEM scar images (very approximately). Impact scar lengths are generally found to be in the range 50-100 μm. If this is combined with the slurry jet velocity (27 $m.s^{-1}$), ignoring minor geometrical factors, a contact time of about 2-5 μs is implied. This implies that Electrochemical Noise electronics would need sampling rates of the order 10^6 s^{-1} to resolve individual impacts. This is consistent with the findings of Oltra *et al* [37] and of Burstein and Sasaki [20], who are the only authors to have attempted to make noise measurements at such rates under erosion-corrosion conditions. Both have identified fast transients. The Gamry instrumentation available for the current work has a maximum sampling rate of 10^3 s^{-1}.

4.4 EROSION – PRELIMINARY CONCLUSIONS.

Erosion measurements have been made in tapwater on the range of HVOF coatings described in Section 4, and on the substrate steel (AISI 1020), at 90^0 and 30^0 impact angles. High energy flow conditions (E_k = 6.5 μJ/nominal particle impact) were used with Redhill 50 sand (mean diameter 235 μm, angular). Short test durations (60 s) were used to ensure that coatings were not penetrated.

Mass loss measurements on eroded samples confirm that aluminium resists erosion poorly. Alloying with silicon improves performance, but not very strongly. Addition of alumina to reinforce the alloy coating made performance worse, but this is to be attributed to the fact that these samples did not have the structure intended; in particular, they exhibited high porosity, apparently, poor alumina/matrix adhesion and a lack of the sandwich structure intended. Since composite development was not a prime object of this work, investigation of this material was discontinued. Instead, hot dip galvanised zinc coated steel was included in later work.

There is a relationship between erosion resistance and microhardness, stronger for 30^0 impacts than for 90^0 impacts. No relationship was found with surface roughness.

Profilometry produces profiles entirely consistent with ductile erosion in all cases. The interior of scars on HVOF coated materials is rougher than is found for the substrate steel. In particular the central hump found in 90^0 impacts is fragmented in the case of the coatings, but is quite smooth for the steel. This probably reflects the splat structure of the HVOF coating (surface oxidation is more likely to be responsible than porosity, since HVOF aluminium metal shows this effect whilst having very low porosity).

Microscopic examination of these samples (optical and electron) shows surfaces consistent with completely ductile erosion mechanisms. At the scar centres very disturbed surfaces produced by plastic flow have the form of lipped platelets; individual impact sites cannot be distinguished. Distant from the scar individual impact sites can be recognised. Small sites are simple microcutting features, but larger sites show long grooves with lateral lipping, indicating plastic flow.

Direct estimation of impact scar volumes from SEM images and comparison with overall volume loss, estimated from sample weight loss, indicates that the larger features seen represent mainly material displacement rather than material loss. Since the larger features are likely to have been made by larger particles, and these in turn will be more significant in the scar centre (since they are less affected by the flow field) this is evidence that material loss is largely *via* plastic flow, resulting in lipping and subsequent lip removal by fracture or otherwise (probably by fatigue fracture in this case; possibly by stress corrosion cracking in a corrosive environment). The efficiency of material removal by impact appears to be very low, casting doubt on the value of parameters such as E_k, V_u, and emphasising the significance of collective effects in dense slurries.

Contact times on impact (depassivation times) are only of the order of a few microseconds, beyond the measurement range of the electrochemical equipment used for this work.

5 STATIC CORROSION

5.1 INTRODUCTION

This Section describes the equipment and procedures used for carrying out corrosion experiments. All the experiments described in this Section were carried out under static corrosion conditions, to characterise the performance of the measurement equipment, to explore the usefulness of various available measurement parameters and to serve as a baseline for future flow corrosion and erosion corrosion experiments. Illustrative results obtained by these means for individual materials are presented. Comparisons between these are made and their significance discussed.

5.2 EQUIPMENT

5.2.1 Potentiostat

A Gamry PC4/750 potentiostat and associated software have been used for electrochemical work, particularly for electrochemical noise measurements for which this system is especially designed

The PC4/750 potentiostat is a pair of printed circuit cards installed in a computer. These comprise a potentiostat card and a controller card. The potentiostat card controls the analog potentiostat circuitry and its isolated power supply. This card is not directly connected to the computer, except *via* its 5V power and *via* instrument earth. It communicates with the computer over serial lines isolated by optocouplers on the other card. The potentiostat card can be switched to act as a potentiostat, a galvanostat or as a zero resistance ammeter (ZRA). The second printed circuit card is the controller card. It contains an ISA bus interface, optocoupled serial bus logic, an isolated power supply, a signal generator (including a sine wave generator for EIS work) and a high performance measurement system. Signal filtering and analog to digital conversion (16 bit ADC) are carried out on the controller card, together with

offset and gain operations. Computer control of the voltage applied to the cell is *via* digital to analog converters (16 bit DACs).

Communication with the electrochemical cell is *via* a 7 core shielded cable. The 5 individual cell leads, connected to the potentiostat analog circuits, are shielded and isolated from instrument earth. There are 2 earth leads (required for different earthing configurations); these and the cable outer shield are connected to instrument earth. The cell connections, in potentiostat configuration, are as shown in Figure 5.1. The working and counter electrodes (WE and CE) are connected as to a precision resistor, i.e. 'sense' leads for measurement of potential drop and current carrying leads are kept separate. The 'sense' leads and that to the reference electrode (RE) are both connected to high impedance inputs ($>10^{12}$ Ω). In potentiostat configuration, with all electrodes 'floating' (as used in these experiments), both earth leads are connected to the Faraday cage. The use of a Faraday cage to prevent interference from through-space electric fields is essential, as is adequate mains filtering to minimise interference from the mains. If a sheet metal (as opposed to wire mesh) Faraday cage is used, this serves also to exclude light from the potentially light-sensitive Ag/AgCl reference electrode.

There is an automatic offset and gain facility built into the system, which allows the use of the most sensitive V and I ranges available under any given circumstances, with autoranging as required. Experience shows that, while this is useful for obtaining 'ranging shots' at data from experiments with unknown outcomes, the autoranging facility introduces switching transients, which cannot be mathematically distinguished from electrochemical noise. It is therefore preferred, once the order of expected voltages/currents is known, to use fixed measurement ranges and gains.

External interference must be minimised. Generally, the filtering and shielding of the instrument appears to be good. Turning the computer monitor off and on results in a

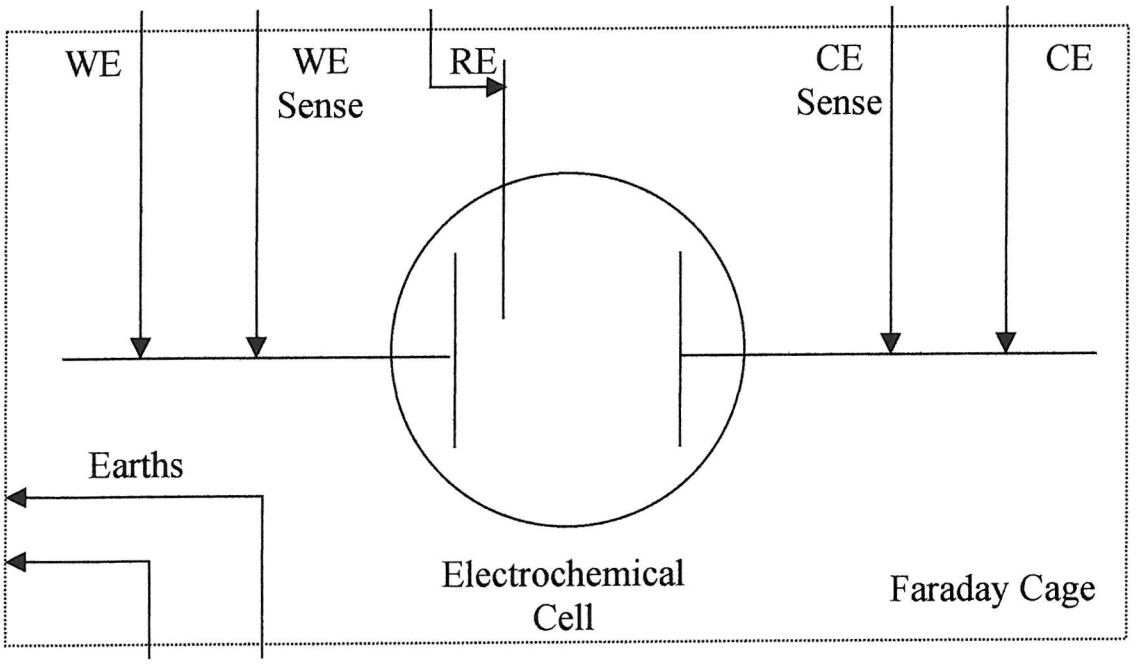

Figure 5.1: Electrochemical Cell connections

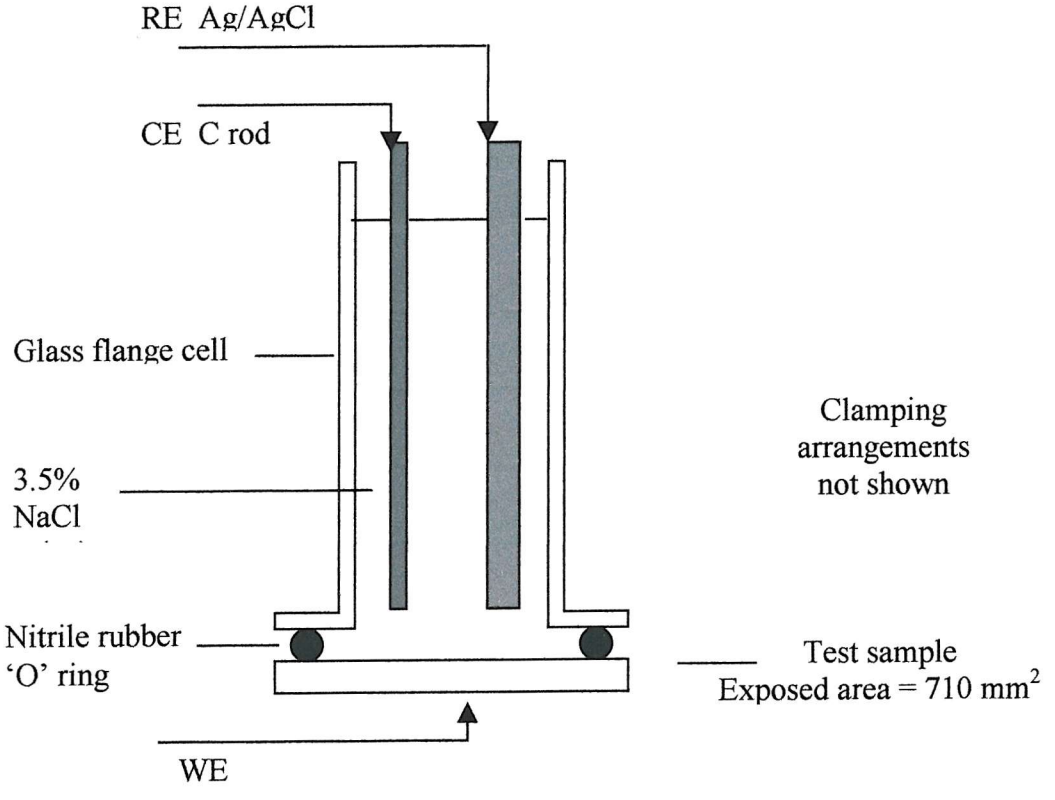

Figure 5.2: Electrochemical Cell construction.

spike at turn-on, but no other effect. Apart from this, external noise is occasionally seen (see, e.g. Section 5.4.4); the source for this has not been located.

The timekeeping precision of the computer appears to be well within 1 minute in 24 hours, i.e. < 0.1 %.

5.2.2 Electrochemical Cell

For reasons explained in Section 2.4.5, experiments have been carried out using a potentiostatted working electrode in a conventional 3 electrode cell, rather than attempting to work with two 'identical' working electrodes.

The cell used for these experiments is shown in Figure 5.2. This cell comprises a glass flange clamped to the working electrode, with an intervening nitrile rubber 'O'-ring. The 'O'-ring both provides a good seal and defines the working electrode area (approximately 710 mm^2). Materials relevant to this project have been used as working electrodes (WE) immersed in static (not de-aerated) 3.5% sodium chloride. The reference electrode (RE) is a robust single junction Ag/AgCl electrode obtained from SENTEK. A carbon rod (Agar Scientific, spectrographic quality) is used as the counter-electrode (CE). All experiments have been carried out in a Faraday cage.

Various issues have been raised concerning the operation of this cell:

- Choice of Reference Electrode. This type of electrode has been chosen with a view to suitability for use in chloride media (3.5% NaCl), robustness (in view of the extension of this work to flowing media) [72], and avoidance of double junctions (to avoid potentiostat instability [180], and unwanted high frequency dispersions in EIS work).

- Field Uniformity. The electrode arrangement, as used, is not symmetrical with respect to the WE. The post-test appearance of the WE (see Section

5.4 below) suggests that the electrode geometry could be improved, for example by using a cylindrical CE disposed around a central RE. For the experiments reported here, the effects due to non-symmetry were minimised by keeping the CE and RE well separated from the WE (about 20 mm). This introduces an iR drop, but in 3.5% NaCl it is not too serious and can be estimated by EIS methods.

- Crevice Corrosion. There is a crevice between the nitrile rubber 'O'-ring and the WE, where unwanted corrosion might occur. In practice, this does not happen, because aqueous solutions do not wet into the crevice, at least not on the time scale of these experiments.

- De-oxygenation of the solution column. No attempt has been made to either fully oxygenate or de-oxygenate the solution column (which would create non-static conditions at the WE surface). While undoubtedly de-oxygenation does occur to some extent, this was not expected to make a significant difference to the results obtained. This appears to be justified for experiments with steel blanks, but possibly not where the WE was aluminium based, (see Section 5.4 below).

5.2.3 Software

Introduction

The software comprises Gamry's CMS100 Framework program, the CMS105 DC Corrosion and CMS300 Electrochemical Impedance modules of this Framework, and the quite separate ESA400 Electrochemical Signal Analyser program. Most of the work reported here is based on the use of the ESA400 software for Electrochemical Noise, with some use of CMS300 for Electrochemical Impedance work.

ESA400 is reviewed for its abilities to perform in terms of the requirements identified from the literature (Sections 2.4.5).

CMS300 is a conventional EIS program, which appears to perform adequately in terms of data acquisition (in a not very demanding application); data export and analysis using the program EQUIVCRT [75] is preferred to Gamry's own program on grounds of convenience and flexibility. These programs are not discussed further.

ENA400 – Electrochemical Noise Analysis software capabilities

Data Acquisition and Pre-processing

Sampling rate. The system is capable of sampling up to 1000 s^{-1}. At the highest sampling rate, performance is degraded, the signal showing quantisation effects. No such problems are apparent when sampling at 100 s^{-1}. Most of the work reported in this Section was carried out at a sampling rate of 20 s^{-1}, occasionally using 100 s^{-1}.

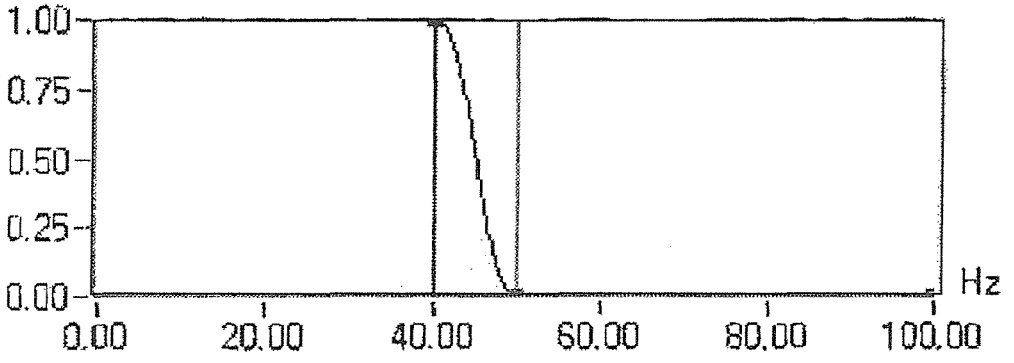

Figure 5.3: 100 s^{-1} filter characteristic: Relative current magnitude *vs* Frequency. Source: Gamry Instruments.

Anti-aliasing. The sampling rates (f_s) are fixed. The analog signal is subjected to anti-aliasing filtering at an appropriate frequency (nominally 0.5 × f_s) before sampling, as is required. Figure 5.3 shows the filter characteristic of the anti-aliasing filter used by Gamry at 100 s^{-1}; this is typical [181]. The filter gives a 0.1% error;

this results in a cut–off at $0.4 \times f_s$ (0 dB) and the signal is reduced to –60 dB at $0.5 \times f_s$. Sampled data may be reliably used up to $0.4 \times f_s$.

Detrending. The software contains a tool for detrending segments of data. This is a least squares linear detrend of the data. It has been found that it is necessary to carry out this operation on all data sets, irrespective of the flatness of the original data, because an offset is introduced by the instrument. This results from the limited resolution (16 bit) of the DAC in the control loop [182].

Resolution and Quantisation. The resolution of the ADCs in the measurement circuits are 16 bit. If the current range is set to 750 μA, the smallest resolved current will be approximately 11 nA. This was adequate for the purposes of the work reported in this Section.

Assessment of Stationarity, and Signal Averaging. Both of these operations require breaking up a given time series into several consecutive shorter series, and applying appropriate parameterisation methods to the latter. ESA400 provides no direct means of doing this, but it is possible to export the raw data to e.g.. MATLAB and carry out any necessary calculation there.

Reporting. ESA400 provides adequate data outputs, but graphical output is very poor. It is preferred to export the results of calculations and plot data as required from MATLAB or EXCEL.

Data Analysis

Data Analysis Capabilities. At least in principle, the ESA400 software is capable of carrying out all the analyses described by Searson and Dawson [100]. The main system limitation, apart from poor documentation/help, is that the computer supplied will not handle data sets much larger than about one million data points; this has not proved to be an important limitation.

The system records noise data (V and I) in records limited only by the storage capacity of the computer. It is subsequently possible to analyse the data in user-defined blocks of arbitrary length (subject to computer capability – analysis capability being much more limited than hard disc memory).

Block Data Statistics. The following block statistics are available for the characterisation of blocks of time series data:

Mean
Variance/Standard Deviation (Population)
Skewness
Kurtosis
Noise Resistance (i.e. $\sigma(V)/\sigma(i)$)

Gamry have chosen to define kurtosis by reference to the kurtosis of a Normal Distribution, taken as a standard, i.e. they subtract 3.0 from the usual statistical definition. For the purposes of this report, 3.0 has been added back to the data, which means that kurtosis cannot have a negative value. Note that both forms of this quantity are found in the literature – a matter that has caused some confusion.

The statistical quantities used in this thesis are defined by:

Mean: $$\mu = \frac{1}{N}\sum_n i_n \qquad (5.1)$$

Variance: $$\sigma^2 = \frac{1}{N}\sum_n (i_n - \mu)^2 \qquad (5.2)$$

Skewness: $$Sk = \frac{1}{N\sigma^3}\sum_n (i_n - \mu)^3 \qquad (5.3)$$

Kurtosis: $$Ku = \frac{1}{N\sigma^4}\sum_n (i_n - \mu)^4 \qquad (5.4)$$

It should be noted that all these quantities are bandwidth sensitive. This is most easily understood, and will be illustrated, in terms of the power spectral density function, to be discussed below. This means that it is essential that, when these quantities, or any derived from them, are quoted, the sampling frequency and sampling time should be quoted also. This has not always been done in the published literature, which makes comparisons of published work extremely moot.

The higher order quantities are strongly affected by time-varying data. Linear trends can be satisfactorily subtracted (and data here is routinely 'linearly detrended' before further processing), but curvilinear baselines ('non-stationarity') lead to meaningless statistics. It should also be noted that skewness and, particularly, kurtosis are very strongly affected by extraneous noise. It is absolutely essential to take all possible steps to isolate the system electrically and to inspect the data obtained to ensure that no extraneous noise has slipped through.

As an example of the effects of extraneous noise, Table 5.1 gives calculated statistical parameters for a typical data set, which contained a single large extraneous current spike (approximately 20× the general noise level, caused by the computer's screen saver! – this interference, once recognised, was removed from later experiments by altering the saver settings). The table shows the effects of editing out 3 grossly outlying data points (out of approximately 4000) – probably this did not remove the tail of the transient completely. This editing has practically no effect on the mean and standard deviation, but has large influences on the skewness and, particularly, on the kurtosis.

	Mean / μA	Variance / $(\mu A)^2$	Skewness	Kurtosis
Raw Data	-19.0	0.017	1.4	18.7
Edited Data	-19.0	0.014	-0.25	6.5

Table 5.1: Influence of external noise on statistical quantities

A further illustration of the effects of interference is to be found in Section 5.4.4.

Probability Density Function (*pdf*). These statistics are quantities which characterise a probability density function (pdf) for the amplitude of the parameter concerned. The program allows direct estimation of this *pdf*. Naturally, all the caveats regarding extraneous noise and curvilinear baselines, which apply to the statistical functions, apply to the *pdf* also. The *pdf* shows whether or not the distribution function is monomodal; if it is not, though the higher order statistical functions can be calculated, they are of very doubtful value.

If the potentiostat is controlling the cell properly, the potential distribution is found to be nearly Gaussian, with (in this cell configuration) a standard deviation of approximately 20 μV; deviation from this seems to be a sensitive measure of lack of control. Rapidly changing cell conditions, lead to lack of stationarity in the output signal.

If the potential distribution is monomodal, but the current distribution is not, as is sometimes observed, then there are implications for the mechanism of current flow; these do not appear to be explored in the literature at all – some comments will be made on these *pdf* plots in relation to particular samples. It may, however, be observed here that if a constant potential is applied to a cell and currents of several different magnitudes flow, as shown by several peaks in the *pdf* plot, then several

different resistances must be present during the course of the experiment, either together or successively.

One possibility is the existence of several different current paths, for example from active areas on the apparent sample surface on the one hand and other active areas deep in the coatings porosity on the other. The *pdf* plot then indicates the distribution of current between these paths.

Another possibility is that the electrochemistry changes within the time scale of the experiment (i.e. the data is non-stationary on this time scale), e.g. as a result of the activation/deactivation of metastable pits.

There is, in principle, quite a lot of information in these plots, not currently exploited.

Noise Resistance. Workers on Electrochemical Noise frequently make use of a quantity called the Noise Resistance, R_N, defined as:

$$\text{Noise Resistance:} \qquad R_N = \frac{\sigma_v}{\sigma_i} \qquad (5.5)$$

It is shown by Chen and Bogaerts [183] that this quantity is equivalent to a polarisation resistance, provided that the corrosion reactions are strictly activation controlled, that the 'mixed potential' is far away from the separate rest potentials of anode and cathode, and that the corrosion process is in a state of dynamic equilibrium. Strictly, this quantity is defined in terms of the type of Electrochemical Noise experiment in which two 'identical' working electrodes are used, and it is not clear that R_N calculated for a potentiostatted system is the same quantity. Of course, if the potentiostat control were perfect, σ_v, and therefore R_N, would always be zero. In practice, this is not the case (σ_v is typically ~ 20 μV, as noted above). R_N values have therefore been calculated, but it is to be understood that these are not necessarily comparable with values obtained by other means elsewhere. It may also be noted

that, since this quantity is derived from σ values, all phase information in the original data is lost. R_N is as bandwidth sensitive as the statistical data it is derived from.

Power Spectral Density (*psd*). The above quantities characterise the signal in the time domain. A series of operations are available to characterise the signal in the frequency domain. These include Power Spectral Density (*psd*) plots as estimated by the Fast Fourier Transform (FFT) and the Maximum Entropy Method (MEM). All the baseline linearity constraints applicable to time domain processing apply here too, with the additional requirement that the 'ends' of the processing window must be made to match up; this normally means that the signal must be multiplied by a 'windowing' function if useable results are to be obtained. Here a Hanning window has been used, though the choice of window does not seem to make very much difference.

FFT *psd* plots are direct transforms of the time domain data. They involve no further assumptions and produce plots that are inherently noisy. Gamry have used an implementation of National Instruments' LabView program to do this. According to National Instruments, [184], FFT psd plots are calculated by a split-radix algorithm with no ensemble averaging. Visual comparison utilising early parts of this work, processed using MATLAB, which uses a Welch algorithm incorporating a Hanning window and ensemble averaging [185], suggests that the real difference is not very great.

MEM calculations aim to arrive at equivalent results, with much less noise, using ideas from Information Theory. The calculation algorithm used is taken from Press et al [186]. However, this method involves the incorporation of an arbitrary number of filter coefficients. The results obtained depend strongly on both the number of filters assumed and the window length used. For this Thesis MEM calculations have not been used, owing to their inherent ambiguity.

The quantities typically of interest from *psd* plots are the slope of the main part of the plot and the 'power' levels associated with any plateaux that may be present. Note that the term 'power' is here used in its signal processing sense (see below), not as normally understood. It is very important to establish that plateaux are real and not artefacts of the measurement or calculation procedures (this is a particular weakness of the MEM procedure); this may require making measurements at several sampling frequencies.

Outlying data points, due to extraneous noise, have relatively little effect on the *psd.* Non-stationarity, in the sense of a curved baseline appears in the *psd* as excess low frequency 'power' – it looks like a very low frequency feature, which can be readily separated from the rest of the *psd* plot, if desired. *Psd* plots are therefore more robust with respect to interference than are time series data; the price paid is that information about transient shape (not accessible in these experiments anyway) is lost.

Power Spectral Density plots are normally plotted in electrochemical work on a double logarithmic basis ($Log(A^2.Hz^{-1})$ *vs* Log(Hz)), in order to identify features which are linear on this basis, and to characterise their slopes. Signal power, however, is more easily characterised from a double linear plot, as is shown schematically in Figure 5.4.

The current power, $\sigma^2(i)$, is the area under the *psd* curve, plotted on a double linear basis ($A^2.Hz^{-1}$ *vs* Hz), between defined frequency limits, '*a*' and '*b*' in Figure 5.4. In the figure above '*a*' represents the reciprocal of the sampling time and '*b*' is the sampling frequency. So, either increasing the sampling frequency (1) or increasing the sampling time (2) will increase $\sigma^2(i)$, i.e. $\sigma^2(i)$ is bandwidth dependent, and sampling frequency and time should always be quoted.

$\sigma^2(i)$, in practice, is the Electrochemical Current Noise variance, as defined above.

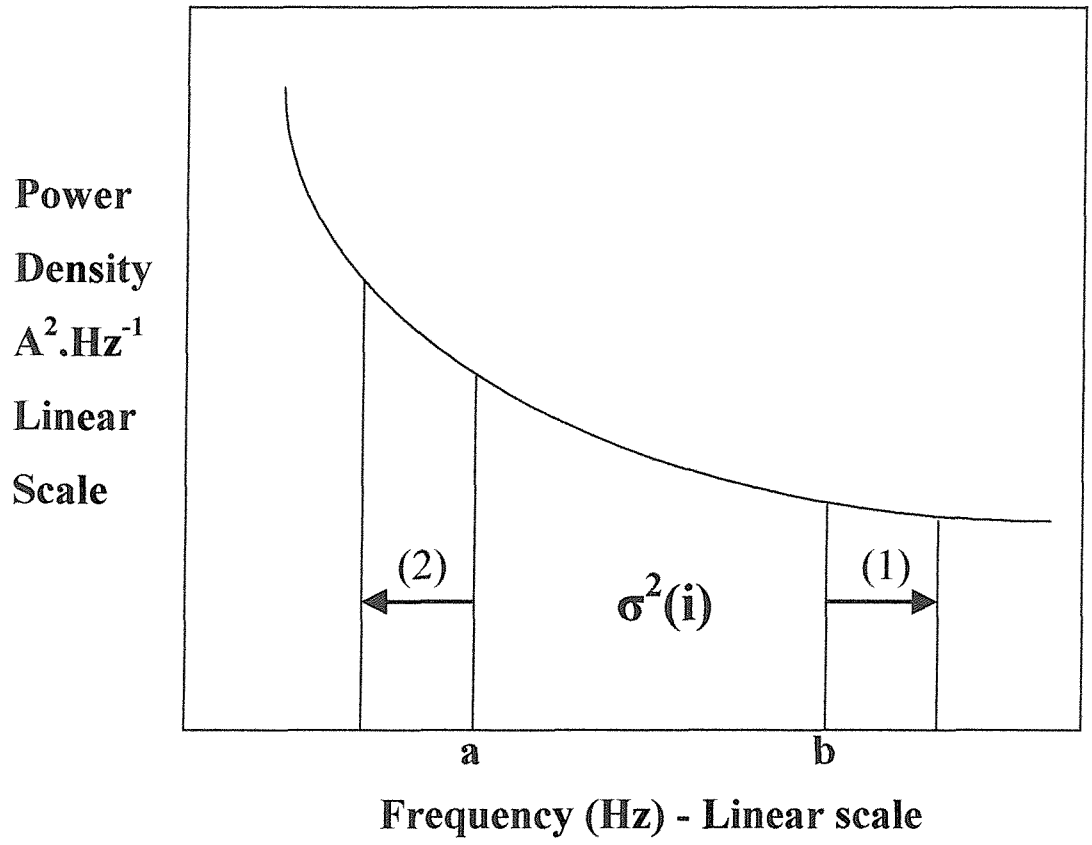

Figure 5.4: Schematic power spectral density curve, showing relationship between *psd* and signal power, and the effects of varying experimental parameters.

Joint Time Frequency Analysis. If the signal is unavoidably time-varying (non-stationary), normal digital signal processing theory does not apply. However, various theories for time varying signals (Joint Time-Frequency Analysis – JTFA) have been developed. There is an implementation of JTFA within ESA400, based on theory given in Chen and Qian [107]. Applying it directly to results obtained in this work does not lead to obviously useful conclusions. More will be said about a specific form of JTFA (the wavelet transform) in Section 6; this is not implementable within ESA400, but an implementation in MATLAB has been developed by this author..

5.3 PROCEDURE

5.3.1 Experimental

After assembling the cell, with the sample of interest as working electrode, and filling it with 3.5% NaCl, a period of 1 hour was allowed to elapse before any measurements were made. The open circuit potential (OCP) of the working electrode relative to the reference electrode was then monitored over two minutes and a value established. This potential was then imposed on the working electrode, using the potentiostat, and the currents flowing between the working and counter electrodes measured and recorded over a period of 600 s at a sampling frequency of 20 s^{-1}; the imposed potential was then released and the electrode allowed to recover. This procedure was repeated at 3, 5 and 24 hours after immersion. All measurements were made within a Faraday cage. After 25 hours, the cell was emptied, dismantled and the surface of the test sample examined.

Samples of the 3 aluminium-based coatings of interest and of hot-dipped galvanised steel were run as well as of the steel substrate. A single experiment was carried out on 304L stainless steel, to show the systems' ability to resolve transients.

5.3.2 Data Analysis – Electrochemical Noise

In order to obtain meaningful data from electrochemical noise measurements, it is essential to obtain time series which are as stationary as possible. It is found, under static conditions, that there is a conflict between different experimental requirements. On the one hand, the WE OCP tends to drift with time (particularly shortly after immersion), so that, if the OCP is measured and then this potential is potentiostatically held over long periods, the progress of the corrosion process is distorted by the measurement – this is clearly unacceptable. On the other hand, it is found that when potentiostatic control is engaged, a current transient occurs, which takes several minutes to decay. This is probably related to the fact that it is

impossible to 'hit' the OCP exactly, particularly with noisy electrodes, and there is some charging of the electrical double layer to be accommodated. It is therefore necessary to pick a compromise measurement time, which is long enough to allow the starting transient to decay, but not so long that the corrosion process is affected excessively. After some experimentation, it has been found that, for the experimental samples tested here, if a measurement time of 600 s is used and the last 200 s of current readings is taken from this, reasonably stationary data are obtained. There is always some residual trend in the data, in addition to the machine induced offset, to be noted in Section 5.4.1, so the 'linear detrend' option is always used. The least satisfactory data, sometimes showing slightly curved baselines (which cannot be removed without distorting the data), are those acquired at the shortest times after immersion, when the OCP is changing most rapidly. To minimise disturbance to the system, at least 30 minutes (usually 2 hours) are allowed to elapse between measurements. These timings are to be assumed in the results reported below, unless otherwise stated.

For a sampling frequency of 20 s^{-1}, the Nyquist frequency is 10 Hz; this is the theoretical maximum frequency for data acquisition without aliasing. However, because of the non-ideal nature of the anti-aliasing filter, a lower high frequency cut-off must be used, as noted above, here 8 Hz.

5.4 RESULTS AND DISCUSSION

5.4.1 Dummy cells and Background Noise

Gamry supply two dummy cells (for DC and AC measurements) to check instrument performance. These were run with the internal calibration routines and the outputs checked with Gamry. They were found to be within specification, except that the mains frequency setting required to be reset from 60 Hz to 50 Hz, which change was made.

The DC cell is a 100 Ω precision resistor. Noise measurement using this cell showed an apparent DC offset of 160 μV (should be zero) at 3 V gain on the voltage channel, after taking about 40 seconds to stabilise. Information from Gamry [182] indicates that this is an artefact, caused by the limited DAC resolution on the voltage control of the potentiostat. Offsets of this order (up to about 1 mV) are not real, and should be removed using the 'linear detrend' option. If this is done a residual noise level of approximately ± 5 μV remains (at 3V voltage gain). This residual noise level is probably gain dependent, but since the present work requires voltage offsets of the order of 1 V, more sensitive ranges are effectively not available. This phenomenon requires that the 'linear detrend' option is always used before processing the data further.

If a noise experiment is carried out with the connectors open circuited (no cell attached to any of the potentiostat leads), the voltage recorded moves out to its compliance voltage (12 Volts), while the current settles to a low level of residual noise (approximately ± 10 pA), which should represent the electrometer noise. This noise was however, found to be superimposed upon a slow drift of about 200 pA over tens of minutes, the cause of which is not known.

Further baseline experiments with real cells attached have been carried out, under conditions similar to those used for measurement of real samples, i.e. with an intact cell attached to the potentiostat, only the WE lead being detached. Under these conditions the Noise Power level $\sigma^2(i)$ is about 10^{-26} A^2 on the 710 mm^2 sample area. This behaviour suggests that very little noise is associated with the carbon CE or the Ag/AgCl RE.

5.4.2 Data Outputs

ENA data have been analysed as time series and *psd* plots. Both these data forms have their value, and should be used together.

Time series are the basic experimental output. This is the format in which interferences and non-stationarity are most obvious. Derived data, particularly higher order statistics such as skewness and kurtosis, are very sensitive to such experimental problems, and should not be used unless it can be positively demonstrated that these influences are absent.

Noise resistance is an interesting quantity, defined in a somewhat arbitrary way. It is not altogether clear what its physical significance is, in the context of a potentiostatted working electrode. Nevertheless, it is easily obtained and appears to behave, at least qualitatively, as would be expected of a polarisation resistance.

Power Spectral Density plots offer a means of reducing time series data to a form from which relatively well defined parameters may be obtained. They also make it possible to remove any consistent interference that may be present, and make the effects of gross non-stationarity separable. However, a complex calculation is involved to obtain the *psd*, and the relationship of *psd* parameters to the physical situation is not self-evident. Also, considerable information is lost (all phase information), notably about the shapes of any resolvable transients (not relevant to this work since individual transients are not resolved). Periodicities in the data, which would show up as distinct peaks, are generally absent; for most systems the plot consists of a single straight line with negative slope, sometimes with a low frequency plateau.

In general, for the purposes of this Section, it has been found that the most useful parameters have been the slope of the *psd* plot and the electrochemical current noise power $\sigma^2(i)$.

5.4.3 Precision

To compare data sets relating to different materials, it is necessary to have an idea of how reliable individual data sets are. It is notable that in the Electrochemical Noise

literature, this issue is not addressed at all. In individual papers, *psd* slopes are typically referred to as 'flat', 'slightly sloped' or 'strongly sloped', and while parameter estimates are quoted, more often for 'slope' than for 'power', they are not actually used for comparative purposes. Perhaps unsurprisingly there is a great deal of confusion about how certain materials (especially steels) behave. Some of this confusion probably arises because the materials are not adequately specified as regards composition, but some is undoubtedly due to inconsistency, both in data acquisition and in data analysis. This is illustrated by the round robin experiment reported by Goellner *et al* [123]; in this case the lack of understanding of several of the participating laboratories was so gross as to make their measurements wholly meaningless.

In the present work, it has been found necessary to define procedures very closely, both for experimental work and for data analysis (Section 5.3). In general, not enough replicate experiments have been carried out to make definitive statements about precision, but an idea can be obtained from situations where the behaviour of a sample does not appear to change with time, and has been measured repeatedly. For present purposes, the behaviour of AISI 1020 steel provides the most informative data. For this see Table 5.2 in section 5.4.5, below. 'Slope' values vary over a range of 5.5 dB/decade, 0.6 dB/decade if the 3 hour immersion figure is excluded. The reason for the anomaly at 3 hours immersion is unknown, but is thought to represent an experimental problem rather than reflecting any underlying difference; however, this cannot be positively asserted. Therefore, somewhat conservatively, 'slope' values will be regarded as different if they differ by more than 5 dB/decade.

5.4.4 Representative Data

Figures 5.5 –5.9 show time traces and *psd* plots for a hot-dipped zinc coating, AISI 1020 steel, a HVOF aluminium coating and for 304L stainless steel immersed in 3.5% NaCl for 1 hour, based on detrended data. Data sets represent 200 s measurements, except for the 304L stainless steel for which 480 s were required to

show the transient structure. The power spectral density plots are all to the same scale, for comparison purposes

Hot-dipped Zinc on Steel

Hot-dipped zinc coated on steel was examined over 24 hours. This sample was not ground before examination. When the cell was dismantled at the end of the experiment, the sample overall appeared slightly polished compared with its as-made condition. A featureless white powder was present on the surface, probably zinc oxide. There were also two dark marks, surrounded by white powder – it is possible that these dark marks represent exposed iron.

Over the course of 25 hours immersion, OCP *vs* Ag/AgCl. changed from –1.023V to –1.032V, a change of 0.009V in the negative direction. This is a very small change and implies that the surface behaviour did not change appreciably during the course of the experiment. To the extent that iron may have become exposed, it has had effectively no influence on this potential.

This series of measurements (Figure 5.5) was severely affected by external interference from an unknown source, which limits the value of the data. However, some information can still be obtained, and this data set also serves to illustrate some of the effects of interference.

The time series plots show, besides the interference, very low amplitude noise superimposed on a slow current drift.

Noise power levels are low ($\sigma^2(i)$ = 8.1 × 10^{-15} A^2), even though a significant proportion of the calculated value is due to the interference, i.e. there is not much noise on this surface. Indeed, the low electrochemical noise level is one reason why this interference is visible. Over 25 hours the noise power increased gradually to 7.3 × 10^{-14} A^2, i.e. about 9 times. The calculated value of skewness is exaggerated and

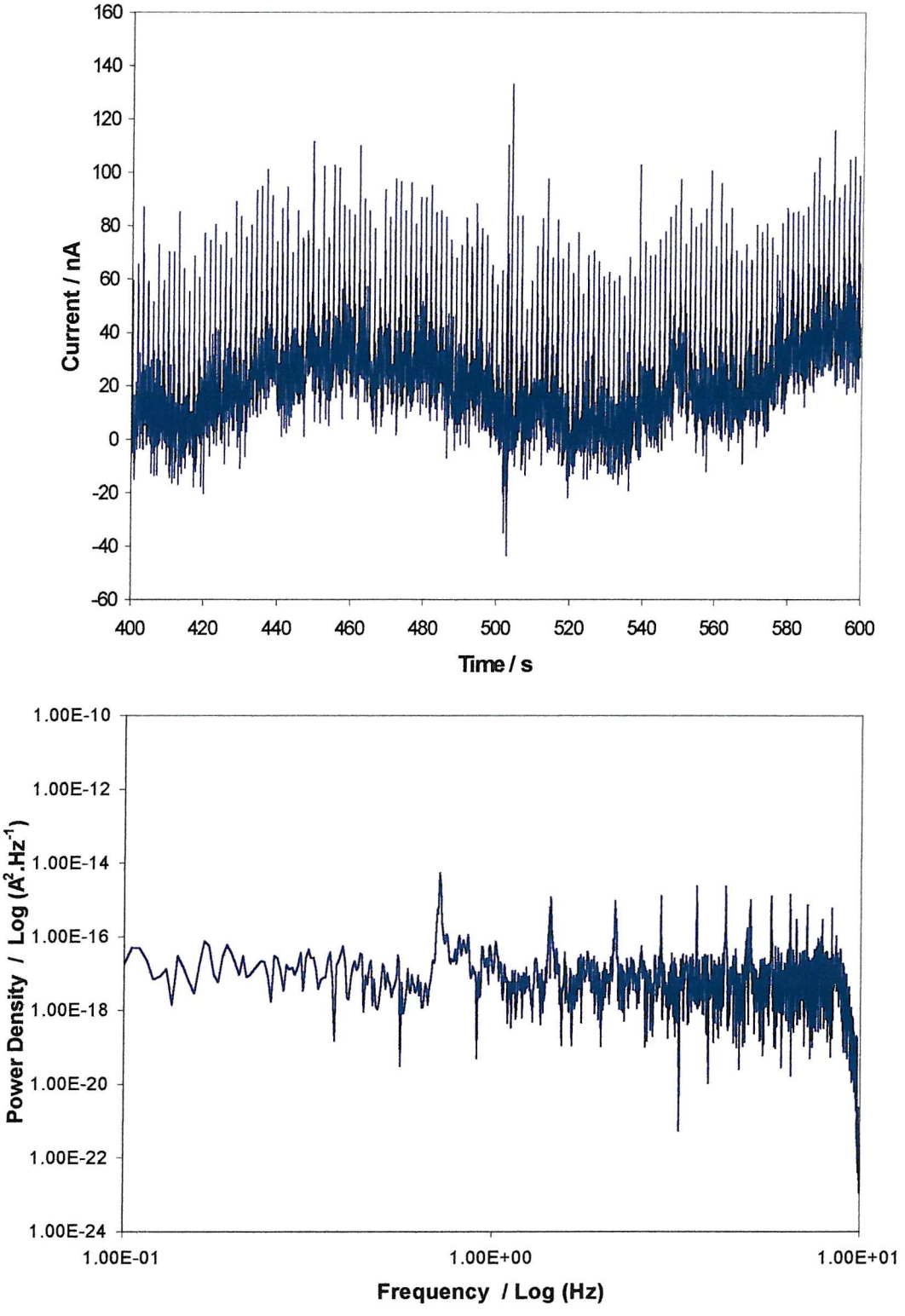

Figure 5.5: Hot-dipped zinc in 3.5% NaCl, 1 hour immersion.
Detrended data. External noise present

the kurtosis is reduced relative to the values they 'should' have because of the interference, though this is not obvious from the raw numbers. Since the standard deviation is distorted, so is the Noise Resistance; this also is not obvious.

The *psd* plots are flat ('white' noise) at a low power level (~ 10^{-17} $A^2.Hz^{-1}$). The interference is concentrated at a few specific frequencies (0.74 Hz and its harmonics). The ease with which artefacts can be recognised and removed means that this form of data presentation is more robust than time series statistics. *Psd* slopes are slightly negative, apparently eventually becoming flat (-3.0 dB/decade for most of the period, increasing to + 0.6 dB/decade at the end of the experiment). This change in the sign of the *psd* slope at the end of the experiment, albeit very small, could be associated with the onset of iron exposure (see next Section), which would be a useful finding if confirmed. Further work would be required to establish whether this connection is real.

Zinc coatings on steel in brine do not appear to have been investigated by Electrochemical Noise before.

AISI 1020 Steel

This steel was used as the substrate on which coatings were applied. Its uncoated behaviour is therefore important. Over the course of 25 hours immersion, the open circuit potential (OCP), *vs* Ag/AgCl, changed from –0.659V to-0.715V, a change of 0.056V in the negative direction. This may be associated with de-oxygenation of the solution column, film formation, or pitting.

When the cell was dismantled at the end of this period, some non-adherent brown rust was present in the solution. The specimen surface exhibited a uniform grey film, with some localised corrosion present.

The time series plot (Figure 5.6 top) shows a featureless noise signal with low power,

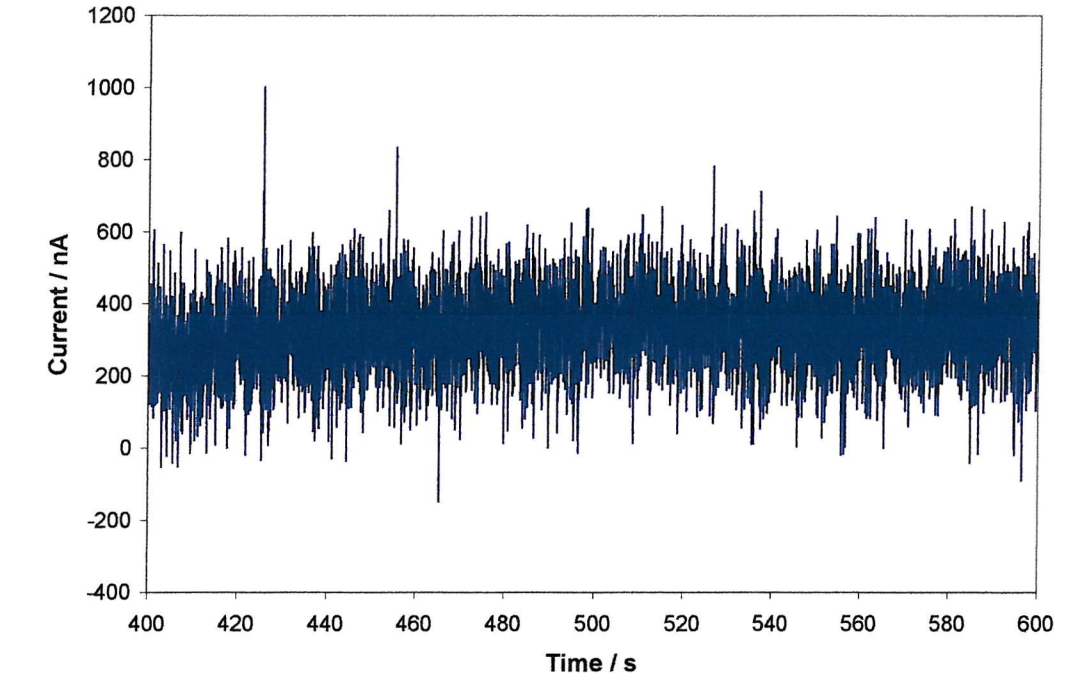

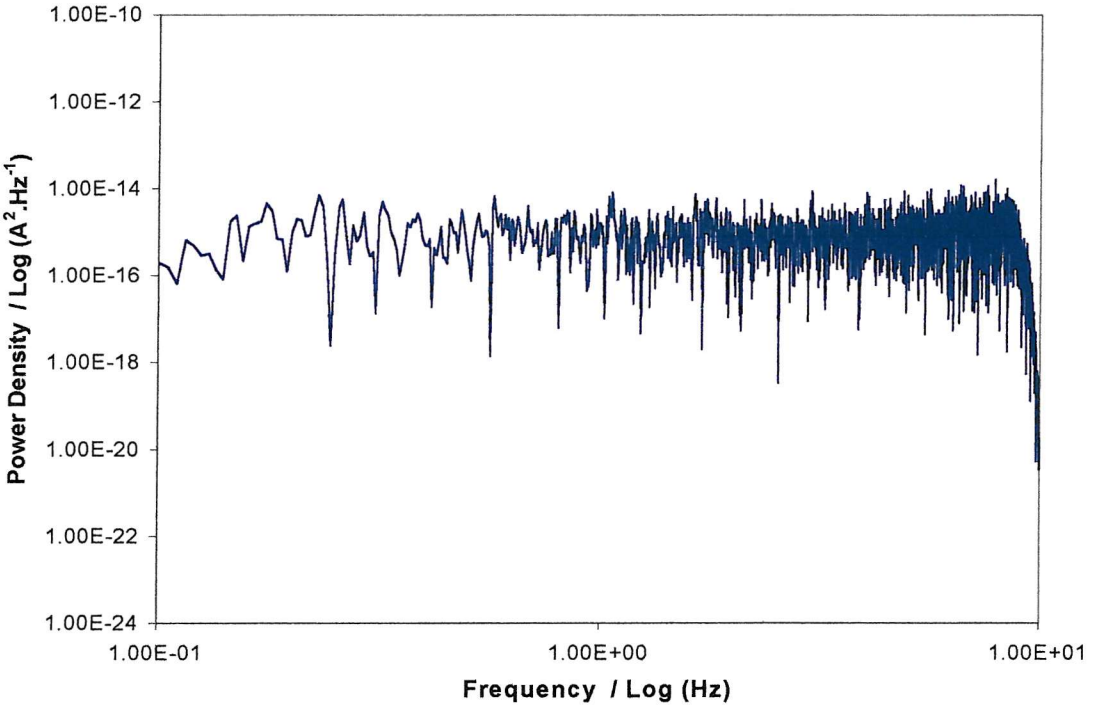

Figure 5.6: AISI 1020 steel in 3.5% NaCl, 1 hour immersion.

Detrended data.

$(\sigma^2(i))$ = 5.2 × 10^{-13}, decreasing to 1.7 × 10^{-14} A^2 over 25 hours, i.e. about ×0.03). There is very little qualitative change, except that the *pdf* plot becomes more Gaussian in shape with time. Most of the change occurred in the first 3 hours.

The *psd* plots exhibit very nearly 'white' noise. The slopes are nearly constant and very close to zero (+ 0.7 -+1.3 dB/decade, discounting one value demonstrably affected by external noise). Note that, although small, these values are consistently positive (the data are anti-correlated, i.e. the data is more likely to change sign than would be the case for a purely random signal). This is different from the behaviour of all the other metals tested and it may be diagnostic of iron exposure (see previous Section), though much more work would be required to confirm this.

HVOF Aluminium on Steel

Aluminium sprayed on steel is the simplest of the HVOF coated samples investigated. As described in Section 3.2.1., flow-out in this sample was good and the aluminium formed a uniform coating with low (<1%, as estimated by image analysis) porosity, probably not extending through the coating thickness.

When the cell was dismantled at the end of the experiment, the generally bright surface was covered by a loose powdery white deposit, probably (hydrous) aluminium oxide. This appeared to plug porosity/pitting. Low power microscopy suggested that corrosion was concentrated at areas where there was porosity/pitting. Over the course of 25 hours immersion, OCP *vs* Ag/AgCl changed from –0.713 V to –0.969 V, a change of 0.256 V in the negative direction. This change is considerably larger than was found for steel, implying that this surface is considerably more sensitive to redox conditions (in practice, oxygen concentration) in the solution than is the steel substrate. It also implies that there will be larger changes in the galvanic currents underlying the noise to be measured, which may make the stationarity requirement harder to achieve.

One hour after immersion, the time series plot (Figure 5.7 top) has an appearance showing rather ragged transients. By 24 hours after immersion, this type of feature has largely disappeared, although there is still some long period variability. Noise power levels were considerably higher than on zinc or steel and irregularly variable over time ($\sigma^2(i)$ in the range 6×10^{-14} to 4.6×10^{-12} A^2), though showing a general tendency to decrease. Possibly longer measurement periods would have improved measurement consistency.

The *psd* plot (Figure 5.7 bottom) shows a straight line plot with a small negative slope, which becomes progressively less negative with time (-12.6 dB/decade, decreasing to –4.3 dB/decade), i.e. the noise becomes 'whiter'.

Overall, over time, noise power decreases and the *psd* slope becomes less steep implying less localisation, while the OCP becomes more negative and white precipitate appears on the surface.

A plausible explanation for these data would involve initial pitting corrosion in oxygenated brine, producing insoluble corrosion product (hydrous aluminium oxide). As the experiment progressed, the oxygen concentration in the solution column decreased, and the general surface of the aluminium moved from passivation into a more active region (more negative potential). Hagyard and Williams [151] indicate that aluminium surfaces are very sensitive to the degree of aeration of the solution, without quantifying this. At the same time, existing pits tend either to become clogged with corrosion product or to grow more open. Large pits/pores may grow at the expense of small ones, reducing heterogeneity. Buzza and Alkire [156] have shown this to occur in 99.999 % aluminium in 1 M NaCl. It is not clear whether the lower purity of the commercial aluminium used here is relevant, or whether there are any pits 'small' enough for this to be a factor. Overall, though, the effect is for the corrosion behaviour to change from pitting to a behaviour more like general corrosion.

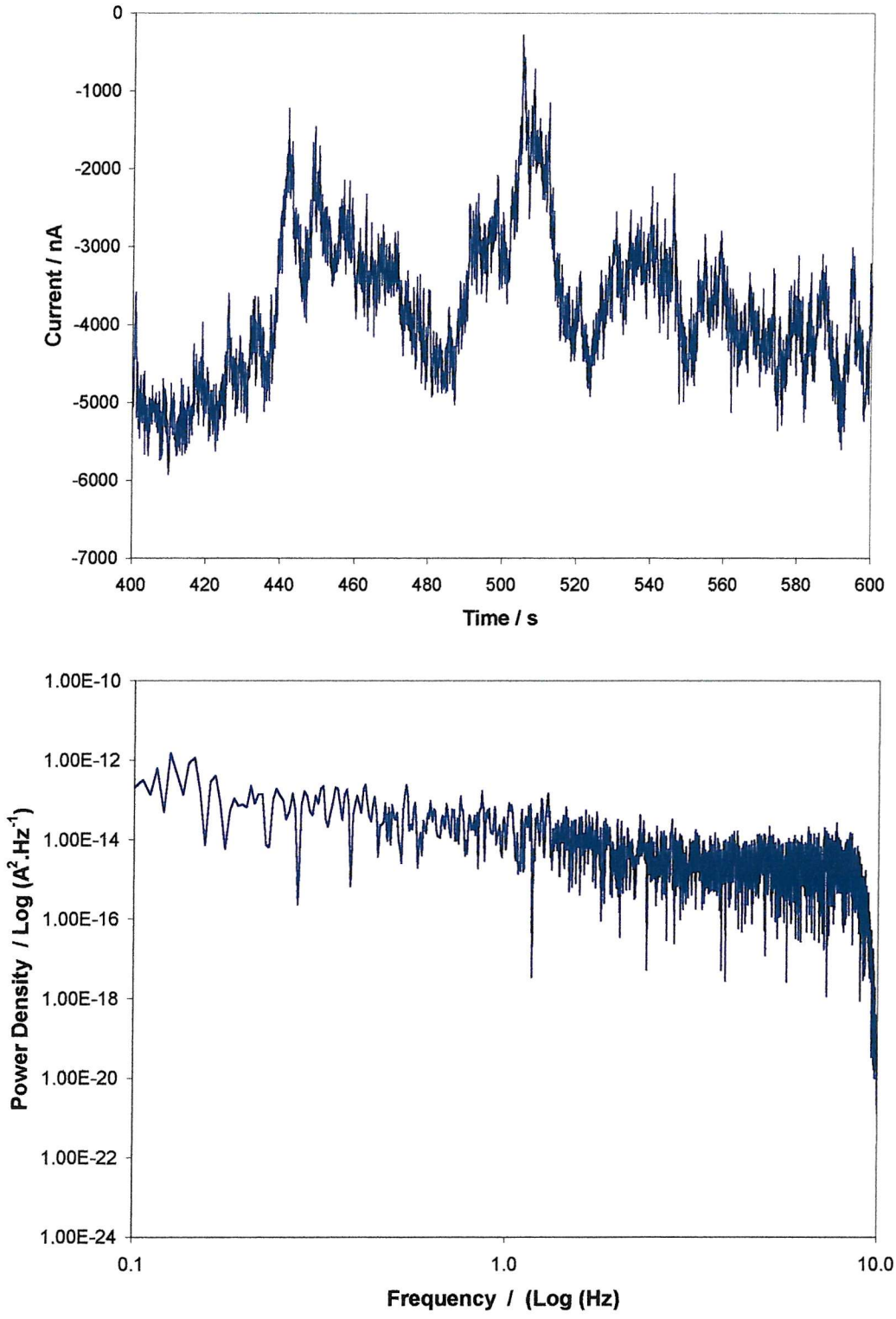

Figure 5.7: HVOF aluminium in 3.5% NaCl, 1 hour immersion.

Detrended data.

HVOF Aluminium/12% Silicon on Steel

HVOF aluminum/12% silicon sprayed on steel has been examined. As described in Section 3.2.1, flow out in this sample was not as good as in the case of pure aluminium, in the sense that the coating contains large unflowed 'melt packets' alloy. However, as estimated by image analysis, porosity appeared to be low (~ 1.2 %).

When the cell was dismantled at the end of the experiment, it was found that the polished surface had acquired a brown appearance, with visible near-circular mottles, possibly related to spraying artefacts. The most likely explanation for this colour change is aluminium depletion, leaving a silicon-rich surface. Attack on the metal appears to be concentrated on the surface porosity initially present (between the alloy splats), though non-uniformly. Some pits now appear very deep (possibly penetrative), with bright, facetted surfaces showing. A small amount of the white powdery deposit seen on pure aluminium is present in some of the larger pits, but the extent of this is, overall, greatly reduced.

Over the course of 25 hours immersion, OCP *vs* Ag/AgCl changed from –0.690V to -0.961V, a change of 0.271 V in the negative direction. This is comparable with (slightly larger than) that observed with commercially pure aluminium.

The time series plots have a generally similar appearance to those obtained for commercially pure aluminium (and are therefore not shown). Noise power is generally somewhat less than for commercially pure aluminium ($\sigma^2(i)$ initially about 2.6×10^{-12} A^2, quickly decreasing to about 2.5×10^{-15} A^2). This suggests (somewhat surprisingly, in view of the finding of Meyer-Rodenbeck [168] that silicon can act as a micro-cathode) that this alloy has superior corrosion resistance to 3.5% NaCl, though localised corrosion remains a possibility. This may be related to the brown surface discoloration observed; an effectively silicon surface.

The *psd* plot is a straight line with negative slope (initially -15.9 dB/decade, decreasing to –2.2 dB/decade after 24 hours).

Qualitatively, this behaviour is similar to that of commercially pure aluminium, as will be discussed further below (Section 5.4.5)

HVOF Aluminium/12% Silicon + Alumina on Steel

The HVOF sprayed (aluminum/12% silicon + alumina) composite, sprayed on steel has been examined. As described in Section 3.2.1, flow out in this sample was poor. The coating contains large unflowed particles of alloy embedded separated by a fine second phase, believed to be the alumina. Additionally, this coating has extensive porosity, estimated by image analysis to be about 6.4%. This is so much larger than that found for the other coatings that there must be a larger chance that the porosity will penetrate right through the coating.

When the cell was dismantled at the end of the experiment, the sample showed little obvious change, other than a somewhat mottled appearance. In particular, the white deposits or surface browning, observed on other samples, were not evident. Low power microscopy suggested that the mottled appearance was related to the distribution of the clearly visible splats across the surface. There were signs of preferential dissolution between the splats.

Over 25 hours immersion, OCP *vs* Ag/AgCl changed from –0.701 V to -0.950 V, a change of 0.249 V in the negative direction. This is very close to that observed with commercially pure aluminium.

The time series plots have a generally similar appearance to those obtained for commercially pure aluminium (and are therefore not shown). Noise power levels ($\sigma^2(i)$ initially 7.7×10^{-14} A^2, quickly decreasing to 8.1×10^{-15} A^2) are comparable to those for the Al/12%Si alloy coating.

The *psd* plot at is a straight line with negative slope (initially -13.0 dB/decade, decreasing to –5.8 dB/decade after 24 hours).

Qualitatively, this behaviour is similar to that of the other HVOF coatings, as will be discussed further below (Section 5.4.5)

304L Stainless Steel

304L grade stainless steel is known to give well-defined noise transients, so a sample was included, to demonstrate that the system can indeed record these. Figure 5.8 (top) shows 8 minutes of measurement.

Well-defined peaks of about 200 nA are seen, each with a relatively slow rise (typically around 20 s) and a sharp fall. Some of the peaks are not completely sharp, suggesting that individual events may not be completely resolved.

Figure 5.8 (bottom) is the power spectral density plot of this time series. It shows a straight-line plot with a slope of –30.6 dB/decade. This is qualitatively similar to the *psd* plots for the aluminium based coatings, but much steeper. This is consistent with the idea that pitting on stainless steel is more localised than that on aluminium.

5.4.5 Material Comparisons

Gross material differences

Table 5.2 consolidates the most useful parameters for the various materials tested. Figure 5.9 shows the trends in *psd* slope values and in OCP with time. In each case the data fall into three distinct groups (note that this is not true for the Noise Power data, to be considered further below). The single measurement made on 304L stainless steel has a *psd* with much the most negative slope (-30.6 dB/decade) and the most noble OCP (-0.115 V vs Ag/AgCl). Conversely, the hot-dipped zinc coating has

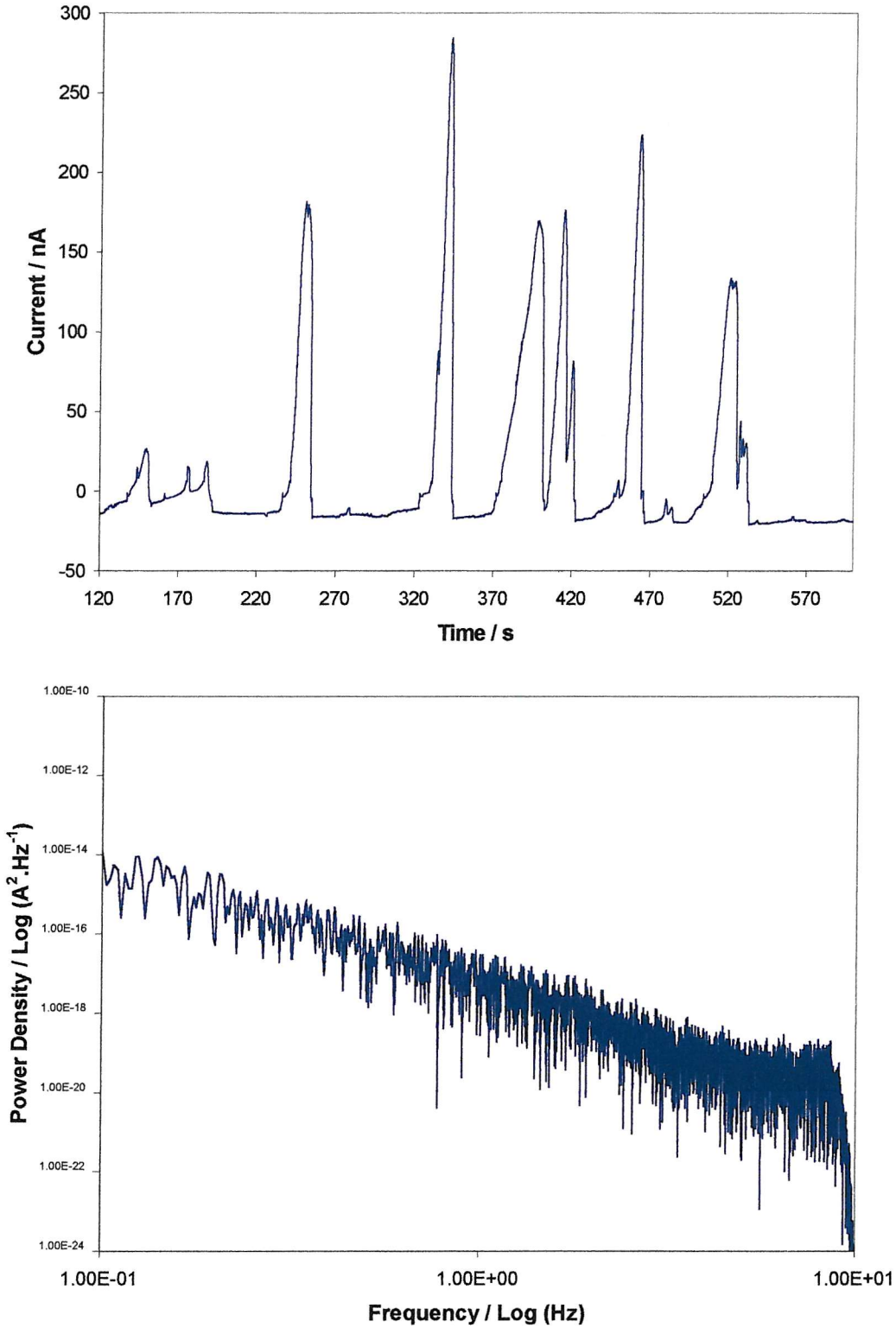

Figure 5.8: 304L stainless steel in 3.5% NaCl, 1 hour immersion.

Detrended data

nearly zero slope and the most active OCP. AISI 1020 steel shares the nearly zero slope, but has a less active OCP. The aluminium-based samples have a range of slopes and OCPs intermediate between those of 304L stainless steel and zinc. They also show a more distinct variability with time, the noise becoming 'whiter' and the OCP more active (more negative).

Figure 5.10 shows these quantities plotted against one another. This indicates a relationship between current *psd* slope and OCP that does not seem to have been remarked upon before.

Time / hours	Zinc	AISI 1020	Al metal	Al/12%Si	Al composite	304L
	PSD Slope (dB/decade)					
1	-3.0	+0.7	-12.6	-15.9	-13.0	-30.6
3	-3.1	-4.2	-11.3	-13.1	-9.9	
5	-3.2	+0.7	-12.6	-10.6	-7.1	
24	+0.6	+1.3	-4.3	-2.2	-5.8	
	Noise Power ($A^2 \times 10^{-15}$ on 710 mm^2)					
1	8.1	520	2400	2600	770	2.9
3	8.1	14	420	2.5	6.4	
5	73	14	4600	0.9	8.1	
24	73	17	63	20	8.1	
	OCP (V *vs* Ag/AgCl)					
1	-1.023	-0.659	-0.713	-0.690	-0.701	-0.115
3	-1.012	-0.681	-0.712	-0.744	-0.731	
5	-1.016	-0.688	-0.711	-0.852	-0.779	
24	-1.032	-0.715	-0.969	-0.961	-0.950	

Table 5.2: Consolidated electrochemical data.

For those samples where a coherent oxide layer is expected (i.e. all the samples except the AISI 1020 samples), the *psd* slope is linearly related to OCP, correlation coefficient $r^2 = 0.94$. Since a variety of different metals is involved, this is not a simple chemical relationship. Conventionally, it is held that the greater the value of the negative slope in the *psd* plot, the greater the degree of 'localisation' of corrosion on the working electrode [105]. Qualitatively, this relationship may be understood by supposing that the most active (in the electrochemical sense) surface, i.e. the zinc surface, has many small sources of noise, where rapid processes occur, whereas the most noble surface, i.e. that of 304L stainless steel, has only a few large sources, where activity is slow. However, why this relationship should be linear is not understood. It is also clear that the relationship does not apply to mild steel (AISI 1020), presumably because the oxide film on mild steel is not coherent.

This relationship could usefully be explored further. To do so would involve:

- tightening up experimental and data analysis procedures to reduce variance as far as possible.
- obtaining a precise estimate of experimental variance by carrying out sufficient replicate experiments.
- extending the range of materials as far as possible, to include at least a range of aluminium alloys, various grades of stainless steel, and perhaps such other materials as titanium (alloys).

Such an investigation could shed light on how material composition and pitting propensity are related. However, this would go beyond the scope of the present project.

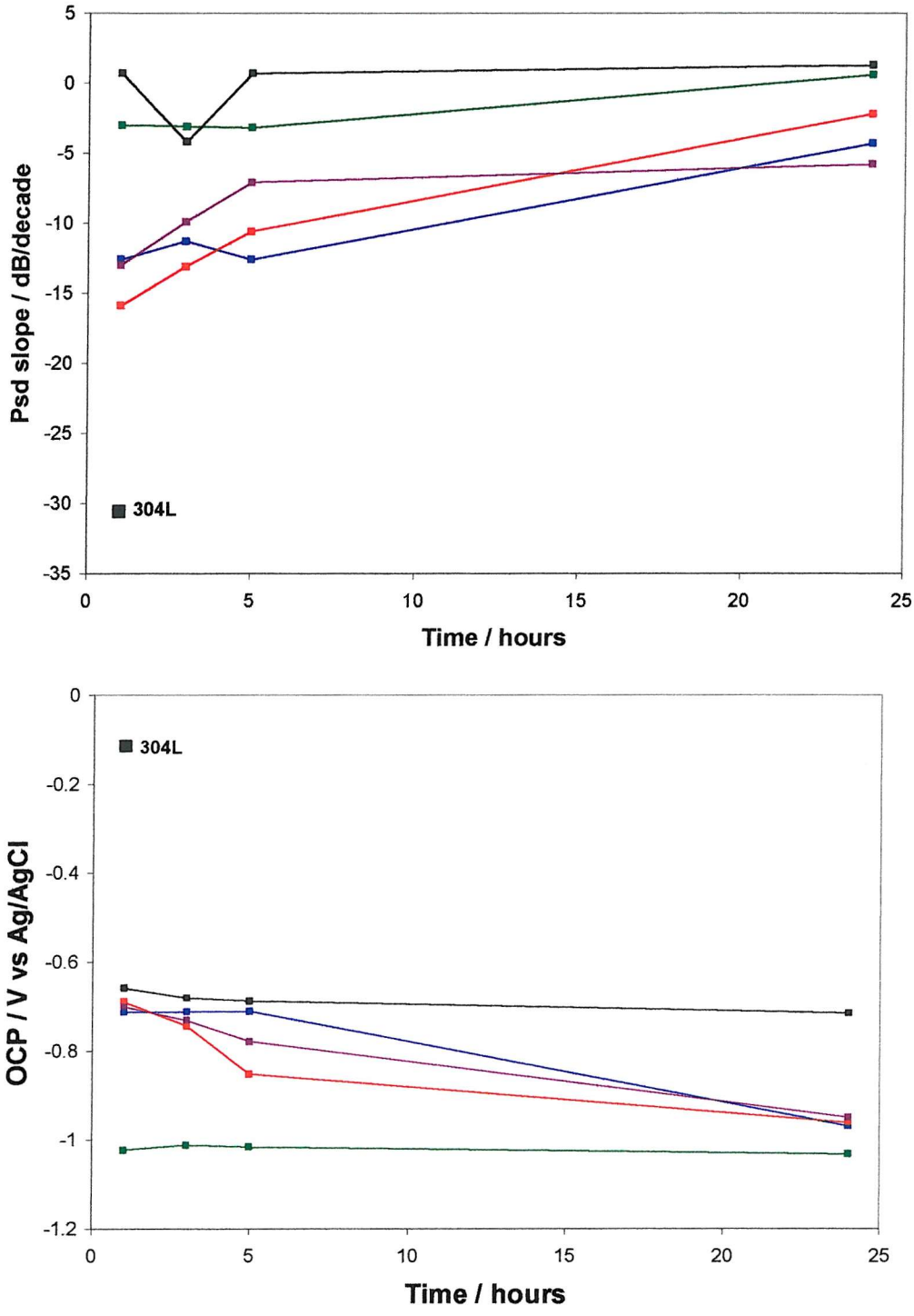

Figure 5.9: Power Spectral Density Slope and OCP trends with time.
(304L, AISI 1020 = Black, Zinc = Green, Aluminium = Blue,
Al/12%Si = Red, Composite = Violet)

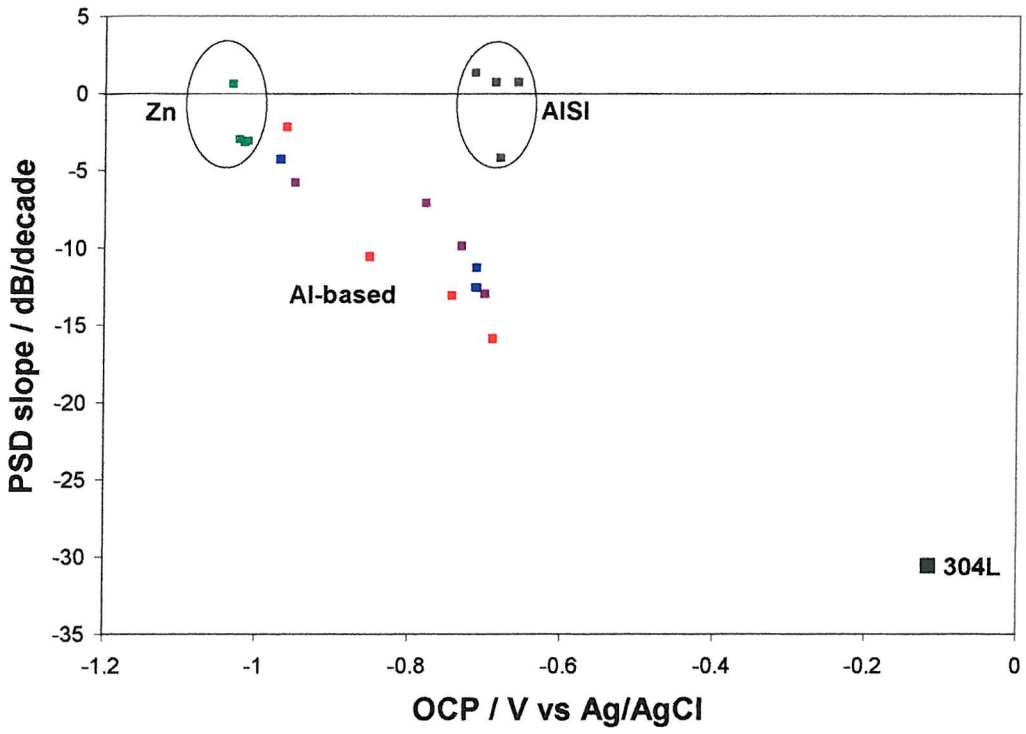

Figure 5.10: Power Spectral Density Slope variation with OCP.
(304L, AISI 1020 = Black, Zinc = Green, Aluminium = Blue,
Al/12%Si = Red, Composite = Violet)

It may also be noted that well-defined transients are associated with steep *psd* plots; this appears to be a mathematical truism, if not a very obvious one. Very crudely, for transients to be easily distinguishable:

- (Slope) >> 10 dB/decade.

Taken together with Figure 5.10, this means that any coating on mild steel that will be anodic, i.e. protective, will never show well defined transients. However, *psd* analysis should still be able to show changes in behaviour.

Aluminium-based materials

It is more difficult to reliably distinguish differences in the relative behaviours of the slopes of the different aluminium-based coatings than it was between different metals, since the differences are of the same order as the assumed measurement variance. In all cases the negative slope of the current *psd* reduces with time; this parallels the negative shift of OCP with time, probably due to de-oxygenation of the solution above the working electrode. The behaviour of the composite coating is different from that of the other coatings, in that the decline in the value of negative slope is less pronounced. If this behaviour is real, it may be related to the greater porosity of the composite coating, which may keep corrosion local. A plausible mechanism for this would involve the blocking of porosity by corrosion product. Figure 5.11 is an SEM image of corrosion product (aluminium oxide/hydroxide) formed on the surface of aluminium under these conditions; there is no reason to believe that such solids do not also form within the coating's internal porosity.

It is of interest that Hagyard and Prior [150], who did obtain well-resolved transients on aluminium, used very pure aluminium (99.99%) in the form of micro-electrodes under very oxidising conditions. All these factors would tend to minimise the number of weaknesses present on an individual sample, and, in terms of Figure 5.10, place their samples well to the right of those measured in this work, i.e. closer to stainless steel and its observed transient behaviour, as found.

Similarly, Brown [187] has reported that compressed air tanks in submarines, internally flame sprayed with aluminium, showed massive pitting corrosion under the coating. This is consistent with the above picture, given that the partial pressure of oxygen in the tanks when full was well over 100× ambient; this may well be sufficient to reverse the aluminium/steel corrosion couple.

There are more reliable differences in Noise Power (see Table 5.2). In this case, there is a clear ranking:

Aluminium >> Al composite > Al/12%Si alloy

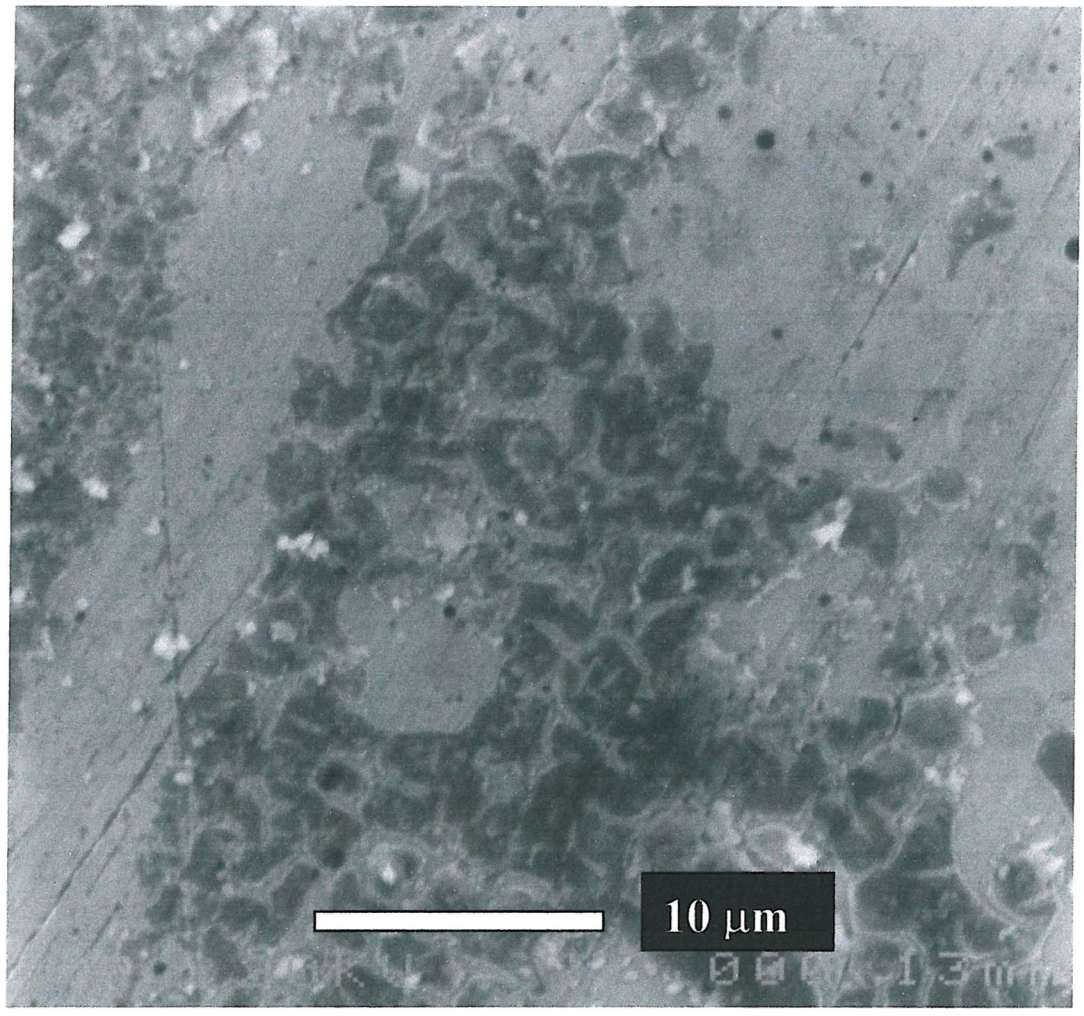

Figure 5.11: SEM image of corrosion product on aluminium surface after 24 hours immersion in 3.5% NaCl.

The Noise Power level on aluminium is greater than on mild steel, whereas on the alloy-based materials it is less. In each case, the Noise Power level decreases with time after the first hour and then becomes roughly constant. The appearance of the alloy sample after immersion suggested surface depletion in aluminium, and it would

not be surprising if an effectively silicon residual surface were less reactive than the original largely aluminium surface. This surface depletion may be less effective within the surface porosity in the composite coating.

These comparisons suggest that, contrary to the suggestion of Meyer-Rodenbeck [165], aluminium/silicon alloys may have significantly better corrosion performance than commercially pure aluminium, without losing their anodic properties with respect to steel, and that porosity must be minimised if these advantages are to be retained. However, care needs to be taken to ensure that good overall performance is not accompanied by severe pitting, which is not excluded by this work.

Al/12%Si *vs* Zinc coatings

The two best coatings, in the sense of having minimal electrochemical noise power, are Al/12%Si and hot-dipped zinc. Their behaviours do, however, differ somewhat. Most notably, the Noise Power decreases in the case of the Al/12%Si coating, but increases for the hot-dipped zinc coating. If it can be firmly demonstrated that this difference corresponds to a real difference in coating performance, and that this difference can be sustained, then this may have practical consequences for material choice.

5.5 CORROSION – PRELIMINARY CONCLUSIONS

Electrochemical Noise measurements have been made on a range of metals and coatings, using a Gamry electrochemical system. An electrochemical cell based on a glass flange has been successfully used for this work. The major problem area in its use has been de-oxygenation of the solution column. Electrode disposition could be improved by making the arrangement more symmetrical.

Electrochemical Noise measurements have been made on a single potentiostatted working electrode. Data acquisition has been carried out, subject to a clearly defined

experimental procedure (Section 5.3.1), with proper attention to anti-aliasing and filtering artefacts, and making an appropriate compromise to obtain adequate time series length, while minimising stationarity problems.

Data Analysis of these time series has been carried out, using simple statistics and power spectral density (*psd*) plots. Strengths and weaknesses of these different modes of data presentation have been discussed. The most useful parameters have proved to be the current noise variance and the slope of the power spectral density plot.

Measurements on hot-dipped galvanised steel, indicated that this coating had the most electrochemically active potential of those tested. *Psd* plots showed nearly 'white' noise at a low Noise Power level. The behaviour of this sample varied little over the course of the experiment, but the small negative slope of the *psd* plot became slightly positive at the end of the experiment. It is possible that this is related to iron becoming exposed, but much more work would be required to confirm this.

Measurements on AISI 1020 0.2% carbon steel produced 'white' noise with no structure. *Psd* plots were flat or slightly positively sloped, with relatively high Noise Power levels. There was very little change in the electrochemistry with time. Visual inspection showed non-adherent oxide and some pitting.

Measurements on steel HVOF coated with commercially pure aluminium (porosity by image analysis < 1%) produced results that developed with time. The most likely reason for this was de-oxidation of the solution column, which produces much larger changes in open circuit potential (OCP) for aluminium-based materials than for any of the other materials tested. At short times, time series showed ragged transients, but these disappeared as time progressed. Similarly, the *psd* plots initially had moderate negative slopes (-12.6 dB/decade), which decreased (to –4.3 dB/decade) in 24 hours. Noise Power was much higher than on steel.

Measurements on steel HVOF coated with Al/12%Si alloy (porosity by image analysis ~ 1%) produced results that developed with time. OCP changed even more rapidly than for commercially pure aluminium, which is thought to have been related to the change of the surface to a brownish colour. *Psd* plots were qualitatively similar to those for commercially pure aluminium, but the Noise Power level reached significantly lower levels. These results are consistent with the idea that corrosion causes surface depletion of aluminium, leaving a less reactive silicon-rich surface.

Measurements on steel HVOF coated with a composite of Al/12%Si alloy and alumina, nominally as a sandwich (but see images in Section 3.2.1; porosity by image analysis ~ 6.4%) produced results which developed with time. The electrochemical noise behaviour was broadly similar to the alloy coating, but the *psd* negative slope did not decline as far, and the Noise Power did not decrease to the same extent. These differences were attributed to the high level of porosity in the sample.

Measurements on 304L stainless steel produced well-defined noise transients. A *psd* plot was steeply sloped (-30.6 dB/decade) with low levels of Noise Power.

Comparison of those metals that form coherent oxide films showed a correlation between the slope of the power spectral density plot and the sample OCP. The mild steel sample (no coherent film) did not fit this pattern. There is room for further investigation of this finding, but this falls outside the scope of the present project.

Comparison of the aluminium-based coatings suggests that adding silicon is likely to be beneficial from a corrosion point of view, contrary to the limited information in the literature, because aluminium depletion leaves a silicon enriched surface, but that it is important to minimise porosity. It will be important to establish that an overall improvement in corrosion performance is not accompanied by severe pitting, which outcome is not excluded by these results.

Trends in the change (reduction) of the negative *psd* slope with time suggest that a key factor in the corrosion behaviour of the aluminium-based samples is the blocking of porosity by corrosion product. If open porosity (steel exposure) is not to be a problem, these results suggest that coating production should be controlled so as to ensure that porosity (as estimated by image analysis) should be restricted to < 1%.

Aluminium-based materials appear to be very sensitive to the oxygen level in the solution, so consideration needs to be given to what levels of oxygenation are likely to be met in service.

The two best coatings tested were the Al/12%Si and zinc coatings.

6 EROSION-CORROSION

6.1 INTRODUCTION

The main experimental part of this work concerns an investigation of the erosion-corrosion behaviour of aluminium, aluminium/12% silicon alloy and zinc coatings on AISI 1020 steel (as previously described – Section 3), and an investigation of the electrochemical noise behaviour associated with this.

The new test rig used for this work is described, with particular emphasis on novel features. A section is devoted to experimental issues which arose, and which were either resolved before the main experimental sequence was begun, or required attention after the event in data handling. In some cases these reveal areas where further attention will be required if future work is to be better controlled; these are set out. The experimental design used is specified. Experimental results are discussed separately in terms of appearance and topography, mass loss and electrochemical behaviour. An attempt is made to relate these, and the nature of the difficulties in doing this is explored. Proposals are made as to how these difficulties may be resolved in the future.

6.2 EXPERIMENTAL

6.2.1 Design of Test Rig

A new erosion-corrosion test rig has been built for this work. The design of this rig is ultimately based on that of Zu *et al* [124], but incorporates improvements made by Puget [125] in that it contains no metallic parts other than the test electrode.

The further improvements made in the new apparatus relate to improving ease of sample handling, and adaptation to allow potentiostatted electrochemical noise measurements to be carried out. Figure 6.1 is a schematic of the key parts of the equipment (omitting reservoirs, pumps and the system's surrounding Faraday cage).

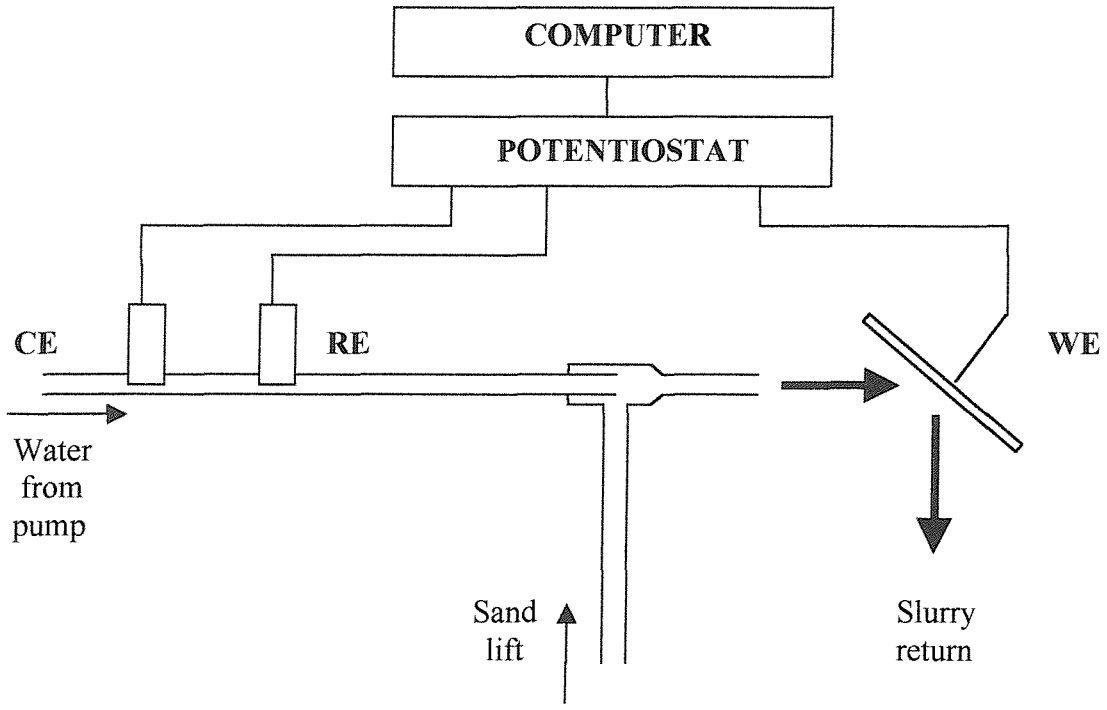

Figure 6.1: Schematic of erosion-corrosion rig for electrochemical noise measurements

Water (or brine) is pumped from a 100 litre reservoir through an electrode block containing counter and reference electrodes to an ejector where sand is picked up from a container below. This arrangement ensures that the vulnerable counter (CE) and reference (RE) electrodes are kept out of the sand stream. The slurry so formed is then projected onto the sample, which constitutes the working electrode (WE) of the system.

Provision is made for two carbon rod counter electrodes, so that noise on the counter electrodes can be estimated under experimental conditions. The reference electrode is a robust single junction Ag/AgCl electrode (Sentek). The working electrode (30 mm diameter working area) is enclosed in a Delrin sample holder designed so that only a defined area is exposed to the slurry; electrical contact is made to the rear of the sample *via* a grub screw and a cable isolated from the experimental environment.

The stand-off distance of the test sample from the jet (37.5 mm in these experiments) and the impingement angle (90^0 or 30^0) can both be adjusted. The jet and the test sample holder are enclosed in a perspex container to guide the used slurry back down into the sand reservoir. The whole apparatus, apart from the circulating pump (the main source of electrical noise) is enclosed in a Faraday cage.

Figure 6.2 shows an overall view of the physical manifestation of this system, with the electrode block/ejector/target chamber at the top, solution reservoir below (the sand reservoir is hidden within this) and the solution circulating pump at the bottom. Solution is taken from the bottom of the solution reservoir, *via* a filter, to the circulating pump. This raises the solution to the top of the rig and drives it through the CE/RE electrode blocks and the lifting/mixing ejector, and projects it on to the test sample. From there the slurry returns by gravity to the sand reservoir, where gravity settling is sufficient to separate the sand from the solution, which returns to its own reservoir by overflow.

Figure 6.3 (upper) shows an overall view of the electrode test block, the ejector, the jet and the sample holder in its enclosure. This photograph was taken before the apparatus had had its associated pipework installed or its Faraday cage built round it. Below this are detailed views of the sample holder showing its relationship with the slurry jet, the form of the front face defining the working area, and the rear of the holder, showing the electrical assembly and the sealing arrangements.

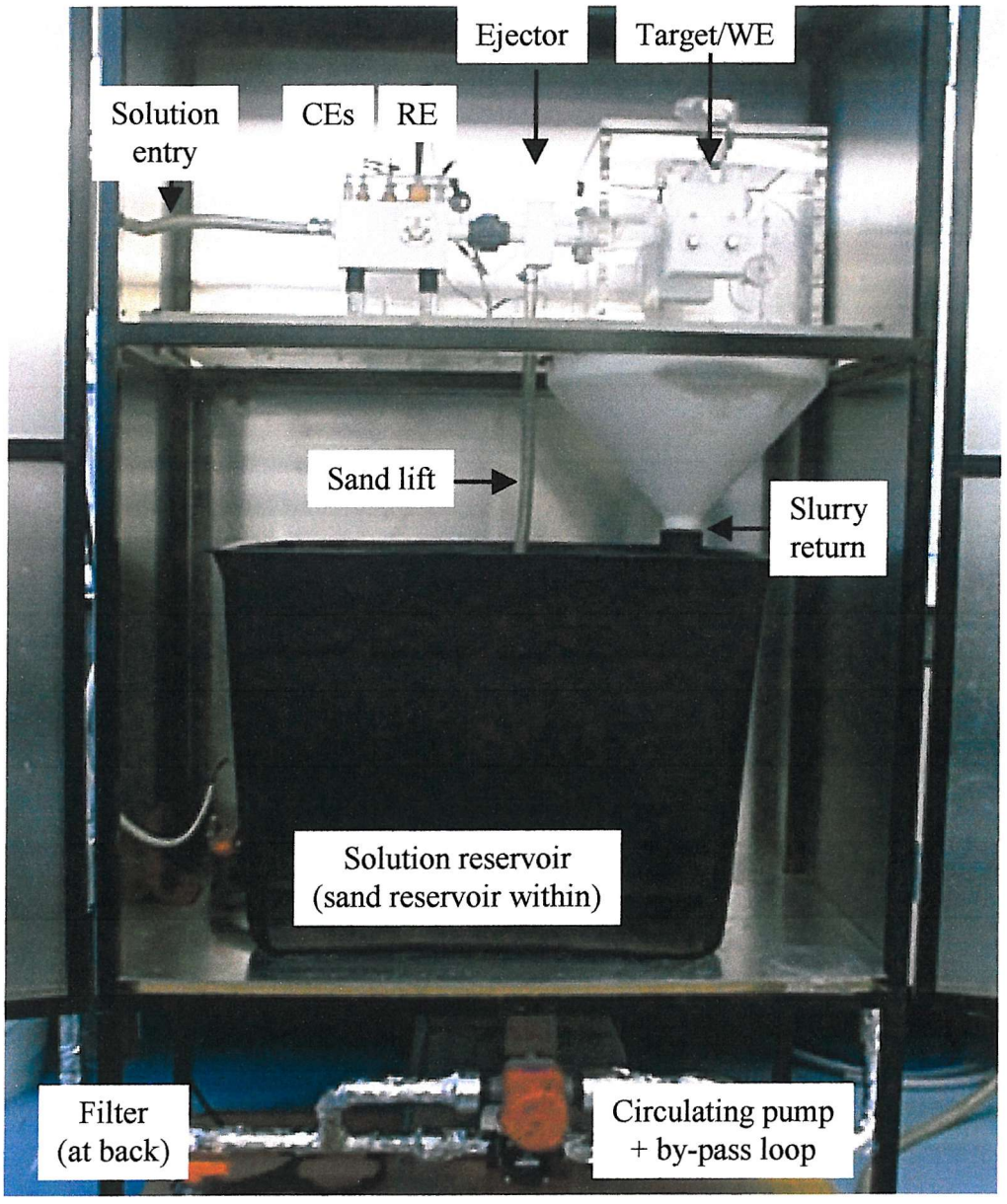

Figure 6.2: Overall view of erosion-corrosion rig.
(enclosed by Faraday cage, except for pump)

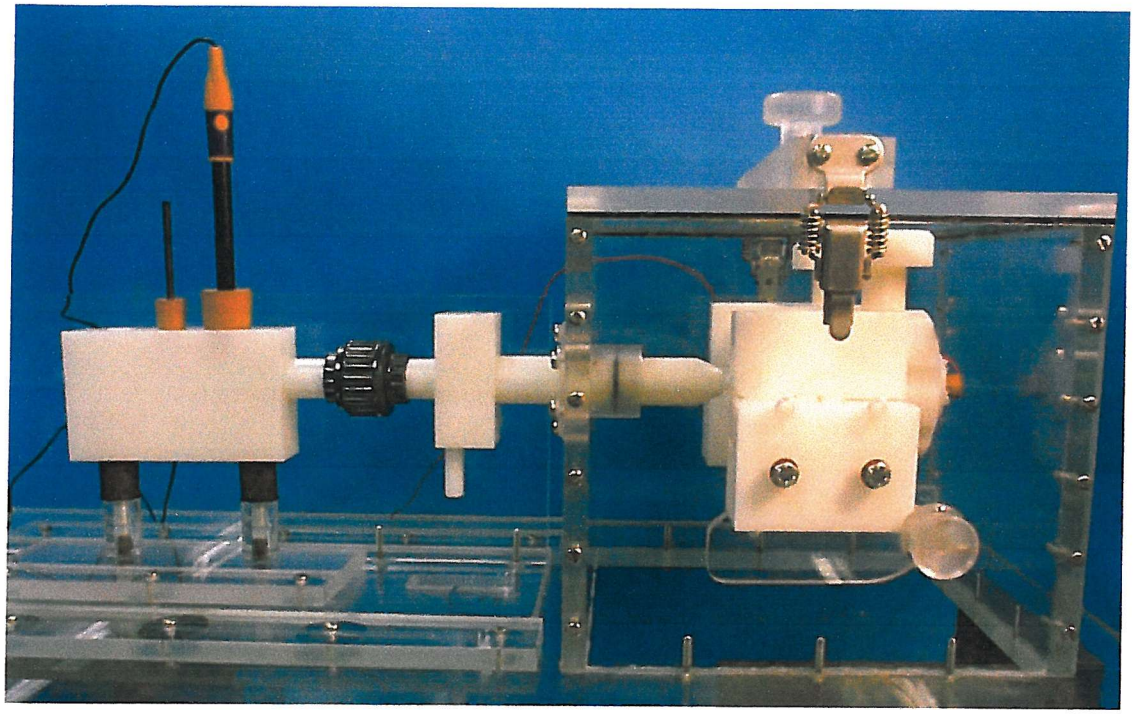

a) General view of electrode block, ejector and sample holder

b) Relation of slurry jet to sample

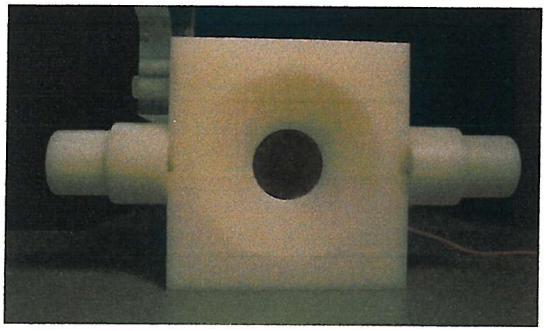

c) Front view of sample in holder

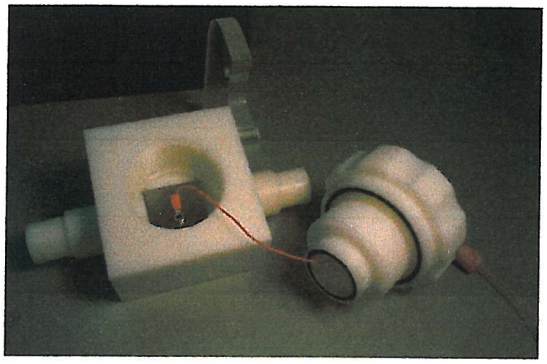

d) Internal construction of sample holder

Figure 6.3: Views of erosion-corrosion rig and sample assembly

6.2.2 Experimental Issues

Introduction

A number of preliminary experiments were carried out in order to establish suitable working conditions for use with the rig and to identify working limits and experimental stability. During the main experimental sequence certain other issues came to light, which have had some influence on the experimental outcomes. For convenience, since these issues are highly interactive, they are all brought together here, with some suggestions as to how future experimental rigs might be improved.

Electrolyte flow

The electrolyte flow rate was determined volumetrically from a timed aliquot from the flow, the liquid being returned to the system after measurement. Steady flow was obtained within a few seconds of starting the pump. Flow is determined by the pump's rated flow rate, the head against which it works and any flow bled off into a by-pass loop. In practice, it was found that to obtain an adequate flow the pump had to be run with no by-pass flow. This is because the pressure drop in the system was higher than expected. This was associated largely with the ejector inlet nozzle (3 mm internal diameter × 75 mm length), though there was probably also some influence from the exit nozzle (5.5 mm internal diameter × 20 mm length) and the sand filter included in the circuit to protect the pump and the counter and reference electrodes. The sand filter was removed and backwashed at intervals to minimise the effects of sand accumulation in this component.

It was found that with the above nozzles a water flow of 85 $mls.s^{-1}$, i.e. 3.6 $m.s^{-1}$, could be sustained and remained consistent over time (at least 1 hour). This flow rate corresponds to a Reynold's number Re ~ 12,000, so the flow is clearly turbulent. The only problem encountered on a trial run was that the circulating pump became rather hot; a larger pump that worked less hard would be desirable.

Unfortunately, this trial run was carried out in June at an ambient temperature of 23 ^{0}C, using clean water. Subsequent experience showed that this flow rate could not be matched in September, using 3.5% NaCl at 18 ^{0}C. Best flow was reduced by about 5%. While this is not in itself a large change, it had a disproportionate effect on the sand flow (see Section 6.2.2 below). The difference appears to be largely a consequence of changes in electrolyte density and viscosity, themselves functions of temperature. Table 6.1 shows published data [188], which show that reduced temperatures increase both density and viscosity; furthermore both these quantities are higher for salt water than for freshwater.

	FRESH WATER			SALT WATER 3.5 % NaCl		
Temperature ^{0}C	Density kg.m^{-3}	Dynamic Viscosity kg.m^{-1}.s^{-1} ($\times 10^{-3}$)	Kinematic Viscosity m^2.s^{-1} ($\times 10^{-6}$)	Density kg.m^{-3}	Dynamic Viscosity kg.m^{-1}.s^{-1} ($\times 10^{-3}$)	Kinematic Viscosity m^2.s^{-1} ($\times 10^{-6}$)
0	999.8	1.52	1.79	1027.3	1.61	1.57
5	999.7	1.42	1.42	1026.9	1.50	1.46
10	999.7	1.31	1.31	1026.2	1.39	1.35
15	999.1	1.14	1.14	1025.2	1.22	1.19
20	998.2	1.01	1.01	1024.0	1.07	1.00
30	995.7	0.80	0.80	1021.0	0.87	0.85

Table 6.1

Density and viscosity of fresh water and seawater at a range of temperatures.

Source: North Carolina State University

Sand flow

Whereas electrolyte flow was, subject to the temperature/composition issue noted above, very consistent, the same cannot be said for sand flow. This proved to be extremely sensitive both to temperature and to exactly how the rig was set up physically. A qualitative understanding of the problem has been obtained, but, nonetheless, this issue is the one that has determined the degree of reproducibility obtainable between runs, weaknesses here have determined the way the experimental outcomes have had to be analysed and this is the main area where improved control is required in the future.

Sand flow was measured by weighing timed dried aliquots taken from the flow loop directly downstream of the target. There is very little 'dead' volume in this loop, and sand 'loss' in the loop was not a problem. Sand removed for these measurements (about 150 gms/run) was replaced with fresh sand. Steady sand flow took about 2 minutes to develop after the pump was started.

Figure 6.4 is a schematic of the sand circuit. All aspects of this circuit need to be controlled. In outline, water is pumped from the reservoir at the bottom of the system to an ejector. Suction induced by this water flow lifts sand from a separate reservoir, *via* a T-valve which allows dilution of the sand flow with water/brine. The sand slurry formed in the ejector is projected on to the target, from which it returns by gravity to the sand reservoir, where sand separates from the electrolyte by sedimentation. Water/brine returns to its own reservoir by overflow.

Particular aspects of this circuit which have required attention (and would benefit from better definition) are:

- Placement of the foot of the sand lift. The sand lift behaviour is very sensitive to this. Best results were obtained when:

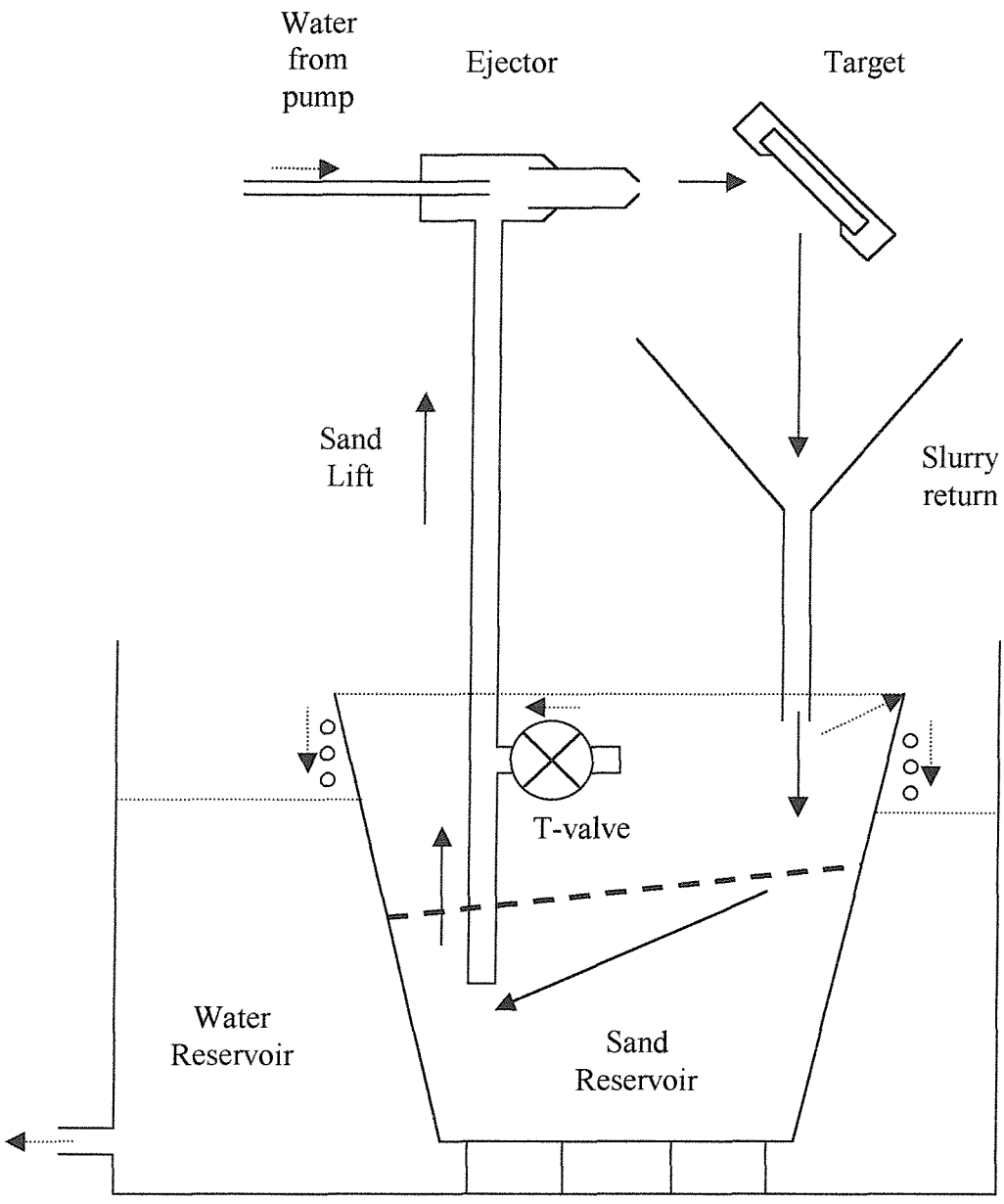

Figure 6.4: Schematic of sand circuit.

- The sand lift tube was kept as near vertical as possible.
- The horizontal separation of the sand lift and the slurry return was minimised.
- The sand lift foot was submerged about 120 mm in the sand. This figure is probably a function of sand size, but this was not investigated. The sand return path within the sand reservoir needs to be steep enough for the sand to flow freely.
- The vertical height of the sand lift was minimised. Ejectors are not efficient pumps and other problems are exacerbated if they are made to work to their limits (see below).

- T-valve opening. It was found that, if the T-valve was opened excessively, very little sand was lifted by the ejector, i.e. very dilute slurries were obtained. If it was closed too far, density oscillations were induced in the sand column. These density oscillations, for reasons to be discussed later, resulted in potential oscillations at the target (or current oscillations if the potential were held constant). This behaviour, if allowed, would obviously mask the electrochemical noise fluctuations that the experiment was designed to investigate. Strong density fluctuations in the sand column could be seen by eye, but electrochemical monitoring, using a 'quiet' target (steel) indicated that some fluctuation could occur, even with no visible change to the sand column. Proper T-valve openings were found by trial and error, using electrochemical monitoring, and were usually about 60-70^0 from open. These openings were found to be extremely sensitive, and differed with salt concentration. In practice, it was usually possible to achieve sand concentrations of 4.5-5.0 %, but it was difficult to do this on colder days.

- Ejector geometry. A schematic of the ejector, showing its important dimensions, is shown in Figure 6.5. The ejector was designed on the basis of the paper of Zu *et al* [124] and the Thesis of Puget [125]. These

suggested that the key dimensions were the inlet and outlet jet diameters and the inlet jet positioning relative to the sand entry. Adjustment of these would allow control of both total flow and sand concentration. On this basis, it was found that an inlet jet of 3.0 mm diameter and an outlet jet of 5.5 mm diameter, with an inlet jet offset of 0.0 mm would allow a water flow of about 85 mls.s^{-1} and a solid concentration of about 4.5-5.0 % on warmer days, but these fell away in cooler weather and sand fluctuations became more of a problem. Some manipulation of the ejector components suggested that the problems were associated with physical constrictions inside the ejector, alleviated in warmer weather by thermal expansion (polymers have large coefficients of thermal expansion).

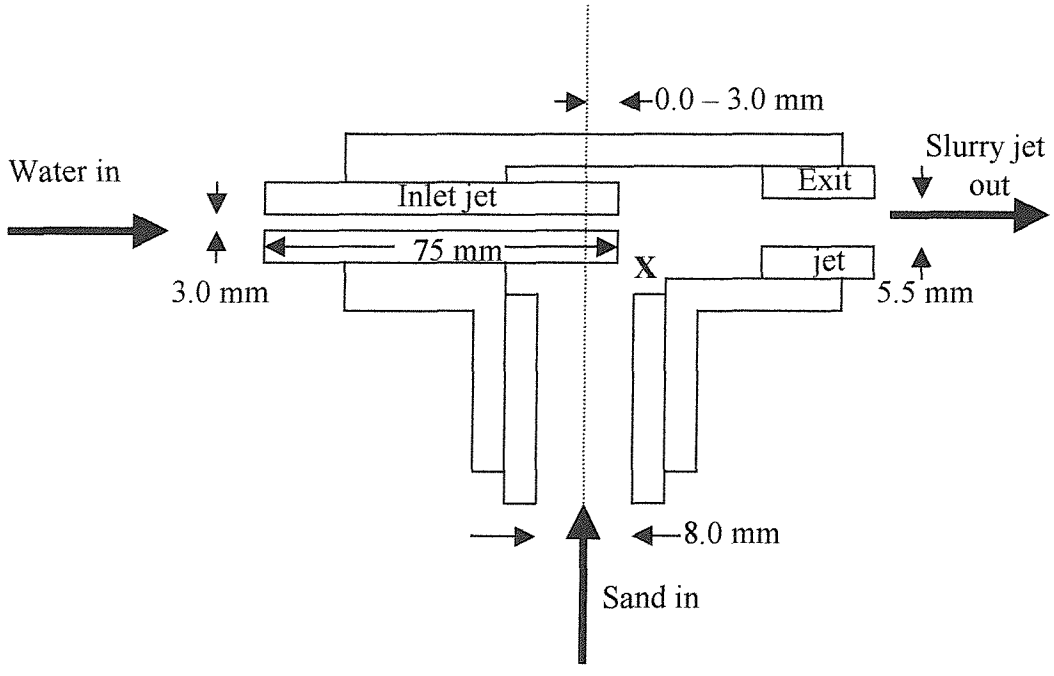

Figure 6.5: Schematic of ejector construction, showing critical dimensions.

- A minor part of this was associated with the excessively long inlet jet (75 mm) causing excess pressure drop in the liquid circuit, hence reduced flow, hence reduced suction at the ejector. However, the main part of the problem was associated with a constriction at the head of the sand lift

(marked X on the schematic). Drilling out the sand lift inlet to the ejector to the maximum extent possible (8.0 mm internal diameter) consistent with its external diameter helped, but some problems remained. It is believed that redesign of the internal shape of the ejector to make it more 'open' would help. It is notable that the schematics of ejectors in Zu *et al* [124] and in Perry [189] suggest that a more 'open' design might be appropriate, but offer no dimensional guidance. Perry offers some theory for ejectors handling fluids only, but implies that no satisfactory theory exists for ejectors handling solids, so design changes would be a matter of trial and error.

- Sand disengagement from the slurry return. It was found that sand carry-over from the sand reservoir to the liquid reservoir could be minimised by extending the slurry return pipe to below the liquid level in the sand reservoir, as shown in Figure 6.4.

Temperature.

It has been noted above that temperature differences affected sand flows very strongly. These temperature differences arose from three different causes:

- Differences in ambient temperature. During the period of these experiments (summer and autumn), the laboratory ambient temperature varied between approximately 18 ^{0}C and 26 ^{0}C.

- Waste heat from the circulation pump. During the course of a 6 hour experiment, electrolyte temperatures would typically rise by about 5 ^{0}C.

- Thermal mass. The system contained 100 kg of liquid and about 25 kg of sand. This was sufficient to ensure that when the rig was run on

consecutive days, the liquid did not lose overnight all the heat gained during the day, so temperatures tended to rise cumulatively.

A very real improvement to the rig performance would be obtained by installing means of temperature control.

Sand Kinetic Energy

Since it proved impossible to maintain sand flow within the desired limits, a parameter is required to characterise the effects of variations in this. A suitable parameter is the Total Incident Sand Kinetic Energy (*TISKE*/J) over the period of the 6 hour experiment.

$$TISKE = \frac{1}{2} M v^2 \qquad (6.1)$$

Here: M is the total mass of sand passed in 6 hours (kg), evaluated as the mass passed per second (Section 6.2.2), multiplied by the number of seconds in the trial (21600).

v is the flow velocity of the slurry ($m.s^{-1}$), evaluated at the nozzle from the volumetric slurry flow ($m^3.s^{-1}$) divided by the exit nozzle cross-sectional area (m^2).

Note that *TISKE* scales as v^3, not v^2, since M contains a v dependence.

TISKE varies with both sand concentration and flow velocity, both of which are themselves dependant on the fluid temperature. This is shown by Figure 6.6.

Figure 6.6 shows how *TISKE* varies with temperature. The solid squares, illustrating the behaviour in softened tap water, show a good linear relationship; *TISKE* rises by about 25% over a 7 ^{0}C temperature interval. When 3.5% NaCl solution was

substituted for water, *TISKE* dropped to the level indicated by the 4 lower crosses, i.e. by about half. Trial-and-error adjustment (screwing in the ejector inlet nozzle by 3 mm) succeeded in bringing the performance back up to the level indicated by the remaining crosses i.e. nearly back to the levels achieved in water. The non-predictability of this behaviour means that *TISKE* has to be considered as a primary variable; this was not part of the original scheme.

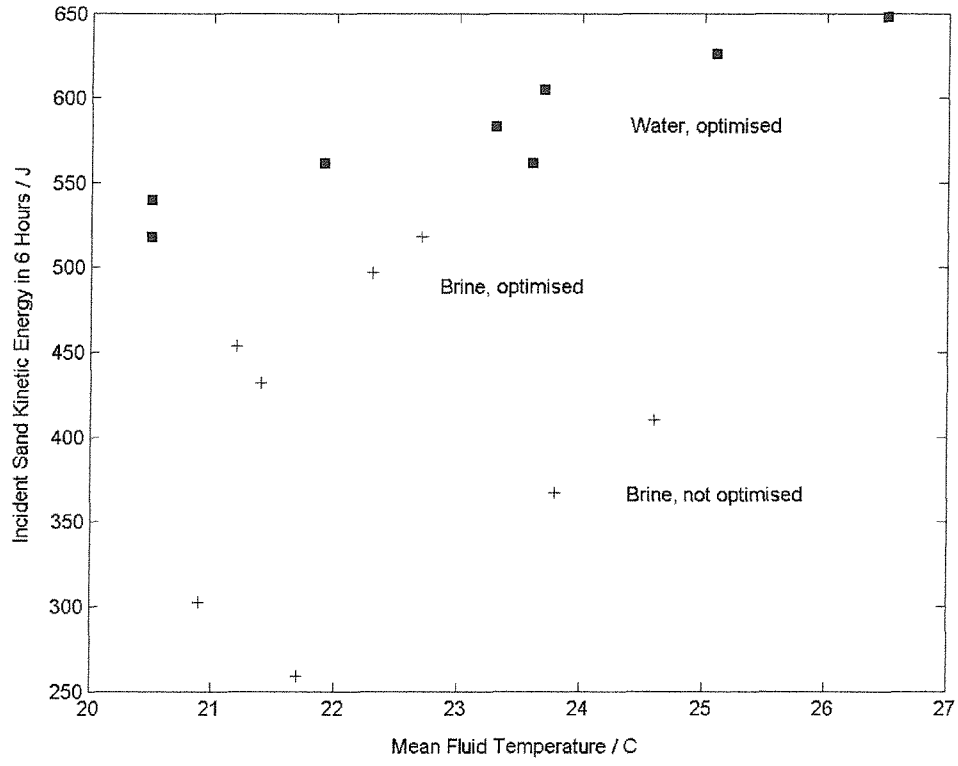

Figure 6.6

Variation of Total Incident Sand Kinetic Energy with mean run temperature.

Experiment time

Trial experiments showed that at the flow rates indicated above, an experiment time of 6 hours would result in a mass loss of about 20 mg from an aluminium based coating, i.e. one readily measurable. The corresponding penetration of about 90 μm, i.e. less than half way through the coating, would ensure that it was the coating

properties that were measured, not those of the substrate. This time was therefore adopted.

Water quality

Ideally, these experiments should have been carried out using deionised water and natural seawater. This was not done, for the following reasons:

- No large scale (multiples of 100 litres) source of deionised water was available. Softened tap water (boiler feed water) was used instead. This was believed to have a low chloride level (negligible compared with seawater), but could not be guaranteed to be completely non-corrosive. Hawthorne [178] has suggested that in some cases measurable levels of erosion corrosion can occur, even at very low chloride levels.

- 3.5 % sodium chloride solution, in boiler feed water, hereafter referred to as 'brine', was used as a proxy for seawater. This was done both for consistency (natural seawater is quite variable) and to avoid complications due the minor components present in natural seawater. The latter comprise inorganic ions, which can lead to the formation of calcareous scales at cathodic areas (these can be quite good cathodic inhibitors, but their incidence tends to be somewhat variable), and organic species, which can lead to the formation of biofilms, beneath which very complicated chemistry can occur.

Sand quality

The sand used was the same as that employed in Section 4, i.e. Redhill 50 sand of mean diameter 250 μm. This was circulated from a reservoir with a large capacity (about 25 kg). Constant recirculation of the sand tends to lead to sand degradation (blunting). This was minimised by replacing all sand removed by sampling with

fresh sand, and by occasionally replacing the entire reservoir contents. No trends attributable to sand blunting were observed.

Electrochemical methods

A main object of this work has been to investigate the application of Electrochemical Noise methods to an erosion-corrosion scenario (see Section 6.3.4 below), but use of certain other electrochemical methods was also considered/used occasionally:

- Potentiodynamic Polarisation. Not used, because it causes gross changes to the sample being measured, and also is slow compared with the rate at which physical changes due to erosion altered the target.

- Linear Polarisation Resistance (LPR). Attempted unsuccessfully. The reasons for this were established to be the excessive iR drop in the system (see EIS measurements, below) and the instability of the OCP of (particularly) aluminium based targets (see below).

- Electrochemical Impedance Spectroscopy (EIS). The potentiostat was not optimised for this method. The available frequency and current measurement ranges were not issues, but the ability to use a substantially longer acquisition time would have been valuable. In practice, EIS was used to determine the solution resistance of the cell. Measurements made at the end of the experimental period established that this was because the internal iR drop in the cell was much larger than expected – about 2700 Ω in 3.5% NaCl and > 100 kΩ in water. Better quality data would result if the cell's internal iR drop were reduced. This iR drop results largely from the same factors that cause excessive pressure drop in the system (mainly the very long inlet jet in the ejector) and would be similarly mitigated by suitable modifications to the cell geometry.

Electrochemical Noise measurements

A number of preliminary experiments (potentiostatted current noise) were carried out to establish levels of background noise, signal stability and sampling rate requirements:

- The entire system (except for the circulating pump) was enclosed in a Faraday cage to isolate the measurement system from external electrical influences. Various earthing arrangements were tried to try to minimise noise levels, but in the end no better solution was found than to connect the Faraday cage to conventional mains earth.

- Power spectral density plots generally showed a smoothly changing curve, with minor sharp interferences at 16, 32, 48 and 50 Hz. These could not be wholly removed, but (except as noted below) were very small and not such as to interfere with the desired measurements.

- Attempts to measure electrochemical noise on the carbon counter electrode used (by measuring noise between the two counter electrodes built into the system for this purpose) showed that this was dominated by a small sinusoidal output at 16 Hz (modified by its harmonics). This is the pump rotation frequency, and it is thought that the fluctuation in electrical output derived from vibration of the electrodes in the flow. While this did not have any significant effect on the test results, a more rigid (and leak-tight!) counter electrode arrangement would be desirable.

- The source of 50 Hz mains pick-up was not established, but by a process of elimination, is thought to have been within the potentiostat itself. 50 Hz pick-up manifested itself in two forms:

- At sampling rates up to 100 s^{-1}, it was very small and could be ignored.

- At sampling rates of 200, 500 and 1000 s^{-1} a 50 Hz signal of constant amplitude (112 nA peak) was imposed on the measured output. Since this amplitude was larger than the signal which it was desired to measure, these higher frequencies could not be used. As it has turned out, this has been an important restriction on the data obtained, so finding means of removing this effect would be an important aspect of any future work.

- Sampling rate. A sampling rate of 20 s^{-1} was used for the previous static corrosion work; this rate has been used for this program also, in the interests of comparability. Since it was felt that more information might be available at higher frequencies, further measurements were made at 100 s^{-1}, the highest rate possible not subject to external interferences (see above).

- Stationarity. As a matter of simple observation, the electrochemical output from this experimental set-up was a great deal more stationary (on the experimental time scale used – 600 s measurement) than that obtained under static conditions. This could have allowed longer experimental runs than were used statically, but 600 s runs were retained in the interests of comparability. This also ensured that adequate time existed between measurements to allow the dissipation of any disturbance to the system caused by the measurements.

Target homogeneity

A problem in interpretation arises because the electrochemical behaviour of the target is not uniform across its area. The potentiostat applies a control potential to the target, which therefore presents an equipotential surface to the impacting jet. To the

extent that, under freely corroding conditions, there might have been local potential differences between different areas of the target, these appear as different current flows from different areas. The measurement system only records the net behaviour of the target as a whole, so, to the extent that internal short-circuiting or signal modification by local capacitances may occur, these are not recorded.

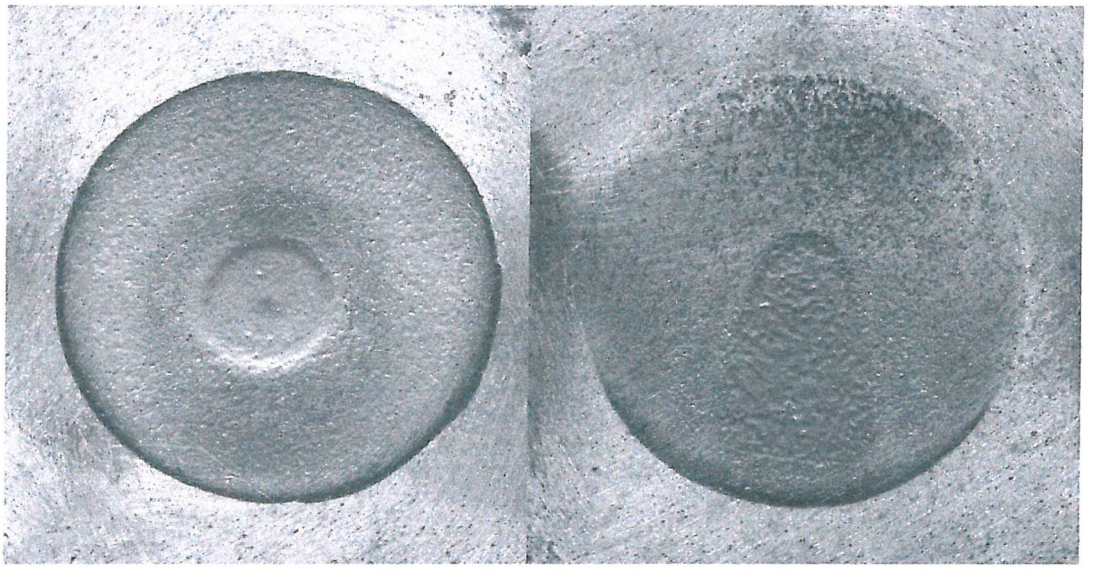

Figure 6.7

Sample 29	Sample 32
90^0 impact	30^0 impact
'Circular' scar	'Comet' scar

Aluminium targets eroded in Brine + Sand.

Diameter of eroded area in each case: 30 mm

The possibilities that may occur are illustrated by the sample targets shown in Figure 6.7. The target becomes very inhomogeneous. Most obviously, there is a pronounced scar and a surrounding area. Under freely corroding conditions, one would expect the scar to become anodic to the surrounding area, because of the removal of protective passivation layers. As has been pointed out by Dawson *et al* [55], a further complication is that the eroded scar may then be partially cathodically protected by the less eroded surroundings. Moreover, both within the erosion scar

and outside it, the behaviour of the sample is not uniform. For normal impact the sample has (approximately) circular symmetry, but for oblique impact this is not the case and there may be distinct differences between the leading edge (top as tested, and also top as shown) of the sample and its trailing edge. These differences may affect erosion, pitting, oxidation and solids deposition, all of which may themselves affect the electrochemical output.

Desirably, means should be found of monitoring local electrochemical behaviour. However, this is a very demanding requirement, which has not been addressed in this work.

6.2.3 Experimental design

The primary objective of this work has been to investigate the applicability of electrochemical noise methods to the erosion-corrosion of protective metallic coatings on steel in seawater. A systematic program of work has therefore been undertaken, using the equipment described and taking into account the experimental issues noted above, including the following variables:

Materials:	HVOF aluminium, HVOF aluminium/12% silicon (polished to 200 μm residual thickness), and hot-dipped zinc coatings (not polished, approximately 80 μm thickness) on AISI 1020 steel, and the steel substrate (as described in Section 3).
Erodents:	Sand + water, Water only, Brine only, Sand + Brine. (Brine here is 3.5% NaCl).
Angles:	90^0, 30^0; 37.5 mm stand-off.
Temperature:	Ambient (plus effects of heating by the circulating pump).
Duration:	6 hours.
Flow:	85 mls.s^{-1} ≡ 3.6 m.s^{-1} (≡ Re = 12,000); Orientation – horizontal, in air.
Sand	Redhill 50 sand, as described in Section 3. 5% w/v concentration, where applicable (≡ Relative separation = 2.1). Renewed periodically.

Evaluated by:	Mass loss
	ECN (hourly, at 20.s^{-1} and 100.s^{-1} sampling rates; potentiostatted runs at OCP).
	Microscopy (optical, SEM)
	Profilometry.

6.3 RESULTS AND DISCUSSION

6.3.1 Introduction

Table 6.2 sets out the scheme of experimental runs carried out. The run numbers in the table are used as identifiers throughout this Section. They reflect the order in which the runs were actually carried out.

An attempt was made to maintain consistent flow conditions between runs. This was not wholly successful. Where possible repeat runs were carried out to ensure that comparability was as good as possible; these repeats are not true replicates. Shortage of coated target materials has meant that a desirable degree of replication has not been achieved, and, together with the flow problems noted, it has not been possible to give the resulting data a full statistical treatment.

Results and discussion are presented under three broad headings: Appearance and Topography, Mass Loss and Electrochemical Noise.

6.3.2 Appearance and Topography

General Appearance of samples

Table 6.3 gives a general idea of the appearance of the various samples at the ends of test runs, as observed by low-power microscopy.

Under impact by water only, most samples showed no visible change. Where there was porosity intersecting the surface in sprayed samples, this was not sealed. A steel target at 30^0 impact appeared to be slightly polished relative to untreated areas.

Under impact by brine only, there was a large difference between the zinc samples and the others. Zinc targets all showed signs of material loss in the form of poorly

Run No.	Fluid	Impact Angle (^{0})	Target
1	Water + sand	90	Steel
2	Water + sand	90	Aluminium
3	Water + sand	90	Zinc
4	Water + sand	90	Aluminium
5	Water + sand	90	Al/12%Si
6	Water + sand	30	Zinc
7	Water + sand	30	Aluminium
8	Water + sand	30	Al/12%Si
9	Water + sand	30	Steel
10	Water + sand	30	Zinc
11	Water only	90	Zinc
12	Water only	90	Aluminium
13	Water only	90	Al/12%Si
14	Water only	30	Zinc
15	Water only	30	Aluminium
16	Water only	30	Al/12%Si
17	Water only	30	Steel
18	Water only	30	Zinc
19	Brine only	90	Zinc
20	Brine only	90	Zinc
21	Brine only	90	Aluminium
22	Brine only	90	Al/12%Si
23	Brine only	30	Zinc
24	Brine only	30	Aluminium
25	Brine only	30	Al/12%Si
26	Brine only	30	Steel
27	Brine only	30	Zinc
28	Brine + sand	90	Zinc
29	Brine + sand	90	Aluminium
35	Brine + sand	90	Aluminium
30	Brine + sand	90	Al/12%Si
36	Brine + sand	90	Al/12%Si
31	Brine + sand	30	Zinc
32	Brine + sand	30	Aluminium
37	Brine + sand	30	Aluminium
39	Brine + sand	30	Aluminium
33	Brine + sand	30	Al/12%Si
38	Brine + sand	30	Al/12%Si
34	Brine + sand	30	Steel

Table 6.2: Key to experimental runs.

Run No.	General Appearance.
1	Circular scar, steep sided, small central hump.
2	Circular scar, small central hump, scar surface matt.
3	Circular scar, pronounced central hump.
4	Circular scar, pronounced central hump, pits around scar.
5	Circular scar, small central hump, scar surface matt.
6	Comet scar, polished w.r.t surrounding area.
7	Comet scar, rough entry, smooth exit.
8	Comet scar, rough entry, smooth exit.
9	Comet scar, polished w.r.t surrounding area.
10	Comet scar, polished w.r.t surrounding area.
11	No visible change.
12	No visible change, surface not sealed.
13	No visible change, surface not sealed.
14	No visible change.
15	No visible change.
16	Possible minor pitting.
17	Impact area slightly polished.
18	No visible change.
19	Radial feature at centre, some pitting around this.
20	Radial flow marks, dark features, white corrosion deposit.
21	Extensive pitting, white corrosion deposit.
22	Extensive pitting, white corrosion deposit.
23	Roughened at impact point, white corrosion deposit.
24	Pitted unevenly across surface, no white deposit.
25	Heavily pitted, white corrosion deposit at 'tail' of target.
26	Bright, with a little pitting at 'top' of target.
27	Rough comet, with possible ridging, white corrosion deposit.
28	Circular scar with radial flow pattern. No corrosion deposit.
29	Circular scar with rough surroundings. No corrosion deposit.
35	Circular scar with rough surroundings. No corrosion deposit.
30	Circular scar with rough surroundings. No corrosion deposit.
36	Circular scar with rough surroundings. No corrosion deposit.
31	Comet scar, white deposit at 'top' of target.
32	Comet scar, smooth, pitted at 'top' of target. No deposit.
37	Comet scar, smooth, pitted at 'top' of target. No deposit.
39	Comet scar, smooth, pitted at 'top' of target. No deposit.
33	Comet scar, little porosity in scar, heavily pitted outside.
38	Comet scar, little porosity in scar, heavily pitted outside.
34	Shallow comet scar, slight pitting at 'top' of target.

Figure 6.3: General appearance of targets after experiments.

defined craters, with obvious flow marks around them, generally radially disposed. Figure 6.7 (Sample 19) shows an example. These zinc samples also showed adherent white deposits around the scar. In the most severe case, (Sample 20), black marks were also present within the scar, Figure 6.8. These are areas where the zinc coating has been wholly removed, revealing the steel beneath.

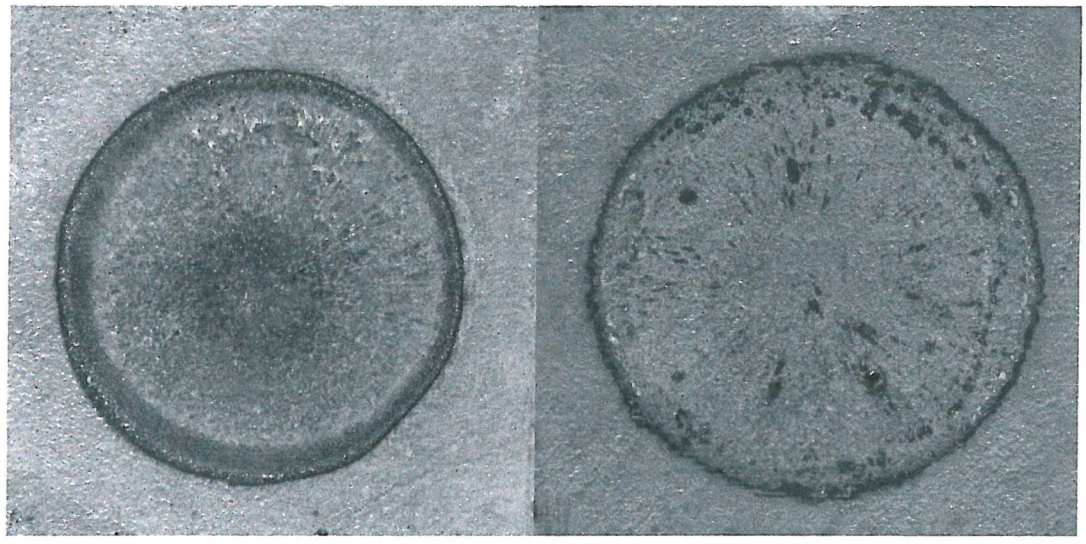

Figure 6.8

Sample 19 Sample 20

Zinc targets eroded in brine.

Diameter of eroded area in each case: 30 mm

Aluminium based samples (metal or alloy) at normal incidence, show pitting together with adherent white deposits; at oblique incidence, pitting is present, but the white deposits are either absent or limited to the 'tail' of the specimen, suggesting removal by the brine flow. Alloy targets are generally more heavily pitted than are pure aluminium targets. A steel target at 30^0 appeared to be slightly polished in the impact area, but with some minor pitting at the 'top' of the sample.

When sand is present, well-defined scars are also present. These have the general form already shown in Figure 6.6, i.e. circular scars at normal impact, 'comet'-shaped scars at oblique impact. The circular scars tended to be steep sided, with relatively

small central peaks. This shape, which differs qualitatively from that commonly reported [19] for ductile erosion at normal impact, is probably a consequence of the effects of slurry density on individual particle flow trajectories [21]. The interior of the scar was typically polished relative to uneroded areas, with the porosity intersecting the surface of the latter removed, presumably by plastic flow. At oblique impact, the entry to the scar is usually rougher than the exit, presumably due to flow effects.

Water+Sand produces just these effects with no deposits or obvious pitting. Brine+Sand produces different results for different target materials. Zinc produces scars surrounded by flow features, suggesting that slurry and flow erosion continue as separate processes. Aluminium based targets produce erosion scars with pitting around them, more pronounced in the case of alloy than for pure aluminium; no white deposits are present – presumably these are washed away. A steel target at 30^0 showed a shallow scar in the impact area and some minor pitting at the 'top' of the sample (where there is better oxygen access than at the 'tail').

These observations show a consistent set of behaviours with the various targets and erodents.

SEM imaging of impact details

SEM images are presented of selected areas of interest only. Electron images of eroded samples are similar to those obtained optically, but the greater depth of field of the SEM allows the better resolution of some features.

Figure 6.9 compares impact features on aluminium made using 'water + sand' at 30^0 nominal impact angle. Areas both inside and outside the visible impact scar are shown, for both the preliminary erosion work discussed in Section 4 (at 27 $m.s^{-1}$, 2.5% w/v sand) and that from the main experimental sequence (at 3.5 $m.s^{-1}$, 5.0% w/v sand).

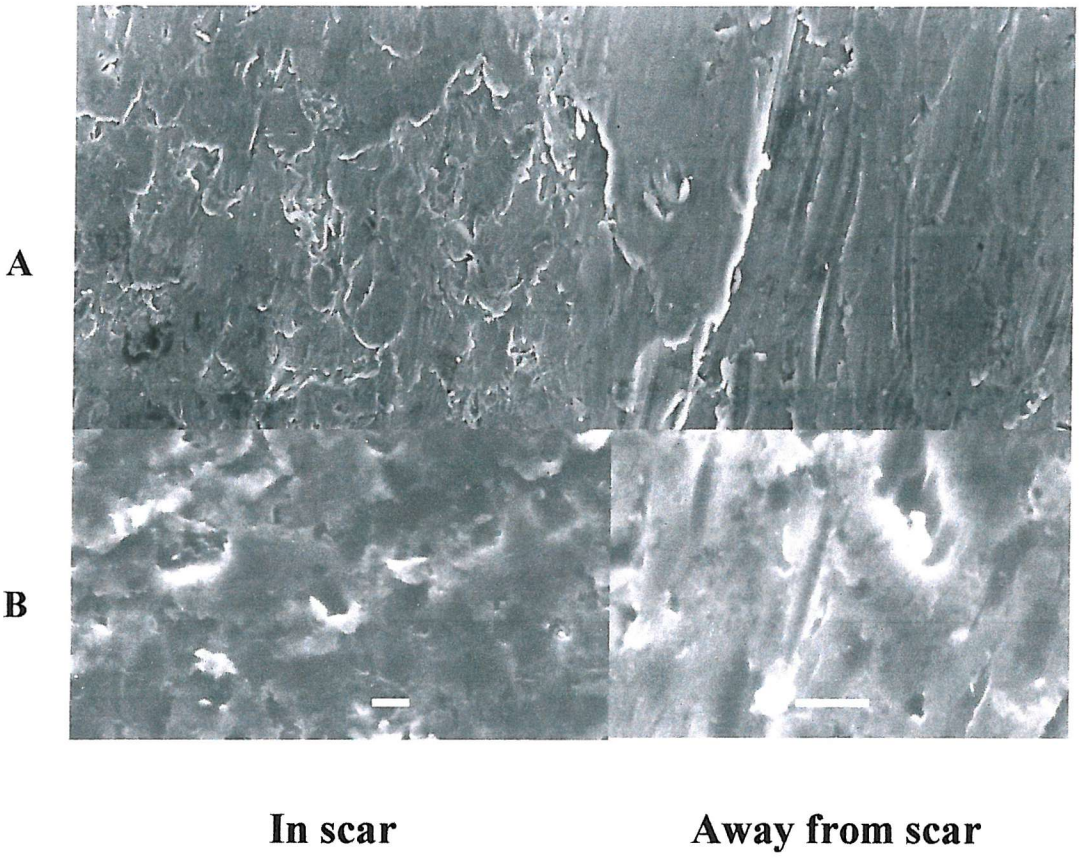

Figure 6.9: SEM images of impact scars: 10 μm scale bars.
Aluminium/water + sand/30^0 impacts.
Condition A: 27 $m.s^{-1}$, 2.5 % w/v sand.
Condition B: 3.6 $m.s^{-1}$, 5.0 % w/v sand.

There are some interesting contrasts.

At 27 $m.s^{-1}$, within the scar, the surface has a platelet-like structure, more commonly associated with gas-blast erosion [39,40]. Outside the scar, long (typically ~ 80 μm) shallow impact features, apparently resulting from very grazing impacts, are found. These features occur quite densely (not quantified) in the vicinity of the scar. They are oriented in the flow direction and have prominent lips on their 'upstream' sides.

At 3.5 $m.s^{-1}$, within the scar, there are no platelets, but the surface is pock-marked by near-vertical impact features, with prominent lips. Outside the scar, symmetrical, relatively short (~ 15-20 μm) impact features occur with much lower frequency than observed at 27 $m.s^{-1}$. Most of these features are readily explained as ploughing/microcutting features of a ductile metal [5], if it is allowed, as seems likely, that that sand particle trajectories are severely modified by inter-particle momentum transfer within the slurry. These slurries are substantially denser than the limit proposed by Oka [27] for non-interference between particles.

Other workers have also seen platelet-like structures. Zu *et al* [124] studied the erosion of aluminium by silica sand in air and in tapwater, and found that sand embedment occurred in air but not in water. Li *et al* [64,130,147], working in 0.5M NaCl observed erosion similar to that seen in this work, with extruded platelets, apparently eventually becoming detached by fatigue cracking. They suggested that the increased mass loss associated with corrosion by NaCl resulted from pitting causing easier lip detachment. A similar mechanism has been proposed by Postelthwaite [148,149] in the context of coal slurries in pipelines.

Hovis *et al* [164] eroding aluminium and aluminium/silicon alloys in air suggested that these alloys may have inferior erosion performance to pure aluminium, because silicon lamellae in the alloy act as 'chip-breakers' in machining processes, whereas aluminium lips can suffer multiple distortions and foldings without fracture. This difference has not been seen in the present work.

The platelet-like structures within the erosion scar at the higher erosion energy are more difficult to explain, but a possibility is suggested by the work of Misra and Finnie [43]. These workers studied three body abrasion of aluminium, and found microcutting-like features under ambient conditions, but more platelet-like structures when they placed their entire apparatus in an oven at ~ 270 ^{0}C (about two-thirds of the absolute melting point of aluminium). They tentatively attributed this to a change in mass loss mechanism, resulting from increased plasticity at higher temperatures.

This may relate to the erosion theory of Sundararajan [32], who links plasticity with lip formation in what would be an appropriate manner. It is at least possible that, in the preliminary erosion work discussed in Section 4, the kinetic energy dissipated as heat in the target was sufficient to raise the local temperature to levels where this sort of generalised plastic flow could occur. At the lower kinetic energy fluxes typical of the main part of the work, insufficient temperature rise occurred for this, and plastic flow remained localised. Obviously, there is not sufficient evidence here to come to a definite conclusion, though an outline calculation (Appendix 6.3.2A) suggests that surface modification by this mechanism or possibly by local boiling/cavitation may indeed be possible. A more systematic investigation would allow definition of whether such a change of mechanism does actually occur. For the main part of this work, all the data refers to circumstances below (in temperature terms) the point at which any such transition may occur.

A further aspect of the erosion features can be seen in Figure 6.10. In water, the features have prominent lips, in brine these are absent. Presumably this is due to stress cracking of these highly strained metal fragments. Loss of these lips would be expected to contribute to increased rates of metal loss in brine, as is in fact found (see below, Section 6.3.3).

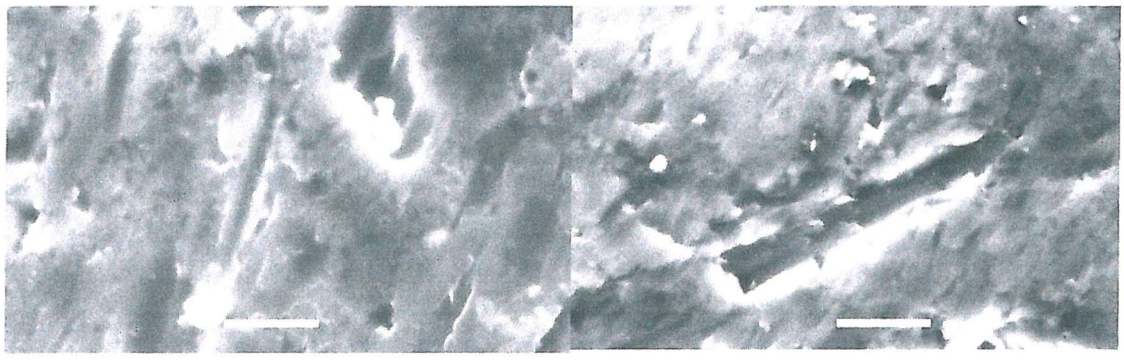

Water + sand. **Brine + sand.**

Figure 6.10: Comparison of SEM images of erosion features in different fluids. Aluminium/30^0 impacts. 10 μm scale bars.

A quite different phenomenon is encountered with zinc, under flow corrosion in 'water + sand' at 30^0 impact. As noted above, the scar entry under these conditions is quite rough. SEM examination shows that this is due to a well defined waviness in the surface, see Figure 6.11, probably caused by instabilities in the fluid flow, as argued by Karimi and Schmidt [70].

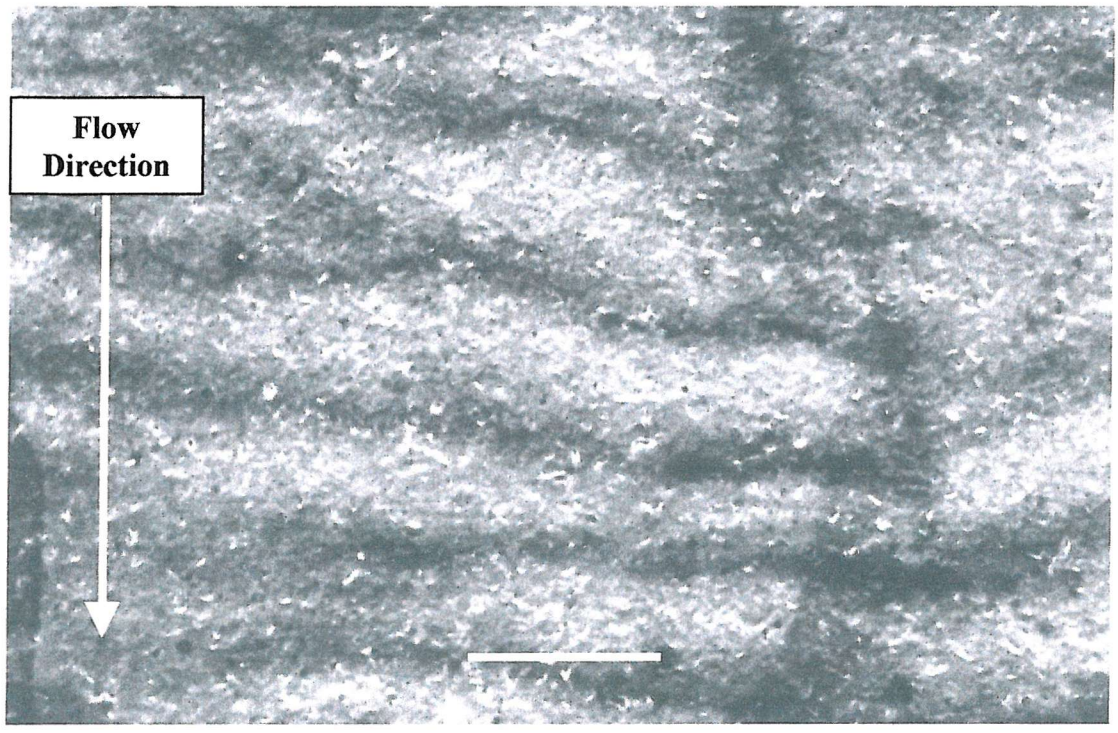

Figure 6.11: Waviness formation on zinc.
Water + sand/30^0 impact.
200 μm scale bar.

Interestingly, this pronounced feature is not seen in 'brine + sand'; presumably the local flow/viscosity regime is sufficiently different for instabilities not to occur.

Profiles of Normal Incidence Scars

Figure 6.12 shows Talysurf sections of representative erosion scars at normal incidence (Water +sand, Brine + sand scars are very similar).

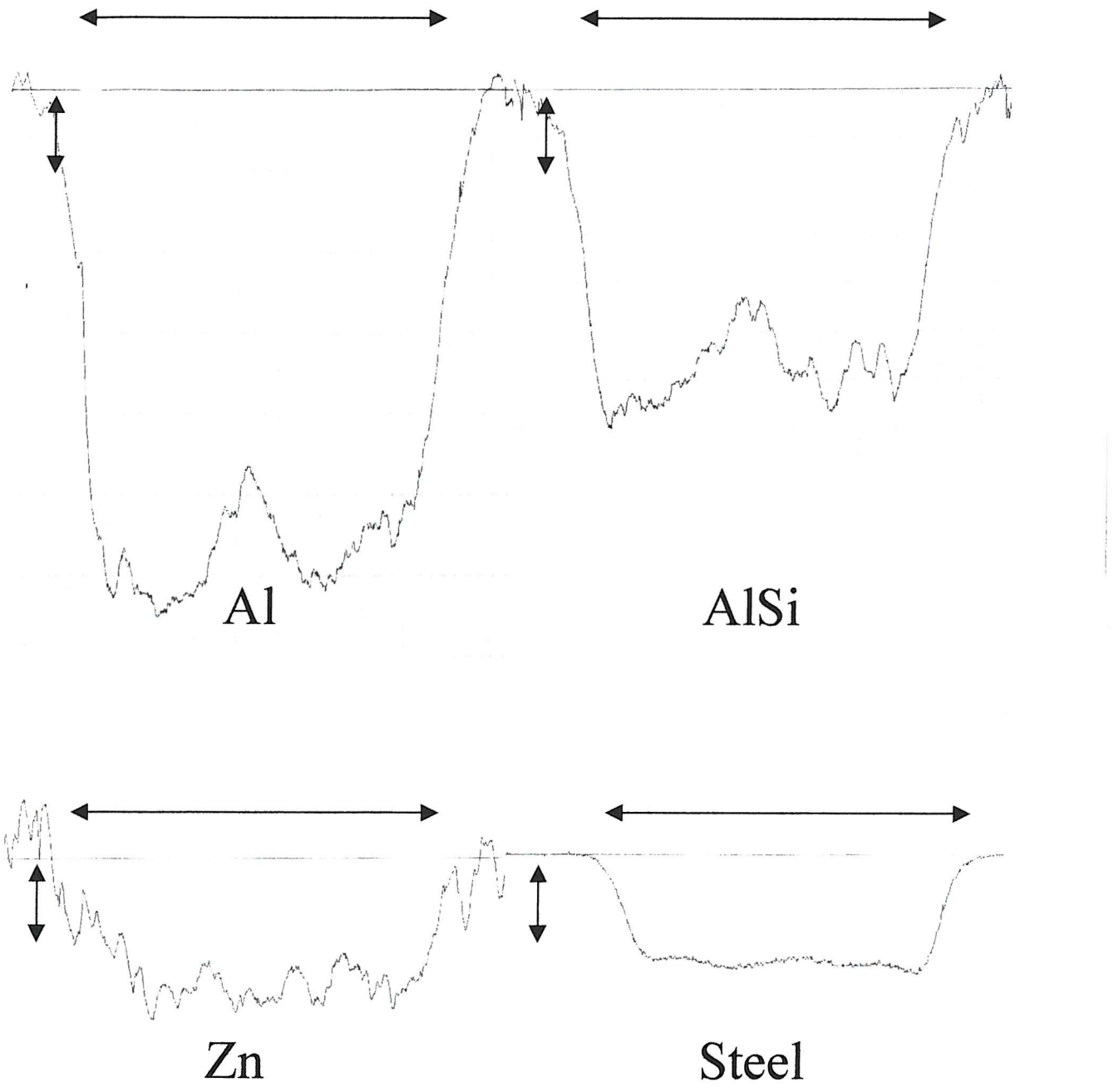

Figure 6.12

2-D Talysurf sections of normal incidence erosion scars.

Horizontal marker = 10 mm

Vertical marker = 20 μm

These sections have been rescaled from the raw data to directly comparable scaling. The aluminium and Al/12%Si alloy sections show a noticeable central peak, as is expected under conditions of ductile erosion, though it is less prominent in the case of the (harder) alloy. The harder zinc and steel samples show little if any central peak. The bottom surface of the zinc scar is noticeably rougher than that for steel; this is possibly related to a coarser grain size in the zinc.

Appearance – Conclusions/Further work

The general scar appearance and profile of each target is consistent with erosion being dominated by ductile processes.

At 30^0 incidence all the samples show similar comet shaped scars, with relatively rough entries and smooth exits. Where individual impact features are visible, these can be accounted for by microcutting/ploughing processes, and subsequent lip loss, at the energy levels involved in the main part of this work. Platelet formation and lip loss may occur at higher energies, but this requires further investigation.

Addition of sodium chloride to the flow appears to promote lip loss, possibly by stress corrosion cracking, though direct evidence of this is lacking.

Under at least some conditions, zinc surfaces can acquire a pronounced surface waviness; this requires further investigation of the conditions under which the phenomenon occurs.

6.3.2A Appendix: Thermal Behaviour

Trial targets (commercially pure aluminium HVOF coated on steel) are eroded by a slurry of sand in water at normal incidence. Observation indicates that the form of the sample surface topography after impact is a function of flow rate. Related work by Misra and Finnie [43] on three body abrasion in air suggests that the differences may be caused by localised heating of the target surface to temperatures of the order of 270^0C.

It is desired to know whether such a local surface temperature could in principle be reached by 'dumping' all the incident surface energy associated with the sand impact into the target, and how this temperature would vary with flow rate. A severely simplified energy balance calculation is attempted.

The experimental set-up is shown schematically in Figure 6.13. The target consisted of a steel blank, dimensions 40 × 40 × 5 mm, approximate mass 60 gm, density 7860 $kg.m^{-3}$, thermal conductivity 80 $W.m^{-1}.K^{-1}$, with a coating of HVOF sprayed aluminium, originally 200 μm thick, density 2700 $kg.m^{-3}$, thermal conductivity 237 $W.m^{-1}.K^{-1}$.

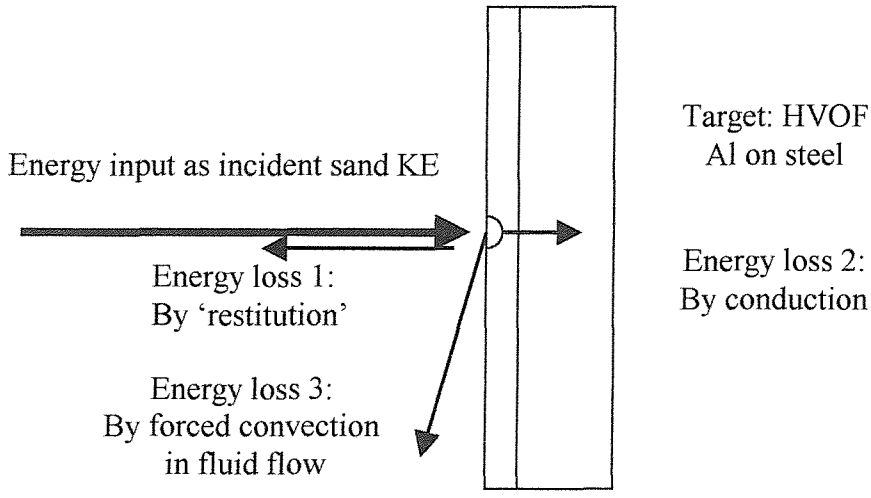

Figure 6.13: Schematic of Energy flows at target surface.

It is envisaged that a calculation can be carried out for steady state conditions for a central area of the target, i.e. 'guard-ring' conditions with no lateral heat flow in the target.

Energy input is envisaged as being via the dissipation of sand kinetic energy on impact.

$$Sand\_Flow = \phi A_{nozzle} \rho_{Slurry} v \qquad \text{kg.s}^{-1} \qquad (6.2)$$

$$Particle\_Flow = \frac{\phi A_{nozzle} \rho_{Slurry} v}{m} \qquad \text{s}^{-1} \qquad (6.3)$$

$$Particle\_KE = \frac{1}{2} m v^2 \qquad \text{J} \qquad (6.4)$$

$$KE\_Flux = \frac{1}{2} \phi A_{nozzle} \rho_{Slurry} v^3 \qquad \text{J.s}^{-1} \qquad (6.5)$$

Where: ϕ = mass fraction sand in the slurry.

A_{nozzle} = cross-sectional area of the jet nozzle (m^2)

ρ_{Slurry} = slurry density ($kg.m^{-3}$)

v = fluid linear velocity ($m.s^{-1}$).

m = mean particle mass (kg).

Note that this kinetic energy *flux* has units of power and scales as ϕv^3. It is independent of the target conditions, particularly target surface temperature. When multiplied by the total run time of the experiment (s), a total incident sand kinetic energy (*TISKE*) (J) is obtained – this will be used in the next Section.

Two particular sets of incident flows have been used in this work.

Condition A (Section 4, steel target holder, flow not visible):

Linear flow rate 27 $m.s^{-1}$ ≡ Volume flow 730 $mls.s^{-1}$.(5.9 mm nozzle).

2.5 % w/v sand in slurry.

Incident sand KE flux = 6450 $mJ.s^{-1}$ or 235 $mJ.s^{-1}.mm^{-2}$.

Condition B (Section 6, polymer target holder, flow visible):

Linear flow rate 3.6 $m.s^{-1}$ ≡ Volume flow 85 $mls.s^{-1}$.(5.5 mm nozzle).

5.0 % w/v sand in slurry.

Incident sand KE flux = 27 $mJ.s^{-1}$ or 1.1 $mJ.s^{-1}.mm^{-2}$.

Sand in both cases is Redhill 50 sand, mean diameter 235 μm, density 2700 $kg.m^{-3}$.
Flow in both cases is large enough to be fully turbulent.

Three routes are envisaged for energy loss.

Restitution. By observation, under condition B this loss mechanism is believed to be small (not observable at condition A). If the coefficient of restitution is independent of v, this loss will be a constant fraction of the incident sand KE flux and will scale as v^3.

Conduction into the mass of the target. Under condition B, the target is held in a polymer holder, from which heat losses by conduction should be (relatively) small. If it is considered that all the impact energy goes toward adiabatic heating of the target, a temperature rise of the target as a whole of about 50^0 C over the course of the experiment can be estimated. In practice, when the test rig was dismantled, the target was not appreciably warm to the touch. It is therefore assumed that in this case, conduction was not an important loss mechanism. Condition A is more difficult to assess, since there is a much larger energy input and also a potentially a much larger heat sink (steel apparatus); probably conduction has some part to play here, but how large has not been assessed. Note that this loss mechanism will scale with the surface temperature rise, ΔT (K), but not with the fluid flow velocity.

Forced convection into the fluid stream represents the third loss and for the purposes of this discussion it will be assumed that this mechanism dominates. A very crude estimate of the energy loss by this route can be made by using the Chilton-Colburn analogy between heat and mass transfer (theory and data from Perry [189]).

For turbulent flow:

$$f/2 = St.Pr^{2/3} \tag{6.6}$$

Where: f	= Fanning friction factor.		(Dimensionless)
St	= Stanton Number	$= h_T/cv\rho_{Slurry}$	(Dimensionless)
Pr	= Prandtl Number	$= c\mu/k$	(Dimensionless)
h_T	= heat transfer coeff	$=q_{conv}/A_{scar}\Delta T$	($J.m^{-2}.s^{-1}.K^{-1}$)
q_{conv}	= convective energy flux		($J.s^{-1}$)
A_{scar}	= area of scar		(m^2)
ΔT	= surface temperature rise		(K)
c_p	= specific heat of slurry		($J.kg^{-1}.K^{-1}$)
v	= exit velocity of slurry		($m.s^{-1}$)
μ_v	= absolute viscosity of slurry		(Pa.s)
k	= thermal conductivity of slurry		($J.m^{-1}.s^{-1}.K^{-1}$)

Note that the exit velocity of the slurry is not known (and is not a constant) but geometry requires it must be of a similar order to the inlet flow. For simplicity, these velocities will be taken as equal.

Expanding the above equation and rearranging it in terms of h_T, then q_{conv}:

$$h_T = \frac{q_{conv}}{A_{scar}\Delta T} = \frac{f}{2} c_p \rho_{Slurry} v \,\mathrm{Pr}^{-\frac{2}{3}} \tag{6.7}$$

$$q_{conv} = \frac{f}{2} c_p \rho_{Slurry} A_{scar} \Delta T \,\mathrm{Pr}^{-\frac{2}{3}} v \tag{6.8}$$

Note that this quantity, the convective energy flux, scales with both ΔT and v. If, neglecting other sources of energy loss, we equate q_{conv} with the energy gain due to impact:

$$\frac{1}{2}\phi A_{nozzle}\rho_{Slurry}v^3 = \frac{f}{2}c\rho_{Slurry}A_{scar}\,\mathrm{Pr}^{-\frac{2}{3}}\,v\Delta T \qquad (6.9)$$

Rearranging and simplifying:

$$\Delta T = \frac{1}{fc}\frac{A_{nozzle}}{A_{scar}}\mathrm{Pr}^{\frac{2}{3}}\,\phi v^2 \qquad (6.10)$$

The surface temperature rise required to drive this process scales with ϕv^2, i.e. with the weight fraction of sand in the slurry and the square of the slurry linear velocity; alternatively, these erosion conditions would induce this surface temperature rise in the absence of other sources of heat loss.

Taking tabulated data from Perry [189] for f,c and Pr for water at ambient temperature, an area ratio of 4, experimental values of ϕ and v and substituting, we have:

For condition A: $\Delta T = 700\ ^0\mathrm{C}$.

For condition B: $\Delta T = 23\ ^0\mathrm{C}$.

Clearly, these are upper limits, not actually reached. Particularly at higher energies, other energy loss mechanisms will become important. If ΔT exceeds 100 ^{0}C, then extra energy loss by boiling (probably nucleate boiling on a rough surface) may occur; the bubbles so formed will then collapse and may cause cavitation damage.

While this calculation is extremely simplified, it does suggest that at sufficiently high slurry energies, both cavitation and possibly surface ductile flow may be involved in influencing the form of surface damage of aluminium (alloy) under sand in water erosion.

6.3.3 Mass Loss

Mass Loss and Scar Depth

Table 6.4 gives the mass losses (mg) and scar depths (μm) found for the various samples. The total incident sand kinetic energy (*TISKE* / J) associated with the sand impacted on the target during the period of the experiment is also estimated from measured sand fluxes and the overall run time.

From a practical point of view, the depth to which corrosion penetrates is at least as important as the mass loss, since it is usually metal penetration that results in component failure. These quantities are not necessarily directly related since mass loss may occur away from the visible erosion scar.

The maximum depths of the erosion scars formed have been estimated from 2-D Talysurf traces (as illustrated in Figure 6.12, Section 6.3.2). It should be noted that the Talysurf stylus is not very sharp and will not penetrate very fine/deep pores or pits, and so underestimates maximum penetration.

Figure 6.14 shows how these scar depths relate to mass loss. It is found that the zinc samples have behaved quite differently form the other materials, as shown.

For solids other than zinc, there is a linear relationship between maximum scar depth, δ_{max} (μm)(n.b. not scar volume) and total mass loss M_T (mg):

$$\delta_{max} = 4.3\, M_T - 0.23 \qquad r^2 = 0.92 \qquad (6.11)$$

There appears to be a slight difference between the behaviour in water and in brine.

In water: $\delta_{max} = 3.8\, M_T - 1.95$ $\qquad r^2 = 0.96$ $\qquad (6.12)$

In brine: $\delta_{max} = 4.3\, M_T - 0.13$ $\qquad r^2 = 0.93$ $\qquad (6.13)$

Run No.	Mass Loss / mg	Scar Depth / μm	*TISKE* / J
1	16.3	21	713
2	39.8	160	583
3	19.9	22	518
4	30.9	109	540
5	15.6	57	562
6	18.8	42	583
7	23.7	95	605
8	15.4	73	626
9	7.5	14	562
10	14.5	45	648
11	3.2	0	0
12	-0.5	0	0
13	-0.1	5	0
14	0.1	0	0
15	0.0	2	0
16	1.5	0	0
17	1.2	1	0
18	4.4	0	0
19	13.7	0	0
20	20.8	0	0
21	1.9	0	0
22	-2.8	10	0
23	6.7	0	0
24	1.0	0	0
25	-0.6	0	0
26	2.5	0	0
27	13.0	0	0
28	27.9	28	497
29	29.1	135	432
35	24.3	135	518
30	11.7	43	346
36	9.5	57	497
31	23.1	30	367
32	17.2	85	410
37	7.9	42	302
39	16.4	67	497
33	7.0	42	259
38	6.4	31	454
34	4.3	5	432

Table 6.4: Mass losses and Scar Depths.

If this distinction is real, then erosion in brine leads to scars about 13 % than in water. This is not unreasonable. However, this difference depends upon just the two highest mass loss points in each case (all aluminium), so the reality of this effect is uncertain.

In each of the above cases, the 'constant' term is very small and is probably to be regarded as effectively zero.

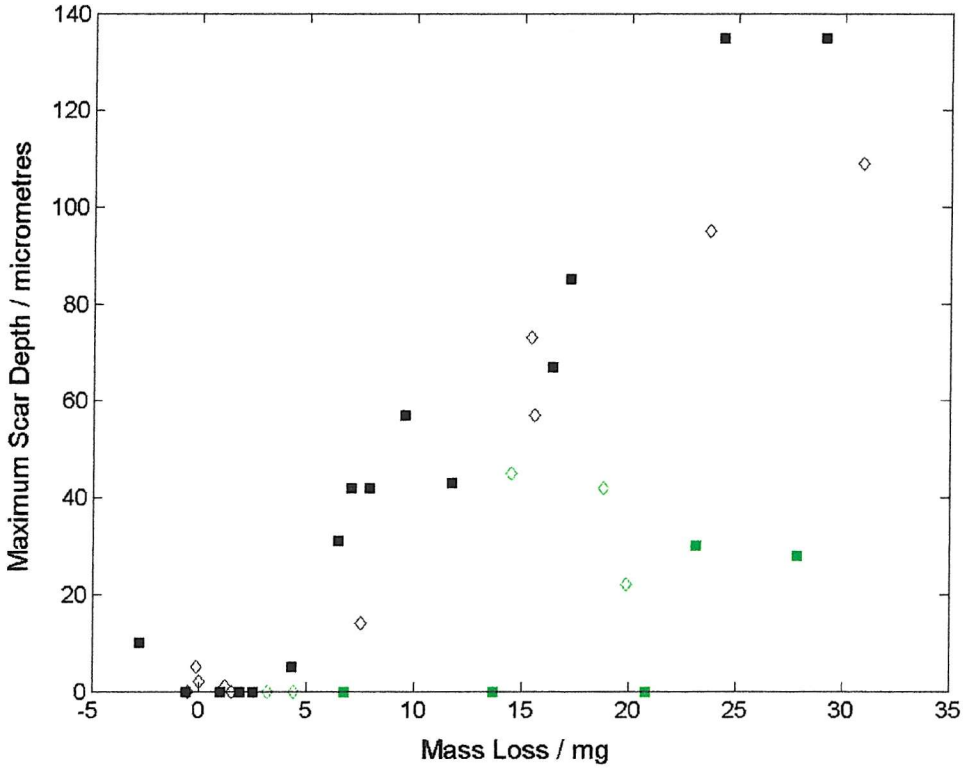

Figure 6.14

Relation of maximum scar depth to mass loss

Codings: Green = Zinc ■ = Brine (+ sand)

Black = All other materials ◊ = Water (+ sand)

The behaviour of zinc targets is completely different. Firstly, in all cases scar depths are much less than for other targets (for a given mass loss). In brine and the absence of sand, there is substantial mass loss but no measurable scar (though there is a local

discoloration where the scar might be expected). This indicates that mass loss is distributed over the whole of the exposed target surface, rather than being localised. In this case the component of momentum parallel to the surface is evidently more important than the normal component. Moreover, in this case 'sand + water' leads to deeper scars than does 'sand + brine'. This is a complex behaviour, which this work is not sufficient to explain, though the formation of a wavy surface in the 'sand + water' case is probably relevant.

Mass Loss vs Kinetic Energy

Originally, it was intended to carry out a material comparison (solids, fluids, impact angle) at fixed flow rates (liquid, sand). However, as explained in Section 6.2.2 above, adequate control of sand flow was not obtained. Therefore, in treating the data some allowance has to be made for this. The simplest means of allowing for the observed variability with both sand concentration and flow velocity is to assume, following van Riemsdijk and Bitter [29], that the amount of material removed is (with some qualifications, see below) proportional to the incident sand kinetic energy, and this is the approach which has been followed here.

Before proceeding further, it should be noted that the above assumption about kinetic energy implies that mass loss is proportional to the square of the flow velocity, i.e. there should be a velocity exponent of 2. Various investigators [30-34] have found, in practice, velocity exponents somewhat greater than 2 and have constructed elaborate theories (not all compatible) to explain this. Mostly, these authors have been considering much higher flow rates (typically, by 2 orders of magnitude) and more dilute slurries or gas blasts. In the present case, the data has been obtained over a fairly narrow range of relatively low flow rates using a relatively dense slurry, and will not support such an interpretation.

Figure 6.15 shows the whole of the mass loss data plotted against *TISKE*, as defined in Section 6.2.2, coded by incident fluid. There is a lot of scatter in the data

(unsurprising considering the range of variables included), but the data clearly fall into groups, with respect to sand kinetic energy.

Firstly, obviously, where there is no sand there is no sand kinetic energy. However, there are mass changes. These are associated with brine flows, not to any large extent with water flows, and will be discussed further below.

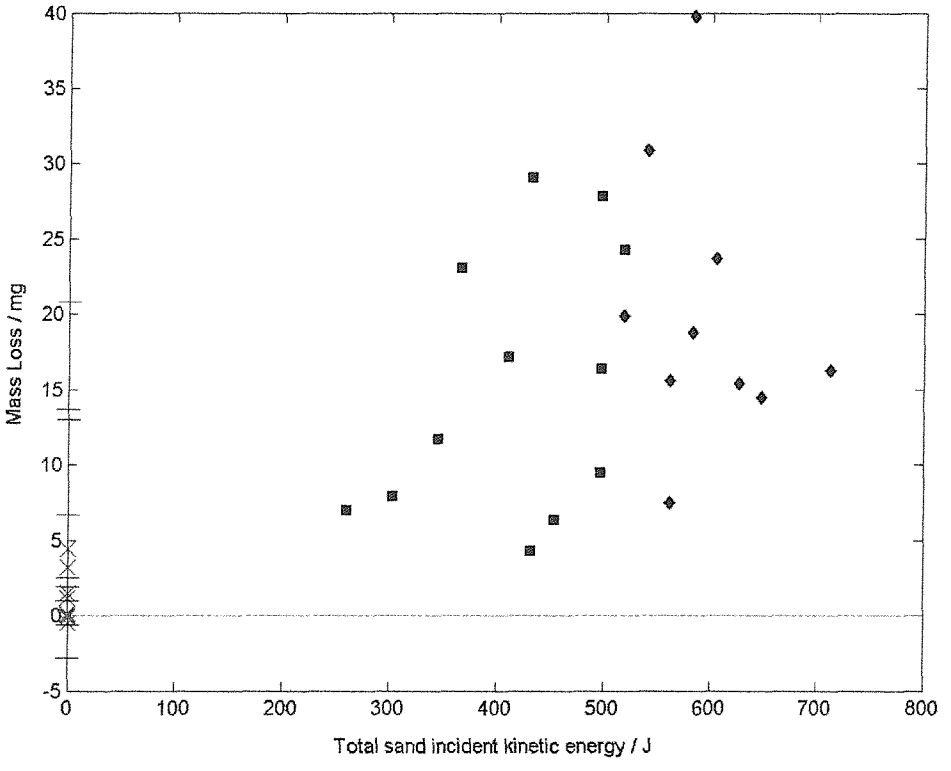

Figure 6.15

Mass Loss as a function of incident sand kinetic energy and erodent type

Fluid Coding: × = Water only

\+ = Brine only

. ◆ = Water+Sand

■ = Brine+Sand

Secondly, where sand is present in the flow non-overlapping data scatters are recorded, depending on whether the fluid present was water or brine. Larger mass

losses were recorded with water, but this may have been a consequence of the larger incident sand kinetic energy. This is why it is necessary to remove this factor.

It is necessary to qualify the simple statement that observed mass loss should be proportional to *TISKE* for various reasons:

- The kinetic energy of the water is neglected. The basis for this is that solid, angular sand particles are able to apply pressure effectively over the small area tips incident on the target surface, whereas the fluid cannot. As will be seen below, this is not necessarily always a sound assumption.

- As noted by van Riemsdijk and Bitter [29], some of the kinetic energy loss will be associated with elastic rebound from the surface. This is expected to be small at low flow rates, and has been neglected here.

- Net mass losses are measured. Where solid corrosion products are present (as in some of these runs), mass loss will be underestimated. Small mass gains are sometimes encountered. No sound method has been found of cleanly removing the corrosion products encountered here; this effect therefore contributes to experimental error – an attempt will be made to estimate it.

- Flow corrosion may be present, as is certainly the case here for zinc targets.

Data for the various target materials, considered separately, have therefore been fitted to an equation of the form:

$$M_T = m\,(TISKE) + c \qquad (6.14)$$

Where the 'c' term is intended to allow for the various effects noted. Neglect of this term could lead to apparent velocity exponents > 2.

Figure 6.16 shows the same data as Figure 6.15, but this time coded by target material.

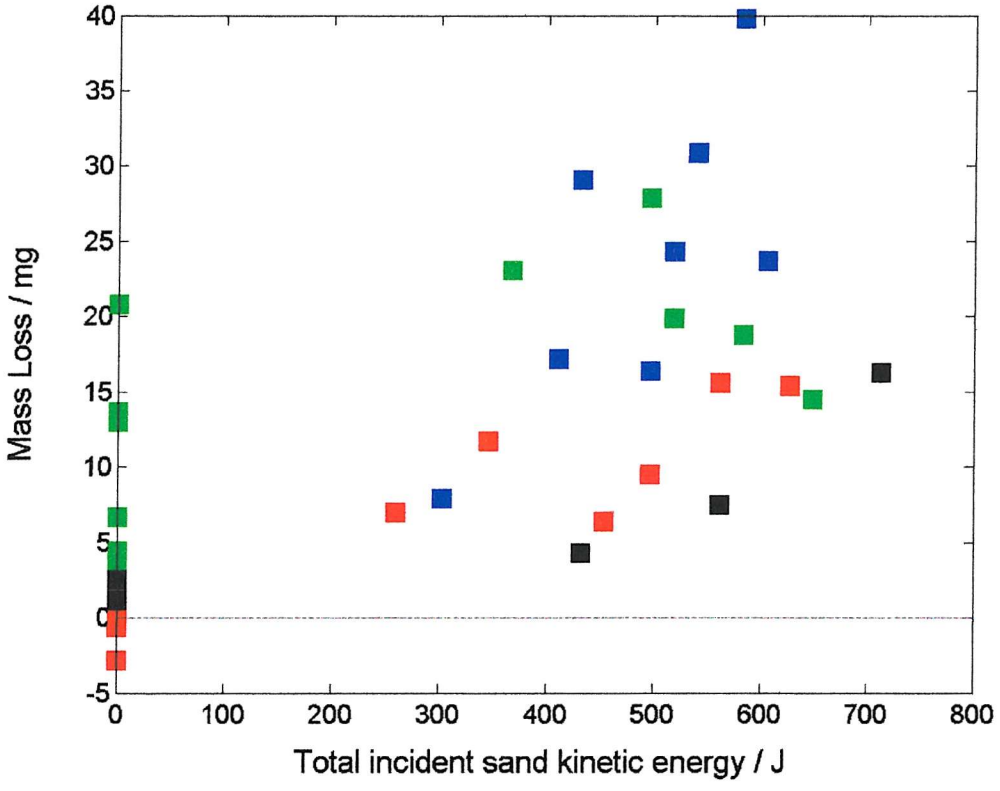

Figure 6.16

Mass Loss as a function of incident sand kinetic energy and target type

Target Solid Coding: Green = Zinc
Blue = Aluminium
Red = Al/12%Si
Black = AISI 1020 Steel

Firstly, concerning the data where no sand is present.

There are large mass losses associated with zinc in brine (and much smaller ones associated with zinc in water). This is evidently flow corrosion and will be considered further below.

Also, erosion of Al/12%Si alloy results in net weight *gains* in brine, but not in water. Reference to Table 6.2 shows that aluminium based targets in brine, but not in water showed pitting and white deposits; these features were more intense for the Al/12%Si alloy than for pure aluminium. This suggests that aluminium is being lost in each case, and redeposited as oxidised corrosion product species (n.b. this redeposition apparently does not occur when sand is present, presumably because of surface scouring by the sand). For aluminium these processes roughly balance and the result is no significant weight change. More intense pitting on the alloy surface, possibly associated with micro-galvanism, as found by Mayer-Rodenbeck [165] in mine waters, results in small net weight gains. These are never greater than 3 mg, and are usually much less.

Regression lines obtained through the data, taken by target materials separately, result in the following relations:

For zinc:	$M_T = 0.020\ (TISKE) + 9.5$	(6.15)
For aluminum:	$M_T = 0.050\ (TISKE) - 0.2$	(6.16)
For Al/12%Si:	$M_T = 0.024\ (TISKE) - 0.3$	(6.17)
For steel	$M_T = 0.016\ (TISKE) + 0.9$	(6.18)

The 'c' values are all small (< 1 mg), with the exception of that for zinc. This suggests that in the absence of flow corrosion, this adjustment can be neglected (though there are just traces of a possible effect due to pitting, leading to negative values of 'c' with insoluble corrosion products and positive value with soluble ones (steel) – much longer runs would be required to substantiate this).

The 'm' values represent the sensitivity of individual material surfaces to erosion intensity, as measured by kinetic energy input. Erosion resistance is often related to material hardness [5,10], so Figure 6.17 shows how this 'm' varies with the inverse of material Vickers Hardness, measured on a transverse section of the coating, as described in Section 3.

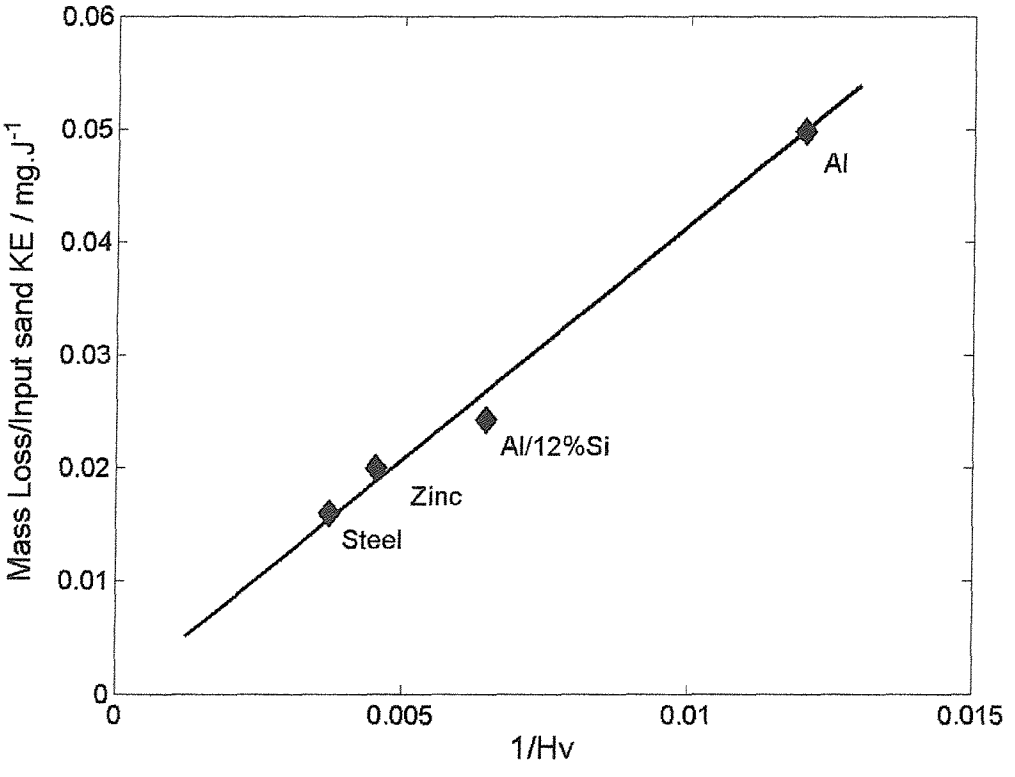

Figure 6.17

Relation between Mass Loss/Incident kinetic energy and inverse Vickers hardness.

Various points should be made about this relationship:

- The goodness of fit is very good, probably fortuitously so.

- The regression line passes close to the origin, as it should.

- That all the data lies on the same line in dictates that the same metal removal mechanism is dominant in each case (probably deformation into

lips and their subsequent fracture – see Section 6.3.2 – not splat removal, since the zinc and steel samples do not contain splats).

- That the zinc data lie on the line indicates that mass loss due to slurry erosion and mass loss due to flow corrosion occur independently.

The equation of the regression line is:

$$M_T/TISKE = 4.05/H_v + 0.0004 \qquad (6.19)$$

Or, neglecting small constants, for a particular material for which this model holds:

$$M_T = 4.05 \times (TISKE/H_v) \qquad (6.20)$$

Which is very simple! However, it neglects the averaging involved in obtaining the relationship. Attention is therefore next given to the residuals in the data, i.e. the differences between actual measured weight losses and those estimated by means of the above equation. Since these behave differently for the different materials, the materials will be considered separately.

Aluminium and Al/12%Si alloy residuals

Figure 6.18 shows the residuals for aluminium and aluminium/12%silicon alloy, plotted against fluid codes, as shown and further coded by material and by impact angle. Data for the alloy have been offset slightly for clarity. Since these data are residuals, they average to zero, and the quantity of interest is the dispersion around this value. In order to aid interpretation, horizontal lines have been inserted at ± 2.5 mg; this figure is essentially arbitrary, but is of the order of the data precision after this degree of manipulation (some more will be said about precision under 'Synergy', below).

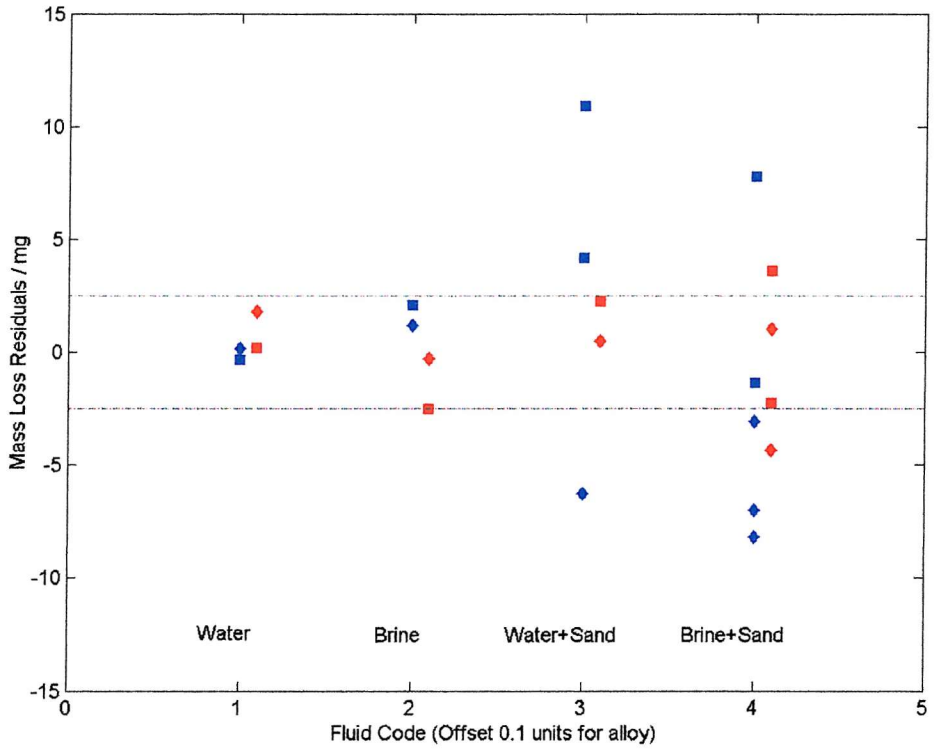

Figure 6.18

Relation of mass loss residuals to fluid, target and impact angle variables for aluminium and Al/12%Si.

Codings: 1 = Water only Blue = Aluminium ■ = 90^0 impact.

2 = Brine only Red = Al/12%Si ◆ = 30^0 impact.

3 = Water+Sand

4 = Brine+Sand

This figure shows that, for these materials:

- The presence of sand causes much more dispersion in mass loss than does that of NaCl in the solution (though note that mass loss does not necessarily relate to penetration – localised pitting corrosion may lead to much deeper penetration than erosion over an area).

- The dispersion in mass loss due to sand erosion is related to impact angle. Erosion at 90^0 leads to substantially greater mass loss than does erosion at 30^0. Note that this is the opposite angle dependency to that found by most other workers in more dilute slurries [15], but is similar to that found for the erosion corrosion of bulk aluminium by coarse (750 μm) silica sand by Li *et al* [147]. Hearley *et al* [44] have also found this dependence in gas-blast erosion of HVOF NiAl coatings. In sufficiently dilute slurries actual local impact angles may bear some relation to nominal impact angles, though even this has been disputed by Clark [21]. In more concentrated slurries (see Oka [27] for what is meant here by 'concentrated'), as used in the present work, it seems likely that inter-particle momentum transfer will ensure that most impacts will actually occur at very grazing impacts. It is supposed (but not here demonstrated – work at a much larger range of impact angles would be required) that the effect found is related to the efficiency with which the sand incident kinetic energy is coupled to the targets solid surface, *via* the component of sand momentum normal to the surface. The relationship is not, however, a direct one, since mass losses are not directly proportional to the size of this component. This is shown by Table 6.5 in which actual mass losses (not residuals) are compared. Only data in horizontal rows should be compared – even this is not ideal since there is still some kinetic energy effect. The numbers in the 'Ratio' column should be 0.5 (= $\sin 30^0/\sin 90^0$) if a direct relation holds; this is evidently not the case – moreover the ratios are clearly material dependent. This angle effect could usefully be investigated further.

- It is evident that the aluminium/12% silicon alloy is much less angle sensitive than is pure aluminium.

- Given the dominance of erosion over corrosion in these materials, it is satisfying to find that the mass loss dependencies on materials and impact angles correspond with those found under pure erosion conditions.

Erodent Fluid	Target Material	Mass Loss / mg		Ratio
		30^0 impact	90^0 impact	
Water+Sand	Aluminum	23.7	30.9	0.77
	Al/12%Si	15.4	15.6	0.99
Brine+Sand	Aluminium	13.8	26.7	0.52
	Al/12%Si	6.7	10.6	0.63

Table 6.5: Mass losses related to nominal impact angle.

Steel residuals

Owing to shortage of material, steel samples were only eroded at 30^0 impact angle. Little residual data was obtained, with variation between samples comparable with measurement precision. Its analysis is therefore not very useful

Zinc Residuals

Figure 6.19 shows mass loss residuals for zinc in the same format as Figure 6.17 for aluminium and Al/12%Si alloy. The form of this plot is, however, quite different. In this case mass loss is clearly more strongly influenced by corrosion than by erosion. However, it remains the case that (with the possible exception of 'water only' data, where mass losses are small anyway) mass losses at 90^0 are greater than those at 30^0.

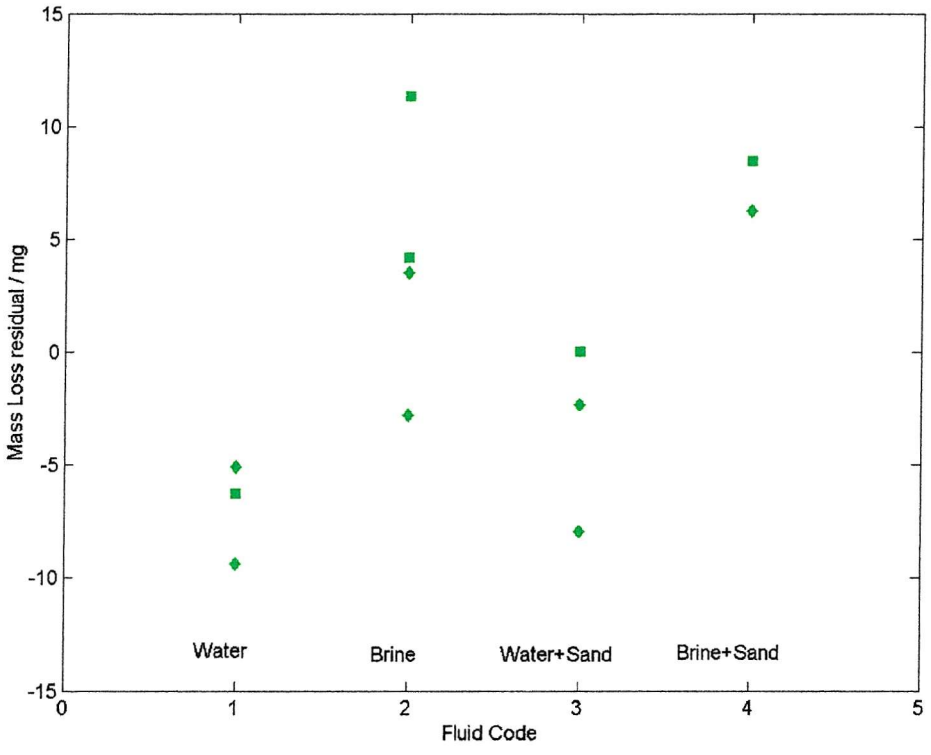

Figure 6.19

Relation of mass loss residuals to fluid, target and impact angle variables for zinc.

Codings: 1 = Water only
2 = Brine only
3 = Water+Sand
4 = Brine+Sand

Green = zinc

■ = 90^0 impact.
◆ = 30^0 impact.

Zinc Flow Corrosion (sand absent)

Zinc is the only one of the materials involved in this work for which flow corrosion is a significant issue. For comparison, a zinc coated sample immersed in brine in a static cell (as used in Section 5) lost 0.8 mg in 6 hours – very much less than under flow conditions. An attempt has been made to gain some further understanding of this by plotting mass losses against flow velocity squared (as a proxy for solution

kinetic energy) for those zinc samples where no sand was present in the erodent stream. This is shown in figure 6.20

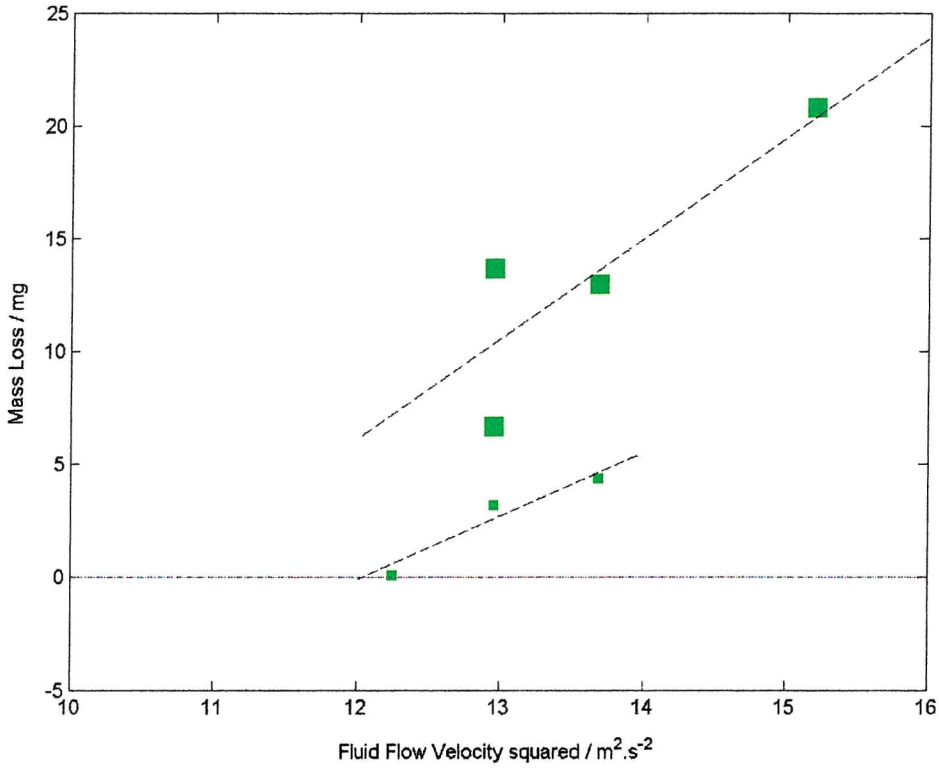

Figure 6.20: Zinc mass losses, related to flow and solution.

Codings: Green = zinc ■ = Brine only

■ = Water only

This plot is made over a limited amount of data and a narrow range of flow conditions. Moreover, flow corrosion seems to be rather variable. However, it is clear from the plot that flow corrosion is strongly promoted by the presence of NaCl in the solution. There also appear to be trends in the variation in mass loss with flow rate (as indicated by the dashed lines), with mass loss in brine being more sensitive to flow than mass loss in water. It is noticeable that, if these trends are real, there is an implication that flow corrosion is unimportant below a cut-off flow rate, around 3 $m.s^{-1}$. It is fortuitous that this happens to be close to the flow rate used here.

This behaviour is entirely consistent with the classical work of Bengough and May [137] (there does not appear to have been any more recent investigation of this phenomenon (!), although some of the work was repeated by LaQue [139,140] in real seawater, with similar results). Bengough and May attribute the non-sensitivity to flow rate at low flow rates in NaCl solutions (< 2 $m.s^{-1}$), to the presence of an adherent oxide film. This flow rate is said to be sensitive to the carbon dioxide level of the solution, carbonate containing films being more easily removed than oxide films. At higher flow rates the flow is sufficient to remove the protective layer and rapid corrosion can occur, the rate increasing with increased oxygen supply. An implication of this is that if a jet is incident on a small area of target the corrosion should be restricted to quite a small area. If the resulting scar is irregular in form, perhaps due to inhomogeneity in the target (the hot-dipped zinc coating in this case), then hydrodynamic effects will result in irregular scars and variable weight losses, as found.

There is a practical implication in this substantial sensitivity to flow corrosion. It is usual to use impressed current cathodic protection for large ships for protection against seawater corrosion, but to use sacrificial zinc anodes for small vessels on grounds of greater economy. The 'zinc' used is an alloy, but very close to pure zinc (~ 0.5 % aluminium, trace cadmium, balance zinc [136]). This distinction, based on vessel size, with the implication that small boats are slow boats, may have been appropriate in 1924 when the Bengough and May work was carried out, but is surely not appropriate today. The limiting speed above which flow corrosion becomes significant is about 3 $m.s^{-1}$, equivalent to about 5.5 knots, which for modern small craft is a very modest speed. It may be that most of the losses on zinc anodes on small craft nowadays result from flow corrosion, rather than their intended anodic protection function. It would be interesting to extend this work using the proper zinc anode alloy to see whether this is the case.

Synergy

There has been considerable interest in the literature (see Section 2.3.5) in the interactions between erosion and corrosion, and their consequences for mass loss, described as 'synergy'. As noted in the Literature Review, there are various different definitions [51,67,68,69]. However, the main problem with 'synergy', by whatever definition, lies in measuring it precisely. This suggests that over-analysing the data is likely to be a problem. Nonetheless, an attempt will be made (slightly unconventionally) to illustrate a particular point.

The areas where difficulties arise are the following:

- Deposition of solid corrosion products. This results in measured mass losses being only *net* mass losses and there may even be mass gains. Unless this effect can be cleanly separated and measured, an error will result in the estimated 'synergy' figure. ASTM [51] recommend that in the presence of deposited solids, no synergy calculation should be attempted. In the present case, deposition of solids seems largely limited to 'Brine only' conditions and results in net gains of 3 mg or less in this case. With this in mind, an attempted calculation will be made.

- ASTM recommends that 'erosion only' conditions be simulated by suppressing the anodic reaction using cathodic protection (1.0 V cathodic of the metal OCP). There are two problems with this:

    - 1.0 V cathodic protection is very large (commercial usage is generally closer to 0.25 V), and likely to induce unwanted cathodic effects, particularly related to hydrogen injection. As has been shown by Naerheim and Kendig [50], the freedom of cathodically protected systems from mass changes should be demonstrated case by case. In the present work, 'erosion only' conditions have been measured using.

'water+sand' (no brine) conditions, rather than by using cathodic protection.

- In any case, it is not clear in a multi-metal system to what potential this protection should be applied – whether to the OCP of the undamaged coating or (as would be normal commercial practice) to the OCP of the substrate – these OCPs may be several hundred millivolts apart.

- It is important that the various measurements used to input data into the synergy calculation be made under strictly comparable conditions. Otherwise, variation between runs may be greater than the synergy effect it is desired to measure. As has been seen above, this condition has not been met in the present work, so the raw data cannot be used for this calculation. An attempt is made to calculate a form of 'synergy' ('Mass loss Synergy' – *Syn-M*) using 'residuals' instead:

  Following Wood [59]:

  $$M_S = M_T' - M_E' - M_C' \qquad (6.21)$$

  Or, in terms of the present work:

  $$Syn-M = \left(M_{B+S}' - M_W'\right) - \left(M_{W+S}' - M_W'\right) - \left(M_B' - M_W'\right) \qquad (6.22)$$

  Where: M_{B+S}, M_{W+S}, M_B, M_W are mass losses in the various fluids, and ' denotes a residual.

- Weighing errors. Equation 6.13 involves 6 pairs of weighings, each, at best, to ± 0.2 mg weighing precision. So, since errors add when quantities are combined by addition or subtraction, equation 6.13 implies that the uncertainty in *Syn-M* is at least several milligrams (not counting any

effects due to solid deposition). So any *Syn-M* values derived here will be of qualitative interest only.

With the above considerations in mind, 'synergy' values have been calculated for each material (except steel), separated by nominal impact angle. These calculations are shown in Table 6.6, with the 'synergy' values (mg) in the bottom row, reduced to single figure precision, since the data will not bear any more.

	Zinc		Aluminium		Al/12%Si	
	90^0	30^0	90^0	30^0	90^0	30^0
M_{W+S}'	0.1	-5.1	7.6	-6.2	2.3	0.5
M_W'	-6.3	-7.2	-0.3	0.2	0.2	1.8
M_B'	7.8	0.4	2.1	1.2	-2.5	-0.3
M_{B+S}'	8.5	6.3	3.3	-6.1	0.4	-1.7
Syn-M	**-6**	**-4**	**-7**	**-1**	**1**	**0**

Table 6.6: Calculation of Mass Loss Synergy / mg.

For the aluminium/12%silicon alloy, the *Syn-M* values are too small to be meaningful. In the other two cases, there is quite a strong angle dependence, with marked *negative* synergy at normal incidence and either no or slightly positive synergy at oblique incidence. It is thought that this effect of nominal impact angle on synergy has not been noticed before.

In the case of HVOF aluminium the most likely cause of negative synergy is the sealing of surface intersecting porosity by ductile flow of the metal under impact, and there is microscopic evidence for this (see Section 6.3.2). Obviously this will not

work for hot-dipped zinc; the data suggest that in this case the main effect is related to flow corrosion in brine, but the situation is too complex to fully resolve with the data available.

Mass Loss Conclusions/Further work

Zinc suffers severely from flow corrosion, other targets do not. A better understanding of this would be useful, particularly with respect to the alloy used to make sacrificial anodes.

All target materials under sand erosion lose mass in a way directly related to sand kinetic energy, and inversely related to hardness.

Corrosion losses are relatively small; solid products sometimes result in net weight gains.

There are greater mass losses at nominally normal incidence than at nominally oblique incidence, due to particle interference effects.

Synergy is difficult to determine precisely, but, as defined here, appears to be angle dependent.

This work requires extension of to more realistic metal coating systems.

6.3.4 Electrochemical Noise data

Introduction

The main part of the electrochemical work reported in this Thesis concerns an investigation of the possibility of using Electrochemical Noise techniques to remotely characterise erosion-corrosion behaviour on HVOF sprayed metallic coatings.

To do this, it has been necessary first to establish stable erosion-corrosion conditions, with appropriate electrochemical monitoring. As described in previous Sections, noise measurements have been made under potentiostatted conditions, resulting in current noise data only. Then, it is necessary to establish what part(s) of the signal contain meaningful information, and what parts are general background noise, so far as this can be done. Then it is desired to associate particular components of the signal with particular aspects of the erosion-corrosion behaviour, and, if possible, mass loss.

In this context, it is important to note that there may be a variety of modes of coating failure. Some or all of the following may be present, along with background noise:

Erosion, leading to electrochemical activity via the creation and repassivation of fresh surface, via:

- Platelet formation and fracture.
- Cutting/Ploughing processes.
- Splat removal.
- Local boiling, resulting in cavitation.

Corrosion, via:

- General corrosion.
- Flow corrosion.

- Pitting, related or otherwise to pre-existing porosity.
- Cracking, especiallyof lips.
- Coating disbondment.
- Galvanic effects between the coating and the substrate, resulting from coating porosity, coating disbondment or coating removal by erosion.
- Hydrogen effects.

Electrochemical behaviour may also be modified by the presence of corrosion product on the sample surface or within the coating porosity.

Note that material may be removed as ions (electrochemically active, faradaic equivalence), as eroded oxide (electrochemically active, but with a time lag) or as metal fragments (not themselves electrochemically active, though the scar left may depassivate/repassivate). Different modes of failure may induce electrochemistry with different efficiencies.

Furthermore, as observed in Section 6.2.2, the targets are inhomogeneous. Different processes may occur on different parts of a target. Internal shorting may occur within a target, resulting in no current in the external circuit or capacative effects may result in phase delays [157]. What is measured is an aggregate of all the separate effects.

Any or all of the effects present may lead to Electrochemical Noise activity. To the extent that more than one of these possible causes of electrochemical activity may be present, more than one feature may be present in the Electrochemical Noise signal. These features may or may not be separable mathematically; in general, if the signal characteristics of two features coincide in both the time and frequency domains, no amount of mathematical processing will separate them. This is a fundamental limitation of the method. In other cases, features may be readily separable, e.g. by frequency, or more sophisticated methods may be required.

General characteristics of the Electrochemical Noise signal

As a preliminary example, Figure 6.21 shows the Electrochemical Noise response obtained at a sampling rate of $100.s^{-1}$ from the erosion-corrosion at 30^0 incidence of hot-dipped zinc coated steel by brine, with addition of sand for part of the time.

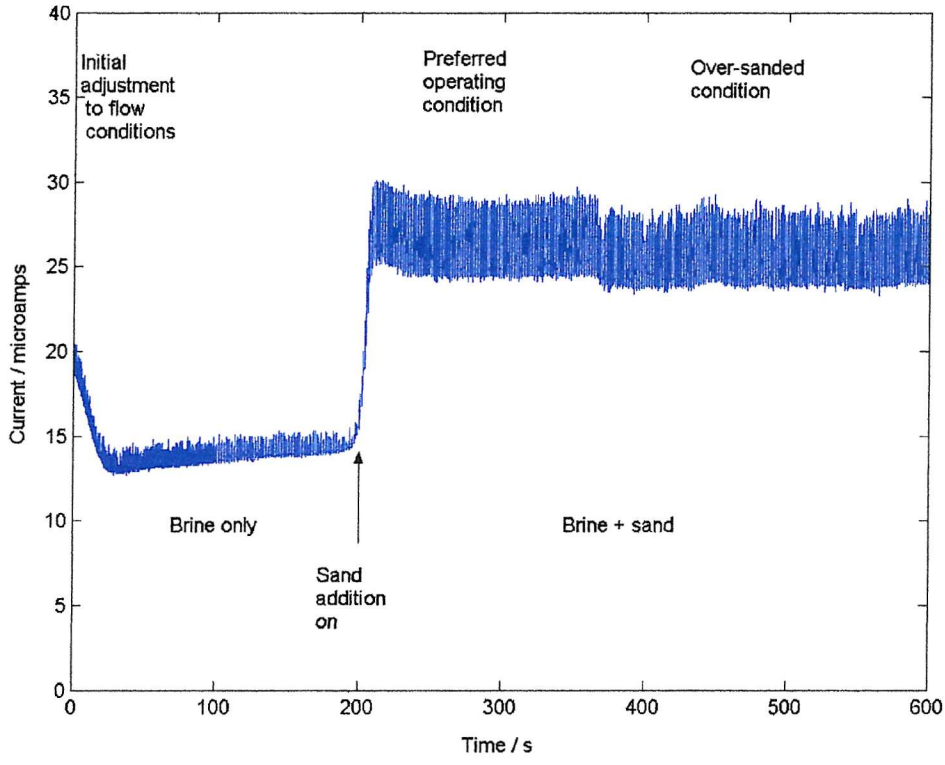

Figure 6.21: Illustrative Electrochemical Noise trace.
Hot-dipped zinc on steel target. 30^0 impact.
Brine, Brine + sand as erodents.
Not detrended.

This figure shows the following features:

- The vertical scale (cell current) is determined by the overall impedance of the system. Since in this case the cell impedance is dominated by the solution resistance (determined by Electrochemical Impedance Spectroscopy to be ~ 2000-3000 Ω in brine, and too large to measure

reliably in water) the overall size of the current is not informative. Neither does the data contain any useful phase information, for the same reason. What is significant is the shape of the plot and parameters which describe this.

- After significant changes to the operating conditions, the system takes an appreciable time to re-equilibrate – typically of the order of 50 s. As a result, in 'real' tests, conditions have been kept as far as possible constant throughout runs. The first part of the recorded data has been omitted from any quantitative analysis in order to minimise any switching effects that may exist; only the last 200 s of 600 s measurements have been used for analysis purposes.

- Apart from these transition periods, the data is much more stationary on a 600 s timescale (that is, statistically uniform across successive time periods) than was observed under static conditions (Section 5).

- In this particular case, under the conditions initially used (brine 'only', i.e. the sand riser was left in the sand reservoir, but with the 'T' valve at the bottom of the riser fully open, leading to 'very small' sand flows, 3.5 $m.s^{-1}$, 30^0 impact, potentiostatted to zinc OCP: -0.950 V *vs* Ag/AgCl under these conditions), the observed current rises uniformly from about 13 μA to 14 μA during the time observed. This current is quite noisy (see further below). This current may arise from at least three sources; on the basis of this experiment alone, it is not possible to distinguish them:

  - A galvanic current, flowing to the counter electrode, resulting from non-perfect estimation of OCP. This is expected to be small if the experiment is properly controlled, but cannot be separately estimated.

  - A small contribution from any residual sand in the flow.

- A contribution from flow corrosion; this is thought to be the major contributor in this case.

- At approximately 200 s, the 'T' valve was partially closed, leading to a uniform sand flow up the riser. These are the 'T' valve settings used in 'real' tests involving sand; they have proved to be very critical. The sand flow was not measured on this occasion, but was assessed visually as being comparable to that used in 'real' tests, i.e. about 0.003 $kg.s^{-1}$. The current stabilised at a substantially higher and noisier level – about 27 μA. The higher current level and its noisier nature (see below) are both thought to be associated with particle impact.

- At approximately 370 s, the 'T' valve was closed almost completely. This might have been expected to increase the sand flow further, but, as explained in Section 6.2.2, the actual effect was to introduce oscillations in the riser and a net reduction in sand flow. Mean current fell slightly – to about 26 μA, while the noisiness remained about the same.

Figure 6.22 shows a detail of the type of noise signal obtained under these conditions (this is a 20 s sequence from the 'brine only' section). The sequence consists of a series of very narrow (short time) transients, basically of one sign only, superimposed on a relatively low level of background noise. The transients are sharp, roughly symmetrical, of variable amplitude and width and appear to occur randomly in time. The signal obtained under 'brine + sand' conditions is qualitatively very similar, except that the transients are larger, overlapping and symmetrical with regard to sign. The detailed behaviour of these transients will be considered in subsequent sections, using data obtained under better controlled conditions.

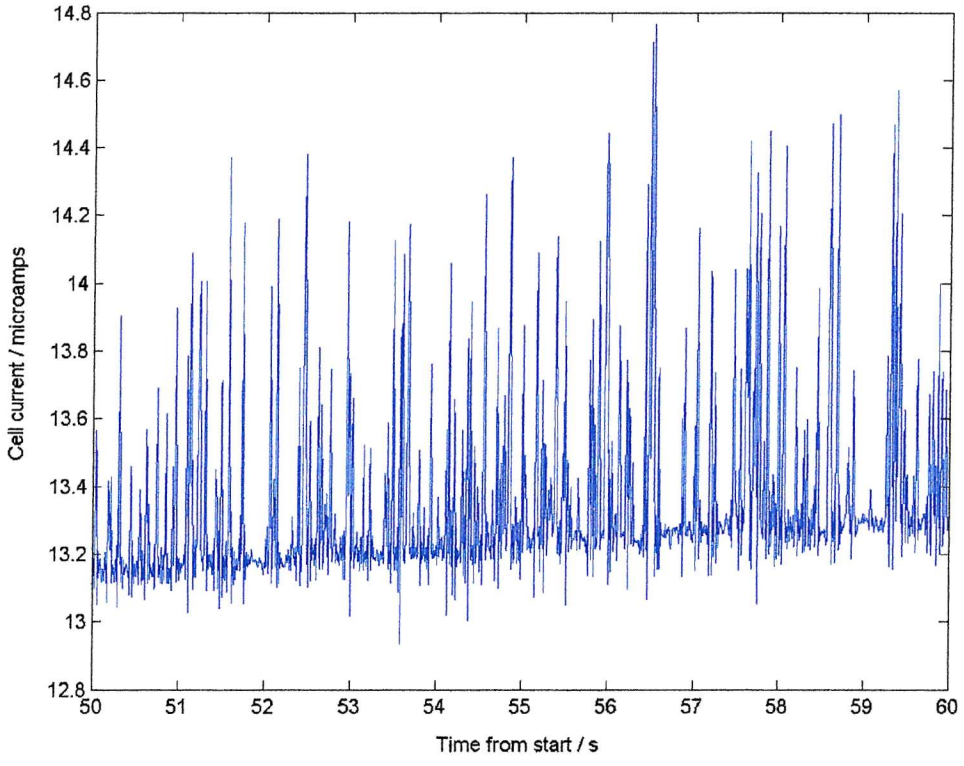

Figure 6.22: Detail of Electrochemical Noise signal.
Hot-dipped zinc on steel target, 30^0 impact, 'brine only'.
Not detrended.

A simple transient model

Before considering real trial data it has been found helpful to see how the statistical properties of some artificial pulse trains behave. Functions available in the MATLAB Signal Processing Toolbox have been used for this. A synthetic pulse train was generated, using symmetrical positive triangular pulses of uniform size, regularly spaced, superimposed upon random background noise. The pulse train was generated from the statements:

```
rand['state',0];
i = h*pulstran[t_p,d,'tripuls',w] + a_n*randn[size[t_p]]
```

where **i** = the generated current function (μA)

	w = pulse width (s)	Typically	= 0.04 s
	h = pulse height (μA)		= 1 μA
	$\mathbf{a}_n$ = noise amplitude (μA)		= 0.05 μA
	d = pulse delay (s)		= Variable.
Also	t_p = length of synthetic pulse train (s)		= 10 s
	fs = Sampling frequency (s^{-1})		= 100 s^{-1}
	fp = Pulse repetition frequency (s^{-1})		= Variable

Statistical and other functions were derived from these pulse trains.

The main findings from this exercise were:

Regularities in the synthetic data lead to large artefacts in power spectral density and probability density function plots, which are therefore not very useful. Conversely, the absence of such artefacts in real data confirms that transient frequencies are essentially random. Modelling randomly occurring transients would be much more complicated and has not been attempted.

Detrending the data does not alter the statistical parameters, other than the mean (this follows from the definitions of the higher statistical functions).

Varying **h** alters mean and standard deviation, but not skewness or kurtosis.

Mean **i** increases linearly with **fp**, as expected. Mean **i** would be a good parameter to use to analyse data, were it not for the fact that in real data it inevitably contains other current components, e.g. from galvanic effects.

i variance increases with **fp**, till **fp** $\approx 1/\mathbf{w}$, then decreases again as the transients become progressively more overlapped.

i skewness decreases steadily with **fp**. For large values of **fp**, the data is very nearly symmetrical. Negative values of skewness are not seen in this model (all the transients put in are positive).

i kurtosis is only large (>>3.0) for well separated transients, i.e. **fp** $< 0.4 \times$ 1/**w**. A minimum value of approximately 2.0 is found when **fp** $\approx$ 1/**w**. At higher values of **fp** kurtosis rise again, but remains below 3.0. So large values of kurtosis only occur when transient events are well separated (as well as being individually 'sharp'). Another way of putting this is to note that processes which broaden transients to the point where they overlap will lead to reductions in kurtosis.

A combination of textbook information [190] and modelling provides the following background:

> A normal distribution has a kurtosis of 3.0
> (this is often used as a standard for comparison for a single peak).
>
> The minimum possible value of kurtosis is 1.0, and is provided by a random variable, which takes only two values with equal probability.
>
> A detrended square wave also takes this value: 1.0.
>
> A sine wave has a kurtosis of 1.5.
>
> A uniform distribution, i.e. a uniform current, not detrended, has a kurtosis of 1.8.

To anticipate consideration of real data, it is found that kurtosis ranges are found to be:

In water:	≤ 3.0
In brine:	≤ 3.0
In water + sand:	4 - 12
In brine + sand:	2 - 9

This implies that (at least some) electrochemistry related to erosion takes place as large, well separated events, whereas background noise and noise related to corrosion occur as more overlapping changes. At first sight the kurtosis values obtained for 'brine + sand' suggest that to a considerable extent the electrochemical situation is the sum of '+ brine' and '+ sand'. The overall signal components may be separable by suitable mathematical manipulation. It will be proposed below that the actual situation is more complicated than this (it is not additive), and involves transient broadening.

In the following a starting assumption will be that electrochemical noise signals have three components – a large amplitude low frequency component associated with (pitting) corrosion [84,85,105], a fairly large amplitude high frequency component associated with erosion [37], and background noise from non-electrochemical sources. Of course, as explained above, there may well be more than this number of modes of metal removal, so this is just a first approximation.

Treatment of Experimental Data

The Electrochemical Noise data from the experimental program is very extensive (almost 500 data sets in total). Analysis of this will be carried out on the following basis with increasing levels of explanation:

- Comparison of representative data sets at one time (aluminium, 90^0 impact, 3.5 hours from start of run, sampled at $100.s^{-1}$, various eroding fluids), to show the main features of the data.
- Time trends.

- Time trace statistics.
- Power Spectral Density.
- Wavelet decomposition.

Representative data

In order to show the main features of the data, a comparison of 4 representative data sets (aluminium, 90^0 impact, 3.5 hours from start of run, sampled at $100.s^{-1}$, various eroding fluids) has been made. (The run numbers correspond to those in Table 6.2, suffix H indicates measurement 3.5 hours from start sampled at $100.s^{-1}$).

Figure 6.23 shows time traces for four erodents.

In the 'water only' case (Run 12H), a featureless signal of very small amplitude is obtained.

When sand is added to this (Run 4H), a similar signal is obtained with superimposed on it a continuous series of very short timescale transients, all of one sign.

In 'brine only' (Run21H), a noisy signal with a slowly varying baseline is obtained.

'Brine + sand' (Run 29H) looks qualitatively rather like 'brine only', but the current magnitude is much larger. This run also shows signs of a current oscillation at about 0.3 Hz; this is an experimental artefact, which appeared at noise currents > 1 μA, and has complicated subsequent analysis.

Superimposed on these traces are the mass loss and noise current values for these runs ('noise current' is used here and hereafter to mean the standard deviation of the current noise trace). The first conclusion is that there is no correlation between mass loss and current noise. Secondly there is a much larger spread of values for current

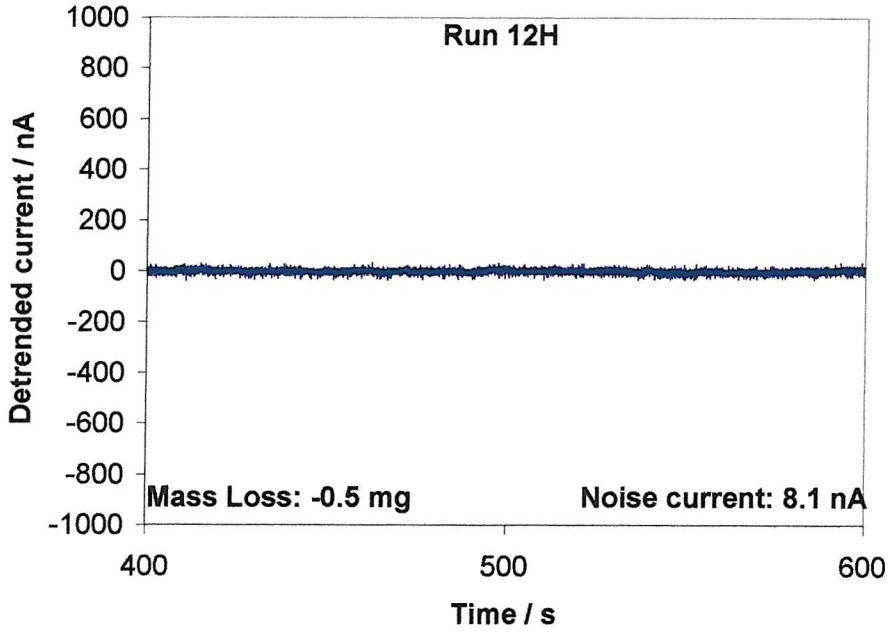

Figure 6.23a: Aluminum/Water only

Normal incidence/3.5 hours/100.s^{-1}

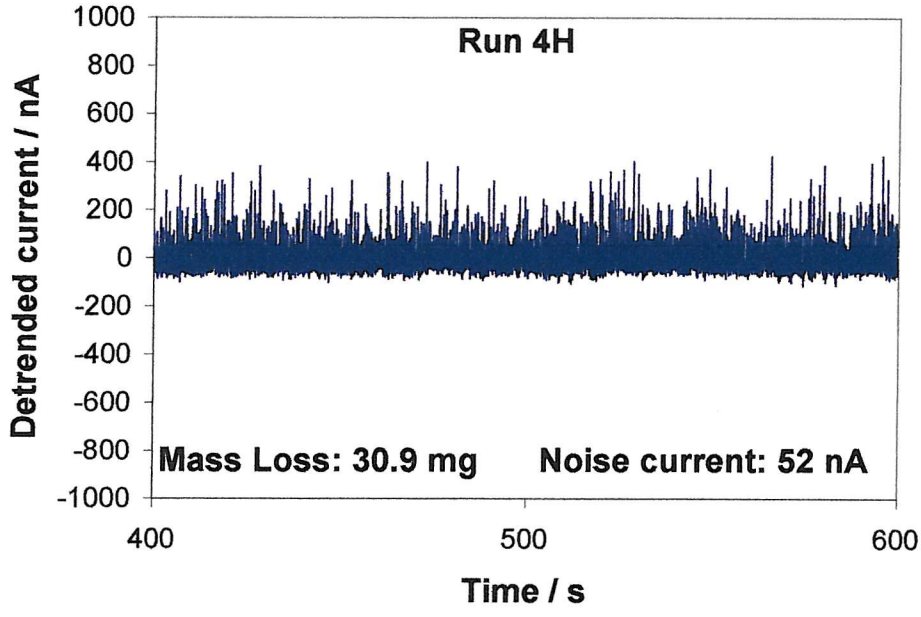

Figure 6.23b: Aluminum/Water + sand

Normal incidence/3.5 hours/100.s^{-1}

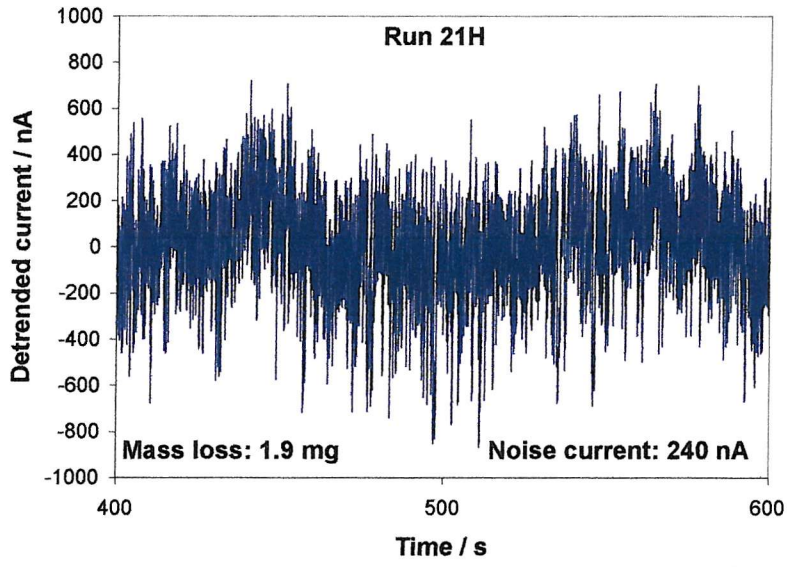

Figure 6.23c: Aluminum/Brine only

Normal incidence/3.5 hours/100.s^{-1}

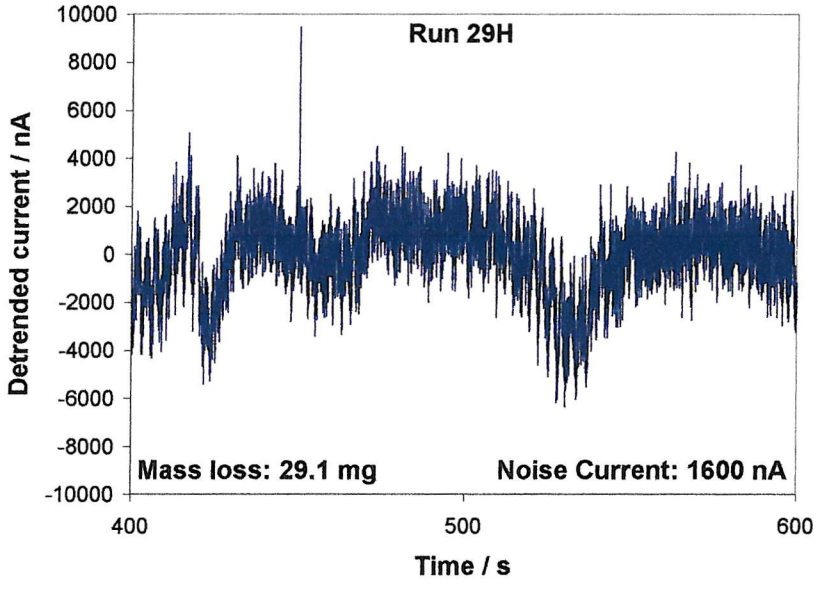

Figure 6.23d: Aluminum/Brine + sand

Normal incidence/3.5 hours/100.s^{-1}

Note difference in vertical scale from other Runs.

Run	Time / hours	Sampling Frequency / s^{-1}	OCP / V vs Ag/AgCl	Current Noise / nA	Skewness	Kurtosis	R_N / Ω
A	0.1	20	-0.753	330	+0.4	3.1	31
B	0.5	100	-0.753	230	-0.2	3.0	44
C	1.1	20	-0.753	172	-0.3	3.2	52
D	1.5	100	-0.753	190	-0.2	2.9	71
E	2.1	20	-0.753	180	-0,2	3.0	42
F	2.5	100	-0.753	210	-0.2	2.9	56
G	3.1	20	-0.754	219	-0.3	2.9	45
H	3.5	100	-0.754	236	-0.3	3.1	55
I	4.1	20	-0.754	240	-0.4	3.1	44
J	4.5	100	-0.754	235	-0.4	3.4	51
K	5.1	20	-0.754	240	-0.5	3.7	31
L	5.5	100	-0.754	250	-0.6	3.5	52

Table 6.7: Statistical data for Run 21.

Aluminium/Brine only/Normal incidence

noise than for mass loss; in particular, the current noise when both sand and brine are present is greatly increased relative to the situation where either factor is present separately - this is not true for mass loss. One way to express this is to say that there is much more 'electrochemical synergy' than there is 'mass loss synergy'. Of this, more below.

Time Trends

As an example, Table 6.7 shows statistical parameters derived for Run 29 over the whole 6 hours of the experimental period. Pairs of Electrochemical Noise measurements were made (at $20.s^{-1}$ and $100.s^{-1}$ sampling rates, 600 s sampling period, final 200 s analysed) at hourly intervals; the members of each pair were made at the same controlled potential. The main point to note about this table is that after the first hour's running the figures do not change rapidly. This is found generally to be true, with the exception of zinc samples (to be considered further later).

During the first hour there is often an anomalously high level of electrochemical activity – this may be related to the removal of residual asperities, or to film formation/modification – after which variance (power) data become approximately constant. Very short period erosion-corrosion tests would be misleading.

As a result, it has been felt justified to consider a run taken from the middle of each experiment (Run H: 3.5 hours from start) as typical, except where there are special features.

Statistical data

The simplest means of comparing the 4 representative data sets chosen is to compare the statistics of the time traces.

The OCP values for these aluminium samples (at 3.5 hours *vs* Ag/AgCl) are significant:

Water only:	-0.555 V	
Water + sand:	-1.139 V	
Brine only:	-0.754 V	(Static: -0.722 V)
Brine + sand:	-0.838 V	

The range of these values is more than 0.5 V, which is large compared with the galvanic potentials in the system and implies that the behaviour of the aluminium/steel system will be very sensitive to environmental conditions. The flow system used for these experiments incorporated a liquid-in-air jet, which imposed very oxidising conditions on the target. It would be expected in these circumstances that in the absence of disruption a stable oxide film would grow on aluminium, and that a disrupted film would repassivate rapidly [45]. The OCP figures are consistent with this, with both impact and the presence of salt leading to more negative (more active) potentials. It is of interest that impact (only) results in a considerably larger potential shift than does salt (only) under these conditions, and that the combined effect of impact and salt is intermediate. This last finding is difficult to understand, but possibly particle impact disrupts the salt crust that exists over stable pits and stabilises their growth [44].

For the case where a direct comparison can be made (brine only), at first sight there is only a small difference in OCP between static and flow conditions. However, while the OCP under flow conditions remained constant (-0.754 V) to within a few mV over 6 hours, under static conditions the OCP drifted from –0.713 V to –0.969 V over a similar period; this is attributed to oxygen being consumed from the vicinity of the metal surface under these conditions.

Two deductions may be made from these observations:

- OCP by itself is not a useful guide to mass loss.

- Control of oxygen levels in future experiments would be desirable; this might most easily be done by employing a submerged jet, similar to that of Oltra *et al* [37].

Commonly used measures [70] of the intensity of Electrochemical Noise are Noise current (the standard deviation of the current signal), or Noise power (the variance of the current signal). A related and also widely quoted quantity is the Noise Resistance (the ratio of the voltage noise standard deviation to the current noise standard deviation; under potentiostatted conditions, this is proportional to the inverse of the noise current). If the $20.s^{-1}$, $100.s^{-1}$ pairs in the table are compared, it is found that the $100.s^{-1}$ data and the $20.s^{-1}$ data differ in magnitude. Usually, the $100.s^{-1}$ currents are larger than those measured at $20.s^{-1}$ and conversely for R_N, showing that these parameters are bandwidth dependent, as explained in Section 5.2.3. This is not always recognised, though the 'frequency dependence' of R_N has been pointed out by Xiao and Mansfeld [99]. It is therefore essential always to specify the data acquisition period and sampling frequency when quoting such data. Another problem with R_N is that it compares current and noise data without making any allowance for such phase differences as may exist.

It is found that if noise current values for the 'brine only' case are compared with the corresponding values for the 'water only' case, consistent ratios are obtained:

For aluminium, Al/12%Si alloy: $\sigma(i_{B+S})/\sigma(i_{W+S}) = \sim 25\text{-}30.$

For zinc, AISI 1020 steel: $\sigma(i_{B+S})/\sigma(i_{W+S}) = \sim 10\text{-}15.$

This difference reflects the greater susceptibility of aluminium (alloys) than the other materials to pitting [154] (though the absolute values of the ratio also contain a contribution from the difference in cell impedance resulting from the greater conductivity of brine).

As noted above, there are large differences in noise current between measurements made with different erodents. It is possible to define an 'electrochemical synergy', analogous to that used for mass loss (but not allowing for mass flow in this case, since, as found by Legat [56], there seems to be no large influence), but based on noise current values, i.e

$$Syn\text{-}E = (\sigma(i_{B+S}) - \sigma(i_W)) - (\sigma(i_{W+S}) - \sigma(i_W)) - (\sigma(i_B) - \sigma(i_W)) \quad (6.23)$$

Use of noise current $(\sigma(i))$ is more appropriate than noise 'power' $(\sigma^2(i))$ in this case, since if the electrochemistry is Faradaic, *Syn-M* and *Syn-E* should correspond.

If synergy is expressed as percentages of 'brine + sand' data, i.e.

$$'Synergy\ \%' = Syn\text{-}E / \sigma(i_{B+S}) \quad (6.24)$$

and similarly for mass loss data, this results in Table 6.8.

Synergy %	Zinc		Aluminium		Al/12%Si	
	90^0	30^0	90^0	30^0	90^0	30^0
Mass loss	-22	17	-26	-7	9	0
Electrochemical	37	70	89	94	92	83

Table 6.8: Comparison of Mass loss and Electrochemical Synergies.

The magnitudes of mass loss data do not in general relate to noise current. Nor is there any relation between the two kinds of 'synergy' data. This seems to arise because the noise current is dominated by a low frequency process (pitting), which

does not contribute greatly to the overall mass loss, whereas mass loss by erosion is not Faradaic. More sophisticated data manipulation is required to take this further.

Skewness and Kurtosis values are not very precise and need to be treated with care. For skewness precision is estimated as $\sqrt{(6/N)}$, i.e. 0.02 for a 20000 point data set, and for kurtosis $\sqrt{(24/N)}$, i.e. 0.03 likewise [70].

Skewness values are generally small and of variable sign; they contain no useful information. The exception to this is the 'water + sand' case, where skewnesses are large; they tend to increase slowly with time. An unexpected feature is that at normal incidence, skewness is positive; at oblique incidence, skewness is negative. The reason for this is unknown, but, as suggested by Dawson *et al*, may relate to the relative sizes and potentials of the scar and its surrounding area [55].

Similarly, in the absence of sand, kurtosis values are consistently close to being Gaussian (= 3.0). Much larger values are found in the 'water + sand' case, and there is some indication of similar behaviour in the 'brine + sand' case, though here the situation is confused by the low frequency 'brine' features. Kurtosis measured at a sampling rate of $100.s^{-1}$ tends to increase; this is much more noticeable than the behaviour at $20.s^{-1}$ sampling; this points toward the importance of high frequency features.

In the 'water + sand' case, an interesting empirical relationship has been found between metal *volume* removed per nominal impact and current noise kurtosis. Figure 6.24 has been composed using data from all the target materials used (aluminium, Al/12%Si alloy, zinc, AISI 1020 steel). Volume loss rises with kurtosis in an apparently almost linear manner from the Gaussian value of 3.0. The linearity is probably fortuitous, since it is difficult to see how losses could relate linearly to such a complicated quantity as kurtosis. Moreover, the significant quantity is probably depassivated impact area, rather than lost volume (though these should be

geometrically related, albeit in a complicated and statistical way). However, the positive trend is real for this erosive system.

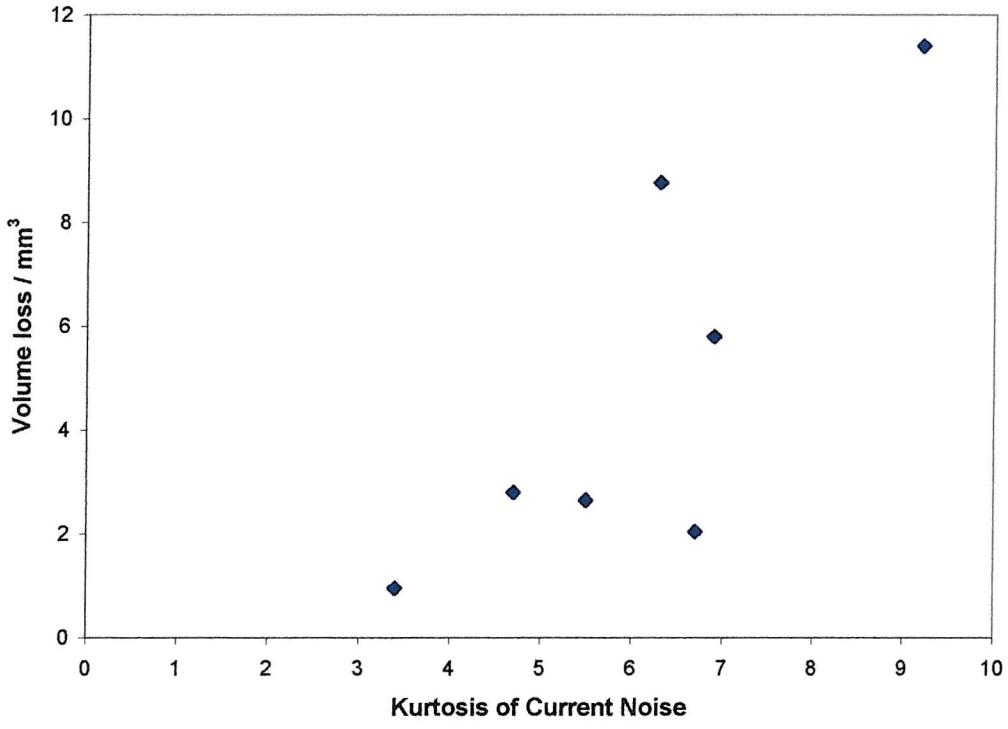

Figure 6.24: Volume loss related to ENA current kurtosis.
'Water + sand' data.

As noted above, such large values of kurtosis are only obtainable when the transients are not only 'sharp' but are also quite well spaced. The model suggests that to be resolvable at a sampling rate of $100.s^{-1}$, but not at $20.s^{-1}$, the transient rate should be in the range 8 – 40 s^{-1}; direct counting suggests about 20 s^{-1}. If these transients represent 'effective' particle impacts, then the rate of 'effective' impacts is very low (at these rather low fluid energies) compared with the nominal rate (about 20,000 s^{-1}), impact efficiency ~ 0.1%. This suggests that only the most energetic particles, possibly having sizes from the high diameter tail of the particle size distribution, actually participate in mass removal. It may be noted that the impact features identified microscopically (Figure 6.9B, Section 6.3.2) are also infrequent (albeit this is not quantified), much more so than was the case at the higher energies (Figure 6.9A) used in Section 4.3.3, where an impact efficiency ~ 1% was estimated by other means. In

general, it would be useful to know more about how impact efficiency varies with sand concentration, size and flow rate – no studies on this have been found in the literature.

In 'brine + sand' this correlation does not work, because the kurtosis is dominated by the behaviour of low frequency components. Instead, a loose correlation is found with current noise, as shown in Figure 6.25. To make this work, two types of point need to be removed, as shown. Both the zinc data points have excess mass loss, attributed to flow corrosion, apparently not predicted by this parameter (at 3.5 hours, but see below). Also, the three highest data.current points have been removed; on inspection all of these showed the oscillatory behaviour in the sand lift, noted earlier; clearly, this invalidates the current measurement.

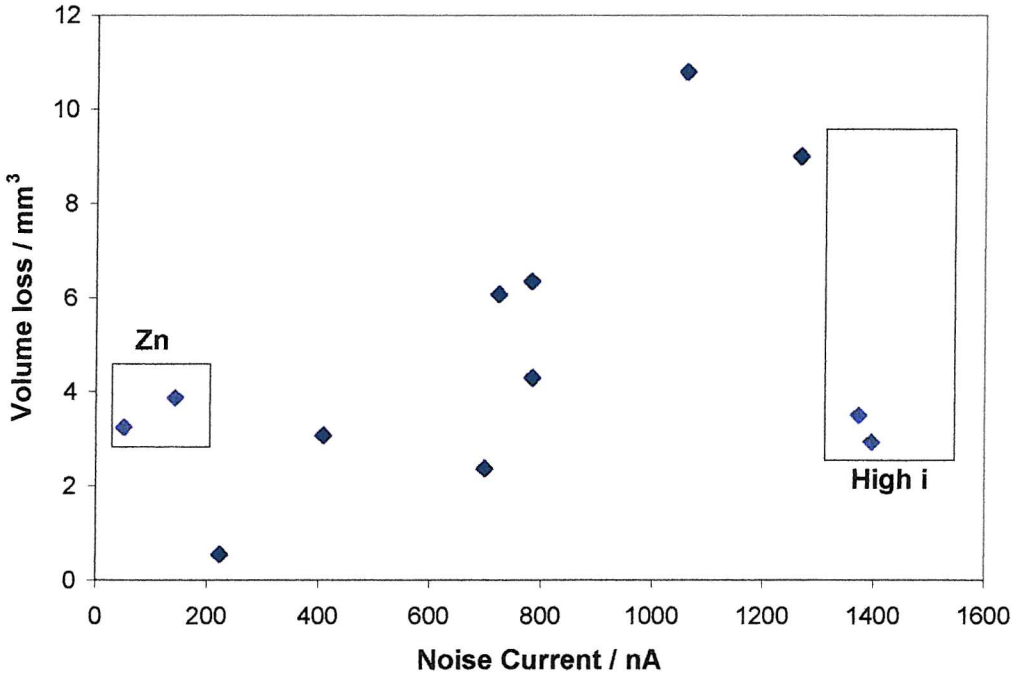

Figure 6.25: Volume loss related to current noise.
'Brine + sand' data

At this level of analysis, this pair of findings (Figures 6.24, 6.25) is difficult to interpret, but more detailed examination of the data will indicate a possible explanation.

There is a further complication in the case of zinc. As mentioned previously, the noise data for the other targets do not change rapidly with time. Zinc behaves differently.

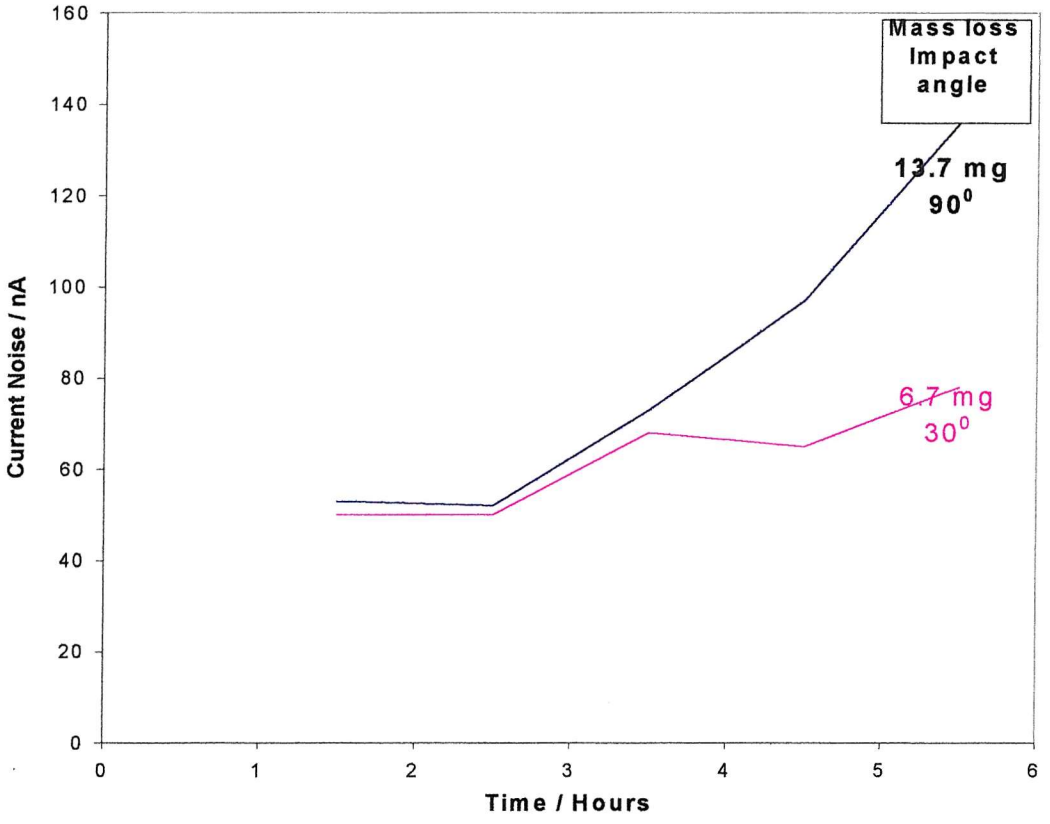

Figure 6.26: Zinc current noise trends with time.
'Brine only' conditions, 2 impact angles

Figure 6.26 shows that under flow corrosion condition ('brine only'), the current noise increases with time, at least after about 3 hours. Also, larger currents at 6 hours are associated with larger total mass losses. This suggests that the flow corrosion phenomenon is self promoting once it gets started. Without mass loss measurements

at intermediate times this cannot be regarded as established, but this observation does suggest a further area of work.

Power Spectral Density (*psd*)/Probability Distribution Function (*pdf*)

Additional information about the structure of the data may be obtained from power spectral density plots and from consideration of the probability density function.

Figure 6.27 compares the power spectral density plots for the four cases. This has been subjected to a 15-point moving average to reduce noise; this implies a reduction in the information in the plot, but plotting unaveraged data (not shown) indicates that no significant feature has been lost. The sharp transients correspond to the pump rotation frequency and its first harmonic.

Substantial differences result from the different experimental conditions. The 'water only' noise (Run 12H) has a *psd* plot that is nearly flat ('white noise'), apart from a deviation at lowest frequencies, and shows power levels small compared with the other plots. This may be regarded as a noise 'floor' for the system (but is not necessarily composed of background electronic noise only, see Section 6.3.4, below). The current probability distribution function is nearly Gaussian (monomodal; skewness = -0.3).

When sand is added to the system (Run 4H), the power spectral density plot is sloped at frequencies above about 5 Hz (-19.6 dB/decade), suggesting localised electrochemical activity, but is flat below this frequency. The current distribution is monomodal, but very skew (= +1.9).

When salt (no sand) is added to the system (Run 21H), the noise amplitude increases (more than for 'water + sand') and a low frequency component is apparent, not present in Run 4H, probably due to pitting [81,82]. At high frequencies (> 5 Hz) the current power spectral density plot is identical with that for 'water + sand'. The

current distribution is monomodal, and nearly Gaussian (skewness = -0.4), being dominated by the low frequency behaviour.

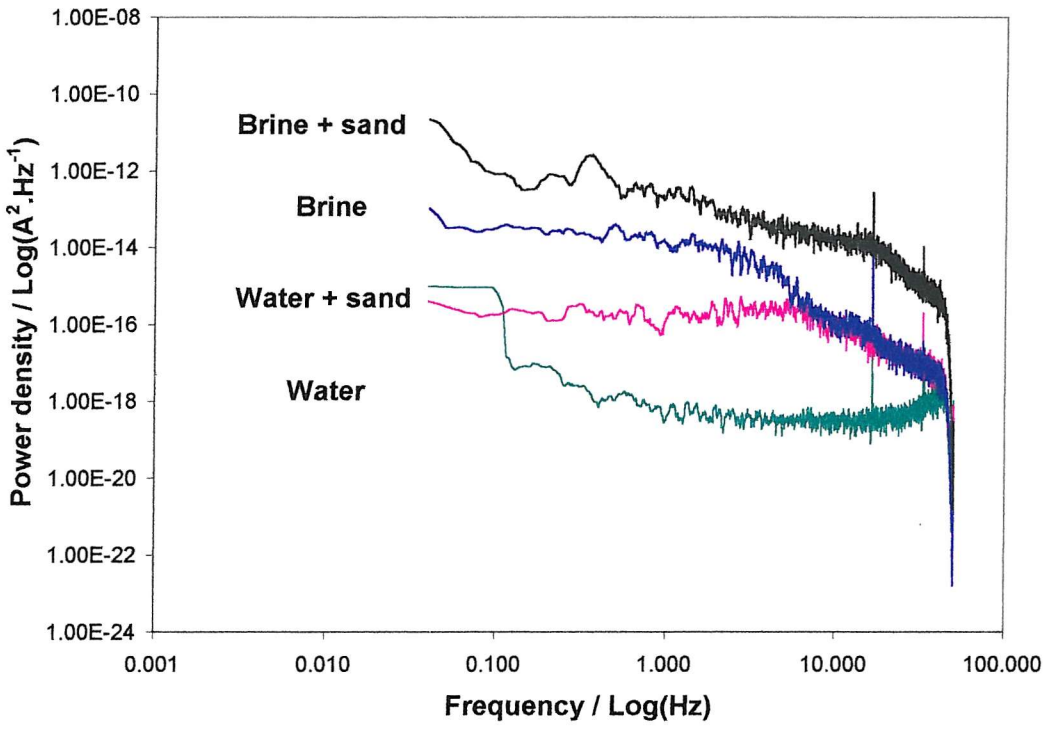

Figure 6.27: Comparative Current Noise power spectral density plots for aluminium targets at normal impact, various erodents. (plots smoothed by 15-point moving average).

A common slope in the high frequency part of the 'water + sand' and 'brine only' plot suggests a common mechanism, or at least a common degree of localisation, at short times. At longer times the curves diverge perhaps because (at least some) pitting features are deeper and are therefore [157] more stable to repassivation than are erosion scars. This suggests that erosion scars behave rather like metastable pits, but under continuous impact do not develop, which is not unreasonable. The lower frequency parts of the *psd* curves, compared with those measured under static conditions (Section 5), are quite ragged, suggesting that, even in the absence of solids, interface conditions are less stable. This may well be related to solution turbulence, but experiments over a range of flow rates would be required to establish

this. Note that these observations could not have been made at the conventional electrochemical noise sampling frequency of $2.s^{-1}$.

When sand and salt are both present (Run 29H) a noise signal is obtained having a noise power that is much larger than in either of the 'one addition' cases. That is, there is much greater 'electrochemical synergy' than there is 'mass loss synergy'; this may point to additional electrochemically active processes being present. There is more power in the current power spectral density plot throughout the frequency range; the transition to the steeper part of the plot appears to have moved up to about 20 Hz. The slope of this (rather short) high frequency section is about –35 dB/decade, i.e. substantially steeper than either of the 'one addition' cases. This seems to suggest that in brine, impact scars are more localised than in water; nevertheless, they are more electrochemically active while they do survive. The current distribution is monomodal and slightly negatively skew (= -0.6), apparently dominated by the low frequency behaviour. The oscillation noted previously is visible at about 0.3 Hz.

Wavelet Decomposition

Introduction. Power spectral densities, calculated using the Fourier Transform, are principally useful for establishing the presence of periodicities (occurrences of constant frequency) in data sets. It has already been noted that the transients in the data sets recorded here are aperiodic. However, there may be other regularities in the data. A technique that has recently become popular for data characterisation, but has not been widely used in electrochemistry, is the use of wavelets, which relate to regularities in timescale (duration) rather than frequency. So, for example, this procedure can pick up regularities in transient width that would be hard to see in a power spectral density plot.

Theory. Since the wavelet transform is relatively unfamiliar, a brief account of the underlying theory and procedure is presented. For further details, see the book by Mallat [117] and the MATLAB Wavelet Toolbox manual [118].

The behaviour of the wavelet transform may be illustrated by reference to that of other better known transforms, as follows:

Fourier Transform

$$F(\omega)=\int_{-\infty}^{\infty} f(t)e^{-j\omega t}dt \tag{6.25}$$

This analyses the whole function *f(t)* in terms of an infinite series of infinite sine (cosine) functions ($e^{-j\omega t}$ exists for all values of *t*) It is good for infinitely extended periodic functions, but is very computationally inefficient for transients and other aperiodic functions. (Most of the computation is devoted to producing zeroes!). It does not locate transients in time or provide any information about them except average bandwidth (and that not very explicitly).

Dirac Transform. (See Figure 6.28a)

$$F(\tau)=\int_{-\infty}^{\infty} f(t)\delta(t-\tau)dt \tag{6.26}$$

Multiplying *f(t)* by a Dirac δ function (a point function) at value τ samples *f(t)* at value τ, i.e. picks out (samples) $f(\tau)$, because the product exists at no other point. If this is done for every value of τ, the integral $F(\tau)$ reproduces *f(t)* exactly.

Wavelet Transform. (See Figure 6.28b)

$$W(u,s)=\int_{-\infty}^{\infty} f(t)\frac{1}{\sqrt{s}}\psi^{*}\left(\frac{t-u}{s}\right)dt \tag{6.27}$$

The **Dirac Transform** samples a point.

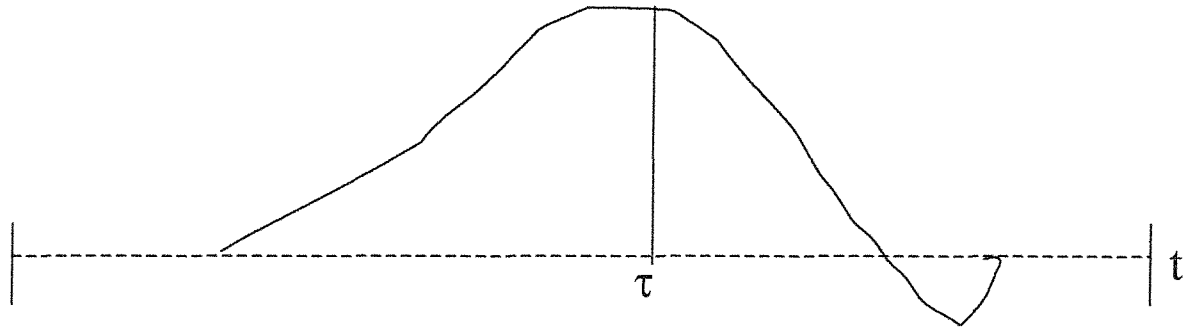

Figure 6.28a: Schematic of Dirac Transform

The **Wavelet Transform** samples and filters a band.

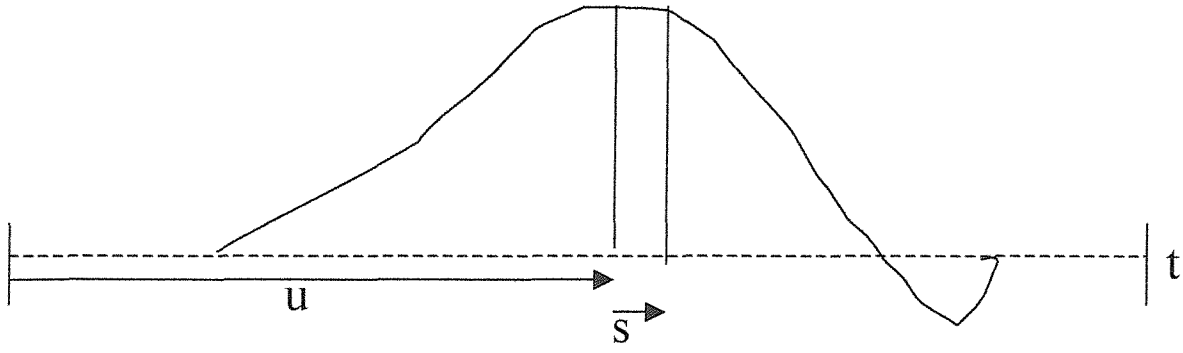

For whole signal: Max $f = f_{sample}$, Min $f = 1/t_{sample}$
For sampled band: Max $f = f_{sample}$, Min $f = 1/s$

The wavelet behaves as a high pass filter.

Figure 6.28b: Schematic of Wavelet Transform.

Multiplying *f(t)* by a wavelet function, defined by:

$$\psi_{u,s}(t) = \frac{1}{\sqrt{s}}\psi\left(\frac{t-u}{s}\right) \qquad (6.28)$$

where: ψ is the particular wavelet waveform used. (see below)

s is a scaling parameter

u is a shifting parameter

selects a band from the signal (the product within the integral is zero outside the band), and applies a filter to it (see below). The integral applies this filter to the whole signal. (ψ^* is the complex conjugate of ψ. Since both the signals and the particular wavelets considered here are wholly real, this complication will be ignored).

As is also shown in Figure 6.28b, the wavelet acts as a high pass filter with a cut-off frequency defined by the scale size of the wavelet.

A wavelet is a waveform of effectively limited duration (it is said to have 'a compact base') that has an average value of zero and an average squared value of unity [117,118]. A variety of wavelets of different forms have been constructed, mostly for image processing applications. Each type of wavelet is characterised by a defining function, which incorporates a scaling parameter (s) and a shifting parameter (u). The scaling parameter defines the (time) scale of the data that the wavelet 'sees'. The shifting parameter moves the (time)-limited wavelet along the data set. The wavelet transform is the integral (sum) over time of the scaled, shifted wavelet multiplied by the signal.

For the purposes of this work the Haar wavelet [191] (Figure 6.29) has been used, because:

- It is the simplest wavelet, it is easy to visualise and it has a compact base.

- It is available within the MATLAB DWT GUI, which is otherwise somewhat limited.
- There is no obvious argument in favour of using one of the more complicated forms, most of which have been developed with other applications in mind.

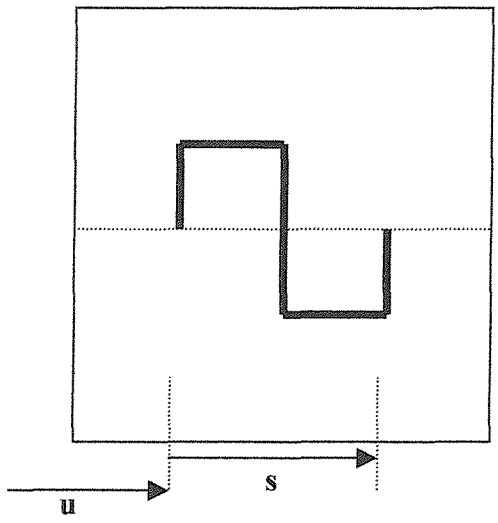

Figure 6.29: Schematic of Haar wavelet.

In principle, integration is required over all possible scales and positions. However, it has been shown [118] that, if repeated application of the wavelet transform at discrete scales based on powers of two (i.e. at scales $1/2^n s$, described as 'dyadic scaling') is used, no accuracy is lost – this procedure is called the discrete wavelet transform (DWT). A wavelet decomposition based on the discrete wavelet transform is equivalent to a multi-narrow-bandpass filter bank [119].

The DWT is used to decompose a time signal into a series of separate signals (one or more 'details' and an 'approximation', in MATLAB's terminology), characterised by different timescales. Figure 6.30 shows two stages of the DWT procedure. The original signal (s_1), here with 20000 data points (as in experimental runs) is first split into a 'detail' containing all the high frequency information and a first level of 'approximation' containing the rest. Because the wavelet transform results in the

same number of points in the filtered signal as in the original (20000), and the 'approximation', obtained by difference, also has this number of points, a procedure known as 'downsampling', which halves the number of points present, is required to ensure that the process does not generate artefacts. The procedure is then repeated to split the first approximation (a_1) into a second detail (d_2) and a second approximation (a_2), and so on as often as desired. The final decomposition contains the same number of points as does the original signal (i.e. no 'new' information). Half of these points are to be found in the finest level of detail, d_1. So, the timescale associated with this level is $2/f_{sample}$ and the other levels are related by dyadic scaling

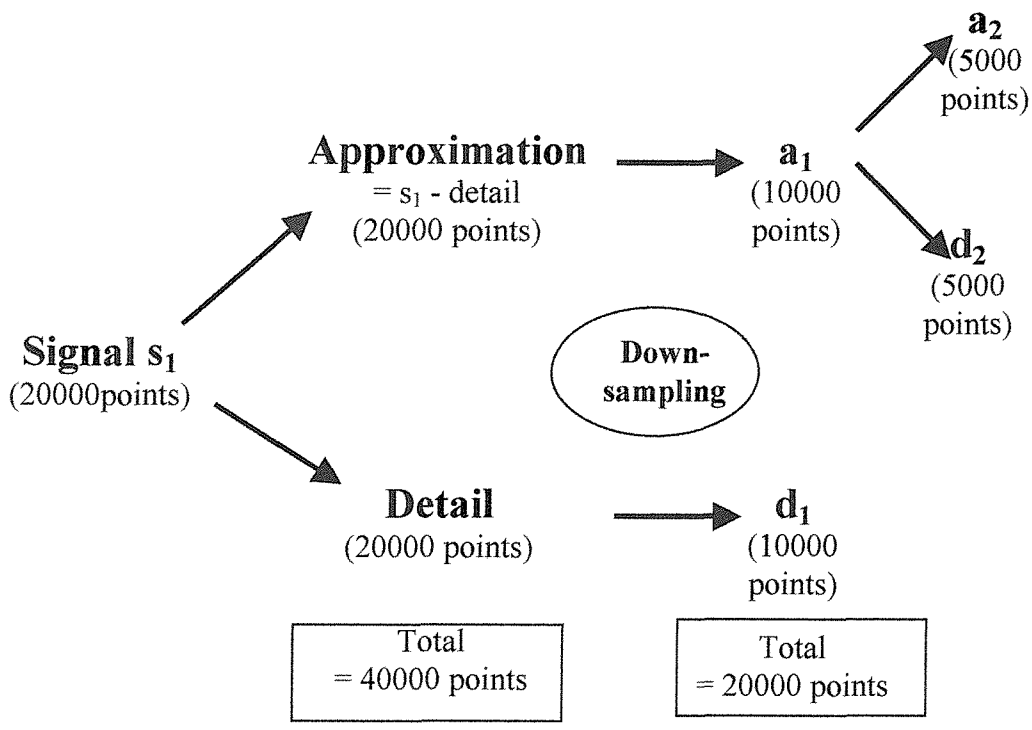

Figure 6.30: Schematic of DWT decomposition procedure.
Adapted from MATLAB Wavelets Toolbox manual .

Note that the wavelet transform removes information from the signal starting at the finest level of detail and getting coarser, the opposite of conventional curve fitting

operations. Note also that all the low frequency variability has been isolated to the 'approximation'. This allows a 'clean' view of the higher frequency features.

In the present work, the sampling frequency has been $100.s^{-1}$, so the timescale associated with d_1 is 0.02 s. Successive 'details' relate to timescales of 0.04 s, 0.08 s, etc, reflecting 'dyadic scaling'. In the following, 10 levels of detailing have been used; d_{10} is associated with a timescale of 10.24 s. Even with this level of detailing most of the low frequency activity falls into the 'approximation'. Following Aballe *et al* [113] and Dong *et al* [114], detail variance (hereafter, 'detail noise power'), calculated from the MATLAB GUI, is plotted against detail number (dyadically scaled timescale) for selected groups of data.

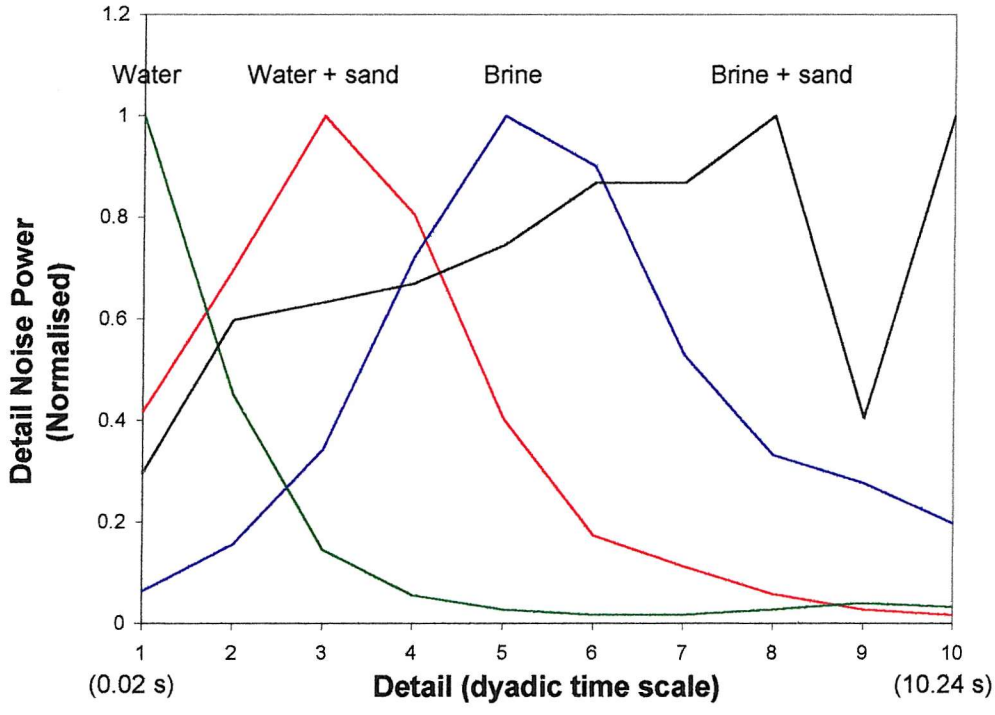

Figure 6.31: Comparison of current noise data for erosion corrosion of aluminium by various erodents at normal incidence; wavelet decomposition of noise power

Aluminium. Figure 6.31 shows data for the four aluminium samples that have been used as representative. In order to present these plots together, the detail noise power

has been normalised in each case by the maximum value for that sample. This is a matter of convenience – it makes no difference to the discussion, which concentrates on timescales.

The labels have been placed to coincide with the maximum values in each trace, so far as they are measurable – the peak for the 'water only' case is evidently off-scale at the short time scale end.

The following points are of note:

- All the features are broad; i.e. there is a wide range of time scales involved in any process underlying these behaviours.

- The 'brine + sand' case is somewhat compromised by an apparent dip at d_9. This is actually probably excess value at d_{10}, as will be discussed later. This feature is notably broader than the others.

- Subject to these comments, it is apparent that:
  - Adding sand to water displaces the peak signal to longer times.
  - Substituting brine for water displaces the peak to even longer times.
  - Adding both sand and salt displaces the peak even further and makes it much broader.

- These observations are consistent with the suggestions that:
  - Adding sand creates flaws.
  - Adding chloride creates and stabilises flaws.
  - Adding both results in a broad range of stabilised flaws.
  - Adding oxygen (not a variable in this work) passivates flaws.

  This is, of course, entirely consistent with the conventional qualitative picture of passive layer damage behaviour [45], and the more quantitative

ideas of Galvele [155] and Pride *et al* [156] concerning the effects of chloride ion concentration on pit growth.

- The transients present in 'brine + sand' experiments are much broader than those in 'water + sand' runs, and therefore overlap more, are less conspicuous and have reduced kurtosis level.

- If these ideas are correct, then the peaks reflect the range of flaw lifetimes in the underlying processes. Erosion-created flaws are estimated as having modal lifetime values of about 0.2 s in water and 2.0 s in brine. However, there are broad spreads about these values and a more tightly controlled experiment would be required to derive a reliable distribution of lifetimes. Given this, then varying the relative sand, chloride and oxygen levels would allow an investigation of repassivation kinetics in dense slurries. This would be complementary to work being carried out elsewhere on single particle erosion-corrosion [19,21] or with inhibitors [115]. Operation at lower oxygen levels may lead to longer flaw lifetimes, hence greater mass loss by 'active' corrosion, or no corrosion when oxygen is completely absent. Mapping the flaw behaviour against the input parameters may be attractive.

- Note that this analysis has required a sampling rate of $100.s^{-1,}$ and that a somewhat higher rate than this would be desirable.

'Water only' runs. Some further aspects of the data are illustrated by considering the different erodents separately. Figure 6.32 shows the results for 'water only' runs

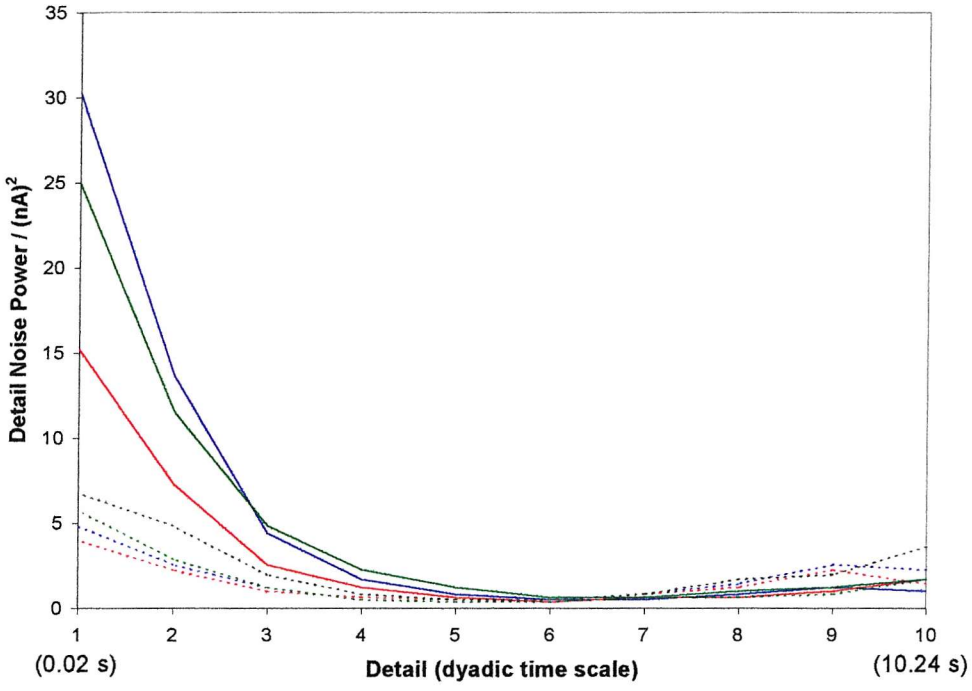

Figure 6.32: 'Water only' runs.
Solid lines: 90^0. Dotted lines: 30^0.
Blue = Aluminium, Red = Al/12%Si, Green = Zinc, Black = Steel.

for all the materials used. The peak current seems to occur at shorter timescales than measured here. Otherwise the most notable feature of the data is that impact angle dependence seems to be much more important than target material dependence. This is unexpected, and not easy to explain. The reason must involve some effect on the solution side of the corroding interface. One possibility is that different flow conditions over the target cause different degrees of disruption to the electrochemical double layer [47]. Another possibility is that this reflects different ease of oxygen access to the surface [71].

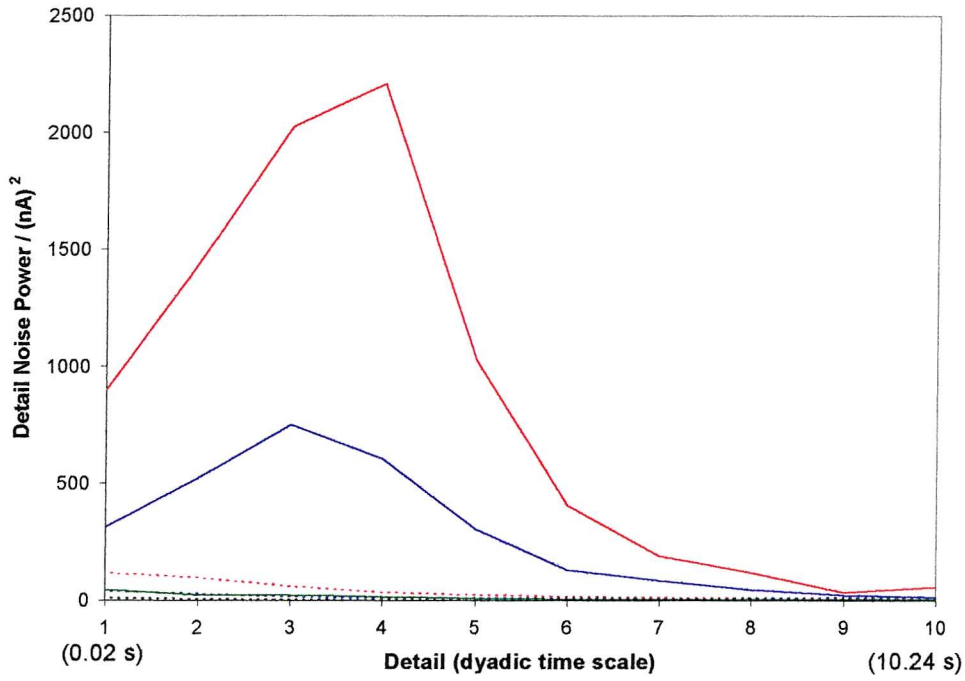

Figure 6.33: 'Water + sand' runs.

Solid lines: 90^0. Dotted lines: 30^0.

Blue = Aluminium, Red = Al/12%Si, Green = Zinc, Black = Steel.

'Water + Sand' runs. Figure 6.33 shows results for all target materials under sand erosion in water. Al/12%Si (particularly) and aluminium under impact at normal incidence show marked peaks at $d_{3/4}$, i.e. at a scale of about 0.12 s. This effect is not present at 30^0 impact, or for the other materials, though it is possible that peaks may exist at shorter timescales. The particularly high currents observed with Al/12%Si may reflect micro-galvanism on freshly exposed surface, as suggested for this alloy in mine-waters by Meyer-Rodenbeck [165]. All samples show greater currents at 90^0 impact than at 30^0.

'Brine only' runs. Figure 6.34 shows results for all target materials in brine. Aluminium (particularly) and Al/12%Si at normal incidence show marked peaks at d_5, i.e. at a scale of about 0.32 s. This effect is present but much weaker at 30^0 impact, but not for the other materials, though it is possible that peaks may exist at shorter timescales. Note that the strongest electrochemical response in this case is for aluminium (contrast 'water + sand'), reflecting the susceptibility of aluminium to pitting in chloride media [153,154]. All samples show greater currents at 90^0 impact than at 30^0.

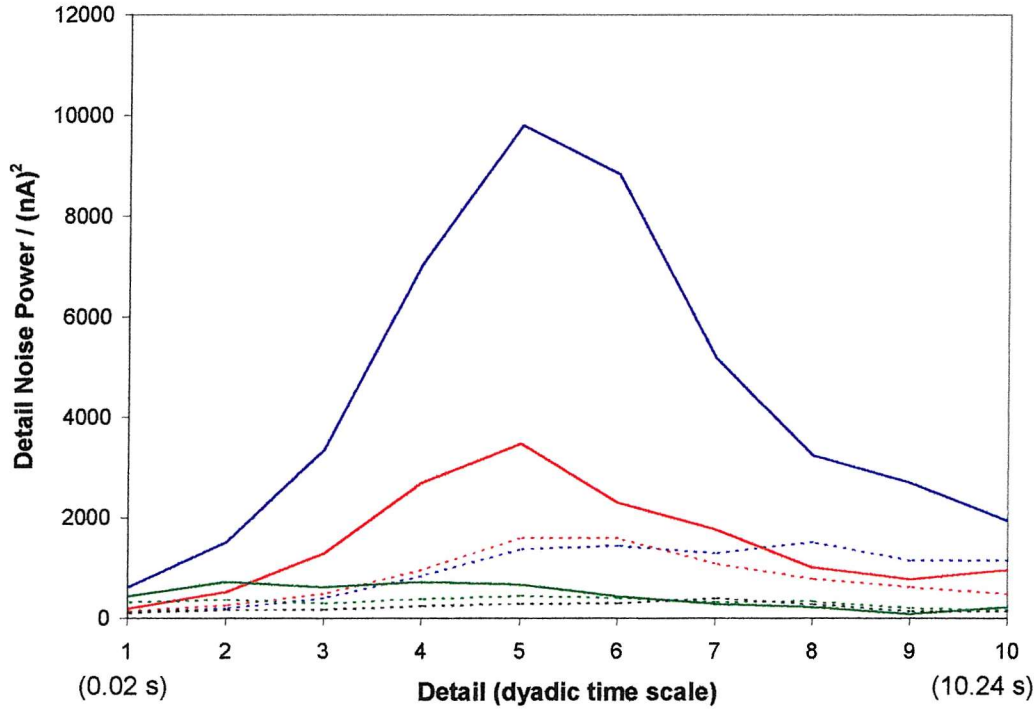

Figure 6.34: 'Brine only' runs.
Solid lines: 90^0. Dotted lines: 30^0.
Blue = Aluminium, Red = Al/12%Si, Green = Zinc, Black = Steel.

'Brine + Sand' runs. Figure 6.35 shows results for all target materials under sand erosion in brine. Aluminium (particularly) and Al/12%Si at normal incidence show the strongest responses, but, relative to the 'brine only' case, the 'peaks' are greatly broadened and are displaced to longer times. This effect is present but is weaker at

30^0 impact. This effect requires an interaction between the sand and the chloride ions. This is unexplored, but a possibility is suggested by the work of Matsumura *et al* [62]. These authors found that they could only explain their erosion-corrosion results on stainless steel by assuming (not unreasonably) chloride adsorption on the surface, and a resulting change in the measured coefficient of friction, which affected performance. Another possibility is that metastable pitting requires the pits to have salt 'lids' [45], which show a variable response to sand impact. For the other materials, there is somewhat more convincing evidence for activity at shorter timescales. Aluminium remains the target with the strongest electrochemical response. In other words, apart from the peak broadening/displacement, 'brine + sand' looks much more like 'brine only' than 'water + sand' electrochemically, in line with the 'electrochemical synergy' finding.

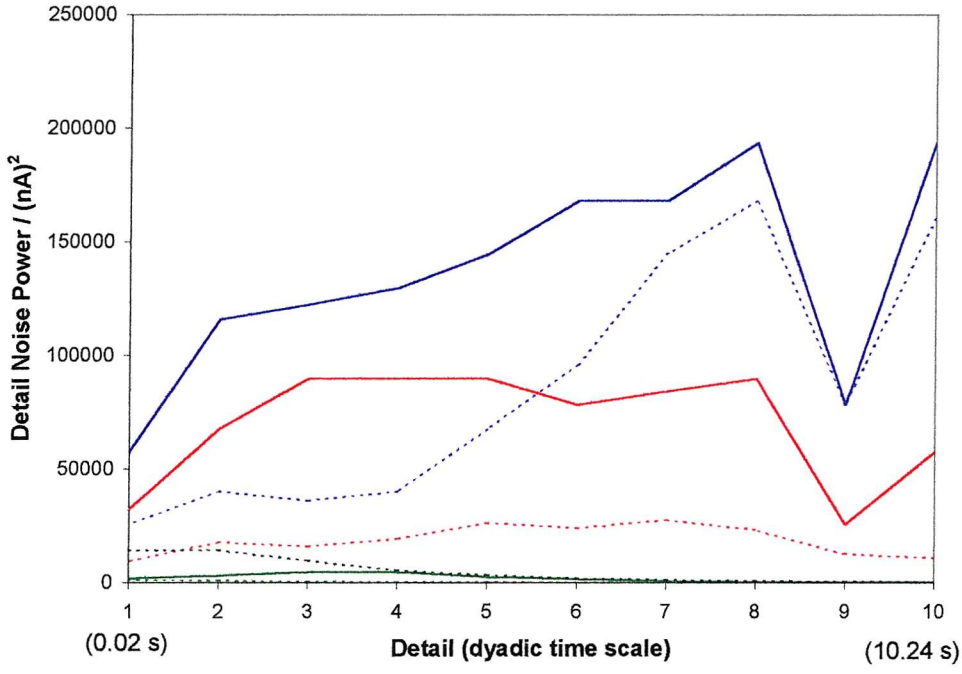

Figure 6.35: 'Brine + sand' runs.

Solid lines: 90^0. Dotted lines: 30^0.

Blue = Aluminium, Red = Al/12%Si, Green = Zinc, Black = Steel.

Several of the traces show a 'dip' at d_9. It is thought that this is more apparent than real, and that really there is too much current recorded at d_{10}. As noted earlier, certain runs suffered from oscillations in the sand lift, and inspection indicates that it is just these runs which show a 'dip' at d_9.

All samples show greater currents at 90^0 impact than at 30^0. As noted in the preceding Sections, this effect occurs with or without either sand or NaCl in the eroding fluid, so these are presumably not responsible. Most likely, as noted under 'water only', this is an oxygen access effect determined by the fluid mechanics of the system. Further investigation with an apparatus similar to that of Dawson *et al* [55] and varying flow rates might resolve this.

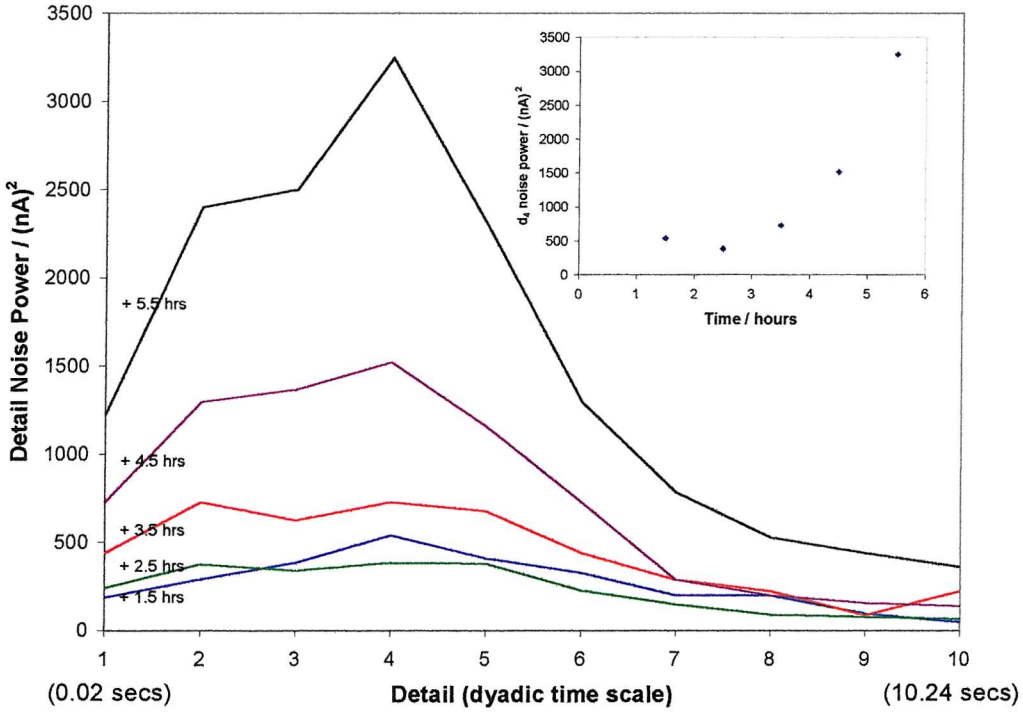

Figure 6.36: Zinc/Brine/Normal incidence
Development of wavelet decompsition.

Zinc. As noted previously, zinc behaviour is different from that encountered with aluminium based materials, in that it develops with time. Figure 6.36 shows how the

wavelet decomposition for zinc corroded by brine at normal incidence (mass loss due to flow erosion = 13.7 mg) develops with time.

Electrochemical activity on the surface, initially uniform with respect to time scale, develops a peak at d_4, i.e. at a timescale of about 0.16 s, which grows with time. The inset shows how d_4 develops with time. There is an apparent induction period of several hours before this effect becomes established, after which activity becomes increasingly marked. This explains why flow corrosion does not show up in the comparative data for noise at 3.5 hours into the run, illustrated in previous sections. This is understandable if zinc flow corrosion increases with the magnitude of surface roughness, as has been suggested by LaQue [139].

The zinc samples were not polished, so flow induced roughness (rippling in the manner of Karimi and Schmidt [70]) will take some time to exceed the sample's initial roughness; once this has occurred the process becomes self-accelerating. This is a proposition that should be testable by using samples of differing initial surface roughnesses.

Electrochemical Conclusions/Further Work.

There is no direct relation between electrochemical noise and mass loss, because there are multiple mechanisms with different efficiencies.

Electrochemical synergy is not the same as mass loss-synergy.

Electrochemical noise data on aluminium and Al/12%Si can be qualitatively explained in terms of flaw formation by sand impact, stabilisation by chloride and repassivation by oxygen.

Wavelet analysis yields qualitative features consistent with an empirical model for impact induced flaw behaviour. It may eventually provide means of estimating repassivation kinetics, especially for Al and its alloys.

Zinc flow corrosion develops slowly, and appears to be self-accelerating as surface roughness increases.

Impact angle has a strong influence on the electrochemical noise behaviour. This is most likely to be related to oxygen transport effects, and, hence, the hydrodynamic properties of the flow. Mass loss also shows angle effects; these may be related.

Better experimental control ([sand], sand size, v, T, $[Cl^-]$, $[O_2,]$ solid target) is required. Reduction of iR and pressure drops are necessary.

Higher sampling rates and automated data collection are required.

Wavelet analysis (best wavelet, scaling, etc) needs to be refined and automated.

Effects of sample heterogeneity need to be understood.

Impact angle effects need to be understood in terms of hydrodynamic/oxygen access factors.

Development of a kinetic model for flaw repassivation on aluminium and its alloys would be useful. In particular, this would help to understand the practical effects of different oxygen levels in the water on corrosion mass loss.

Further work on the relation of zinc surface roughness to flow corrosion would be useful.

7 CONCLUSIONS

Detailed conclusions appear at the end of each Section, so only an overall summary appears here.

Materials

The sponsor requirement is for economic coatings on (mild) steel to resist erosion-corrosion by sand in flowing seawater. There is particular interest in the use of metallic coatings.

Coatings need to be: Erosion resistant
Corrosion resistant
Cheap enough

The primary function of a coating is to act as a barrier. It must therefore have a good resistance to erosion, resistance to which correlates very roughly with hardness. Once the coating has been penetrated, behaviour depends on electrochemistry. Coatings should be anodic to the substrate (or at least not cathodic), so that they can protect the substrate galvanically.

The work in this thesis has been carried out using model anodic coatings on AISI 1020 steel. These were HVOF sprayed coatings made from commercially pure aluminium, aluminium/12%silicon (eutectic) alloy, and a novel layered composite sprayed alternately with this alloy and alumina, hot-dipped zinc coatings. Samples of the substrate have been included for comparison.

Characterisation of HVOF coatings showed that dense coatings were obtained when metal or alloy were sprayed (~ 1% porosity or less), but that the composite had much higher levels of porosity (~6.5%). Flow-out of alloy particles was sometimes poor.

Erosion

Mass loss measurements on eroded samples confirm that aluminium resists erosion poorly. Alloying with silicon improves performance, but not very strongly. Addition of alumina to reinforce the alloy coating made performance worse, but this is to be attributed to the fact that these samples were not structurally as intended; in particular, they exhibited high porosity and, apparently, poor alumina/matrix adhesion. Since composite development was not a prime objective of this work, investigation of this material was discontinued.

Profilometry and microscopic examination of these samples (optical and electron) shows surfaces consistent with completely ductile erosion mechanisms. At the scar centres very disturbed surfaces produced by plastic flow have the form of lipped platelets; individual impact sites cannot be distinguished. Distant from the scar individual impact sites can be recognised. Small sites are simple microcutting features, but larger sites show long grooves with lateral lipping, indicating plastic flow.

Mass loss is largely *via* plastic flow, resulting in lipping and subsequent lip removal by fracture (probably fatigue fracture).

Static Corrosion

Static corrosion measurements have been carried out in 3.5% NaCl solutions. Because of the impossibility of maintaining identical electrode pairs, ENA measurements (current only) have been made on a single potentiostatted sample electrode. In practice the most useful results were obtained from power spectral density curves of this current noise; considerable effort has been put into ensuring that these data are reliable.

Comparison of the psd plots of the different metals showed regularities in the negative slopes, which, with the exception of the mild steel sample, are linearly related to sample OCP. This suggests that, for surfaces that form coherent oxide films, an active underlying metal (e.g. zinc) will have many small reactive sites with rapid processes occurring, whereas for a noble metal (e.g. stainless steel) there will be a smaller number of larger sites with slower processes occurring. However, no conclusion has been reached as to the reason for the linear form of the relationship.

Coatings on mild steel, which are protective (i.e. anodic to the substrate) are expected not to show well-defined transients. Nevertheless electrochemical noise series for aluminium will have some structure, recoverable by analysis of *psd* plots. It may be possible to detect coating breakdown by analysing changes in this structure.

Comparison of the aluminium-based coatings suggests that adding silicon is likely to be beneficial from a corrosion point of view, contrary to the limited information in the literature, because aluminium depletion leaves a silicon enriched surface, but that it is important to minimise porosity.

Trends in the change (reduction) of the negative *psd* slope with time suggest that a key factor in the corrosion behaviour of the aluminium-based samples is the blocking of porosity by corrosion product. If open porosity (steel exposure) is not to be a problem, these results suggest that coating production should be controlled so as to ensure that porosity (as estimated by image analysis) should be restricted to < 1%.

Aluminium based materials appear to be sensitive to the oxygen level in the solution, so consideration needs to be given to what levels of oxygenation are likely to be met in service, and if necessary, equipment in which this variable can be controlled should be developed.

The two best coatings tested in terms of static corrosion were the Al/12%Si and zinc coatings.

Erosion-Corrosion

A new test rig with no metal parts has been built, designed to characterise erosion corrosion both gravimetrically and electrochemically. Electrochemical characterisation is primarily by Electrochemical Noise methods, using a potentiostatted working electrode. Considerable effort has gone into characterising the behaviour of this equipment.

Zinc suffers from flow corrosion; other targets do not.

All target materials under sand erosion lose mass in a way directly related to sand kinetic energy, and inversely related to hardness.

Corrosion losses are quite small, relative to erosion, under the test conditions used; solid products sometimes result in net weight gains.

For the aluminium-based targets erosion scar depth is proportional to mass loss, but this relation does not hold for zinc coatings.

Mass loss by erosion appears by microscopic examination to be entirely ductile.

There are greater mass losses at nominally normal incidence than at nominally oblique incidence, not usually associated with ductile erosion though this behaviour has been seen by some other workers with similar materials. The discrepancy is thought to result from the use of relatively dense slurries, in which real particle trajectories deviate considerably from nominal ones because of particle/particle interactions; real impact angles are thought to be much more grazing than nominal ones.

Erosion-corrosion synergy is difficult to determine precisely, but appears to show a pronounced dependence on nominal impact angle, which is not understood.

There is no direct relation between Electrochemical Noise and mass loss, because there are multiple mass loss mechanisms with different efficiencies. Pure erosion, in particular, is not Faradaic.

Electrochemical synergy is not the same as mass loss synergy; synergy determination should rely on one type of measurement or the other, not a mixture.

Power spectral density plots are not as linear under flow conditions as they are under static corrosion conditions, despite the data being more stationary on the time scale of the overall measurement (200 s). It is thought that this results from continuous disruption of the interface in the former case. Erosion scars behave like corrosion pits at high frequencies, but show less 'power' at longer times; this is consistent with the likelihood that erosion scars are relatively more open than are corrosion pits and repassivate more easily.

Electrochemical noise data on aluminium and Al/12%Si can be qualitatively explained in terms of flaw formation by sand impact, stabilisation by chloride and repassivation by oxygen, plus a lower frequency component associated with pitting.

Wavelet analysis allows separation of surface mechanisms separated by differing time scales, and the removal of any low frequency drift. It may eventually provide means of estimating repassivation kinetics, especially for Al and its alloys, by correlating modal time scales for the repassivation process with changes to input parameters (sand kinetic energy, chloride level, aeration). The breadth of the time scale peak may also allow estimation of the dispersion of this behaviour in a dense slurry.

Sampling frequencies up to 100 s^{-1} allowed characterisation of depassivation/repassivation features resulting from erosion behaviour that would not have been accessible at the more conventional sampling frequency of 2 s^{-1}. This sampling frequency was not high enough to properly characterise the behaviour in water.

Zinc flow corrosion develops slowly, and appears to be self-accelerating as surface roughness increases.

There are effects of impact angle, which may be related to oxygen access effects, via the system hydrodynamics. These effects may be related to the observed angular dependence of mass loss synergy, and they require further investigation.

8 FURTHER WORK

Materials

The materials used in this work have been model coatings, chosen largely because of their availability. Coatings for practical use should have a better balance of erosion and corrosion behaviours. Possible candidates for this include:

Hypereutectic aluminium/silicon alloys
Zinc/aluminium alloys
Aluminium/Nickel
Iron/Silicon
Aluminium (alloy) treated with rare earth compounds, e.g. of Ce, Y
Al/yttria dispersions
Zn alloys, e.g. Zn/Fe, Zn/Ni.

Since porosity is clearly an important factor in performance, consideration of coating means other than spraying, e.g. hot-dipping, electroplating, should be considered.

Tests in this work were carried out in 3.5% NaCl. The work could usefully be extended to real seawater from various locations.

Test Equipment

The most important requirement for improved performance in any future test rig will be improved control of flow, particularly sand flow. Partly in order to achieve this, positive temperature control is desirable. Since real seawater temperatures vary in the range 0-50^0 C, the ability to cover this range would be useful.

Since aluminium alloys are sensitive to aeration levels, it would be useful to have a test rig in which aeration (and possibly also CO_2) could be positively controlled. This would require a submerged jet arrangement.

Interpretation would be eased by the use of closely sieved sand fractions.

Since the Electrochemical Noise behaviour has turned out to be very complicated, a useful simplification would be to repeat the work in this Thesis using solid targets (i.e. not coatings, not HVOF sprayed). This would avoid complication due to substrate or porosity effects.

The test rig, as built, has an excessive pressure drop and an excessive iR drop, both associated with the detail of the ejector design. There is scope for considerable improvement in this area.

The spatial behaviour of the target is not well characterised, either in terms of the distribution of incident kinetic energy, or of its electrochemical response. The distribution of incident kinetic energy is probably best approached by Computational Fluid Dynamics modelling, which might usefully develop the two interpenetrating fluids solid-in-gas approach of Gustavsson. For the electrochemical response, development of an approach based on some form of segmented electrode would be appropriate.

The experimental technique used in this work involved a great deal of repetitive data collection under manual control. Much of this could usefully be automated, as could data analysis, once a stable analytical regime is finalised.

Extension of electrochemical measurement to higher sampling frequencies would be useful.

Erosion

Better understanding of the apparent change in erosion mechanism on aluminium with increasing input sand kinetic energy would be useful. How does this depend on local temperatures? How do local temperatures depend on impact conditions, heat loss mechanisms.

A better understanding of the relationship between impact efficiencies, relative separations and input kinetic energies in slurries of various densities would be useful.

A better understanding of the mass loss mechanisms of composites under erosion would be useful.

As noted above, a better CFD understanding of the behaviours of dense slurries would be useful. Interpenetrating fluid models look promising.

Static Corrosion

A better understanding of the effects of aeration on the Electrochemical Noise behaviour of aluminium (alloys) is required.

Better definition of the experimental finding relating the slope of the power spectral density curve to the open circuit potential of a working electrode is required. This needs extension to a wider range of materials (Al alloys, steels – stainless and otherwise- and other materials, e.g. Ti alloys). The distinction made between metals with adherent and non-adherent oxide coatings needs to be confirmed. Supporting theory needs to be established.

Flow/Erosion-corrosion

The very marked flow corrosion of zinc could usefully be further investigated, particularly in terms of relating mass loss to Electrochemical Noise behaviour as a function of time.. This should be extended to the zinc alloys conventionally used as sacrificial anodes in ships/boats.

Erosion-corrosion behaviour of suitable target materials could be mapped in terms of variations with respect to relevant input parameters. These are likely to be sand kinetic energy, chloride concentration and aeration level. Nominal impact angle could be used as a secondary parameter. Output parameters (mapped parameters) could be mass loss, penetration depth, or one of a number of electrochemical quantities. Of the latter, modal time scale for the erosion depassivation/repassivation process, derived from wavelet decomposition, looks attractive. This could lead to characterisation of repassivation kinetics; it would be interesting to see know how these relate to alloy composition.

9 REFERENCES

1 A.J. Speyer, R.J.K. Wood, K.R. Stokes and A.J. Sturgeon, "Corrosion of aluminium-based coatings for use in marine pipework", presented at *Eurocorr 2000,* London, 2000.

2 A.J. Speyer, R.J.K. Wood and K.R. Stokes, "Erosion of aluminium-based claddings on steel by sand in water", *Wear,* 250 (2001), 802-808

3 R.J.K. Wood, J.A. Wharton, A.J. Speyer and K.S. Tan, "Investigation of erosion-corrosion processes using electrochemical noise measurements", *Tribology International,* 35 (2002), 631-641.

4 R.J.K. Wood and A.J. Speyer, "Erosion-corrosion of Marine Coatings", to be submitted to a special Tribo-corrosion issue of *Wear* (2002).

5 I.M. Hutchings, "Tribology: Friction and Wear of Engineering Materials", Edward Arnold (1992).

6 T. Young, "A Course of Lectures on Natural Philosophy and the Mechanical Arts", Printed for J. Johnson, 1807.

7 Lord Rayleigh, "The Sand-Blast", *Nature,* 93, (1914), 188.

8 R.J.K. Wood "Design Guide on Wear Minimisation in Slurry Systems" for AEA Technology (Harwell), Mechanical Engineering Consultancy, University of Southampton (1994).

9 A. Forder, MPhil/PhD Transfer Thesis, University of Southampton (1997). Report No ME/97/02.

10 H.C. Meng and K.C. Ludema, "Wear models and predictive equations: their form and content", *Wear* 181-183 (1995), 443-457.

11 I. Finnie, "Erosion of Surfaces by Solid Particles" *Wear* 3 (1960), 87-103.

12 K. Wellinger, "Sandsrahlverschleiss an Metallen", *Z. Metallkunde* 40 (1949), 361.

13 J.G.A. Bitter, "A Study of Erosion Phenomena: Part I", *Wear* 6 (1963), 5-21.

14 J.G.A. Bitter, "A Study of Erosion Phenomena: Part II", *Wear* 6 (1963), 169-190.

15 F. Lin and H. Shao, "The effect of impingement angle on slurry erosion", *Wear* 141 (1991), 279-289.

16 R.S. Lynn, K.K. Wong, and H.McI Clark, "On the particle size effect in slurry erosion" *Wear* 149 (1991), 55-71.

17 A.J. Sparks and I.M. Hutchings, "Effects of erodent recycling in solid particle erosion testing", *Wear,* 162-164 (1993), 139-147.

18 G.W. Stachowiak, "Particle angularity and its relationship to abrasive and erosive wear." *Wear* 241, (2000), 214-219.

19 M.T. Benchaita, P. Griffith and E. Rabinowicz, "Erosion of a metallic plate by solid particles entrained in a liquid jet", *J. Eng. Ind* 105 (1983), 215-227.

20 G.T. Burstein and K. Sasaki, "The birth of corrosion pits as stimulated by slurry erosion", *Corrosion Science,* 42 (2000), 841-860.

21 H.McI. Clark, "Particle velocity and size effects in laboratory slurry erosion measurements, OR do you know what your particles are doing?", *Tribology International* 35, (2002), 617-624.

22 A. Neville and X. Hu, "Assessment of electrochemical response from high alloy stainless steels during slurry impingement and single impacts to improve understanding of erosion-corrosion", *British Corrosion J.,* 37(1), (2002), 43-47.

23 H. McI. Clark, "The influence of the flow field in slurry erosion", *Wear,* 152 (1992), 223-240.

24 J.A.C. Humphrey, "Fundamentals of fluid motion in erosion by solid particle impact", *Int J. Heat and Fluid Flow,* 11 (1990), 170-195.

25 S. Turenne, M. Fiset and J. Masounave, "The effect of sand concentration on the erosion of materials by a slurry jet", *Wear,* 133 (1989), 95-106.

26 P.H. Shipway and I.M. Hutchings, "A method for optimising the particle flux in erosion testing with a gas-blast apparatus", *Wear,* 174 (1994), 169-175.

27 Y.I. Oka, M. Nishimura, K. Nagahashi and M. Matsumura, "Control and evaluation of particle impact conditions in a sand erosion test facility", *Wear,* 250 (2001), 736-743.

28 M. Gustavsson, "Fluid Dynamic mechanisms of particle flow causing ductile and brittle erosion", *Wear,* 252 (2002), 845-858.

29 A.J. van Riemsdijk and J.G.A. Bitter, "Erosion in gas-solid systems", *Fifth World Petroleum Congress*, New York (1959), Section VII, 43-57.

30 I. Finnie and D.H. McFadden, "On the velocity dependence of the erosion of ductile metals by solid particles at low angles of incidence", *Wear,* 48 (1978), 181-190.

31 M. Hashish, "An improved model of erosion by solid particle impact", *Proc. 7th Int. Conf. on erosion by liquid and solid impact,* Paper 66.

32 G. Sundararajan, "A comprehensive model for the solid particle erosion of ductile materials"; *Wear*, 149 (1991), 111-127.

33 J.A. Laitone, "Aerodynamic effects in the erosion process", *Wear* 56 (1979), 239-246.

34 H.Hojo, K. Tsuda, K. Shirato and T. Yabu, "Erosion behaviour of plastics by slurry jet method", *Kagaku Kogaku Ronbunshu* 14 (1988) 161-166.

35 R.W. Lyczkowski, S. Folga, S.L. Chang, J.X. Bouillard, C.S. Wang, G.F. Berry and D. Gidaspow, "State-of-the-art computation of dynamics and erosion in fluidised bed tube banks" in *Proc. 10th Int Conf. on Fluidised Bed Combustion,* ASME, New York, 1989, Vol1, 465-478.

36 I.M. Hutchings, "Mechanisms of the erosion of metals by solid particles", in ASTM STP 664 "Erosion: Prevention and useful applications", (1979), 59-76.

37 R. Oltra, C. Gabrielli, F. Huet and M. Keddam, "Electrochemical investigation of locally depassivated iron. A comparison of various techniques", *Electrochimica Acta,* 31(12), (1986), 1501-1511.

38 I. Finnie, J. Wolak and Y. Kabil, "Erosion of metals by solid particles", *ASTM J. Materials,* 2 (1967), 682-700.

39 A.V. Levy, "The platelet mechanism of erosion of ductile metals", *Wear*, 108 (1986),1-21.

40 A.V. Levy, "Solid particle erosion and erosion-corrosion of materials", ASM International (1995).

41 I. Finnie, A. Levy, and D.H. McFadden, "Fundamental mechanisms of the erosive wear of ductile metals by solid particles", in ASTM STP 664 "Erosion: Prevention and Useful Applications", (1979) 36-58.

42 A.K. Cousens and I.M. Hutchings, "A critical study of the erosion of an aluminium alloy by solid spherical particles at normal impingement", *Wear,* 88, (1983), 335-348.

43 A. Misra and I. Finnie, "An experimental study of three-body abrasive wear", *Wear,* 85 (1983), 57-68.

44 J.A. Hearley, J.A. Little and A.J. Sturgeon, "The erosion behaviour of NiAl intermetallic coatings produced by high velocity oxy-fuel thermal spraying", *Wear,* 233-235 (1999), 328-333.

45 M.G. Fontana, "Corrosion Engineering", McGraw-Hill (1987).

46 K.R. Trethewey and J. Chamberlain, "Corrosion for Science and Engineering", Longman (1996).

47 D.A. Jones, "Principles and Prevention of Corrosion", 2nd Edition, Prentice-Hall (1996).

48 N. Sato, "The stability of localised corrosion", *Corrosion Science,* 37(12), (1995), 1947-1967.

49 R. Francis, "Galvanic Corrosion – A Practical Guide for Engineers", NACE International, (2001).

50 Y. Naerheim and M.W. Kendig, "The influence of electrochemical potential on wear", *Wear,* 104 (1985), 139-150.

51 "Standard Guide for Determining Synergism between Wear and Corrosion", ASTM Standard G 119-93, (1993).

52 J.F. Douglas, J.M. Gasiorek and J.A. Swaffield, "Fluid Mechanics", 3rd Edition, Longman (1995).

53 V.V. Rao and O.Trass, "Mass transfer from a flat surface to an impinging turbulent jet" *Canadian J. of Chemical Engineering*, June 1964, 95-99.

54 D.A. Dawson and O. Trass, "Mass transfer in a turbulent radial wall jet" *Canadian J. of Chemical Engineering*, June 1966, 121-129.

55 J.L. Dawson, C.C. Shih, D.G. John and D.A. Eden, "Electrochemical testing of differential flow induced corrosion using jet impingement rigs", NACE Corrosion Paper 453, 1987.

56 K.D. Efird, E.J. Wright, J.A. Boros and T.G. Hailey, "Correlation of steel corrosion in pipe flow with jet impingement and rotating cylinder tests", *Corrosion*, 49(12), (1993), 992-1003.

57 A. Legat, "Influence of electrolyte movement on electrochemical noise", *Corrosion,* 56(11) (2000), 1086-1092.

58 H.G. Zelders, "La corrosion superficielle dans le circuit de lavage des charbonnages des mines de l'état Néerlandais", *Metaux et Corrosion,* 65 (1949), 65-76.

59 R.J.K. Wood and S.P. Hutton, "The synergistic effect of erosion and corrosion: trends in published results", *Wear* 140 (1990), 387-394.

60 E. Heitz, "Chemo-Mechanical effects of flow on corrosion", *Corrosion* 47 (2), (1991), 135-145.

61 A.W. Batchelor and G.W. Stachowiak, "Predicting synergism between corrosion and abrasive wear", *Wear,* 123 (1988), 281-291.

62 M. Matsumura, Y. Oka, H. Hiura and M. Yano, "The role of passivating film in preventing slurry erosion of austenitic stainless steel", *ISII International*, 31 (1991), 168-176.

63 P. Novak and A. Macenauer, "Erosion-corrosion of passive metals by solid particles", *Corrosion Science,* 35 (1-4), (1993), 635-640.

64 Y. Li, G.T. Burstein and I.M. Hutchings, "The influence of corrosion on the erosion of aluminium by aqueous silica slurries", *Wear,* 186-187, (1995), 515-522.

65 M.M. Stack, "Looking beyond the millennium: critical issues in the evaluation of materials performance for resistance to erosive wear in corrosive conditions", *Wear*, 235 (1999), 484-496.

66 K. Sasaki and G.T. Burstein, "Observation of a threshold impact energy required to cause passive film rupture during slurry erosion of stainless steel", *Philosophical Magazine Letters,* 80 (2000), 489-493.

67 M. Matsumura, Y.Oka and M. Yamawaki, "Slurry erosion and corrosion of commercially pure iron in a fountain jet testing facility – Mechanism of erosion-

corrosion under comparable intensity of erosion and corrosion", *Proc. 7th Int. Conf. on Erosion by Liquid and Solid Impact*, (Cambridge) Paper 40-1 (1987).

68 Z. Yue, P.Zhou, and J. Shi, "Wear of Materials", ASME, New York (1987).

69 M.M. Stack, S. Zhou and R.C. Newman, "Identification of transitions in erosion-corrosion regimes in aqueous environments", *Wear,* 186-187, (1995), 523-532.

70 A. Karimi and R.K. Schmidt, "Ripple formation in solid-liquid erosion", *Wear,* 156 (1992), 33-47.

71 Southampton Electrochemistry Group, "Instrumental Methods in Electrochemistry", Ellis Horwood (1985).

72 D.J.G. Ives and G.J. Janz, "Reference Electrodes", Academic Press, (1961).

73 E.M. Rosen and D.C. Silverman, "Corrosion prediction from polarisation scans using an artificial neural network integrated with an expert sstem", *Corrosion,* 48(9), (1992), 734-744.

74 R. Cottis and S. Turgoose, "Electrochemical Impedance and Noise", NACE International, (1999).

75 B.A. Boukamp, 'EQUIVCRT' User's Manual, University of Twente. Also, *Solid State Ionics,* 20 (1986), 31.

76 D.C. Silverman, "Rapid Corrosion Screening in poorly defined systems by Electrochemical Impedance Technique", *Corrosion",* 46(7), (1990), 589-598.

77 J.E.B. Randles, *Disc Faraday Soc.*, 1, (1947), 11.

78 W.P. Iverson, "Transient voltage changes produced in corroding metals and alloys", *J.Electrochem. Soc.* 115 (1968), 617-618.

79 G.C. Barker, "Noise connected with electrode processes", *J. Electroanalytical Chem.*, 21 (1969), 127-136.

80 M. Fleischmann and J.W. Oldfield, *J. Electroanalytical Chem.* 27 (1970), 207

81 V.A. Tyagai, *Electrokhimiya,* 10 (1974), 3.

82 G. Blanc, I. Epelboin, C. Gabrielli and M. Keddam, "Electrochemical Noise generated by anodic dissolution or diffusion processes", *J. Electroanalytical Chem.*, 75 (1977), 97-124.

83 D.E. Williams, C. Westcott and M. Fleischmann, *J. Electrochemal. Soc.*, 132 (8), (1985), Part I 1796-1804, Part II 1804-1811.

84 U. Bertocci, "Separation between deterministic response and random fluctuations by means of the cross-power spectrum in the study of Electrochemical Noise", *J. Electrochemical Soc.*, 128 (3), 1981, 520-523.

85 J. C. Uruchurtu and J.L. Dawson, "Noise Analysis of pure aluminium under different pitting conditions", *Corrosion,* 43 (1), 1987, 19-26.

86 K. Hladky, "Corrosion Monitoring", USP 4,575,678. (1983).

87 D.A. Eden, D.G. John and D.L. Dawson, "Corrosion Monitoring", USP 5,139,627 (1992).

88 R.A.Cottis and S. Turgoose, "Electrochemical Noise measurements – A theoretical basis", *Materials Science Forum*, 192-194 (1995), 663-672.

89 R.G. Kelly, M.E. Inman and J.L. Hudson, "Analysis of electrochemical noise for type 410 stainless steel in chloride solutions", in "Electrochemical Noise Measurements for Corrosion Applications" ASTM STP 1277, (1996), 101-113.

90 P.C. Pistorius, "Design Aspects of Electrochemical Noise Measurements: Electrode Size and Sampling Rate", *Corrosion,* 53(4), (1997), 273-283.

91 K. Hladky and J.L. Dawson, "The measurement of localised corrosion using Electrochemical Noise" *Corrosion Science,* 21(4), (1981), 317-322.

92 A. Neville, T. Hodgkiess and J.T. Dallas, "A study of the erosion-corrosion behaviour of engineering steels for marine pumping applications", *Wear,* 186-7 (1995), 495-507

93 P.C. Pistorius, "The effects of some fundamental aspects of the pitting corrosion of stainless steel on Electrochemical Noise measurements", in *"Electrochemical Noise Measurements for Corrosion applications",* ASTM STP 1277, Ed J.R. Kearns et al, 1996, 343-358.

94 A. Burkert, A. Heyn, J. Gollner, I. Garz, E. Vera and G.K. Wolf, "Examination of IBAD-aluminium-layers by electrochemical noise analysis", *Materialwissenschaft und werkstofftechnik,* 29(9), (1998), 496-505.

95 M. Danielson, "Modeling of certain electrode parameters on the electrochemical noise response", *Corrosion* 53(10), (1997) 770-777.

96 J.G. Proakis and D.G. Manolakis, "Digital Signal Processing", Prentice Hall International, (1996).

97 I.N. Bastos, F. Huet, R.P. Nogueira and P. Rousseau, "Influence of aliasing in Time and Frequency Electrochemical Noise measurements.", *J. Electrochem. Soc.* 147 (2), (2000), 671-677.

98 U. Bertocci, J. Frydman, C Gabrielli, F. Huet and M. Keddam, "Analysis of Electrochemical Noise by power spectral density applied to corrosion studies", *J. Electrochem. Soc.*, 145 (1998), 2780-2786.

99 J.R. Kearns, D.A. Eden, M.R. Yaffe, J.V. Fahey, D.L. Reichert and D.C Silverman, "ASTM Standardisation of Electrochemical Noise measurement", ASTM STP 1277, Ed J.R. Kearns et al, (1996), 446-470.

100 P.C. Searson and J.L. Dawson, "Analysis of Electrochemical Noise generated by corroding electrodes under open-circuit conditions", *J. Electrochem. Soc.*, 135 (1988), 1908-1915.

101 C. Gabrielli, F. Huet, M. Keddam and R. Oltra, *Corrosion,* 46(4), (1990), 266-278.

102 T.Schauer, H. Greisiger and L. Dulog, "Details on MEM analysis of electrochemical noise data and correlation with impedance measurements for organic coatings on metals", *Electrochimica Acta,* 43(16-17), (1998), 2423-2433.

103 H. Xiao and F. Mansfeld, *J. Electrochem. Soc.*, 141 (1994), 2332.

104 R.A. Cottis and C.A. Loto, "Electrochemical Noise generation during SCC of a high-strength carbon steel" *Corrosion,* 46 (1990), 12-19.

105 A. Legat and V. Dolecek, "Corrosion Monitoring System based on measurement and analysis of Electrochemical Noise" *Corrosion,* 51(4), (1995) 295-300.

106 H. Greisiger and T. Schauer, "On the interpretation of the electrochemical noise data for coatings", *Progress in Organic Coatings,* 39 (2000), 31-36.

107 D. Chen and S Qian, "Joint Time-Frequency Analysis, Methods and Applications", Prentice-Hall PTR, (1996).

108 A. Aballe, M. Bethencourt, F.J. Botana and M. Marcos, "Using wavelets transform in the analysis of electrochemical noise data", *Electrochimica Acta,* 44 (1999), 4805-4816.

109 A. Aballe, M. Bethencourt, F.J. Botana and M. Marcos, "Wavelet transform based analysis for electrochemical noise", *Electrochemistry Communications,* 1 (1999), 266-270.

110 Ding Hong-bo, Pan Zhong-xiao, Yu Xing-zeng, Zheng Fu-yang and Renato Seeber, "The preliminary study for the interpretation of Electrochemical Noise with continuous wavelet transform", *The Journal of Corrosion Science and Engineering,* Volume 1, Paper 10, review version at http://www.cp.umist.ac.uk/JCSE, submitted 24/01/99.

111 X.D. Dai, R.L. Motard, B. Joseph and D.C. Silverman, "Corrosion process monitoring using wavelet analysis", *Ind. Eng. Chem. Res.* 39 (2000), 1256-1263.

112 K.Darowicki and A. Zielinski, "Joint time-frequency analysis of electrochemical noise", *J. Electroanalytical Chem.* 504, (2001), 201-207.

113 A. Aballe, M. Bethencourt, F.J. Botana, M. Marcos and J.M. Sanchez-Amaya, "Use of wavelets to study electrochemical noise transients", *Electrochimica Acta,* 46 (2001), 2353-2361.

114 Z. Dong, X. Guo, J Zheng and L. Xu, "Calculation of noise resistance by use of the discrete wavelets transform", *Electrochem. Comms,* 2 (2001), 561-565.

115 A. Aballe, M. Bethencourt, F.J Botana, M. Marcos and R.M. Osuna, "Electrochemical Noise applied to the study of the inhibition effect of $CeCl_3$ on the corrosion behaviour of Al-Mg alloy AA5083 in seawater", *Electrochimica Acta,* 47 (2002), 1415-1422.

116 J. Smulko, K. Darowicki and A. Zielinski "Detection of random transients caused by pitting corrosion", *Electrochimica Acta* 47 (2002), 1297-1303.

117 S. Mallat, "A Wavelet Guide to Signal Processing", 2nd Edition, Academic Press, (1999).

118 MATLAB Wavelet Toolbox Manual, Version 2, The Mathworks, (2000).

119 G. Strang and T. Nguyen, "Wavelets and filter banks", Wellesley-Cambridge Press, (1996).

120 N. Huang, Z. Shen and H.H. Liu, "The Empirical Mode Decomposition and the Hilbert Spectrum for non-linear and non-stationary time series analysis", *Proc. Roy. Soc. London A,* 454 (1998), 903-995.

121 J.Goellner, A. Burkert, A. Heyn and J. Hickling, "Using electrochemical noise to detect corrosion: Evaluation of a round-robin experiment." *Corrosion,* 55(5), (1999), 476-492.

122 B.K. Prasad, O.P. Modi, A.K. Jha and A.K. Patwardhan, "Effects of some material and experimental variables on the slurry wear characteristics of zinc-aluminium alloys", *J. Materials Eng. And Performance* 10(1), (2001), 75-80.

123 B.W. Madsen, "Measurement of erosion-corrosion synergism with a slurry wear test apparatus", *Wear,* 123 (1988), 127-142.

124 J.B. Zu, I.M.Hutchings and G.T. Burstein, "Design of a slurry erosion test rig", *Wear,* 140 (1990), 331-344.

125 Y. Puget, "The performance of cost-effective coatings in aggressive saline environments", NACE Corrosion 98, Paper 688, (1998).

126 J. Tuzson, "Laboratory slurry erosion tests and pump wear calculations", *ASME J. Fluids Eng.* 106 (1984), 135-140.

127 Y. Xie, HMcI Clark and H.M. Hawthorne, "Modelling slurry particle dynamics in the Coriolis tester", *Wear,* 225-229, (1999), 405-416.

128 H. McI. Clark, J. Tuzson and K.K. Wong, "Measurements of specific energies for erosive wear using a Coriolis tester", *Wear,* 241 (2000), 1-9.

129 C.H. Pitt and Y.M. Chang, "Electrochemical determination of erosive wear of high carbon steel grinding balls", *Minerals and Metallurgical Processing,* 2(3) (1985), 166-173.

130 Y. Li, G.T. Burstein and I.M. Hutchings, "Influence of environmental composition and electrochemical potential on the slurry erosion-corrosion of aluminium", *Wear,* 181-183 (1995), 70-79.

131 "Corrosion tests of flame-sprayed coated steel, 19 year Report", American Welding Society, Miami, Florida, USA, (1974).

132 US Army Corps of Engineers, "Thermal Spraying: New Construction and Maintenance", Manual No 1110-2-3401, (1999), posted at www.usace.army.mil/inet/usace-docs/eng-manuals/em1110-2-3401/bmdoc.pdf

133 US Military standard DOD-STD-2138, "Metal sprayed coated systems for corrosion protection on board naval ships" (1981).

134 A.R. Parks, "Aluminium sprayed coatings on board US Navy ships – A ten year overview", (1997), posted at www.intmetl.com/us_navy.htm

135 T. Race, V. Hock and A. Beitelman, "Performance of selected metalised coatings and sealers on lock and dam facilities", (1997), posted at www.intmetl.com/lock_and_dam.htm

136 US Specification Mil-A-18001H, or, equivalently, ASTM Standard B418 Type 1.

137 G.D. Bengough and R. May, "Seventh Report to the Research Committee of the Institute of Metals: Part II The Corrosion of Zinc", *J. Inst. Metals,* 32 (1924), 143-148.

138 P.T. Gilbert and F.L. LaQue, "Jet impingement tests", *J. Electrochem. Soc.,* 101(9), (1954), 448-455.

139 F.L. LaQue, "Marine Corrosion: Causes and Prevention", John Wiley, (1975).

140 L. Diaz-Ballote and L.F. Garfias-Mesias, "Electrochemical Noise analysis of galvanised steel immersed in saturated $Ca(OH)_2$ solutions", NACE Corrosion 1998 Paper 373.

141 A.J. Bryant and R.A.P. Fielding, "Aluminium at sea", *Light Metal Age,* 59 (2001), 48-65.

142 A. Venugopal, R.D. Angal and V.S. Raja, "Electrochemical evaluation of steps in the anodic dissolution of Al-Zn-In anode in 3.5% NaCl solution", *Bulletin of Electrochemistry* 12(1-2), (1996) 93-96.

143 W.H. Thomason, "Cathodic Protection of submerged steel with thermal sprayed aluminium coatings", *Materials Performance,* March 1985, 20-28.

144 K.P. Fischer, W.H. Thomason, T. Rosbrook and J. Murali, "Performance history of thermal sprayed aluminium coatings in offshore service", *Materials Performance,* April 1995, 27-35.

145 K. Niemi, P. Sorsa, P. Vuoristo and T. Mantyla, "Thermally sprayed alumina coatings with strongly improved wear and corrosion resistance", *Proc. 7th National Thermal Spray Conf., Boston, Mass,* (1994) 533-536.

146 J.B. Zu, G.T. Burstein and I.M. Hutchings, "A comparative study of the slurry erosion and free-fall particle erosion of aluminium", *Wear,* 149 (1991), 73-84.

147 Y. Li, G. T. Burstein and I.M. Hutchings, "The influence of corrosion on the erosion of aluminium by aqueous silica slurries", *Wear,* 186-187, (1995), 515-522.

148 J. Postlethwaite, E.B. Tinker and M.W. Hawrylak, "Erosion–corrosion in slurry pipelines, *Corrosion,* 30 (8), (1974) 285-290.

149 J. Postlethwaite, "Effect of chromate inhibitor on the mechanical and electrochemical components of erosion-corrosion in aqueous slurries of sand", *Corrosion,* 37(1), (1981) 1-5.

150 T. Hagyard and M.J. Prior, "Potential of aluminium in aqueous chloride solutions: Part 2.", *Trans. Faraday Soc.,* 57 (1961), 2295-2298.

151 T. Hagyard and J.R. Williams, "Potential of aluminium in aqueous chloride solutions: Part 1.", *Trans. Faraday Soc.*, 57 (1961), 2288-2294.

152 S.T. Pride, J.R. Scully and J.L. Hudson, "Metastable Pitting of aluminium and criteria for the transition to stable pit growth", *J. Electrochem. Soc.*141(11), 3028-3040.

153 Z. Szklarska-Smialowska, "Pitting corrosion of aluminium", *Corrosion Science*, 41 (1999), 1743-1767.

154 Z. Szklarska-Smialowska, "Pitting Corrosion of Metals", NACE 1986.

155 J.R. Galvele, "Transport processes and the mechanism of pitting of metals", *J. Electrochem. Soc.* 123(4), (1976), 464-474.

156 D.W. Buzza and R.C. Alkire, "Growth of corrosion pits on pure aluminium in 1M NaCl", *J. Electrochem. Soc.*, 142 (4), (1995), 1104-1111.

157 R. Oltra, G.M. Indrianjafy and R. Roberge, "Effect of transient electrical coupling phenomena on the initiation of pits by a pulsed laser.", *J. Electrochemical. Soc.* 140 (2), (1993), 343-347.

158 H.S. Isaacs and A.J. Davenport, "The influence of surface capacitance on the measurements of localised corrosion transients", *J. Electrochem. Soc.* 137 (7), (1990), 2196-2198.

159 F. Mansfeld, C. Chen, C.B. Breslin and D. Dull, "Sealing of anodised aluminium alloys with rare earth metal solutions", *J. Electrochem. Soc.* 145 (1998), 2792-2798.

160 F. Mansfeld, "Use of rare earth metal solutions for corrosion protection of aluminium alloys and mild steel", *Russian J. of Electrochemistry,* 36 (2000), 1063-1071.

161 Zollner Pistons, "Hypereutectic Aluminium: a piston material for modern high specific output gasoline engines", (1998), posted at http://www.zpistons.com/Resources/Tech_papers/871994.

162 S.C. Lim, M. Gupta, Y.F. Leng, and E.J. Lavernia, "Wear of a spray-deposited H.M. Hawthorne, B. Arsenault, J.P. Immarigeon, J. G. Legoux and V.R. Parameswaran, "Comparison of slurry and dry erosion behaviour of some HVOF thermal sprayed coatings", *Wear,* 225-229, (1999), 825-834.hypereutectic aluminium-silicon alloy", *J. Materials Processing Technology* 63 (1997) 865-870.

163 S. Anand, T.S. Srivatsan, Yue Wu and E.J. Lavernia, "Processing, microstructure and fracture behaviour of a spray-atomised and deposited aluminium-silicon alloy.", *J. Materials Science* 32 (1997) 2835-2848.

164 S.K. Hovis, J. Talia and R.O. Scattergood, "Erosion mechanisms in aluminium and Al-Si alloys", *Wear,* 107 (1986), 175-181.

165 G. Meyer-Rodenbeck, T. Hurd and A. Ball, "On the abrasive-corrosive wear of aluminium alloys", *Wear,* 154 (1992), 305-317.

166 A.K. Bhattamishra, I. Chattoraj, D.K. Basu and P.K. De, "Study on the influence of the Si/Fe ratio on the corrosion behaviour of come Al-Fe-Si alloys", *Z. MetallKd,* 91, (2000), 393-396.

167 S. Turenne, D. Simard and M. Fiset, "Influence on structural parameters on the slurry erosion resistance of squeeze-cast metal-matrix composites", *Wear,* 149 (1991), 187-197.

168 S. Turenne, Y. Chatigny, D. Simard, S. Caron and J. Masounave, "The effect of abrasive particle size on the slurry erosion of particulate reinforced aluminium alloy", *Wear,* 141 (1990), 147-158.

169 J.A. Bester and A. Ball, "The performance of aluminium alloys and particulate reinforced aluminium metal matrix composites in erosive-corrosive slurry environments", *Wear,* 162-164, (1993), 57-63.

170 C. Monticelli, F. Zucchi, F. Bonollo, G. Brunoro, A Frignani and G. Trabanelli, "Application of electrochemical noise analysis to study the corrosion behaviour of aluminium composites", *J. Electrochemical Soc.*, 142 (2), (1995), 405-410.

171 C. Monticelli, F. Zucchi, G. Brunoro, A Frignani and G. Trabanelli, "Corrosion and corrosion inhibition of alumina particulate/aluminium alloys metal matrix composites in neutral chloride solutions", *J. Applied Electrochemistry,* 27 (1997) 325-334.

172 Z. Ahmad and B.J.A. Aleem, "Degradation of aluminium metal matrix composites in salt water and its control", *Materials and Design,* 23 (2002), 173-180.

173 T. Zhang and D.Y. Li, "Improvement in the resistance of aluminium with yttria particles to sliding wear in air and in a corrosive medium", *Wear,* 251 (2001), 1250-1256.

174 H. Mulki and T. Mizuno, "Contact mechanics of zinc coated steel sheets", *Wear,* 199 (1996), 260-267.

175 Galvanizers Association, "The Engineer's and Architect's guide to hot-dip galvanizing", Undated.

176 R.J.K. Wood, "The sand erosion performance of coatings", *Materials and Design,* 20 (1999), 179-191.

177 A.A. Townsend, "Turbulence", Chapter 10 in V. Streeter, "Handbook of Fluid Dynamics", McGraw-Hill, 1961.

178 H.M. Hawthorne, B. Arsenault, J.P. Immarigeon, J. G. Legoux and V.R. Parameswaran, "Comparison of slurry and dry erosion behaviour of some HVOF thermal sprayed coatings", *Wear,* 225-229, (1999), 825-834.

179 M.M. Jung, "Assessment of curved, rotationally symmetric surfaces in three dimensions", PhD Thesis, University of Southampton (1999).

180 Gamry Instruments Inc., "CMS 100 Electrochemical Measurement System, Hardware Operator's Manual, v3.01" (1998).

181 A. Krebs, Gamry Instruments, Inc., Personal communication, 16/02/00.

182 E. Oliver, Gamry Instruments, Inc., Personal communication, 14/07/99.

183 J.F. Chen and W.F. Bogaerts, "The physical meaning of noise resistance", *Corrosion Science,* 37 (11), (1995), 1839-1842.

184 J. Barson, National Instruments UK, Personal communication, 10/09/99.

185 The Mathworks, MATLAB Signal Processing Toolbox User's Guide, Version 5, revised 1998.

186 W.H. Press, S.A. Teukolsky, W.T. Vetterling and B.P. Flannery, "Numerical Recipes in C, The Art of Scientific Computing", Cambridge University Press, 1992.

187 R. Brown (BAe Systems), "High pressure air cylinders: reducing through life costs", unpublished presentation to Marine Corrosion Club, 5/7/00.

188 E. Leithold, North Carolina State University, posted at http://www.eos.ncsu.edu/eos/info/mea/mea411_info/VISCOUS (2001).

189 "Perry's Chemical Engineer's Handbook", 6th edition, McGraw-Hill, Eds R.H. Perry and D.W. Green, 1984.

190 M.G. Bulmer, "Principles of Statistics", Oliver and Boyd, (1965).

191 A. Haar, "Zur Theorie der orthogonalen functionensysteme", *Math. Annalen*, 68 (1910), 331-371.